Tidal Dynamics of Laterally Heterogeneous Planetary Bodies

Thesis by
Alexander C. Berne

In Partial Fulfillment of the Requirements for the
Degree of
Doctor of Philosophy

CALIFORNIA INSTITUTE OF TECHNOLOGY
Pasadena, California

2026
Defended March 31, 2025

Alexander C. Berne
ORCID: 0000-0001-7857-8513

To Anna

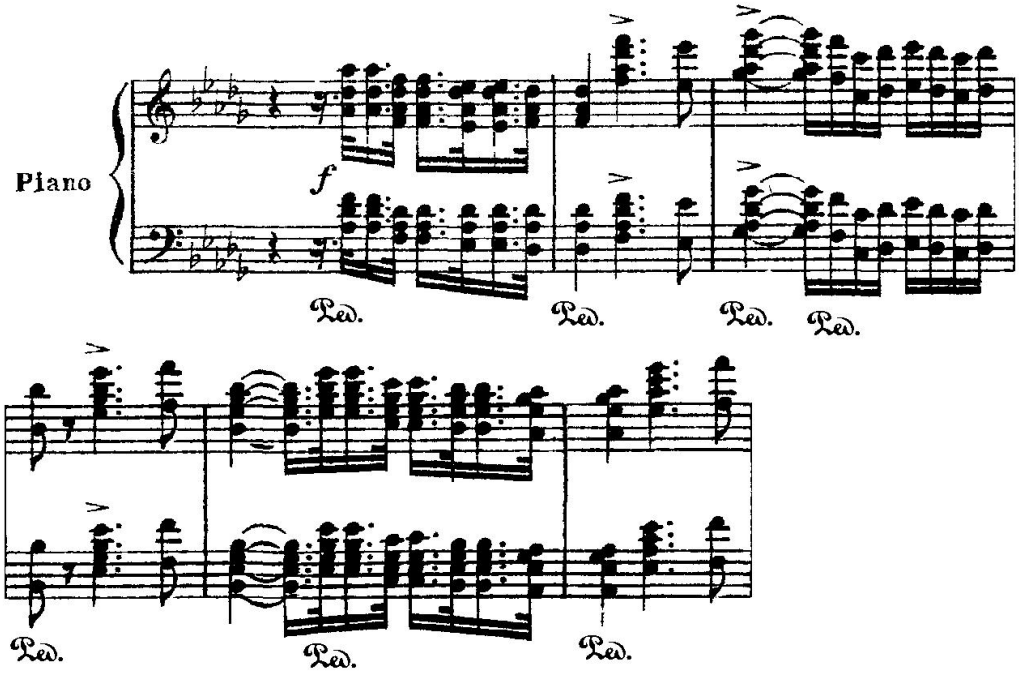

Tchaikovsky's Piano Concerto No. 1

ACKNOWLEDGEMENTS

Much like a glacier, my Ph.D. has undergone periods of rapid acceleration and slow, grinding forward motion over the last five years. Also considering COVID-19, massive fires, torrential rain, then even more massive fires, it goes without saying that completion of my degree would not have been possible without the support of many, many wonderful people.

First and foremost, I would like to thank Mark Simons, who, from the very beginning of my time at Caltech, encouraged my various (sometimes wandering) projects and goals. Mark has taught me not what to think, but *how* to think, in more ways than can be described here. Just as one small example, I will never be able to visually inspect a linear scale that plots density, shear modulus, or layer thickness without some amount of internal angst. I hope that my future work in the field carries forward his tendency to question first-order assumptions built into every problem.

I am also deeply grateful to Joann Stock, who sparked my ongoing interest in the tectonic history of California. To Dave Stevenson, who has always entertained—and even encouraged—my (sometimes very speculative) investigations of deep planetary interiors. To Mike Gurnis, who inspired my fascination with geodynamics early on and with whom I've had many very thought provoking coffee hour discussions. And to Jennifer Jackson, who has kept me grounded, reminding me that theoretical models must, in the end, be reconciled with experimental reality.

I would like to specifically thank James Keane at JPL who has heard me complain about true polar wander papers on many different occasions. I am grateful not only for your illustrations, but also your unique insight, guidance, and passion for understanding Solar System phenomena. I will miss our weekly meetings. I'd also like to thank Ryan Park, who has provided an engineer's perspective on my research (and dealt with my repeated requests to explain to me what a 'spacecraft arc' is exactly). I would also like to thank many others at JPL, including Erin Leonard, Steve Vance (and his lab members), Ceri Nunn, Ashley Schoenfeld, and Julie Castillo-Rogez. My work would also not be possible without the many very dedicated collaborators on my research projects, including Marc Rovira-Navarro, Isamu Matsuyama, Francis

Nimmo, Joseph Spitale, Douglas Hemingway, and many others.

I want to thank the very hard working PhD students and postdocs at Caltech. Among these I'd like to specifically acknowledge office mates, Ben and Cijin, who have dealt with my repeated incursions into their thinking space at odd hours of the day (and sometimes night). To Tobie, the student with whom I probably had the most in-depth conversations through my time as a Ph.D. student (I look forward to seeing you in Germany). To Yida Li, a great conversationalist on the subject of subduction initiation. To Yuan-Kai Liu, who I am amazed has managed to pursue a Ph.D. *and* raise two kids. To Rishav Mallick, to whom I still have not managed to satisfactorily explain why scientists use spherical harmonics to describe 6-km resolution lunar gravity fields. To Amir, who has chatted with me many times regarding the politics of the Planetary Science community. To Leonid Periaslov, Anna Gulcher, Tina Seeger, Jimmy Atterholt, Jiaqi Fang, Jack Wildling, Ettore Biondi, Adriana Pina, Maria Camarca, Benjamin Idini, Valeria Villa, Chenxi Kong, Xiaozhuo Wei (Wǒ jiào línxiǎodōng), and many others.

I would like to acknowledge the absolutely fantastic Seismolab (and GPS) administrative staff, who are the real muscle behind the department. To Donna Mirales, who has dealt with all sorts of requests on my behalf to a combination of NASA, GMG, AGU, LPSC, Caltech, and so on. To Rosemary, who was extremely helpful in dealing with my (often last minute) requests to submit grant applications. To Kim Baker-Gatchalian, Monica Nolasco, Scott Dungan, Julie Lee, and many others, thank you for supporting me, I will miss you all.

To Sihan Chen, though it's been many years since we have regularly seen each other, you have been a great best friend.

My family is my rock. My parents John and Jennifer have seen me progress from a unkempt high school student to a marginally less unkempt adult at the end of my doctorate. I am very thankful to have you both by my side. To Starr, who encouraged me to continue my doctorate (despite my complaints). To Patrick, who introduced me to Kerbal Space Program, as well as all of my siblings. To Katie and Craig (thank you for your car rides to Mt Wilson and elsewhere), Susie and George (and our memories of your house in Ventura). To Steven Brindle, who served as an

early inspiration to pursue a doctorate. I'd like to thank my parents-in-law— Cathy and Uwe, for your support through the years. And of course, I want to thank my grandparents Cynthia and Tom, who have (going back many years) stimulated my love for California and interest in science.

To Anna. Thank you for your support through the years. My life changed the moment when, in the middle of the COVID lockdowns, I said: *I think am going to California for 5 years* and you said *I think you mean,* ***we're*** *going to California for 5 years*. It has been great to have you along for the ride.

ABSTRACT

Planetary bodies experience deformation in response to tidal forces from external gravitating objects. Changes to planetary gravity fields produced by this forcing depend on internal rheological structure. For example, a spherically symmetric body's response to tides depends on the presence, thicknesses, and effective shear moduli of internal layers (e.g., the core, an ocean) and follows the spatial pattern of driving gravitational potentials. However, bodies that exhibit substantial deviation from spherical symmetry can exhibit a more complicated response to forcing that includes power both at short (i.e., regional-scale) and long (i.e., global-scale) wavelengths. In this thesis, we explore the impact of lateral heterogeneities in internal rheological structure on the tidal responses of Enceladus, the second major moon of Saturn, and Earth's Moon.

We begin by exploring the impact of faults and lateral variations in ice shell thickness on the long-wavelength gravitational response of Enceladus (Chapter 2). Using finite element models of Enceladus' crust, we demonstrate substantial deviation between the longest-wavelength components of response to tidal forcing (i.e., the diurnal degree-2 Love numbers) and those expected for a spherically symmetric model of Enceladus. We further show that structural heterogeneities predominantly produce deformation over spatial scales similar to the size of these features. Based on this finding, we develop a methodology to precisely characterize regional variations in crustal thickness using local observations of surface strain at Enceladus (Chapter 3). We demonstrate that this strain can be readily inferred using measurements of the motion of the surface over the tidal cycle (e.g., via interferometric synthetic aperture radar or InSAR). We then adapt our finite element models to explore relationships between slip on fault structures over Enceladus' south polar region (i.e., the Tiger Stripes) and geological activity observed for the body (Chapter 4). We find a close correspondence between the double-peaked and asymmetric timing of strike-slip motion and observed diurnal variations in the brightness of a large plume emanating from Encealdus' South Pole. Based on this finding, we suggest that rifts along the Tiger Stripes experience periodic localized extension to modulate cryovolcanic activity. Finally, we use observations of the spherical harmonic degree-3 variability in the lunar gravity field to infer the presence of a 2-3% internal hemispheric, near-to-far- side variation in shear modulus of the Moon's mantle (Chapter 5). We demonstrate that a 100-200K hemispheric difference in mantle temperature can

explain this inferred shear modulus structure, and suggest that internal asymmetries may be a remnant of processes which formed surface mare basalts ~4 Gya. Our work demonstrates future potential for the use of tidal tomography to characterize the deep interior structure and geodynamics of planetary bodies throughout the solar system.

PUBLISHED CONTENT AND CONTRIBUTIONS

Berne, A., M. Simons, J. T. Keane, and R. S. Park (2023a). "Inferring the Mean Thickness of the Outer Ice Shell of Enceladus From Diurnal Crustal Deformation". In: *Journal of Geophysical Research: Planets* 128 (6). https://doi.org/10.1029/2022JE007712
A.B. led and concieved the project, ran numerical analyses, and wrote the manuscript.

Berne, A., M. Simons, J. T. Keane, and R. S. Park (2023b). "Using Tidally-Driven Elastic Strains to Infer Regional Variations in Crustal Thickness at Enceladus". In: *Geophysical Research Letters* 50 (22). https://doi.org/10.1029/2023GL106656
A.B. led the project, participated in its conception, ran numerical analyses, and wrote the manuscript.

Park, R. S., A. Berne, A. S. Konopliv, J. T. Keane, I. Matsuyama, F. Nimmo, M. Rovira-Navarro, M. P. Panning, M. Simons, D. J. Stevenson, and R. C. Weber (2025). "Thermal Asymmetry in the Moon's Mantle Inferred from Monthly Tidal Response". In: *Nature* 641.8065. https://doi.org/10.1038/s41586-025-08949-5
Though not the first author, A.B. led and concieved the project, carried out analyses, and wrote the introduction and latter two-thirds of the manuscript (included in this thesis)., pp. 1188–1192.

Berne, A., M. Simons, J. T. Keane, E. S. Leonard, and R. S. Park (2024). "Jet activity on Enceladus linked to tidally driven strike-slip motion along tiger stripes". In: *Nature Geoscience* 17.5. https://doi.org/10.1038/s41561-024-01418-0
A.B. led the project, participated in its conception, ran numerical analyses, and wrote the manuscript.

This thesis focuses on the publications presented above.

PUBLISHED CONTENT AND CONTRIBUTIONS

Bagheri, A., M. Simons, S. Vance, R. Park, A. Berne, and M. Melwani-Daswani (2025). "Exploring the interior structure of Enceladus and its relationship to sustained habitability". In: *The Planetary Science Journal (Under Review)*.
Alex Berne used 3D finite element models to compute degree-2 Love numbers for Enceladus across a range of interior structures (e.g., core sizes, ice shell thicknesses).

Park, R. S., J. E. Riedel, E. Brandon, N. E. Harvey, S. Manafi, M. C. Smart, Z. J. Towfic, A. Berne, W. I. Bertiger, J. T. Keane, A. S. Konopliv, N. Mastrodemos, M. Simons, S. D. Vance, and A. T. Vaughan (2025). "Gravity Imaging Radio Observer (GIRO) for Planetary Science and Mission Opportunities". In: *The Planetary Science Journal* 6.5. https://doi.org/10.3847/PSJ/adceea
A.B. carried out forward calculations of the amplitude of the time variable gravity field up to spherical harmonic degree 20 at Enceladus (for comparison to the measurement sensitivity of the GIRO probes)., p. 127.

Rovira-Navarro, M., I. Matsuyama, D. Dirx, A. Berne, D. Calliess, and S. Foyelle (2025). "Prospects of Using Tidal Tomography to Constrain Ganymede's Interior". In: *Geophysical Research Letters* 52.11. https://doi.org/10.1029/2025GL114708
A.B. performed an analysis of the sensitivity of potential spacecraft measurements of Ganymede's gravity field to 3D structure at depth, e2025GL114708.

Spitale, J., M. Tigges, A. Berne, A. Rhoden, T. Hurford, and K. Webster (2025). "Curtain-Based Maps of Eruptive Activity in Enceladus's South-Polar Terrain at 15 Cassini Epochs". In: *The Planetary Science Journal* 6.3. https://doi.org/10.3847/PSJ/adb7d7
A.B. carried out a quantitative analysis comparing outputs from a finite element model of Enceladus' tiger stripes and observations of jet activity., p. 67.

Rovira-Navarro, M., I. Matsuyama, and A. Berne (May 2024). "A Spectral Method to Compute the Tides of Laterally Heterogeneous Bodies". In: *Planetary Science Journal* 5 (5). https://doi.org/10.3847/PSJ/ad381f
A.B. carried out benchmarks of results from the semi-analytic model in this work using finite element models of Enceladus.

The references above represent additional publications that have resulted from work presented in this thesis.

TABLE OF CONTENTS

LIST OF ILLUSTRATIONS

Number *Page*

LIST OF TABLES

Chapter 1

INTRODUCTION

1.1 Motivation

The interior of planetary bodies is perhaps the most fundamental structural component of these systems, yet it is also challenging to observe directly. On Earth, first-order constraints on the deep interior (e.g., a separate core, mantle, and crust) were established through seismological observations in the late 19th and early 20th centuries (Gutenberg and Richter, 1938; Markušić and Ivančić, 2020). Modern advancements in seismic data collection and analysis have since revealed details within these layers, including the structure of subducting slabs and the complexities of the core-mantle boundary (e.g., Romanowicz and Dziewonski, 2009). However, aside from a few notable exceptions (e.g., the InSight mission to Mars (Banerdt et al., 2020) and Apollo-era seismology on the Moon (Nunn et al., 2020)), current studies of extraterrestrial planetary interiors are largely confined to describing first-order structure due to the logistical challenge of deploying seismometers in outer space. As a result, remote sensing techniques (e.g., gravity field observations) remain the primary tool for probing the structure and evolution of these bodies.

1.2 Static Gravity

Gravity fields are sensitive to the internal distribution of mass for planetary bodies. We can correspondingly generalize these fields as a volume integral over a spatially variable internal density (Jekeli, 2007):

$$W(\mathbf{r}) = \int_v \frac{G}{||\mathbf{r} - \mathbf{r}'||} \rho(\mathbf{r}') dv(\mathbf{r}'), \tag{1.1}$$

where $W(\mathbf{r})$ is the gravitational potential at position $\mathbf{r}$, and $\mathbf{r}'$, $\rho(\mathbf{r}')$, and v represent the position vector, density distribution, and volume of the gravitating body, respectively. G denotes the universal gravitational constant. At very low spatial resolutions (i.e., long-wavelengths), it is often more convenient to express Equation 1.1 as an expansion into orthonormal spherical harmonic basis functions which describe perturbations to the gravitational potential relative to a spherical reference figure of mass M (i.e., the total mass of the body) (Kaula, 1963):

$$W(r,\theta,\phi) = \frac{GM}{r}\left(1 + \sum_{l=2}^{\infty}\left(\frac{R}{r}\right)^{l}\sum_{m=0}^{l} P_{lm}(\sin\theta)\left[C_{lm}\cos m\phi + S_{lm}\sin m\phi\right]\right), \tag{1.2}$$

where P_{lm} are associated Legendre polynomials evaluated at degree l and order m; C_{lm} and S_{lm} are unnormalized and dimensionless coefficients; R is the mean radius of the gravitating body; and r, θ, and ϕ are spherical coordinates (radial distance, latitude, and longitude relative to the system's center of mass) for observations that are external to the gravitating body. Note that the spatial wavelength λ for a given harmonic is related to l according to $\lambda \approx 2\pi R/l$.

Inferring separate internal mass layers using Equation 1.2 suffers from the non-unique trade-off of the impact of layer thickness, shape, and density on coefficients C_{lm} and S_{lm}. To resolve this ambiguity, hydrostatic conditions (i.e., bodies are fully relaxed into their equilibrium shape) are often assumed *a priori*. For example, hydrostatic satellites that synchronously orbit their parent body should exhibit a characteristic ratio between zonal and positive sectoral components of their $l = 2$ gravity field (i.e., C_{20} and C_{22}; Murray and Dermott, 2000):

$$\frac{C_{20}}{C_{22}} \approx -10/3. \tag{1.3}$$

If Equation 1.3 is satisfied, a satellite's moment of inertia factor (MOI) can be determined via the Darwin-Radau relation (Darwin, 1899; Murray and Dermott, 2000; Hemingway et al., 2018):

$$\mathrm{MOI} = \frac{2}{3}\left(1 - \frac{4}{5}\sqrt{\frac{1 - qC_{22}}{1 + 4qC_{22}}}\right) - \frac{20}{9}C_{22}, \tag{1.4}$$

where $q = \omega^2 R/g$ is the ratio of outward centrifugal acceleration due to rotation (i.e., of angular velocity ω) and inward surface gravitational acceleration g. MOI has a theoretical maximum value of 0.4 for homogeneous bodies. As such, an observed MOI < 0.4 hints at internal differentiation (e.g., the presence of a core) (Iess et al., 2014).

Despite its elegance, Equation 1.4 often fails for small bodies since hydrostatic equilibrium is the exception, rather than the rule, for these systems. For example, the gravity field of Saturn's moon Enceladus (R = 252 km) is moderately non-hydrostatic ($C_{20}/C_{22} = -3.61$; Park et al., 2024) and a prominent equatorial bulge on the Earth's Moon (R = 1737 km) results in an extreme departure of its gravity field from hydrostatisticity ($C_{20}/C_{22} = -2.62$; Zuber et al., 2013; Qin et al., 2018).

1.3 Time-Variable Gravity

Time-varying components of gravity fields can provide additional constraints on the structure of planetary interiors. The amplitude of these variations are typically a few orders of magnitude smaller than the static gravity field and can arise from periodic tidal interactions with external (i.e., disturbing) bodies (Kaula, 1969). Time-varying gravity fields can therefore be modeled as perturbations to coefficients C_{lm} and S_{lm} in Equation 1.2 (i.e., ΔC_{lm} and ΔS_{lm}) using parameters known as Love numbers k_{lm} (Love, 1909; Konopliv et al., 2013):

$$\Delta C_{lm} - i\Delta S_{lm} = V_{lm} k_{lm}. \tag{1.5}$$

V_{lm} are complex terms that describe the forcing potential:

$$V_{lm} = \frac{1}{2l+1} \sum_j \frac{GM_j}{GM} \frac{R^{l+1}}{r_j^{l+1}} P_{lm}(\sin\theta_j) e^{-im\phi_j}, \tag{1.6}$$

where θ_j, ϕ_j, and r_j are the latitude, longitude, and distance of external body j relative to the satellite's center of mass. Note that Equation 1.6 implies the presence of gravity fields at all l and m. However, the most substantial components of the tidal potential (i.e., arising from the obliquity/eccentricity of planetary orbits and their rotation) exist at $l = 2$ and rapidly diminish with increasing spherical harmonic degree according to $\sim R^{l-2}/r^{l-2}$. For the Earth-Moon tides, this relation implies V_{3m}/V_{2m} ~1/220 whereas for Saturn-Enceladus tides V_{3m}/V_{2m} ~1/944 (Zhong et al., 2012).

Unlike static gravity fields, time-variable gravity is sensitive to the mass *and* the rheological structure (e.g., the stiffness) of planetary bodies. The Love numbers of a theoretical body with uniform density are therefore analogous to its compliance: high k_{lm} indicate a structurally weak interior (and vice versa for small k_{lm}). This property makes k_{lm} particularly useful for detecting mechanically weak internal layers such as subsurface oceans. Note that, unlike k_{lm}, analogous measurements of the time-variable shape of planetary surfaces (i.e., shape Love numbers h_{lm}) are largely insensitive to the internal density of these systems (e.g., Ermakov et al., 2021).

Equation 1.5 assumes a one-to-one relationship between an applied gravity field and a response at a given l and m. However, bodies with substantial lateral heterogeneity in rheological structure will exhibit coupling between forcing at harmonics l', m' and

response for harmonics at different l, m (i.e., mode coupling; Dahlen and Tromp, 1998, Rovira-Navarro and Matsuyama, 2022). We can generalize Equation 1.5 to consider mode coupling effects by introducing 'effective Love numbers' $K^{l,m}_{l',m'}$ (also called Green's functions in Chapter 2):

$$\begin{aligned}\Delta C_{lm} - i\Delta S_{lm} = \sum_{l'=2}^{\infty}\sum_{m'=0}^{l'} \frac{1}{2l'+1}\sum_j \frac{GM_j}{GM}\frac{R^{l'+1}}{r_j^{l'+1}} P_{l'm'}(\sin\theta_j) \\ \times\Big[\Big(K^{l,m}_{l',m'}\cos(m'\phi_j) + K^{l,m}_{l',-m'}\sin(m'\phi_j)\Big) \\ - i\Big(K^{l,-m}_{l',m'}\cos(m'\phi_j) + K^{l,-m}_{l',-m'}\sin(m'\phi_j)\Big)\Big]. \end{aligned} \tag{1.7}$$

Traditional Love numbers k_{lm} in Equation 1.5 can generally be derived from $K^{l,m}_{l',m'}$ in Equation 1.7. This relationship is trivial for spherically symmetric bodies (i.e., $k_{lm} = K^{l,m}_{l,m}$). In contrast, a body with substantial near-to-far side asymmetries (e.g., an $l = 1, m = 1$ variation in internal shear modulus) subject to degree-2 tidal forcing will exhibit k_{30}, k_{31}, k_{32}, and k_{33} that depend on several 'off-diagonal' (i.e., $l', m' \neq l, m$) values of $K^{l,m}_{l',m'}$ (Zhong et al., 2012):

$$\begin{aligned} k_{30} &\approx K^{30}_{30} + \frac{V_{21}}{V_{30}}K^{30}_{21} \\ k_{31} &\approx K^{31}_{31} + \frac{V_{20}}{V_{31}}K^{31}_{20} + \frac{V_{22}}{V_{31}}K^{31}_{22} \\ k_{32} &\approx K^{32}_{32} + \frac{V_{21}}{V_{32}}K^{32}_{21} \\ k_{33} &\approx K^{33}_{33} + \frac{V_{22}}{V_{33}}K^{33}_{22}, \end{aligned} \tag{1.8}$$

where V_{lm} are derived from Equation 1.6. Note that Equation 1.8 describes deformation evaluated only at very long spatial wavelengths. By contrast, geologic faults (e.g., the Tiger Stripes at Enceladus) or lateral variations in crustal thickness tend to drive deformation in response to tidal forcing over much shorter spatial scales. It is therefore typically more convenient to describe deformation arising from these features using local parametrizations of displacement (e.g., surface strain rate; Berne et al., 2023b). Even so, deformation arising from faults or lateral variations in crustal thickness may bias the interpretations of long-wavelength time-varying gravity (e.g., k_{2m}) for inferring first-order structure (e.g., mean crustal thickness; Berne et al., 2023a).

1.4 Modeling Deformation for Laterally Heterogeneous Bodies

Methods to predict the response of a laterally heterogeneous body to tidal forcing require some special attention. The degree-2 tidal potentials in Equation 1.5 induce sufficient deformation to result in self-gravitation of deformed bodies. Accounting for these self-gravitational effects requires simultaneously solving, at a minimum, both the quasi-static equation of motion and Poisson's equation:

$$\nabla \cdot \boldsymbol{\sigma} = \rho \nabla (W + V), \tag{1.9}$$

$$\nabla^2 W = 4\pi G \rho, \tag{1.10}$$

where $\boldsymbol{\sigma}$ is the stress tensor, ρ is the spatially variable density, and V is the total gravitational potential arising from external (i.e., disturbing) bodies. Lateral heterogeneity in elastic structure enters Equations 1.9-1.10 through the constitutive relation:

$$\boldsymbol{\sigma} = \frac{1}{2}\mathbb{C} : \left(\nabla \mathbf{u} + (\nabla \mathbf{u})^T\right), \tag{1.11}$$

where $\mathbb{C}$ is the spatially variable fourth-order tensor for linear elasticity and $\boldsymbol{u}$ is the displacement field. For spherically symmetric structures, Equations 1.9-1.11 can be solved using semi-analytic methods (e.g., Wahr et al., 2006; Martens et al., 2019). However, predicting deformation for bodies with 3D structure typically requires numerical treatment due to the difficulty associated with generalizing solutions to Equations 1.9-1.11 for complicated geometries. Finite element models (FEMs) can approximate solutions to Equations 1.9-1.11 by discretizing domains into values over a set of mesh nodes. Numerical treatments also readily allow for modeling fault dynamics (e.g., friction) using so-called split nodes (i.e., duplicate node sets at overlapping positions) along crack interfaces (Melosh and Raefsky, 1981).

1.5 Thesis Overview

In this thesis, we will explore both challenges and opportunities for characterizing the internal structure and dynamics of bodies with lateral heterogeneities. We focus our attention on two natural planetary satellites: Enceladus and the Moon.

We begin by discussing the impact of lateral variations in elastic structure on Enceladus' diurnal degree-2 Love numbers, k_{2m} and h_{2m} (Chapter 2). k_{2m} and h_{2m} describe the longest wavelength response of the interior to tidal forcing and, for

Enceladus, are most sensitive to the characteristics (e.g., mean thickness) of the outer ice shell. Using a numerical finite element model of deformation arising from eccentricity tides at Enceladus, we demonstrate that lateral variations in crustal thickness and geologic faults can substantially impact k_{2m} and correspondingly bias inferences of mean crustal thickness derived from this parameter by up to 40%. We also show that crustal thinning over Enceladus' South Polar region preferentially impacts sectoral harmonics (i.e., k_{22} and h_{22}) over zonal harmonics (i.e., k_{20} and h_{20}), thereby enabling determination of the importance of lateral structure via quantification of Love number ratios k_{22}/k_{20} and h_{22}/h_{20}. Note that we consider only purely elastic bulk rheologies for planetary interiors throughout this thesis. However, viscous structure may induce temporal phase lags in Enceladus' degree-2 deformation relative to forcing at this wavelength. We discuss the possibility of measuring and interpreting this phase-lagged tidal signal in the conclusion (Chapter 6).

In Chapter 3, we examine the impact of regional-scale structure on surface strain at Enceladus. We find that this strain correlates with local variations in crustal thickness, prompting the development of a method to recover thickness from potential future observations of surface motion (e.g., via interferometric radar measurements or InSAR). Building on the finite element models described in Chapter 2, our recovery minimizes differences between strains from candidate crustal thickness models and that produced by synthetic 'true' crustal models. Using our approach, we demonstrate recovery of thickness for several fiducial models with ~ 2 km accuracy relative to true thickness values across the crust. Nonetheless, recoveries of crustal thickness become inaccurate at short wavelengths ($l \geq 12$) due to our approach's inability to account for the complicated impact of bending effects in Enceladus' ice shell at these scales.

In Chapter 4, we examine the dynamics of Enceladus' south polar (i.e., Tiger Stripe) faults. Enceladus has a large plume comprised of water-ice crystals that emanate from several jets distributed over these Tiger Stripes. Moreover, the brightness of Enceladus' plume varies periodically over the satellite's 32.9 hr orbit, suggesting a relationship between tidal forcing of the Tiger Stripes and geologic activity. Using an adapted version of our finite element models, we find that strike-slip motion along the Tiger Stripes closely tracks both the timing of plume brightness variations and spatial distribution of observed heat flow. Static friction also modulates periodic strike-slip motion resulting in an asymmetric and double-peaked timing structure

for this motion. We suggest that strike-slip motion may periodically open small rifts along the Tiger Stripes to regulate jet activity, similar to pull-apart zones along tectonic faults in terrestrial settings (e.g., the Salton Basin along the San Andreas Fault).

In Chapter 5, we use observations from the Gravity Recovery and Interior Laboratory (GRAIL) mission to constrain the structure and dynamics of the Moon's deep interior. GRAIL captured the time-variability of $l = 2$ and $l = 3$ components of the lunar gravity field (i.e., k_{2m} and k_{3m}). As discussed previously, lunar k_{3m} are sensitive to the presence of lateral heterogeneity in the mantle and are observed to be about ~70% higher than values expected for a spherically symmetric interior. Based on this finding, we infer the presence of an approximately 2-3% variation in the shear modulus across a hemispherical, $l = 1$, $m = 1$ (near-to-farside) pattern in the deep lunar interior. The lack of an associated long-wavelength anomaly in lunar density structure suggests that this degree-1 variation in stiffness represents a predominantly thermal asymmetry in the mantle. This asymmetry may be a remnant of processes that formed surface mare flood basalts around 4 Gya.

Chapters 2–4 of this thesis are published as articles in peer-reviewed journals and are fully reproduced here (including supplementary sections) with very minor alterations to ensure consistent formatting. As a result, the content of methods sections overlap substantially between these chapters, especially regarding the development of finite-element models and descriptions of time-variable gravity fields. Chapter 5 is currently under review (presented content has undergone one round of revisions) and we present only portions related to interior modeling (i.e., including a very brief discussion on the methodology for gravity field inversions used to derive k_{3m} from GRAIL measurements) in this thesis.

We finish with conclusions and suggestions for future directions.

References

Banerdt, W. B., S. E. Smrekar, D. Banfield, D. Giardini, M. Golombek, C. L. Johnson, P. Lognonné, A. Spiga, T. Spohn, C. Perrin, S. C. Stähler, D. Antonangeli, S. Asmar, C. Beghein, N. Bowles, E. Bozdag, P. Chi, U. Christensen, J. Clinton, G. S. Collins, I. Daubar, V. Dehant, M. Drilleau, M. Fillingim, W. Folkner, R. F. Garcia, J. Garvin, J. Grant, M. Grott, J. Grygorczuk, T. Hudson, J. C. Irving, G. Kargl, T. Kawamura, S. Kedar, S. King, B. Knapmeyer-Endrun, M. Knapmeyer, M. Lemmon, R. Lorenz, J. N. Maki, L. Margerin, S. M. McLennan, C. Michaut, D. Mimoun, A. Mittelholz, A. Mocquet, P. Morgan, N. T. Mueller, N. Murdoch,

S. Nagihara, C. Newman, F. Nimmo, M. Panning, W. T. Pike, A. C. Plesa, S. Rodriguez, J. A. Rodriguez-Manfredi, C. T. Russell, N. Schmerr, M. Siegler, S. Stanley, E. Stutzmann, N. Teanby, J. Tromp, M. van Driel, N. Warner, R. Weber, and M. Wieczorek (2020). *Initial results from the InSight mission on Mars*. DOI: 10.1038/s41561-020-0544-y.

Berne, A., M. Simons, J. Keane, and R. Park (2023b). "Using Tidally-Driven Elastic Strains to Infer Regional Variations in Crustal Thickness at Enceladus". In: *Geophysical Research Letters* 50 (22). DOI: 10.1029/2023GL106656.

Berne, A., M. Simons, J. Keane, and R. Park (2023a). "Inferring the Mean Thickness of the Outer Ice Shell of Enceladus from Diurnal Crustal Deformation". In: *Journal of Geophysical Research E: Planets* . DOI: 10.1029/2022JE007712.

Dahlen, F. A. and J. Tromp (1998). *Theoretical global seismology*. DOI: 10.1063/1.882788.

Darwin, G. H. (1899). "The theory of the Figure of the Earth carried to the second order of small quantities". In: *Monthly Notices of the Royal Astronomical Society* 60 (2). ISSN: 0035-8711. DOI: 10.1093/mnras/60.2.82.

Ermakov, A. I., R. S. Park, J. Roa, J. C. Castillo-Rogez, J. T. Keane, F. Nimmo, E. S. Kite, C. Sotin, T. J. W. Lazio, G. Steinbrügge, S. M. Howell, B. G. Bills, D. J. Hemingway, V. Viswanathan, G. Tobie, and V. Lainey (2021). "A Recipe for the Geophysical Exploration of Enceladus". In: *Planetary Science Journal* 2 (4). ISSN: 26323338. DOI: 10.3847/PSJ/ac06d2.

Gutenberg, B. and C. F. Richter (1938). "P' AND THE EARTH'S CORE." In: *Geophysical Journal International* 4. ISSN: 1365246X. DOI: 10.1111/j.1365-246X.1938.tb01761.x.

Hemingway, D., L. Iess, R. Tajeddine, and G. Tobie (2018). *The Interior of Enceladus*. University of Arizona Press. DOI: 10.2458/azu_uapress_9780816537075-ch004.

Iess, L., D. J. Stevenson, M. Parisi, D. Hemingway, R. A. Jacobson, J. I. Lunine, and P. Tortora (2014). "The gravity field and interior structure of Enceladus". In: *Science* 344.6179. ISSN: 10959203. DOI: 10.1126/science.1250551.

Jekeli, C. (2007). "3.02 - Potential Theory and Static Gravity Field of the Earth". In: *Treatise on Geophysics: Volume 1-10*. Vol. 1-10. DOI: 10.1016/B978-044452748-6.00054-7.

Kaula, W. M. (1963). *Determination of the Earth's gravitational field*. DOI: 10.1029/RG001i004p00507.

Kaula, W. M. (1969). "Tidal Friction with Latitude-Dependent Amplitude and Phase Angle". In: *The Astronomical Journal* 74. ISSN: 00046256. DOI: 10.1086/110912.

Konopliv, A. S., R. S. Park, D. N. Yuan, S. W. Asmar, M. M. Watkins, J. G. Williams, E. Fahnestock, G. Kruizinga, M. Paik, D. Strekalov, N. Harvey, D. E. Smith, and M. T. Zuber (2013). "The JPL lunar gravity field to spherical harmonic degree 660 from the GRAIL Primary Mission". In: *Journal of Geophysical Research: Planets* 118 (7). ISSN: 21699100. DOI: 10.1002/jgre.20097.

Love, A. E. H. (1909). "The yielding of the earth to disturbing forces". In: *Proceedings of the Royal Society of London. Series A, Containing Papers of a Mathematical and Physical Character* 82 (551). ISSN: 0950-1207. DOI: 10.1098/rspa.1909.0008.

Markušić, S. and I. Ivančić (2020). "History of seismology in Croatia". In: *Earth Sciences History* 39 (1). ISSN: 19446187. DOI: 10.17704/1944-6187-39.1.160.

Martens, H. R., L. Rivera, and M. Simons (2019). "LoadDef: A Python-Based Toolkit to Model Elastic Deformation Caused by Surface Mass Loading on Spherically Symmetric Bodies". In: *Earth and Space Science* 6 (2). ISSN: 23335084. DOI: 10.1029/2018EA000462.

Melosh, H. J. and A. Raefsky (1981). "A simple and efficient method for introducing faults into finite element computations". In: *Bulletin of the Seismological Society of America* 71.5. ISSN: 0037-1106. DOI: 10.1785/bssa0710051391.

Murray, C. D. and S. F. Dermott (2000). *Solar System Dynamics*. DOI: 10.1017/cbo9781139174817.

Nunn, C., R. F. Garcia, Y. Nakamura, A. G. Marusiak, T. Kawamura, D. Sun, L. Margerin, R. Weber, M. Drilleau, M. A. Wieczorek, A. Khan, A. Rivoldini, P. Lognonné, and P. Zhu (2020). *Lunar Seismology: A Data and Instrumentation Review*. DOI: 10.1007/s11214-020-00709-3.

Park, R. S., N. Mastrodemos, R. A. Jacobson, A. Berne, A. T. Vaughan, D. J. Hemingway, E. J. Leonard, J. C. Castillo-Rogez, C. S. Cockell, J. T. Keane, A. S. Konopliv, F. Nimmo, J. E. Riedel, M. Simons, and S. Vance (Jan. 2024). "The Global Shape, Gravity Field, and Libration of Enceladus". In: *Journal of Geophysical Research: Planets* 129 (1). ISSN: 21699100. DOI: 10.1029/2023JE008054.

Qin, C., S. Zhong, and R. Phillips (2018). "Formation of the Lunar Fossil Bulges and Its Implication for the Early Earth and Moon". In: *Geophysical Research Letters* 45 (3). ISSN: 19448007. DOI: 10.1002/2017GL076278.

Romanowicz, B. and A. Dziewonski (2009). "Seismology and Structure of the Earth". In: *Treatise on Geophysics* 1.

Rovira-Navarro, M. and I. Matsuyama (2022). "A Spectral Method to Study the Tides of Laterally Heterogenous Bodies". In: *AGU Fall Meeting Abstracts*.

Wahr, J., M. T. Zuber, D. E. Smith, and J. I. Lunine (2006). "Tides on Europa, and the thickness of Europa's icy shell". In: *Journal of Geophysical Research E: Planets* 111.12. ISSN: 01480227. DOI: 10.1029/2006JE002729.

Zhong, S., C. Qin, G. Geruo, and J. Wahr (2012). "Can tidal tomography be used to unravel the long-wavelength structure of the lunar interior?" In: *Geophysical Research Letters* 39 (15). ISSN: 00948276. DOI: 10.1029/2012GL052362.

Zuber, M. T., D. E. Smith, M. M. Watkins, S. W. Asmar, A. S. Konopliv, F. G. Lemoine, H. J. Melosh, G. A. Neumann, R. J. Phillips, S. C. Solomon, M. A. Wieczorek, J. G. Williams, S. J. Goossens, G. Kruizinga, E. Mazarico, R. S. Park, and D. N. Yuan (2013). "Gravity field of the moon from the Gravity Recovery and Interior Laboratory (GRAIL) mission". In: *Science* 339 (6120). ISSN: 10959203. DOI: 10.1126/science.1231507.

Chapter 2

INFERRING THE MEAN THICKNESS OF THE OUTER ICE SHELL OF ENCELADUS FROM DIURNAL CRUSTAL DEFORMATION

A. Berne et al. (2023a). "Inferring the Mean Thickness of the Outer Ice Shell of Enceladus From Diurnal Crustal Deformation". In: *Journal of Geophysical Research: Planets* 128 (6).

2.1 Abstract

The thickness of the outer ice shell plays an important role in several geodynamical processes at ocean worlds. Here, we show that observations of tidally-driven diurnal surface displacements can constrain the mean ice shell thickness, $\tilde{d}_{ice}$. Such estimates are sensitive to any significant structural features that break spherical symmetry such as faults and lateral variation in ice shell thickness and structure. We develop a finite-element model of Enceladus to calculate diurnal tidal displacements for a range of $\tilde{d}_{ice}$ values in the presence of such structural heterogeneities. Consistent with results from prior studies, we find that the presence of variations in ice shell thickness can significantly amplify deformation in thinned regions. If major faults are also activated by tidal forcing—such as Tiger Stripes on Enceladus—their characteristic surface displacement patterns could easily be measured using modern geodetic methods. Within the family of Enceladus models explored, estimates of $\tilde{d}_{ice}$ that assume spherical symmetry *a priori* can deviate from the true value by as much as $\sim 41\%$ when structural heterogeneities are present. Additionally, we show that crustal heterogeneites near the South Pole produce differences of up to 35% between Love numbers evaluated at different spherical harmonic orders. A $\sim 41\%$ range in estimates of $\tilde{d}_{ice}$ from Love numbers is smaller than that found with approaches relying on static gravity and topography ($\sim 250\%$) or analyzing diurnal libration amplitudes ($\sim 85\%$) to infer $\tilde{d}_{ice}$ at Enceladus. As such, we find that analysis of diurnal tidal deformation is a relatively robust approach to inferring mean crustal thickness.

2.2 Introduction

Enceladus, a moon orbiting Saturn approximately every 32.9 hrs, is demonstratively geologically active (Porco et al., 2006; Spencer et al., 2006; Hansen et al., 2006; Ingersoll et al., 2020). Erupting jets at the body's surface align with the position of four prominent, evenly spaced surface fractures (informally known as 'Tiger Stripes') (Porco et al., 2006). These fractures produce jets or geysers that are the source of a water-ice-dominated plume emanating from the South Polar Terrain (SPT). The Tiger Stripes correlate with the position of anomalously high heat flux and regional thinning at the SPT (Spencer et al., 2006; Porco et al., 2014). Moreover, jet activity varies with orbital phase to produce maxima in plume brightness near orbital apoapse and periapse (Ingersoll et al., 2020). The correlation of the plume brightness oscillation period and Enceladus's orbital period strongly suggests that diurnal tides regulate heat and mass transport in the outer ice shell (Hurford et al., 2007). We explore the interactions between crustal structure and diurnal deformation to improve our understanding of the interior dynamics of Enceladus.

Constraints on ice shell structure, in particular outer shell mean thickness $\tilde{d}_{ice}$, provide a first-order constraint on the thermal properties, interior structure, and potential for habitability of any ocean world. $\tilde{d}_{ice}$ is an essential parameter for understanding the total heat budget (Roberts and Nimmo, 2008), the potential for convection within the ice shell (Mitri and Showman, 2005), the radial extent of the core and ocean (Hemingway and Mittal, 2019), and the rate at which oxidized material cycles between the surface and the ocean through burial processes (Zolotov and Shock, 2004). $\tilde{d}_{ice}$ also constrains plausible tidal heating mechanisms on Enceladus including viscous dissipation in the crust (Souček et al., 2019) and turbulent ocean flow (Hay and Matsuyama, 2019; Tyler, 2020).

Several approaches currently exist to infer $\tilde{d}_{ice}$. Static gravity and topography admittance modelling (Iess et al., 2014; McKinnon, 2015; Hemingway and Mittal, 2019; Akiba et al., 2022) and diurnal shell libration amplitude measurements (Thomas et al., 2016; Van Hoolst et al., 2016) yield estimates of $\tilde{d}_{ice}$ for Enceladus between 17–60 km ($\sim$ 250%) and 14–26 km ($\sim$ 85%), respectively. These methods rely on the presence of large-scale non-hydrostatic surface topography and a hydrostatic core, or alternatively, a short orbital period (i.e., that is comparable to the resonant frequency of the ice shell of a few days). Here, we explore an alternative approach that relies on the analysis of the response to short-period (i.e., diurnal) tidal forcing. Inferences of $\tilde{d}_{ice}$ from analysis of diurnal tides are relatively insensitive to

assumptions regarding the core and are not contingent upon fortuitous structural or orbital conditions (e.g., a short orbital period or the presence of non-hydrostatic topography) at Enceladus.

Differential gravitational attraction to a central, parent body (e.g., a planet) produces tides on orbiting satellites. Over timescales substantially greater than that of the orbital period (i.e., long-period), satellites deform as viscous fluids and the ultimate response to tidal forces is sensitive to radially varying internal density structure (e.g., Hubbard and Anderson, 1978). Bodies with eccentric orbits around their parent bodies experience an additional tidal force (i.e., the eccentricity or diurnal tide) which operates at a period equal to that of the orbit. At this timescale, any non-fluid interior layers may deform viscoelastically. For ocean-world bodies (i.e., where the outer ice shell and silicate core are mechanically decoupled by an intervening liquid ocean) deformation of the outer shell in response to diurnal tides is then relatively insensitive to the deep internal structure but is highly sensitive to $\tilde{d}_{ice}$. Measurement of time-varying gravity or surface displacement can therefore be used to directly infer $\tilde{d}_{ice}$.

The radial response of a body to time-dependent forcing can be described using gravitational and shape Love numbers (k_l and h_l respectively) that depend on spherical harmonic degree l (Love, 1909). The $l = 2$ diurnal Love numbers k_2^d and h_2^d track the very long-wavelength elastic response of bodies to diurnal tides and are sensitive to long-wavelength elastic structure (i.e., $\tilde{d}_{ice}$). We will demonstrate that there only exists a unique relationship between a body's response and a load at $l = 2$ for the limiting case of a fully spherically symmetric body. More generally, inferences of $\tilde{d}_{ice}$ from diurnal Love numbers at Enceladus require accounting for the potential impact of non-spherically symmetric structure.

For an arbitrary 3D structure, we can formulate a general linear relationship between spherical harmonics V_{lm} (i.e., of degree l and order m) of a driving gravitational potential $V(\mathbf{\Omega})$ which deforms (i.e., drives mass movement) within a body and generates harmonics $U_{l'm'}$ of an induced gravitational potential $U(\mathbf{\Omega})$:

$$V(\mathbf{\Omega}) = \sum_{l=0}^{\infty} \sum_{m=-l}^{l} V_{lm} Y_{lm}(\mathbf{\Omega}) \tag{2.1a}$$

$$U(\mathbf{\Omega}) = \sum_{l'=0}^{\infty} \sum_{m'=-l'}^{l'} U_{l'm'} Y_{l'm'}(\mathbf{\Omega}), \tag{2.1b}$$

where $Y_{lm}(\mathbf{\Omega})$ denote real spherical harmonics, the prime ($'$) denotes induced components, and $\mathbf{\Omega}$ is the angular position variable comprising a co-latitude and longitude pair (θ, ϕ) in a reference frame whose origin is fixed to Enceladus's center of mass (Note: we restrict our analysis to the induced gravitational response but could easily apply the methodology discussed in this section to derive the induced topographic response). For a linear elastic solid, deformation is linearly related to forcing (see also Supplementary S1.1). The tidal forcing harmonics V_{lm} accordingly map to harmonics $U_{l'm'}$ via linear Green's functions $\gamma_{lm}^{l'm'}$ which describe the elastic structure of a body:

$$\begin{bmatrix} U_{l'm'} \\ \vdots \\ \vdots \\ U_{\infty\infty} \end{bmatrix} = \begin{bmatrix} \gamma_{lm}^{l'm'} & \cdots & \cdots & \gamma_{\infty\infty}^{l'm'} \\ \vdots & \ddots & & \vdots \\ \vdots & & \ddots & \vdots \\ \gamma_{lm}^{\infty\infty} & \cdots & \cdots & \gamma_{\infty\infty}^{\infty\infty} \end{bmatrix} \begin{bmatrix} V_{lm} \\ \vdots \\ \vdots \\ V_{\infty\infty} \end{bmatrix} \tag{2.2}$$

Equation 2.2 demonstrates that the response of a body (i.e., defined as $U_{l'm'}/V_{lm}$) will generally vary in time due to the changing shape of an applied load (i.e., time-variable V_{lm} components) *despite* a fixed elastic structure. For diurnal tides, the driving potential is composed of three harmonics V_{20}, V_{22}, and $V_{2\,\text{-}2}$ (Murray and Dermott, 2000) and Equation 2.2 simplifies to:

$$\begin{bmatrix} U_{l'm'} \\ \vdots \\ \vdots \\ U_{\infty\infty} \end{bmatrix} = \begin{bmatrix} \gamma_{20}^{l'm'} & \gamma_{22}^{l'm'} & \gamma_{2\,\text{-}2}^{l'm'} \\ \vdots & \vdots & \vdots \\ \vdots & \vdots & \vdots \\ \gamma_{20}^{\infty\infty} & \gamma_{20}^{\infty\infty} & \gamma_{2\,\text{-}2}^{\infty\infty} \end{bmatrix} \begin{bmatrix} V_{20} \\ V_{22} \\ V_{2\,\text{-}2} \end{bmatrix} \tag{2.3}$$

$U_{lm} \neq 0$ for $l \neq 2$ indicate a coupling between forcing and response across spatial scales (i.e., 'mode coupling'; Dahlen and Tromp, 1998). To derive Love numbers, we restrict our analysis to the U_{20}, U_{22}, and $U_{2\,\text{-}2}$ components of the induced gravitational potential field (Note that $U_{lm} = 0$ for $l = 1$ in a reference frame whose origin is fixed to Enceladus's center of mass). Equation 2.3 then simplifies to:

$$\begin{bmatrix} U_{20} \\ U_{22} \\ U_{2\,\text{-}2} \end{bmatrix} = \begin{bmatrix} \gamma_{20}^{20} & \gamma_{22}^{20} & \gamma_{2\,\text{-}2}^{20} \\ \gamma_{20}^{22} & \gamma_{22}^{22} & \gamma_{2\,\text{-}2}^{22} \\ \gamma_{20}^{2\,\text{-}2} & \gamma_{22}^{2\,\text{-}2} & \gamma_{2\,\text{-}2}^{2\,\text{-}2} \end{bmatrix} \begin{bmatrix} V_{20} \\ V_{22} \\ V_{2\,\text{-}2} \end{bmatrix} \tag{2.4}$$

The individual components $\gamma_{lm}^{l'm'}$ in Equation 2.4 contain information regarding the sphericity of a body's elastic structure. For a non-rigid body, diagonal components

(i.e., $\gamma_{20}^{20}, \gamma_{22}^{22}, \gamma_{2\,-2}^{2\,-2}$) are always non-zero and are principally sensitive to bulk elastic properties (e.g., $\tilde{d}_{ice}$; Wahr et al., 2006). Off-diagonal components (i.e., γ_{22}^{20}, γ_{20}^{22}, $\gamma_{2\,-2}^{22}$, $\gamma_{2\,-2}^{20}$, $\gamma_{22}^{2\,-2}$, $\gamma_{20}^{2\,-2}$) represent coupling between forcing and response at mutually distinct harmonics. At spatial wavelengths significantly greater than $\tilde{d}_{ice}$, the outer ice crust of spherically symmetric ocean worlds conform to the shape of driving potential surfaces (i.e., following the thin-plate approximation originally derived from beam theory; Levinson, 1984). According to Equation 2.4, distinct diagonal components or non-zero off-diagonal components therefore imply the presence of non-spherically symmetric structure. For a spherically symmetric body, $\gamma_{22}^{20} = \gamma_{20}^{22} = \gamma_{2\,-2}^{22} = \gamma_{2\,-2}^{20} = \gamma_{22}^{2\,-2} = \gamma_{20}^{2\,-2} = 0$ and $\gamma_{20}^{20} = \gamma_{22}^{22} = \gamma_{2\,-2}^{2\,-2} = k_2^d$. Equation 2.4 then simplifies to:

$$\begin{bmatrix} U_{20} \\ U_{22} \\ U_{2\,-2} \end{bmatrix} = \begin{bmatrix} k_2^d & 0 & 0 \\ 0 & k_2^d & 0 \\ 0 & 0 & k_2^d \end{bmatrix} \begin{bmatrix} V_{20} \\ V_{22} \\ V_{2\,-2} \end{bmatrix} \tag{2.5}$$

We can define 'effective' Love numbers k_{2m}^d as quantities which track U_{2m} normalized by V_{2m} (i.e., $k_{2m} = U_{2m}/V_{2m}$). According to Equation 2.5, a unique relationship between harmonics U_{2m} and V_{2m} exists only for spherically symmetric structures (i.e., $k_{2m}^d \rightarrow k_2^d$). More generally, k_{2m}^d are sensitive to non-spherically symmetric structure and the overall shape of the load (i.e., combination of V_{20}, V_{22}, and $V_{2\,-2}$) such that $k_{20}^d \neq k_{22}^d \neq k_{2\,-2}^d$ (i.e., 'order splitting' or 'spectral leakage') (Behounkova et al., 2017; Ermakov et al., 2021; Vance et al., 2021). Several structures are expected to break spherical symmetry at Enceladus including lateral variations in thickness of the ice shell, structurally weak (e.g., highly fractured or damaged) zones, or the presence of major fault structures (Behounkova et al., 2017). We therefore expect that diurnal Love numbers are not directly sensitive to $\tilde{d}_{ice}$ at Enceladus and inferences of $\tilde{d}_{ice}$ from k_{2m}^d (or h_{2m}^d) should account for the potential influence of structural heterogneities in the outer ice crust.

Several studies describe the relationship between elastic structure and diurnal deformation at Enceladus. Wahr et al. (2006) develop analytic expressions to calculate k_{2m}^d and h_{2m}^d from eccentricity tides at ocean worlds using an approach that only applies to spherically symmetric models. Beuthe (2018) extends this analysis of k_{2m}^d and h_{2m}^d to allow for variations in crustal thickness but assumes a thin-shelled approximation and does not include the potential impact of faults. The most sophisticated models to date by Souček et al. (2016), Behounkova et al. (2017), Souček et al.

(2019), and Sládková et al. (2021) simulate deformation using finite-element models (FEM) of the outer ice shell with both variations in ice thickness and weak zones. These studies do not specifically address the relationship between deformation and $\tilde{d}_{ice}$ and exclude effects from a broader range of structural heterogeneities inferred from surface geology at Enceladus including large circum-tectonic boundaries and extensional fractures extending radially outward from the South Polar Terrain (i.e., chasma).

Here, we explore how estimates of $\tilde{d}_{ice}$, based on analysis of diurnal tides, are potentially impacted by structural heterogeneities within the ice crust of Enceladus. We simulate deformation on tidally-loaded quasi-spherical shells using a FEM and compare results from six sets of end member models of Enceladus:

1. A spherically symmetric ice shell.
2. An ice shell with variations in thickness.
3. An ice shell with faults at Tiger Stripe locations.
4. An ice shell with 'weak zones' (regions of reduced shear modulus) at locations corresponding to the position of additional structures inferred from Enceladus's geology (i.e., chasma and circum-tectonic boundaries).
5. An ice shell with both variations in thickness and faults.
6. An ice shell with faults, variations in thickness, and weak zones.

We parameterize the response of the shell by calculating Love numbers k^d_{20}, k^d_{22}, $k^d_{2\,\text{-}2}$ and h^d_{20}, h^d_{22}, $h^d_{2\,\text{-}2}$, from deformed geometries and compare these predicted values with those predicted from models without structural heterogeneities. We then explore the challenge of inferring $\tilde{d}_{ice}$ from Love numbers posed by the presence of structural heterogeneities in the crust. We conclude by highlighting the potential for analyzing diurnal tides to determine $\tilde{d}_{ice}$ both for Enceladus and for other ocean worlds.

2.3 Methods

We develop a quasi-spherical FEM of Enceladus that allows for structural heterogeneities in the ice shell and that can be used to predict the elastic response of the body to diurnal tidal loads. We first build an FEM mesh that reflects desired structural heterogeneities. We then use a modified version of the finite-element

code PyLith (Aagaard et al., 2007) to calculate displacements on models subjected to tidal forcing. In post-processing, we extract $l = 2$ Love numbers from model displacements. We describe each of these steps in detail below.

Model Preparation

We consider six types of models that differ in the style of structural heterogeneity assumed: (1) a *Base* model without structural heterogeneities; (2) a model with large scale faults (i.e., *Faulted*); (3) a model with Lateral Thickness Variations (i.e., *LTV*); (4) a model with weak zones at locations coincident with major geologic structures (i.e., *WZ*); (5) a combined model with faults and Lateral Thickness Variations (i.e., *Faulted+LTV*); and (6) a combined model with faults, Lateral Thickness Variations, and weak zones (i.e., *Faulted+LTV+WZ*). For each model, we develop a mesh with tetrahedral elements using the software package CUBIT (Skroch et al., 2019; CoreForm, 2020) and refine cell size in regions which locally exhibit high strain (e.g., near faults). Minimum and maximum cell sizes (i.e., tetrahedra cell edge lengths) are 1 and 12 km respectively throughout the mesh. For tetrahedra along the faults, we limit maximum cell size to 3 km and achieve a vertical resolutions as fine as 1 - 2 km across each interface. Example snapshots of our mesh geometry are shown in Figure 2.1. We perform a mesh convergence test to verify our choice of element sizing parameters and to provide accurate Love number values on models with structural heterogeneities (see supplementary section S1.3 for details).

- For the *Base* models, we mesh a spherical shell with a specified input thickness $\tilde{d}_{ice}$. All of our models have baseline elastic parameters consistent with the rheology of ice (Jaccard, 1976; Shaw, 1985; Neumeier, 2018). We assign a base shear modulus value for ice of $G = 3.3$ GPa and a bulk modulus of $\mu = 8.6$ GPa (i.e., consistent with the formulation described in Souček et al. (2016) with $G = 3.3$ GPa and Poisson's ratio $\nu = 0.33$). For this analysis, we ignore viscous effects since viscous strain at the forcing period relevant for Enceladus (32.9 hours) is expected to be negligibly small (<1% of the total shell strain (Wahr et al., 2009), see also Supplemetary Section S1.6). Short-period elastic deformation of the core is also expected to be several orders of magnitude smaller than shell deformation (Schubert et al., 2007). We therefore treat the core as a rigid body and ignore any impact that deformation of the core or related 3D mantle structures (e.g., ocean plumes driven by hydrothermal activity at the core-ocean boundary; Choblet et al., 2017) may

have on the response of the ice shell to eccentricity tides.

- For the *Faulted* models, we introduce fault surfaces that are through-going (i.e., they extend through the full thickness of the ice shell) and are frictionless. The explicit inclusion of fault surfaces within the FEM formulation uses a 'split-node' formulation whereby we duplicate nodes along the fault plane and introduce special cohesive cells between node sets (Melosh and Raefsky, 2009; see also Supplementary S1.1). Split-node formulations allow for robust calculations of fault-induced deformation and self-consistent predictions of fault slip. Our *Faulted* model specifically refers to a shell with four faults at the South Pole consistent with the mapped extent of Tiger Stripes at Enceladus. We extract the surface trace of the Tiger Stripes from existing maps of Enceladus (Schenk, 2008). We assume that effective hydrostatic normal stresses within water-filled cracks exceed extensional forces across fault geometries (Sládková et al., 2021 cf. Equation S14). We therefore ignore any potential impact of fault opening on deformation for *Faulted* models in this work (for details, see Supplementary S1.1).

- To construct the *LTV* models, we apply topography, H_{top}, to the outer surface of our base model geometry and modify the inner surface (i.e., the ice-ocean boundary), H_{bottom}, assuming isostatic (Airy) compensation. Given surface gravitational acceleration g_0, outer shell ice of density ρ_{ice}, ocean water of density ρ_w, gravitational acceleration at the ice-ocean interface g_{int}, mean radius of the outer surface R_0 (see Table 2.1 for chosen values of these parameters) (Hemingway and Matsuyama, 2017), and $\tilde{d}_{ice}$ we can write:

$$H_{bottom} = H_{top} \frac{\rho_{ice}}{(\rho_{ice} - \rho_w)} \frac{g_0}{g_{int}} \frac{R_0^2}{(R_0 - \tilde{d}_{ice})^2}. \tag{2.6}$$

Table 2.1: Assumed parameter values used in Equation 2.6. Parameter values taken from Schenk et al. (2018).

Parameter	Value	Units
ρ_{ice}	925	kg/m^3
ρ_w	1007	kg/m^3
g_0	0.113	m/s^2
g_{int}	0.120	m/s^2
R_0	252.1	km

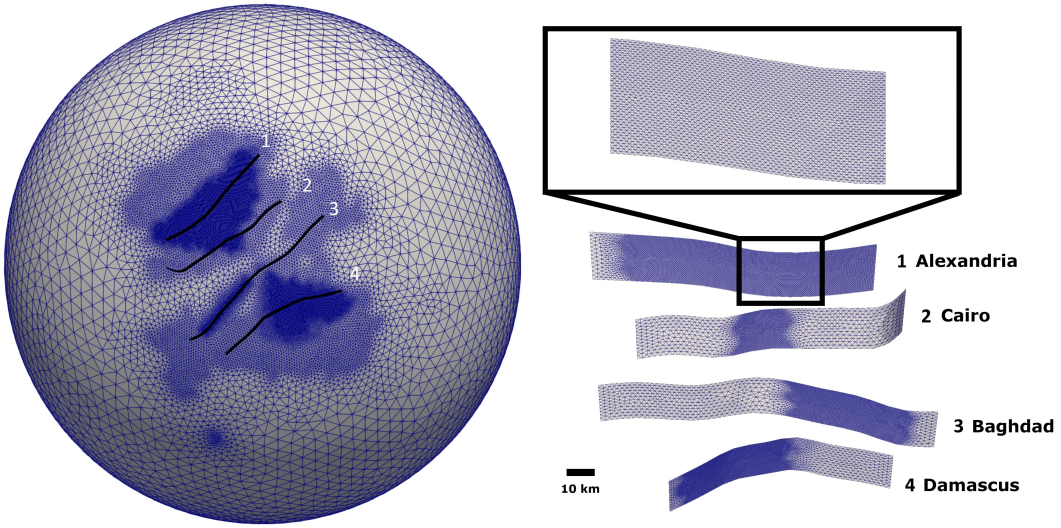

Figure 2.1: Example snapshots of mesh geometry from *Faulted* models (see main text). Left panel: South polar view of 3D mesh geometry discretized with tetrahedral elements. We refine cell sizes in regions that are expected to exhibit high strain upon tidal loading (in this case, near Tiger Stripes). The trace of the Tiger Stripes is shown as black lines on the outer surface of our geometry. Right panel: Perspective view of 2D discretization along Tiger Stripe surfaces. Inset image shows close-up view of mesh along Tiger Stripe 1 (i.e., Alexandria Sulcus). Labels for individual Tiger Stripes are shown in left and right panels. Cell edges are colored blue. An approximate distance scale is shown in the right panel for reference.

Our *LTV* models use topography extracted from the shape model given by Nimmo et al. (2011) up to a maximum spherical harmonic degree $L_{max} = 8$. Our *Faulted+LTV* model includes both types of structural heterogeneities.

- Our *WZ* models incorporate 1-km wide through-going 'weak zones' at locations corresponding to the south polar circum-tectonic boundary, chasma, and Tiger Stripes. Yin and Pappalardo (2015) report that extensional, compressional, and shear stresses drive the formation of fractures in the circum-tectonic boundary surrounding the SPT whereas only extensional stresses appear to form the chasma that radiate away from the SPT. Although the fracture depth of faults observed at the circum-tectonic boundary and chasma remains poorly constrained based on current observations (Yin and Pappalardo, 2015), we would expect that all modes of fracture (extensional, compressional, and shear) in a finite-width volume would result in local 'damaged' regions of the ice shell which are less capable of accommodating tidally-driven stresses (i.e., exhibit a lower shear modulus) compared to the surrounding unfractured medium. In the most extreme feasible scenario, highly fractured regions of the crust (i.e., with porosity 0 % - 60%; we do not expect ice porosities > 60% due to pore compaction arising from hydrostatic confinement at depth; Durham et al., 2005) would penetrate to depths where liquid water from the subsurface ocean permeates the pore space of ice (Ingersoll and Nakajima, 2016). The pore pressure of fluid within a fractured ice matrix at depth within Enceladus's crust is not zero (i.e., the ice-water mixture exhibits 'undrained' conditions; Rovira-Navarro et al., 2022). The effective elastic bulk modulus for such a system is similar to the bulk modulus of the solid ice phase (Rovira-Navarro et al., 2022 cf. Equation 18c). We therefore formulate weak zones as regions with an elastic shear modulus G_{WZ} reduced to negligible values $\sim 10^{-5}\, G$ but maintain a constant ice bulk modulus and density throughout our geometry.

  Deformation driven by the presence of frictionless faults (i.e., 2D interfaces) is distinct from that arising from crustal weak zones (i.e., finite-width 3D volumes) in models. Water-filled fault interfaces subject to effective hydrostatic normal stresses that exceed tidally-driven stresses will resist extensional deformation in a manner similar to that of the surrounding elastic medium (see Supplementary section S1.1.1.4 of this chapter; Sládková et al., 2021; Rovira-Navarro et al., 2022). By contrast, 3D volumes that contain weakened material will exhibit less resistance to normal stresses than the surrounding

elastic medium due to a locally reduced elastic Young's modulus (i.e., which is sensitive to G_{WZ} for our formulation for weak zones; see also Segall, 2010). Reduced resistance to normal stresses along weak zones in *WZ* models should enable deformation patterns comparable to those expected from mode-1 crack opening (i.e., similar to the deformation produced by Tiger Stripes in Souček et al., 2016). We do not consider the potentially distinct responses of highly fractured areas of the ice shell to extensional and compressional tidal stresses in this study. Our *Faulted+LTV+WZ* models incorporate weak zones, faults, and lateral variations in crustal thickness. Note that *Faulted+LTV+WZ* models in this work incorporate both 2D interfaces and 3D weak zones at Tiger Stripe locations.

Tidal Loading

For Enceladus, the driving potential (to the first order in eccentricity) produced by time-dependent eccentricity tides $V(r, \theta, \phi, t)$ at a point in a reference frame whose origin is fixed to Enceladus's center of mass (i.e., the ($\theta = 90°$, $\phi = 0°$) datum lies at the sub-Saturnian point, where θ is co-latitude and ϕ is longitude) is written as a combination of radial $V_{rad}(r, \theta, \phi, t)$ and librational $V_{lib}(r, \theta, \phi, t)$ terms (Murray and Dermott, 2000):

$$V_{rad}(r, \theta, \phi, t) = r^2 \omega^2 e \cdot \cos(\omega t) \, \frac{3}{4} \left(\mathrm{P}_{22}(\mu) \cos 2\phi - 2\, \mathrm{P}_{20}(\mu) \right) \tag{2.7a}$$

$$V_{lib}(r, \theta, \phi, t) = r^2 \omega^2 e \cdot \sin(\omega t) \, \mathrm{P}_{22}(\mu) \sin 2\phi. \tag{2.7b}$$

Each term in Equation 2.7 is scaled by the factor $\omega^2 e$, where $\omega = 5.307 \cdot 10^{-5}$ s^{-1} is Enceladus's orbital angular velocity and $e = 0.0047$ is the body's orbital eccentricity. Time $t = 0, \frac{2\pi}{\omega}$ corresponds to orbital periapse. $P_{20}(\mu)$ and $P_{22}(\mu)$ are associated Legendre Functions with the nested function $\mu = \cos(\theta)$. We apply body forces, ocean tractions, topographic surface traction forces, and self-gravitational forces produced by the driving potential from Equation 2.7 and calculate displacement fields arising from these loads. We ignore inertial forces for our analysis and obtain solutions for displacements at mesh nodes across the full 3D spherical geometry. We enforce zero rigid body rotations and translations for simulations (for details, see Supplementary section 1.1 of this chapter).

We use the 3D visco-elasto-plastic FEM code PyLith (Aagaard et al., 2007). PyLith is a well-established and extensively benchmarked tool developed in the terrestrial

crustal dynamics community for studying tectonic processes on Earth. PyLith allows for complex bulk rheology, various formulations for fault behavior, and complex geometrical meshes. PyLith was originally designed for quasi-Cartesian problems; as such we have modified it to allow for modeling full spheres in a no-net-rotation/translation reference frame with central time-dependent body forces appropriate for eccentricity tides. We benchmark our tidal loading formulation as implemented in PyLith applied to our *Base* model against the program SatStress (Wahr et al., 2009) (see Supplementary section S1.1-1.2 of this chapter).

Calculation of Love numbers

We post-process the resulting deformation fields to evaluate the $l = 2$ diurnal Love numbers k^d_{2m} and h^d_{2m}. The 'diurnal' Love numbers are distinct from 'fluid' Love numbers k^f_{2m} and h^f_{2m}. 'Fluid' Love numbers are sensitive to the arrangement of a body's interior layers which deflect in response to long-period static tides in order to achieve hydrostatic equilibrium (Goldreich and Mitchell, 2010). In contrast, diurnal Love numbers depend on the elastic response of the body to short-period eccentricity tides (see Equation 2.7) and are superimposed onto the long-period tide. Moreover, diurnal Love numbers are usually at least an order of magnitude smaller than fluid Love numbers (Beuthe, 2018; Hemingway and Mittal, 2019). Relative to the fluid Love numbers, the diurnal Love numbers are less sensitive to deeper interior structure at ocean worlds (Wahr et al., 2009).

For h^d_{2m}, we expand the outer surface of our deformed geometry into spherical harmonics and separately compute coefficients H_{2m}. We calculate V_{20}, V_{22}, and $V_{2\,\text{-}2}$ using the $l = 2$ components of the tidal potential from Equation 2.7:

$$V_{20} = -\frac{3}{2} r^2 \omega^2 e \cdot \cos(\omega t) \tag{2.8a}$$

$$V_{22} = \frac{3}{4} r^2 \omega^2 e \cdot \cos(\omega t) \tag{2.8b}$$

$$V_{2\,\text{-}2} = r^2 \omega^2 e \cdot \sin(\omega t). \tag{2.8c}$$

From V_{2m}, H_{2m}, and the definition of the effective Love numbers (see introduction), we have:

$$h^d_{2m} = g_0 H_{2m} / V_{2m}. \tag{2.9}$$

Following a similar procedure for k^d_{2m}, we compute coefficients U_{2m} of the spherical harmonic expansion of the induced gravitational potential field (see Equation 2.1) associated with the deformed geometry:

$$k_{2m}^{d} = U_{2m}/V_{2m}. \tag{2.10}$$

As mentioned earlier, Love numbers defined in this way will depend on the time-varying shape and amplitude of the driving potential (i.e., see Equations 2.4 and 2.8). Thus, we expect values of k_{2m}^{d} and h_{2m}^{d} to vary over the tidal cycle at Enceladus. Since we aim to minimize the impact of non-spherically symmetric structure on inferences of $\tilde{d}_{ice}$, we evaluate deformation at two unique points in the tidal cycle: $t = 0$ and $t = \frac{\pi}{2\omega}$. At $t = 0$ (or $\frac{\pi}{\omega}$), $V_{2\,-2} = 0$ (according to Equation 2.8) which eliminates the potential impact of the off-diagonal components $\gamma_{2\,-2}^{22}$, $\gamma_{2\,-2}^{20}$, $\gamma_{22}^{2\,-2}$, and $\gamma_{20}^{2\,-2}$ (from Equation 2.4) on values of k_{20}^{d} or k_{22}^{d}. Similarly, at $t = \frac{\pi}{2\omega}$ (or $\frac{3\pi}{2\omega}$), $V_{20} = V_{22} = 0$ which eliminates the impact of all off-diagonal components on values of $k_{2\,-2}^{d}$.

Ice Shell Thickness and Elastic Thickness

Mean ice shell thickness $\tilde{d}_{ice}$ described in our analysis is distinct from mean elastic thickness typically referenced in studies of plate flexure (e.g., Nimmo and Pappalardo, 2004; Conrad et al., 2019). Elastic thickness as inferred from flexure studies denotes the thickness of the crust that exhibits predominantly elastic (i.e., non-viscous) deformation over very long timescales (e.g., topographic loading; Mancktelow, 1999). For ocean world crusts, elastic thickness is typically a fraction ($< 70\%$) of the thermal thickness of the ice shell (i.e., the radial distance between the surface and the phase boundary between the ocean and the ice shell at 273 K). In contrast, $\tilde{d}_{ice}$ is the thickness of the ice shell that deforms elastically upon *cyclic* loading over diurnal timescales. Analyzing Love numbers from fully viscoelastic ice shells that are cyclically deformed over a 32.9 hour period produces estimates of $\tilde{d}_{ice}$ that are only slightly ($< 0.2\%$) smaller than values of the thermal thickness of the crust at Enceladus (for details, see Supplementary section S1.6 of this chapter).

Previous FEMs

Our FEMs are similar to, but distinct from, those described in the papers Souček et al., (2016), Behounkova et al., (2017), and Sládková et al., (2021). We employ a tidal forcing formulation which is identical to that described in Souček et al., (2016) to generate body, ocean traction, and topographic loading forces. However, we include the effect of self-gravitation in our models (which modifies final calculated values of k_{2m}^{d} and h_{2m}^{d} by up to 3%; Beuthe, 2018). Souček et al., (2016) employ weak zones (i.e., finite width regions with reduced elastic moduli) as proxies the behavior of fault interfaces. In contrast, we adopt a split-node approach at the fault-plane to simulate

deformation which enables straightforward calculations of fault slip. Souček et al., (2016), Behounkova et al., (2017), and Sládková et al., (2021) also focus on the implications of deformation for tidal heating, while we focus here on the inference of shell structural parameters in the presence of structural heterogeneities. Finally, our models additionally consider the effect of fault zones beyond the Tiger Stripes and thereby identify the extent to which other major structural heterogeneities (e.g., chasma and circum-tectonic boundaries) may affect diurnal deformation patterns at Enceladus.

The most significant difference between models by Souček et al., (2016) Behounkova et al., (2017), and Sládková et al., (2021) and those described in this work relates to respective formulations for weak zones. Souček et al., (2016) and Behounkova et al., (2017) reduce shear modulus to effectively negligible values while maintaining a constant Poisson's ratio within damaged regions. Such a formulation results in negligibly small values for weak zone bulk modulus. FEMs in Sládková et al., (2021) maintain constant weak zone elastic parameters but reduce viscosity within a finite-width volume to mimic static Coulomb friction along Tiger Stripes. Note that for zero static friction, the behavior of the Tiger Stripes in models by Sládková et al., (2021) approaches the behavior of weak zones in Souček et al., (2016) and Behounkova et al., (2017). The elastic moduli for weak zone formulations by Souček et al., (2016) and Behounkova et al., (2017) are consistent with those expected for a 'drained' two-phase system (Rovira-Navarro et al., 2022 cf. Equation 18b). We expect that 'undrained' conditions exist for ice-water mixtures subject to hydrostatic pressures at depth (Rovira-Navarro et al., 2022; Sládková et al., 2021). We therefore choose to maintain a constant bulk modulus in weak zones for this work (see previous discussion in section 2.1 for *WZ* models). Note that we are able to broadly reproduce the results of Souček et al., (2016) by employing weak zones only at Tiger Stripe locations and reducing both bulk and shear modulus to effectively negligible values in Supplementary S1.2.

2.4 Results

Figures 2.2 and 2.3 show snapshots of the radial displacement fields from each of the six model classes. The upper panels show absolute displacements on our *Base* model whereas the subsequent panels show the radial displacement fields for models incorporating structural heterogeneities relative to our *Base* model. Not surprisingly, there is a substantial increase in localized deformation near zones of structural heterogeneities (i.e., broadly consistent with model results from Souček et al.,2016;

Behounkova et al., 2017; and Sládková et al., 2021). For the *LTV* model, we find that the highest increases in displacement values occur near the South Pole where the ice shell is thinnest. In the *Faulted* model, radial displacements are maximum near fault tips (also at the South Pole). In our *WZ* and *Faulted+LTV+WZ* model, localized radial deformation is partitioned between the Tiger Stripes, chasma, and circum-tectonic boundaries in a complex manner with further increases in displacement near the Tiger Stripes due to extensional and shear strain localization along weak zones. Note that the addition of lateral variations in crustal thickness alters the geometry of weak zones in *Faulted+LTV+WZ* models relative to those in *WZ* models resulting in distinct displacement fields produced by weak zones in either case. Long-wavelength increases in displacement amplify values of the Love numbers for all models that incorporate structural heterogeneities. Moreover, surface deformation at this scale does not follow the pattern of the disturbing potential from Equation 4.3. This difference causes values of k^d_{20}, k^d_{22}, and $k^d_{2\,\text{-}2}$ (or h^d_{20}, h^d_{22}, and $h^d_{2\,\text{-}2}$) to diverge from each other (i.e., 'order-splitting').

Figure 2.4 shows additional snapshots of fault slip along the Tiger Stripes as evaluated by our *Faulted* model and crustal thickness variations in our *LTV* model. Displacements surrounding the South Pole in the *Faulted* model follow a double-couple pattern (i.e., a symmetric pattern of alternating maximal and minimal radial displacement around the fault tips; Segall, 2010) consistent with left-lateral strike-slip motion observed along the Tiger Stripes in Figure 2.4. Regional thinning at the North and South Poles in our *LTV* model also drives quadrupole displacement patterns across Northern and Southern hemispheres. However, the higher amplitude and greater regional extent of crustal thinning at the SPT (i.e., compared to that near the North Pole) results in relatively higher radial displacements over the Southern Hemisphere in *LTV* models.

Our *Faulted*, *Faulted+LTV*, *WZ*, and *Faulted+LTV+WZ* models predict significantly lower localized displacement along the length of the Tiger Stripes (i.e., ~ 20 cm) than do FEMs by Souček et al. (2016) and Behounkova et al. (2017) ($\sim$ 1-7 m). In the case of *Faulted* and *Faulted+LTV* models, the effect of clamping opening and closing motion across fault structures (see Supplementary section S1.1 of this chapter) suppresses mode-1 deformation surrounding Tiger Stripes (Segall, 2010). In contrast, reducing the shear modulus along weak zones in *WZ* and *Faulted+LTV+WZ* models produces discontinuities in radial displacement across the Tiger Stripes similar to those produced by mode-1 crack opening displacement (Segall, 2010). However, the

inclusion of a non-zero bulk modulus in weak zones for *WZ* and *Faulted+LTV+WZ* models reduces the magnitude of extensional and compressional strain over the Tiger Stripes as compared to the predicted impact of weak zones in FEMs by Souček et al., (2016) (see sections 2.1 and 2.5 of the methods for details).

Results for k_{20}^d, h_{20}^d, $k_{2\text{-}2}^d$. and $h_{2\text{-}2}^d$ from each model category are shown in Figure 2.5. Results similar to those shown in Figure 2.5 illustrating the behavior of k_{22}^d and h_{22}^d are also shown in Figure 2.6. Note that non-spherically symmetric models have enhanced values of Love numbers across all $\tilde{d}_{ice}$ values consistent with the amplification of deformation shown in models with structural heterogeneities (see Figures 2.2 and 2.3). Love number results in Figures 2.5 and 2.6 imply that inferences of elastic structure which assume Enceladus is spherically symmetric (i.e., the *Base* model) will underestimate $\tilde{d}_{ice}$ if structural heterogeneities are present in the crust. To evaluate this model error, $\Delta\%\tilde{d}_{ice}$, we determine the percentage difference between $\tilde{d}_{ice}$ assigned to the *Base* models and the mean thickness of selected models with heterogeneities (i.e., $\tilde{d}_{ice}^{Het}$) which each produce the same value of h_{2m}^d or k_{2m}^d:

$$\Delta\%\tilde{d}_{ice} = \frac{\tilde{d}_{ice}^{Het} - \tilde{d}_{ice}}{\tilde{d}_{ice}} \cdot 100\%. \tag{2.11}$$

Figures 2.5 and 2.6 show $\Delta\%\tilde{d}_{ice}$ for each model category with structural heterogeneities. Results demonstrate that Tiger Stripes in the *Faulted* models minimally ($< 3\%$) impact values of $\Delta\%\tilde{d}_{ice}$. By contrast, weak zones and variations in crustal thickness (in *WZ* and *LTV* models) bias inferences of $\tilde{d}_{ice}$ from Love numbers by up to $\sim 18\%$ and $\sim 20\%$ respectively. The most extreme case (*Faulted+LTV+WZ* models) yields values of $\Delta\%\tilde{d}_{ice}$ as high as $\sim 41\%$. Small differences between the shape of h_{2m}^d or k_{2m}^d curves (and $\Delta\%\tilde{d}_{ice}$ curves evaluated from h_{2m}^d or k_{2m}^d) arise from slight differences in radial displacement patterns at the outer surface and the ice-ocean boundary across models.

Note the distinct values of k_{22}^d and h_{22}^d compared to k_{20}^d and h_{20}^d or $k_{2\text{-}2}^d$ and $h_{2\text{-}2}^d$ (i.e., 'order-splitting') in models with structural heterogeneities in Figures 2.5 and 2.6. To directly quantify the impact of structural heterogeneities on order-splitting, we additionally plot values of k_{22}^d/k_{20}^d and h_{22}^d/h_{20}^d vs. $\tilde{d}_{ice}$ in Figure 2.6. We track k_{22}^d/k_{20}^d and h_{22}^d/h_{20}^d since these quantities implicitly account for the baseline impact of $\tilde{d}_{ice}$ on Love numbers and are especially sensitive to the presence of structural heterogeneities near the South Pole of Enceladus (see discussion).

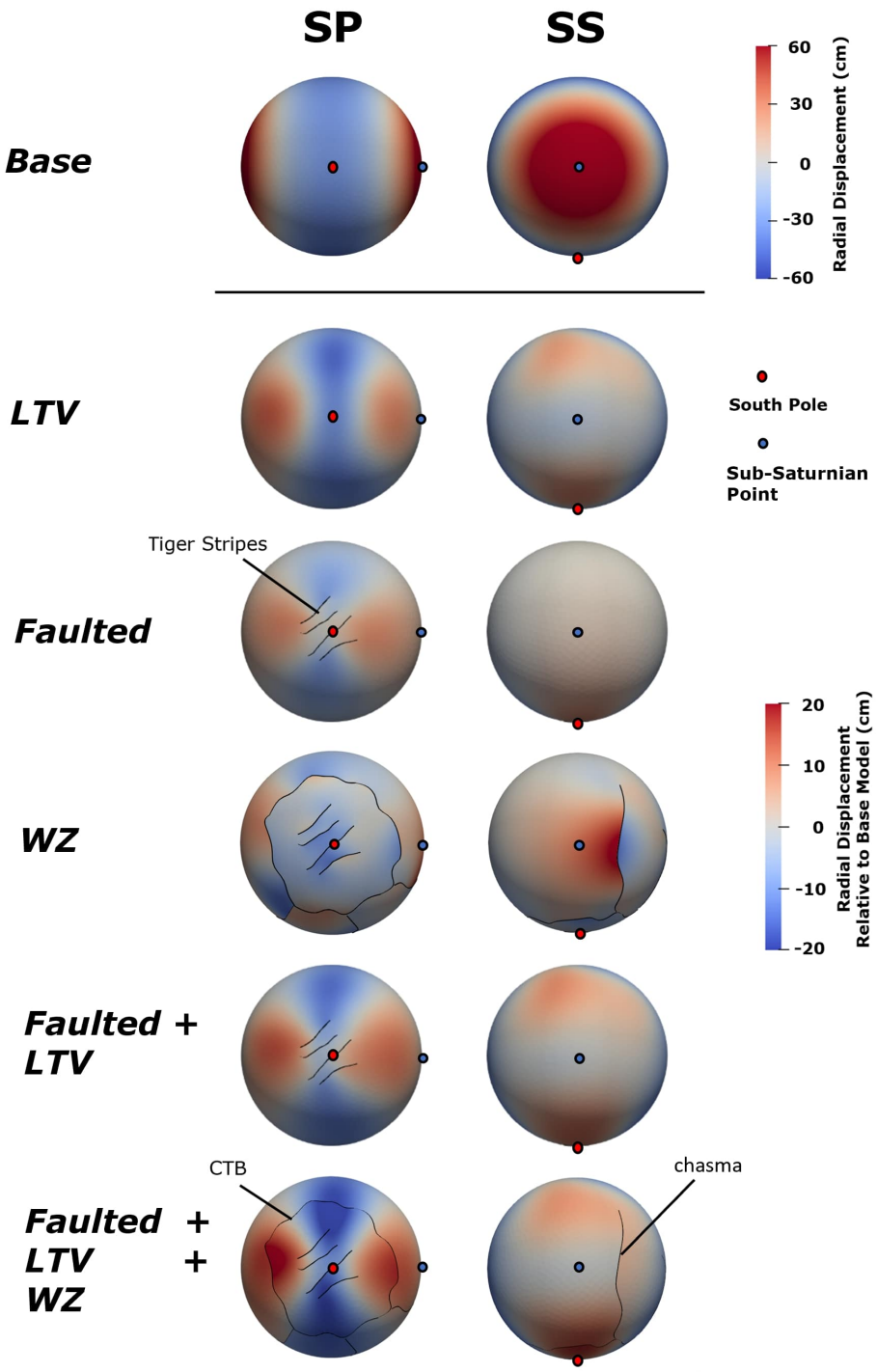

Figure 2.2: Snapshots of radial displacement from each model class viewed facing the South Pole (SP, left column) and the sub-Saturnian point (SS, right column) evaluated at $t = 0$ (periapse). The top row shows the radial displacement in the *Base* model due to tidal forcing. The remaining rows present the differences in radial displacement between models with structural heterogeneities and the *Base* model. Each model shown assumes $\tilde{d}_{ice} = 25$ km. Tiger Stripes, the south polar circum-tectonic boundary (CTB), and chasma are labelled. Figure 2.3 shows the same models at a different time in Enceladus's orbit. To view model results for horizontal displacements at $t = 0$, refer to Supplementary section S1.7.

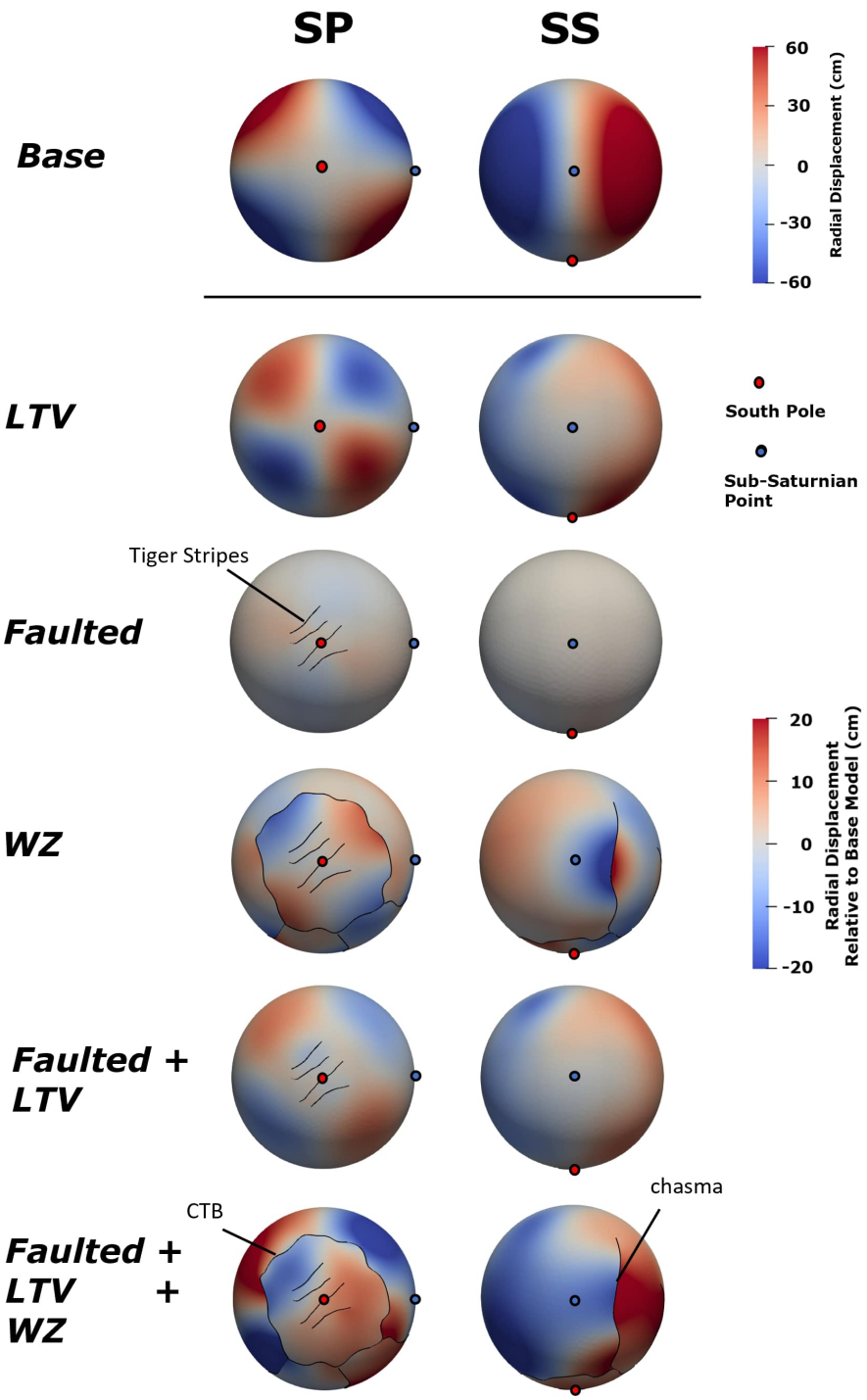

Figure 2.3: Snapshots of radial displacement from each model class viewed facing the South Pole (SP, left column) and the sub-Saturnian point (SS, right column) evaluated at $t = \frac{\pi}{2\omega}$. The top row shows the radial displacement in the *Base* model due to tidal forcing. The remaining rows present the differences in radial displacement between models with structural heterogeneities and the *Base* model. Each model shown assumes $\tilde{d}_{ice} = 25$ km. Tiger Stripes, the south polar circum-tectonic boundary (CTB), and chasma are labelled. Figure 2.2 shows the same models at a different time in Enceladus's orbit.

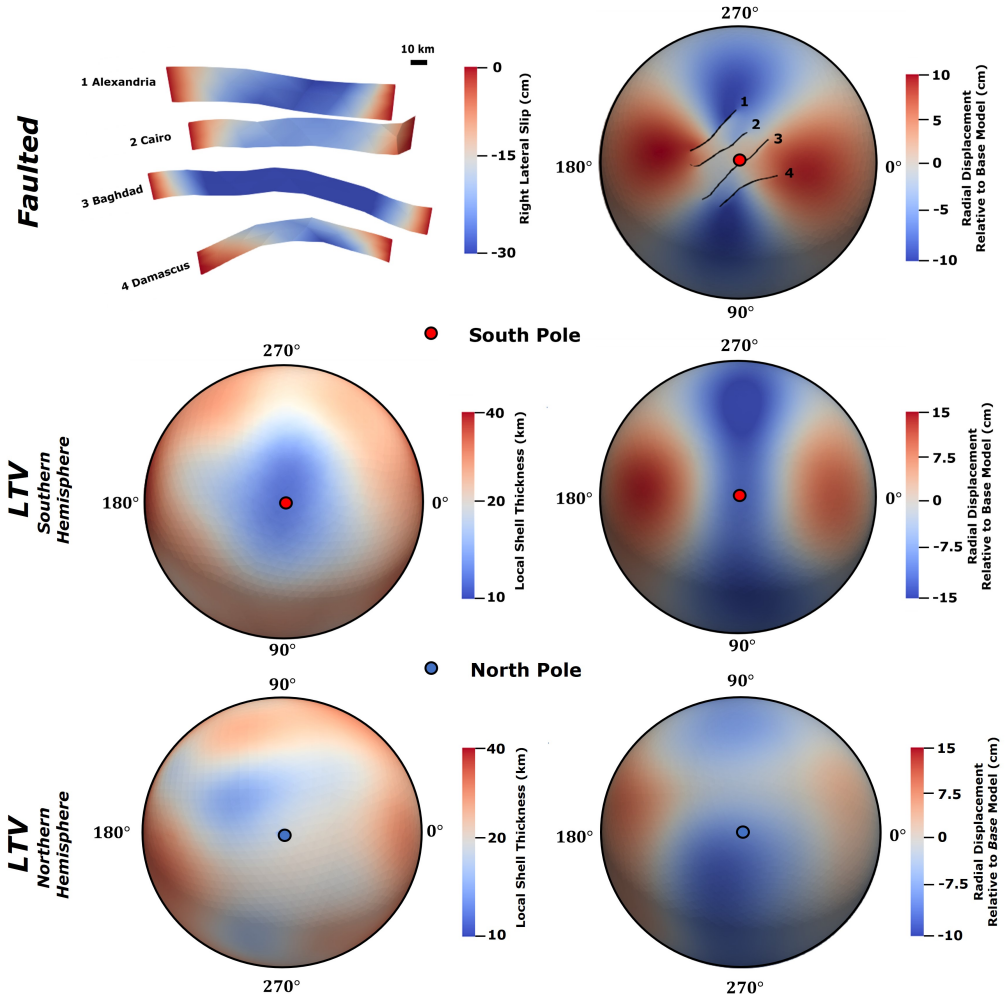

Figure 2.4: Snapshots of slip along the Tiger Stripes and regional thinning respectively corresponding to deformation shown in *Faulted* (top row) and *LTV* (center and bottom rows) models in Figure 2.2. The upper left image shows a perspective view of fault slip on the Tiger Stripes, where negative (blue) values indicate left-lateral slip. The upper right shows a south polar projection (where 0° corresponds to the sub-Saturnian longitude), with fault locations overlaid on radial displacements (this is rescaled from the third row of Figure 2.2). The center and bottom rows respectively show images of polar projections showing crustal thickness variations (left) and radial displacements (right) evaluated from the *LTV* model (i.e., rescaled from the second row of Figure 2.2) in the Northern and Southern Hemispheres. Local thickness values are plotted in $\log_{10}$ scale. Each model shown assumes $\tilde{d}_{ice}$ = 25 km and is evaluated at t = 0 (periapse). South and North Poles marked for reference. Longitude labels denote degrees East of the sub-Saturnian point. See Supplementary Figure 2.14 or an additional plot of crustal thickness variations used for *LTV* models.

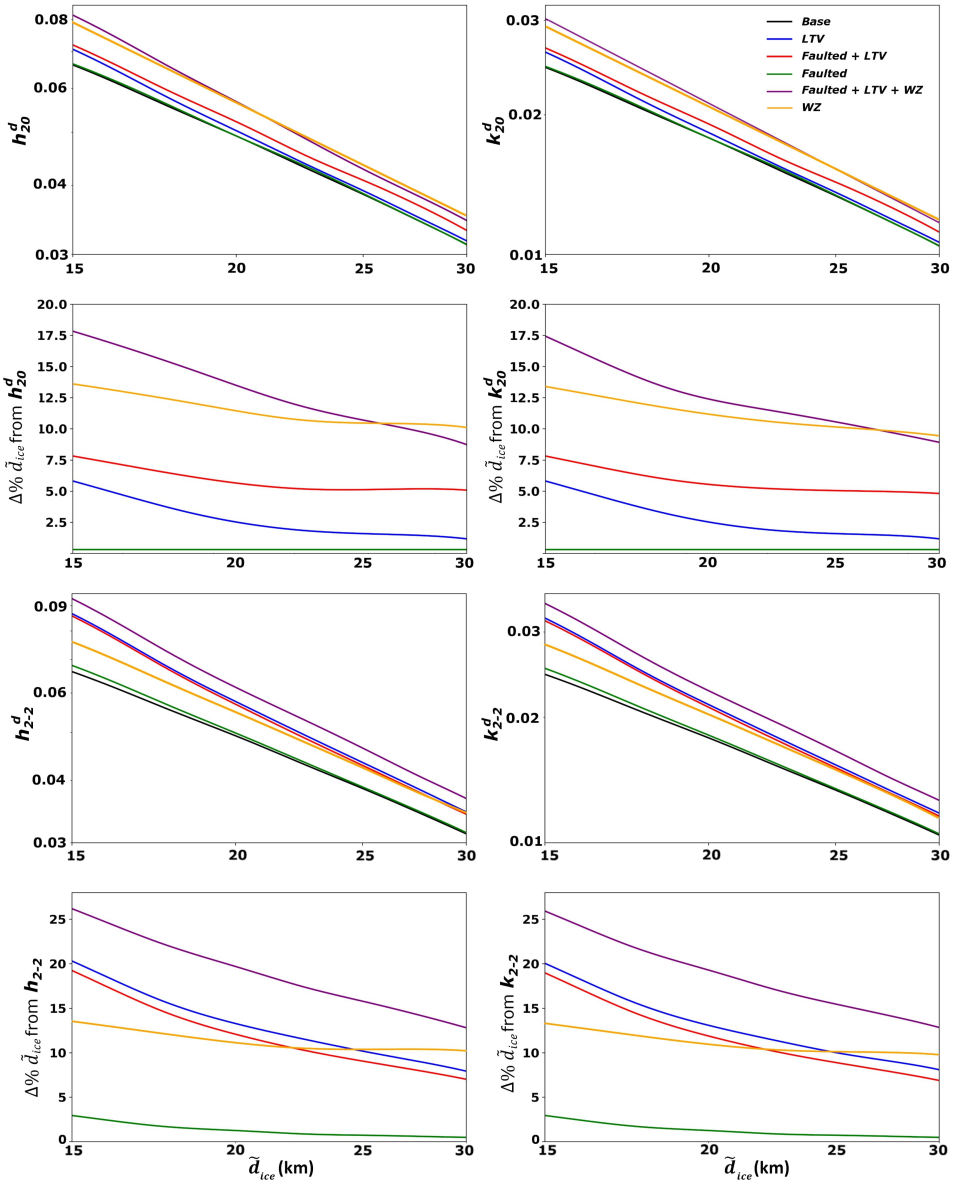

Figure 2.5: The relationship between deformation and mean ice shell thickness, $\tilde{d}_{ice}$. First row: h^d_{20} and k^d_{20} vs. $\tilde{d}_{ice}$ for *Base* models (black lines), *LTV* models (blue lines), *Faulted* models (red lines), *Faulted+LTV* models (green lines), and *Faulted+LTV+WZ* (purple lines). We plot both axes in $\log_{10}$ scale and generate curves by evaluating h^d_{20} and k^d_{20} at t=0 (periapse) for 40 equally spaced $\tilde{d}_{ice}$ values between 15 and 30 km. Second row: Percentage range of $\tilde{d}_{ice}$ values corresponding to a fixed Love number values for each model category relative to the *Base* model. Curves in these plots are generated by evaluating $\Delta\%\tilde{d}_{ice}$ from Equation 2.11. X-axes are plotted in $\log_{10}$ scale. Third and Fourth Rows: similar to first and second rows (respectively) but for $h^d_{2\text{-}2}$ and $k^d_{2\text{-}2}$ evaluated at $t = \frac{\pi}{2\omega}$.

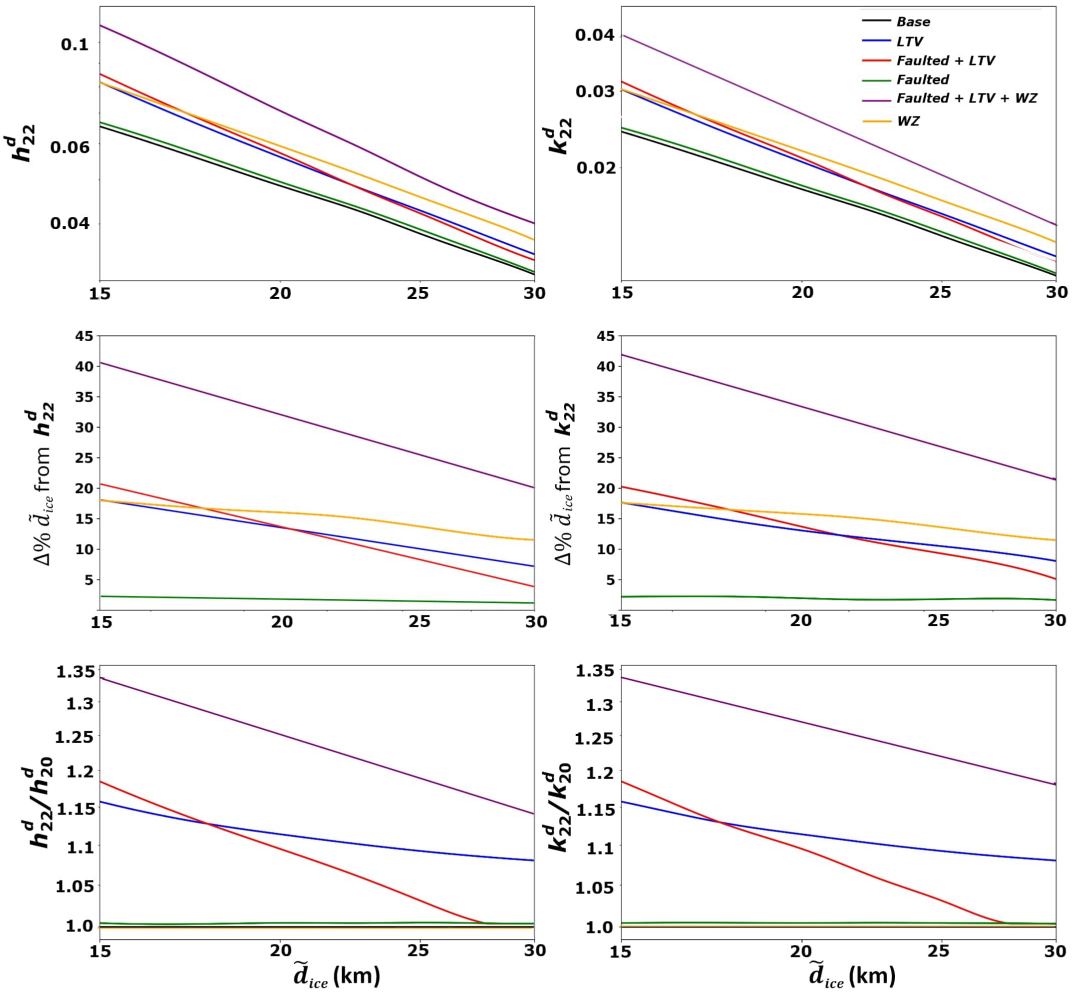

Figure 2.6: First row: Similar to first row of Figure 2.5 but for h^d_{22} and k^d_{22} instead of h^d_{20} and k^d_{20}. Second row: Similar to second row of Figure 2.5 for h^d_{22} and k^d_{22} instead of h^d_{20} and k^d_{20}. Third Row: 'order-splitting' associated with l = 2 Love numbers. We evaluate k^d_{22} and h^d_{22} or k^d_{20} and h^d_{20} at t=0 (periapse) for 40 equally spaced $\tilde{d}_{ice}$ values between 15 and 30 km to compute k^d_{22}/k^d_{20} and h^d_{22}/h^d_{20}. X-axes are plotted in $\log_{10}$ scale.

2.5 Discussion

We explore the dependence of diurnal Love number values on the presence of structural heterogeneities and $\tilde{d}_{ice}$ at Enceladus. Of the simplified structural heterogeneities considered, weak zones appear to have the most significant impact on the diurnal response of the ice shell to tides across the range of possible $\tilde{d}_{ice}$ (15–30 km) at Enceladus. The large spatial extent of the weak zones (i.e., 200–500 km in length or comparable to the radial length scale of Enceladus) and capacity to accommodate both additional normal- and shear-strain drives higher Love number values than those produced from the presence of variations in the thickness of the crust and faults in isolation. We find that for cases with less pronounced weak zones (i.e., where $G_{WZ}/G > 10^{-5}$), the amplification of deformation drops dramatically (see Supplementary section S1.4 of this chapter for details). These findings are consistent with results from Souček et al. (2016) and Behounkova et al. (2017) despite differences in the implementation of weak zones between the respective models (see section 2.4).

The diurnal response of Enceladus to eccentricity tides is also highly sensitive to variations in the thickness of the ice crust. *LTV* models show deviation in inferred $\tilde{d}_{ice}$ values relative to *Base* models of up to 20%. The amplification of deformation in thinned regions (see Figures 2.2 and 2.4) is highly dependent on $\tilde{d}_{ice}$. As $\tilde{d}_{ice}$ approaches 15 km, ice shell thickness approaches zero locally and strain increases rapidly near the South Pole. The resulting enhanced deformation drives the observed large increase in Love numbers at $\tilde{d}_{ice} < 20$ km (Figure 2.5 and 2.6).

As implemented here, faults have less impact on long-wavelength deformation than do variations in the thickness of the ice crust or weak zones. Fault structures in isolation bias inferred $\tilde{d}_{ice}$ values from diurnal Love number values by up to 3%—rather insignificant. This observation follows from Figures 2.2 and 2.4 which shows that fault-induced deformation creates a strong double-couple deformation pattern as expected from slip on Tiger Stripes. Slip-induced deformation produces substantial radial displacement at scales comparable to the size of associated faults but reduced displacement at longer wavelengths. As such, for the Tiger Stripes along-fault slip only modestly increases diurnal Love number values. Moreover, we expect the influence of Tiger Stripe slip on diurnal Love number values to decrease as maximum principal stresses rotate around the South Pole and fault slip decreases (see Figure 2.3).

We find significant order-splitting (i.e., $k^d_{22}/k^d_{20} \neq 1$ and $h^d_{22}/h^d_{20} \neq 1$) in models

with structural heterogeneities. Moreover, Figures 2.2 and 2.6 suggest k_{22}^d/k_{20}^d and h_{22}^d/h_{20}^d are highly sensitive to the scale of non-spherically symmetric structure near the South Pole. For *LTV* models, radial displacement patterns exhibit strong, long-wavelength quadrupole symmetry about the South Pole (i.e., generating an $m = 2$ pattern) causing larger values of k_{22}^d/k_{20}^d and h_{22}^d/h_{20}^d. In contrast, slip along Tiger Stripe faults produces shorter-wavelength quadrupole deformation resulting in relatively smaller values of k_{22}^d/k_{20}^d and h_{22}^d/h_{20}^d. In *Faulted+LTV* models, slip-induced short wavelength deformation dominantly accommodates strain when $\tilde{d}_{ice}$ >25 km (i.e., resulting in k_{22}^d/k_{20}^d values trending towards 1, whereas at smaller values of $\tilde{d}_{ice}$, the effect of LTVs dominate such that k_{22}^d/k_{20}^d and $h_{22}^d/h_{20}^d >> 1$). Weak zones combined with lateral variations in thickness (i.e., in *Faulted+LTV+WZ* models) produce the highest levels of quasi-quadrupole deformation near the South Pole and so drive the largest values of k_{22}^d/k_{20}^d and h_{22}^d/h_{20}^d (up to $\sim$ 1.35 or 35%).

The non degree-2 deformation patterns visible for our range of models (see Figures 2.2 - 2.4) imply that significant mode coupling occurs when structural heterogeneities are present in the crust of Enceladus (see Introduction; Qin et al., 2014; Zhong et al., 2021; Lau et al., 2015). Consistent with Love number results in Figures 2.5 - 2.6, we find that the lateral extent of structural heterogeneities scales with the spatial wavelength of non degree-2 deformation (see Supplementary section S1.5 of this chapter for details). We expect that spatial variations in the rheological properties along faults or weak zones (e.g., changes in the shear modulus, the coefficient of static friction) complicate inferences of $\tilde{d}_{ice}$ from non-degree 2 tidal deformation produced by these structures. However, the impact of lateral variations in crustal thickness on displacement fields (e.g., Love numbers and mode coupling) is more uniquely sensitive to $\tilde{d}_{ice}$ at Enceladus (see previous discussion and Figures 2.5 and 2.6). Inferring both $\tilde{d}_{ice}$ and lateral variations in crustal thickness from deformation evaluated across multiple spatial wavelengths is therefore a compelling topic for future research, but is beyond the scope of the current work.

The predicted amplitude of tidally-driven radial surface displacements falls within a readily measurable range at Enceladus. Figures 2.2, 2.3, 2.5, and 2.6 show that the maximum amplitude of the time-variable component of radial surface displacement is approximately 50 – 150 cm, with differences of 5 – 20 cm between models. The maximal values for the time-variable components of horizontal displacement also differ between models, with a range of 15 – 20 cm relative to background values of about 5 – 10 cm near the South Pole (see Supplementary section S1.7 of this

chapter). These values are substantially larger than the demonstrated sensitivity of Interferometric Synthetic Apreture Radar (InSAR) to measurements of ground displacement (e.g., Simons and Rosen, 2015). Moreover, radial surface displacements of 5 – 20 cm can induce 2 – 80 μGal time-variable gravity anomalies which is greater than the expected detection limit of gravity measurements acquired from line-of-sight tracking between multiple orbiting spacecraft (e.g., Ramillien et al., 2004 and Dai et al., 2016). An orbiting spacecraft capable of repeated geodetic measurements over several months could gather snapshots of gravity and the radial position of the surface at multiple points over Enceladus. This data could be analyzed to create a quasi-continuous time-series of geodetic signals over the body, enabling computation of h^d_{2m} and k^d_{2m}. Therefore, a dedicated geodetic mission to Enceladus could be envisioned to acquire the necessary measurements for analyzing diurnal tides as discussed in this work.

We ignore the potential impact of lateral variations in elastic moduli on tidal deformation. However, the elastic shear modulus of ice in Enceladus's crust is sensitive to the $\sim 40^{\circ}$K elevated temperature over the SPT (Howett et al., 2010). A ~ 40 K temperature variation corresponds to a change in ice shear modulus of about 2 - 3% (Proctor, 1966; Neumeier, 2018). For comparison, variations in crustal thickness of up to 100% of $\tilde{d}_{ice}$ near the SPT in *LTV* model alters Love numbers by up to $\sim$ 20% (see Figures 2.5 - 2.6). The impact of variations in elastic shear modulus on Love numbers is similar to that corresponding to the presence of lateral variations in crustal thickness (Wahr et al., 2006 cf. Equation 4-9). We therefore expect that variations in shear modulus of 2 - 3% over the SPT induce $\sim$ 0.1 - 0.2% (i.e., essentially negligible) differences in Love number values for Enceladus.

We assume a density structure for the crust and ocean (see Table 2.1), however the ocean density, ρ_w, is particularly uncertain. This uncertainty biases inferred values of $\tilde{d}_{ice}$ derived from diurnal Love numbers since ρ_w scales the restoring force at the ice-ocean interface (see section 2.2 and Supplementary section S1.1 of this chapter). Uncertainties in estimates of ρ_w are approximately 5% (i.e., ρ_w = 1000–1050 kg/m^3; Čadek et al., 2016) and thus uncertainty in ρ_w can modify diurnal Love numbers by up to 4%. Propagated uncertainty from imprecise estimates of ρ_w is therefore slightly larger than model uncertainty associated with the presence of Tiger Stripes (3%) but substantially smaller than that produced from neglecting the potential influence of weak zones or variations in ice shell thickness. Moreover, changing the input value of ρ_w should not produce order-splitting and so does not

alter inferences of short-wavelength shell structure from comparisons of diurnal Love numbers.

Spherically symmetric (i.e., 1D) models for tidal deformation can adequately describe the relationship between Love numbers and $\tilde{d}_{ice}$ for many ocean worlds (Wahr et al., 2006). For example, Europa and Ganymede exhibit relatively small amplitudes of lateral variations in crustal thickness ($\sim$ a few km) compared to likely mean thickness values $>$ 20 km (McKinnon and Melosh, 1980; Howell, 2021). These two worlds also lack discernible large-scale fault structures or weak zones (Hoppa et al., 2000; McKinnon and Melosh, 1980; Cameron et al., 2019). As such, the use of 3D models to improve estimates of $\tilde{d}_{ice}$ is not necessary for these bodies since the inherent uncertainty posed by imperfect estimates of bulk structure (e.g., ocean density, Nimmo et al., 2007) is likely to outweigh that arising from the presence of structural heterogeneities. In contrast, structural heterogeneities at Enceladus drive a $\sim$20-40% change in Love numbers which is much greater than the previously discussed $<$ 5% uncertainty posed by the impact of uncertainty in ocean density or elastic moduli (Howett et al., 2010; Čadek et al., 2016). Thus, 3D models are crucial for using tidal deformation to characterize $\tilde{d}_{ice}$ at Enceladus.

2.6 Conclusion

We evaluate the relationship between mean ice shell thickness, $\tilde{d}_{ice}$, and diurnal Love numbers for a range of shell models with structural heterogeneities. We find that structural heterogeneities at Enceladus broaden the range of possible $\tilde{d}_{ice}$ values corresponding to a measured Love number by about 41% in the most extreme case. The maximal range of plausible $\tilde{d}_{ice}$ values increases less than 30% for $\tilde{d}_{ice}$ values above 20 km (likely values of $\tilde{d}_{ice}$ at Enceladus are between 21–26 km; Thomas et al., 2016). Moreover, if weak zones are not present then the range of plausible $\tilde{d}_{ice}$ values further reduces to less than $\sim$ 20%. As such, we demonstrate that analysis of diurnal tides could serve as a useful tool for characterizing interior structure from future geodetic investigations at Enceladus.

2.7 Open Research

The data used in this study were generated using the software package PyLith (Aagaard et al., 2007; Aagaard et al., 2022). PyLith is an open-source finite element code for modeling geodynamic processes and is available on GitHub and Zenodo repositories (Aagaard et al., 2022). The specific PyLith version used in this study was v2.2.2. PyLith input files, post-processing scripts, and selected output files for

this work are available on (Berne et al., 2023). The mesh geometries utilized in this study were created using CUBIT (v15.2), a node-locked licensed software which is available through the developer Sandia National Laboratories (Skroch et al., 2019; CoreForm, 2020).

2.8 Acknowledgements

We would like to express our gratitude to the reviewers and editors for their valuable contributions in revising content in this chapter. This research was supported by the Future Investigators in NASA Earth and Space Science and Technology (FINESST) Program (80NSSC22K1318). We also thank the Keck Institute for Space Studies (KISS) at California Institute of Technology for organizing two workshops about "Next-Generation Planetary Geodesy" which provided insight, expertise, and discussions that greatly assisted the research. We also thank Matthew Knepley, Brad Aagaard, and Charles Williams for providing invaluable advice to modify PyLith for the simulations described this work. A portion of this research was supported by a Strategic Research and Technology Development task led by James T. Keane and Ryan S. Park at the Jet Propulsion Laboratory, California Institute of Technology, under a contract with the National Aeronautics and Space Administration (80NM0018D0004).

References

Aagaard, B., C. Williams, and M. Knepley (2007). "PyLith: A Finite-Element Code for Modeling Quasi-Static and Dynamic Crustal Deformation". In: *Eos* 88(52).

Aagaard, B., C. Williams, and M. Knepley (2022). "PyLith: A Finite-Element Code for Modeling Quasi-Static and Dynamic Crustal Deformation". In: *geodynamics/pylith v2.2.2 (v2.2.2) [Computer software]. Zenodo,https://doi.org/10.5281/zenodo.3269486* .

Akiba, R., A. I. Ermakov, and B. Militzer (2022). "Probing the Icy Shell Structure of Ocean Worlds with Gravity–Topography Admittance". In: *The Planetary Science Journal* 3 (3). DOI: 10.3847/psj/ac4d2b.

Behounkova, M., O. Soucek, J. Hron, and O. Cadec (2017). "Plume activity and tidal deformation on enceladus influenced by faults and variable ice shell thickness". In: *Astrobiology* 17.9. ISSN: 15311074. DOI: 10.1089/ast.2016.1629.

Berne, A., M. Simons, J. T. Keane, and R. S. Park (2023a). "Inferring the Mean Thickness of the Outer Ice Shell of Enceladus From Diurnal Crustal Deformation". In: *Journal of Geophysical Research: Planets* 128 (6).

Berne, A., M. Simons, J. T. Keane, and R. S. Park (2023b). “Using Tidally Driven Elastic Strains to Infer Regional Crustal Thickness and Ocean Salinity at Enceladus”. In: *54th Lunar and Planetary Science Conference*. Vol. 2806, p. 1899.

Beuthe, M. (2018). “Enceladus’s crust as a non-uniform thin shell: I tidal deformations”. In: *Icarus* 302. ISSN: 10902643. DOI: 10.1016/j.icarus.2017.11.009.

Čadek, O., G. Tobie, T. Van-Hoolst, A. Lefèvre, G. Mitri, M. Běhounková, and A. Trinh (2016). “Enceladus’s internal ocean and ice shell constrained from Cassini gravity, shape, and libration data”. In: *Geophysical Research Letters* 43 (11). ISSN: 19448007. DOI: 10.1002/2016GL068634.

Cameron, M. E., B. R. Smith-Konter, G. C. Collins, D. A. Patthoff, and R. T. Pappalardo (2019). “Tidal stress modeling of Ganymede: Strike-slip tectonism and Coulomb failure”. In: *Icarus* 319. ISSN: 10902643. DOI: 10.1016/j.icarus.2018.09.002.

Choblet, G., G. Tobie, C. Sotin, M. Běhounková, O. Čadek, F. Postberg, and O. Souček (2017). “Powering prolonged hydrothermal activity inside Enceladus”. In: *Nature Astronomy* 1 (12). ISSN: 23973366. DOI: 10.1038/s41550-017-0289-8.

Conrad, J. W., F. Nimmo, P. M. Schenk, W. B. McKinnon, J. M. Moore, C. B. Beddingfield, R. A. Beyer, K. D. Runyon, L. A. Young, S. A. Stern, H. A. Weaver, C. B. Olkin, and K. Ennico (2019). “An upper bound on Pluto’s heat flux from a lack of flexural response of its normal faults”. In: *Icarus* 328. ISSN: 10902643. DOI: 10.1016/j.icarus.2019.03.028.

CoreForm (2020). “ "CUBIT" https://coreform.com/products/coreform-cubit/ ”. In.

Dahlen, F. A. and J. Tromp (1998). *Theoretical global seismology*. DOI: 10.1063/1.882788.

Dai, C., C. K. Shum, J. Guo, K. Shang, B. Tapley, and R. Wang (2016). “Improved source parameter constraints for five undersea earthquakes from north component of GRACE gravity and gravity gradient change measurements”. In: *Earth and Planetary Science Letters* 443. ISSN: 0012821X. DOI: 10.1016/j.epsl.2016.03.025.

Durham, W. B., W. B. McKinnon, and L. A. Stern (2005). “Cold compaction of water ice”. In: *Geophysical Research Letters* 32 (18). ISSN: 00948276. DOI: 10.1029/2005GL023484.

Ermakov, A. I., R. S. Park, J. Roa, J. C. Castillo-Rogez, J. T. Keane, F. Nimmo, E. S. Kite, C. Sotin, T. J. W. Lazio, G. Steinbrügge, S. M. Howell, B. G. Bills, D. J. Hemingway, V. Viswanathan, G. Tobie, and V. Lainey (2021). “A Recipe for the Geophysical Exploration of Enceladus”. In: *Planetary Science Journal* 2 (4). ISSN: 26323338. DOI: 10.3847/PSJ/ac06d2.

Goldreich, P. M. and J. L. Mitchell (2010). "Elastic ice shells of synchronous moons: Implications for cracks on Europa and non-synchronous rotation of Titan". In: *Icarus* 209 (2). ISSN: 00191035. DOI: 10.1016/j.icarus.2010.04.013.

Hansen, C. J., L. Esposito, A. I. Stewart, J. Colwell, A. Hendrix, W. Pryor, and R. Wast (2006). "Enceladus' water vapor plume". In: *Science* 311 (5766). ISSN: 00368075. DOI: 10.1126/science.1121254.

Hay, H. C. and I. Matsuyama (2019). "Nonlinear tidal dissipation in the subsurface oceans of Enceladus and other icy satellites". In: *Icarus* 319. ISSN: 10902643. DOI: 10.1016/j.icarus.2018.09.019.

Hemingway, D. and I. Matsuyama (2017). "Isostatic equilibrium in spherical coordinates and implications for crustal thickness on the Moon, Mars, Enceladus, and elsewhere". In: *Geophysical Research Letters* 44.15. ISSN: 19448007. DOI: 10.1002/2017GL073334.

Hemingway, D. and T. Mittal (2019). "Enceladus's ice shell structure as a window on internal heat production". In: *Icarus* 332. ISSN: 10902643. DOI: 10.1016/j.icarus.2019.03.011.

Hoppa, G., R. Greenberg, B. R. Tufts, P. Geissler, C. Phillips, and M. Milazzo (2000). "Distribution of strike-slip faults on Europa". In: *Journal of Geophysical Research E: Planets* 105.E9. ISSN: 01480227. DOI: 10.1029/1999JE001156.

Howell, S. M. (2021). "The likely thickness of europa's icy shell". In: *Planetary Science Journal* 2.4. ISSN: 26323338. DOI: 10.3847/PSJ/abfe10.

Howett, C. J., J. R. Spencer, J. Pearl, and M. Segura (2010). "Thermal inertia and bolometric Bond albedo values for Mimas, Enceladus, Tethys, Dione, Rhea and Iapetus as derived from Cassini/CIRS measurements". In: *Icarus* 206 (2). ISSN: 00191035. DOI: 10.1016/j.icarus.2009.07.016.

Hubbard, W. B. and J. D. Anderson (1978). "Possible flyby measurements of Galilean satellite interior structure". In: *Icarus* 33 (2). ISSN: 10902643. DOI: 10.1016/0019-1035(78)90153-7.

Hurford, T. A., P. Helfenstein, G. V. Hoppa, R. Greenberg, and B. G. Bills (2007). "Eruptions arising from tidally controlled periodic openings of rifts on Enceladus". In: *Nature* 447 (7142). ISSN: 14764687. DOI: 10.1038/nature05821.

Iess, L., D. J. Stevenson, M. Parisi, D. Hemingway, R. A. Jacobson, J. I. Lunine, and P. Tortora (2014). "The gravity field and interior structure of Enceladus". In: *Science* 344.6179. ISSN: 10959203. DOI: 10.1126/science.1250551.

Ingersoll, S. P. Ewald, and S. K. Trumbo (2020). "Time variability of the Enceladus plumes: Orbital periods, decadal periods, and aperiodic change". In: *Icarus* 344. ISSN: 10902643. DOI: 10.1016/j.icarus.2019.06.006.

Ingersoll and M. Nakajima (2016). "Controlled boiling on Enceladus. 2. Model of the liquid-filled cracks". In: *Icarus* 272. ISSN: 10902643. DOI: 10.1016/j.icarus.2015.12.040.

Jaccard, C. (1976). "P. V. Hobbs Ice physics. Oxford, Clarendon Press, 1974. xvii, 837 p. £29." In: *Journal of Glaciology* 17 (75). ISSN: 0022-1430. DOI: 10.3189/s0022143000030847.

Lau, H. C., H. Y. Yang, J. Tromp, J. X. Mitrovica, K. Latychev, and D. Al-Attar (2015). "A normal mode treatment of semi-diurnal body tides on an aspherical, rotating and anelastic Earth". In: *Geophysical Journal International* 202 (2). ISSN: 1365246X. DOI: 10.1093/gji/ggv227.

Levinson, M. (1981). "A new rectangular beam theory". In: *Journal of Sound and Vibration* 74 (1). ISSN: 10958568. DOI: 10.1016/0022-460X(81)90493-4.

Love, A. E. H. (1909). "The yielding of the earth to disturbing forces". In: *Proceedings of the Royal Society of London. Series A, Containing Papers of a Mathematical and Physical Character* 82 (551). ISSN: 0950-1207. DOI: 10.1098/rspa.1909.0008.

Mancktelow, N. S. (1999). "Finite-element modelling of single-layer folding in elasto-viscous materials: The effect of initial perturbation geometry". In: *Journal of Structural Geology* 21 (2). ISSN: 01918141. DOI: 10.1016/S0191-8141(98)00102-3.

McKinnon, W. B. (2015). "Effect of Enceladus's rapid synchronous spin on interpretation of Cassini gravity". In: *Geophysical Research Letters* 42 (7). ISSN: 19448007. DOI: 10.1002/2015GL063384.

McKinnon, W. B. and H. J. Melosh (1980). "Evolution of planetary lithospheres: Evidence from multiringed structures on Ganymede and Callisto". In: *Icarus* 44.2. ISSN: 00191035. DOI: 10.1016/0019-1035(80)90037-8.

Melosh, H. J. and A. Raefsky (1981). "A simple and efficient method for introducing faults into finite element computations". In: *Bulletin of the Seismological Society of America* 71.5. ISSN: 0037-1106. DOI: 10.1785/bssa0710051391.

Mitri, G. and A. P. Showman (Oct. 2005). "Convective–conductive transitions and sensitivity of a convecting ice shell to perturbations in heat flux and tidal-heating rate: Implications for Europa". In: *Icarus* 177.2, pp. 447–460. ISSN: 0019-1035. DOI: 10.1016/J.ICARUS.2005.03.019.

Murray, C. D. and S. F. Dermott (2000). *Solar System Dynamics*. DOI: 10.1017/cbo9781139174817.

Neumeier, J. J. (2018). "Elastic Constants, Bulk Modulus, and Compressibility of H2O Ice i h for the Temperature Range 50 K-273 K". In: *Journal of Physical and Chemical Reference Data* 47 (3). ISSN: 00472689. DOI: 10.1063/1.5030640.

Nimmo, F., B. G. Bills, and P. C. Thomas (2011). "Geophysical implications of the long-wavelength topography of the Saturnian satellites". In: *Journal of Geophysical Research E: Planets* 116.11. ISSN: 01480227. DOI: 10.1029/2011JE003835.

Nimmo, F. and R. Pappalardo (2004). "Furrow flexure and ancient heat flux on Ganymede". In: *Geophysical Research Letters* 31 (19). ISSN: 00948276. DOI: 10.1029/2004GL020763.

Nimmo, F., P. C. Thomas, R. T. Pappalardo, and W. B. Moore (2007). "The global shape of Europa: Constraints on lateral shell thickness variations". In: *Icarus* 191 (1). ISSN: 00191035. DOI: 10.1016/j.icarus.2007.04.021.

Porco, D. Dinino, and F. Nimmo (2014). "How the geysers, tidal stresses, and thermal emission across the south polar terrain of Enceladus are related". In: *Astronomical Journal* 148 (3). ISSN: 00046256. DOI: 10.1088/0004-6256/148/3/45.

Porco, P. Helfenstein, P. C. Thomas, A. P. Ingersoll, J. Wisdom, R. West, and S. Squyres (2006). "Cassini observes the active south pole of enceladus". In: *Science* 311 (5766). ISSN: 00368075. DOI: 10.1126/science.1123013.

Proctor, T. M. (1966). "Low-Temperature Speed of Sound in Single-Crystal Ice". In: *Journal of the Acoustical Society of America* 39 (5A). ISSN: NA. DOI: 10.1121/1.1909980.

Qin, C., S. Zhong, and J. Wahr (2014). "A perturbation method and its application: Elastic tidal response of a laterally heterogeneous planet". In: *Geophysical Journal International* 199 (2). ISSN: 1365246X. DOI: 10.1093/gji/ggu279.

Ramillien, G., A. Cazenave, and O. Brunau (2004). "Global time variations of hydrological signals from GRACE satellite gravimetry". In: *Geophysical Journal International* 158 (3). ISSN: 0956540X. DOI: 10.1111/j.1365-246X.2004.02328.x.

Roberts, J. H. and F. Nimmo (Apr. 2008). "Tidal heating and the long-term stability of a subsurface ocean on Enceladus". In: *Icarus* 194.2, pp. 675–689. ISSN: 0019-1035. DOI: 10.1016/J.ICARUS.2007.11.010.

Rovira-Navarro, M., R. F. Katz, Y. Liao, W. van der Wal, and F. Nimmo (2022). "The Tides of Enceladus' Porous Core". In: *Journal of Geophysical Research: Planets* 127 (5). ISSN: 21699100. DOI: 10.1029/2021JE007117.

Schenk, P. M. (2008). "Cartographic and Topographic Mapping of the Icy Satellites of the Outer Solar System". In: *International Archives of the Photogrammetry, Remote Sensing and Spatial Information Sciences* 37.

Schenk, P. M., R. N. Clark, C. J. A. Howett, A. J. Verbiscer, and J. H. Waite (2018). *Enceladus and the Icy Moons of Saturn*. DOI: 10.2458/azu_uapress_9780816537075.

Schubert, G., J. D. Anderson, B. J. Travis, and J. Palguta (2007). "Enceladus: Present internal structure and differentiation by early and long-term radiogenic heating". In: *Icarus* 188.2. ISSN: 00191035. DOI: 10.1016/j.icarus.2006.12.012.

Segall, P. (2010). *Earthquake and volcano deformation*. DOI: 10.5860/choice.48-0287.

Shaw, G. H. (1985). "Elastic properties and equation of state of high pressure ice". In: *The Journal of Chemical Physics* 84 (1). ISSN: 00219606. DOI: 10.1063/1.449897.

Simons, M. and P. A. Rosen (2015). "Interferometric Synthetic Aperture Radar Geodesy". In: *Treatise on Geophysics: Second Edition*. Vol. 3. DOI: 10.1016/B978-0-444-53802-4.00061-0.

Skroch, M., S. Owen, M. Staten, R. Quadros, B. Hanks, B. Clark, and C. Stimpson (2019). *CUBIT Geometry and Mesh Generation Toolkit 15.4 User Documentation*.

Sládková, K. P., O. Souček, and M. Běhounková (2021). "Enceladus' Tiger Stripes as Frictional Faults: Effect on Stress and Heat Production". In: *Geophysical Research Letters* 48 (19). ISSN: 19448007. DOI: 10.1029/2021GL094849.

Souček, O., M. Běhounková, O. Čadek, J. Hron, G. Tobie, and G. Choblet (2019). "Tidal dissipation in Enceladus' uneven, fractured ice shell". In: *Icarus* 328. ISSN: 10902643. DOI: 10.1016/j.icarus.2019.02.012.

Souček, O., J. Hron, M. Běhounková, and O. Čadek (2016). "Effect of the tiger stripes on the deformation of Saturn's moon Enceladus". In: *Geophysical Research Letters* 43.14. ISSN: 19448007. DOI: 10.1002/2016GL069415.

Spencer, J. R., J. C. Pearl, M. Segura, F. M. Flasar, A. Mamoutkine, P. Romani, and R. M. Lopes (2006). "Cassini encounters Enceladus: Background and the discovery of a south polar hot spot". In: *Science* 311 (5766). ISSN: 00368075. DOI: 10.1126/science.1121661.

Thomas, P. C., R. Tajeddine, M. S. Tiscareno, J. A. Burns, J. Joseph, T. J. Loredo, and C. Porco (2016). "Enceladus's measured physical libration requires a global subsurface ocean". In: *Icarus* 264. ISSN: 10902643. DOI: 10.1016/j.icarus.2015.08.037.

Tyler, R. H. (2020). "Heating of Enceladus due to the dissipation of ocean tides". In: *Icarus* 348. ISSN: 10902643. DOI: 10.1016/j.icarus.2020.113821.

Van Hoolst, T., R. M. Baland, and A. Trinh (2016). "The diurnal libration and interior structure of Enceladus". In: *Icarus* 277. ISSN: 10902643. DOI: 10.1016/j.icarus.2016.05.025.

Vance, S., M. Behounkova, B. G. Bills, P. Byrne, O. Cadek, J. Castillo-Rogez, G. Choblet, K. Hughson, T. Hurford, S. Kedar, J. Keane, E. Kite, A. H. Lobo, A. G. Marusiak, M. M. Daswani, M. P. Panning, R. S. Park, B. E. Schmidt, K. Sladkova, K. M. Soderlund, C. Sotin, O. Soucek, S. Stähler, G. Steinbrügge, S. Tharimena, A. Thompson, G. Tobie, W. Song, and S. Wang (2021). "Distributed Geophysical Exploration of Enceladus and Other Ocean Worlds". In: *Bulletin of the AAS* 53 (4). DOI: 10.3847/25c2cfeb.a07234f4.

Wahr, J., Z. A. Selvans, M. E. Mullen, A. C. Barr, G. C. Collins, M. M. Selvans, and R. T. Pappalardo (2009). "Modeling stresses on satellites due to nonsynchronous rotation and orbital eccentricity using gravitational potential theory". In: *Icarus* 200.1. ISSN: 00191035. DOI: 10.1016/j.icarus.2008.11.002.

Wahr, J., M. T. Zuber, D. E. Smith, and J. I. Lunine (2006). "Tides on Europa, and the thickness of Europa's icy shell". In: *Journal of Geophysical Research E: Planets* 111.12. ISSN: 01480227. DOI: 10.1029/2006JE002729.

Yin, A. and R. Pappalardo (2015). "Gravitational spreading, bookshelf faulting, and tectonic evolution of the South Polar Terrain of Saturn's moon Enceladus". In: *Icarus* 260. ISSN: 10902643. DOI: 10.1016/j.icarus.2015.07.017.

Zhong, S., C. Qin, G. Geruo, and J. Wahr (2012). "Can tidal tomography be used to unravel the long-wavelength structure of the lunar interior?" In: *Geophysical Research Letters* 39 (15). ISSN: 00948276. DOI: 10.1029/2012GL052362.

Zolotov, M. Y. and E. L. Shock (2004). "A model for low-temperature biogeochemistry of sulfur, carbon, and iron on Europa". In: *Journal of Geophysical Research E: Planets* 109.6. ISSN: 01480227. DOI: 10.1029/2003JE002194.

2.9 Supplementary Information

S1

In S1, we describe the governing equations for our tidal loading boundary value problem and our solution method (1.1), benchmark our solutions against analytic and numerical tidal loading models (1.2), and verify that results on models with heterogeneities are not subject to inaccuracy due to our choice of mesh sizing parameters (1.3) or our choice of weak-zone elastic moduli (1.4). We also investigate the extent that structural heterogeneities that induce non degree-2 harmonics in radial displacement fields (1.5), examine whether the mean ice thickness tracked in this study (i.e., $\tilde{d}_{ice}$) approximates the thermal thickness of Enceladus's ice shell (1.6), and illustrate the impact of structural heterogeneities on horizontal displacements at Enceladus (1.7).

1.1 Governing Equations

1.1.1.1 Strong Form of the Equation of Motion

Following Aagaard et al. (2007), we formulate and solve a boundary value problem appropriate for tidal loading. We start by defining the strong form of the quasi-static equation of motion for a geometry with fault surfaces:

$$\sigma_{ij,j} + f_i = 0 \text{ in } W \tag{2.12a}$$

$$\sigma_{ij} n_j = T_i \text{ on } S, \tag{2.12b}$$

where i describe cartesian directions i for a body subject to stresses σ_{ij} and specific forces f_i over the volume W and T_i describes tractions on all surfaces S. We subdivide S into the surface at the outer domain boundary S_0, the surface at the inner (i.e., ice-ocean) domain boundary S_{int}, and surfaces corresponding to fault interfaces S_f of our geometry.

1.1.1.2 Constitutive Relation for Elasticity

We write a constitutive relation for elasticity (i.e., Hooke's law) using the rank-4 stiffness tensor C_{ijkl} to map displacements u_{kl} to stresses σ_{ij}. We assign parameters in C_{ijkl} that are appropriate for linear isotropic material with a shear modulus G and bulk modulus μ (see Table 2.3 of the main text; the symbol denotes derivative with respect to a direction):

$$\sigma_{ij} = C_{ijkl}(u_{k'l} + u_{l'k}). \tag{2.13}$$

1.1.1.3 Tidal Loading

Building on the procedure of Souček et al. (2016) (see S1), we formulate three components of tidal loading: 'body', 'ocean', and 'topographic' forces. We additionally treat a fourth 'self-gravitational' force for this work. As per Newton's second law, the body force f_i^b arising from diurnal tides is the gradient of the driving potential (i.e, see Equation 2.7 of the main text) scaled by ice density ρ_{ice} ($\mathbf{e}_i$ denotes the unit vector parallel to the evaluated direction):

$$f_i^b = \rho_{ice} \nabla V \cdot \mathbf{e}_i. \tag{2.14}$$

The ocean force is a traction T_i^o on S_{int} which scales the driving potential V with ocean density ρ_w ($\mathbf{e}_s$ denotes the unit vector perpendicular to the surface of the geometry):

$$T_i^o = \rho_w V (\mathbf{e}_s \cdot \mathbf{e}_i) \text{ on } S_{int}. \tag{2.15}$$

The topographic force arises from the traction induced by deformation at the boundaries of the domain (see Equation S5 in Souček et al., 2016). We form the topographic force by generating tractions on S_0 (i.e., $T_i^{t,0}$) and S_{int} (i.e., $T_i^{t,int}$). For small displacements, we can write $T_i^{t,int}$ and $T_i^{t,0}$ as a function of radial displacements at domain boundaries (i.e., $u_i(\mathbf{e}_i \cdot \mathbf{e}_s)$), ρ_{ice}, ρ_w, and gravitational acceleration at the inner and outer surfaces g_{int} and g_0 (see Table 2.3 in the main text):

$$T_i^{t,0} = u_i(\mathbf{e}_i \cdot \mathbf{e}_s)\rho_{ice} g_0 (\mathbf{e}_s \cdot \mathbf{e}_i) \text{ on } S_0 \tag{2.16a}$$

$$T_i^{t,int} = u_i(\mathbf{e}_i \cdot \mathbf{e}_s)(\rho_{ice} - \rho_w) g_{int} (\mathbf{e}_s \cdot \mathbf{e}_i) \text{ on } S_{int}. \tag{2.16b}$$

For the self-gravitational force, we evaluate a body force f_i^{sg} and a traction at the inner surface T_i^{sg}:

$$f_i^{sg} = \rho_{ice} \nabla V_{sg} \cdot \mathbf{e}_i \tag{2.17a}$$

$$T_i^{sg} = \rho_w V_{sg} (\mathbf{e}_i \cdot \mathbf{e}_s) \text{ on } S_{int}, \tag{2.17b}$$

where V_{sg} is a gravitational potential arising from deformation (i.e., mass movement) at the boundaries of the domain. To compute V^{sg}, we combine solutions to the Poisson's equation (i.e., potentials) arising from boundary displacements (i.e.,

V^{sg}_{int} and V^{sg}_{0}) that are expanded into spherical harmonics (i.e., via the linear transformation H_{qw} where q and w are spherical harmonic degree and order). We evaluate potentials at radial locations r. $\mathcal{G}$ is the universal gravitational constant (i.e., as discussed in Hemingway and Mittal (2019) cf. Equation 4). We ignore effects due to the changes in density on V^{sg}:

$$V^{sg} = V^{sg}_{int} + V^{sg}_{0} \tag{2.18}$$

$$V^{sg}_{int} = \sum_{l}\sum_{k} \frac{4\pi\mathcal{G}r}{2l+1}(\rho_w - \rho_{ice})\Big(\frac{R_0}{r}\Big)^{l+2} H_{qw} u_i(\mathbf{e}_i \cdot \mathbf{e}_s) \ \text{ on } S_{int} \tag{2.19a}$$

$$V^{sg}_{0} = \sum_{l}\sum_{k} \frac{4\pi\mathcal{G}r}{2l+1}\rho_{ice}\Big(\frac{r}{R_0 - \tilde{d}_{ice}}\Big)^{l-1} H_{qw} u_i(\mathbf{e}_i \cdot \mathbf{e}_s) \ \text{ on } S_0. \tag{2.19b}$$

1.1.1.4 Fault Displacement

To consider the impact of frictionless faults in the crust (e.g., Tiger Stripes) on deformation, we assume that fault surfaces within our geometry S_f are tractioless (i.e., dislocations fully cancel tidally-driven tractions along the fault plane). Following the formulation described in Segall, 2010 (Chapter 1), we relate displacements on either end of a fault surface (i.e., u^+_i and u^-_i) to tractions T^f_i over S_f according to:

$$T^f_i = C_{ijkl} M_{kli}(u^+_i - u^-_i) \cdot \mathbf{e}_i \ \text{ on } S_f, \tag{2.20}$$

where M_{kli} is a rank-3 tensor containing linear Green's functions relating slip to co-local strains along a fault plane in a 3D elastic medium (Segall, 2010). For this work, we ignore deformation arising from mode-1 crack displacement (i.e., fault opening or penetration, Aagaard et al., 2007). As such, we apply an additional constraint to 'clamp' motion normal to fault surfaces:

$$(u^+_i - u^-_i) \cdot \mathbf{e}_s = 0 \ \text{ on } S_f. \tag{2.21}$$

We assume 'clamped' fault surfaces based on the expectation that the magnitude of tidally-driven elastic stresses within Enceladus's ice shell (tens of kPa) is much smaller than the magnitude of hydrostatic normal stresses across the fault plane (a few MPa). We compute fault slip d_s by applying a rotation matrix R_{si} to transform vectors u^+_i and u^-_i from the global cartesian coordinate system to a local fault coordinate system:

$$d_s = R_{si}(u_i^+ - u_i^-) \text{ on } S_f. \tag{2.22}$$

1.1.2 Numerical Approximation and Solution Method

1.1.2.1 Weak Form of Equation of Motion

We construct the weak form of the quasi-static equation of motion by dotting the strong form of the equation of motion (Equation 2.12) with a weighting function ϕ_i:

$$\int_W (\sigma_{ij,j} + f_i)\ \phi_i\ dW = 0. \tag{2.23}$$

1.1.2.2 Galerkin Approach

Following the Galerkin approach, we formulate our weighting function ϕ_i as an n-dimensional combination of linear basis (i.e., shape) functions N^n scaled by coefficients c_i^n. We also formulate our trial solution (i.e., for displacement u_i) as an m-dimensional combination of linear basis functions N^m scaled by coefficients a_i^m:

$$\phi_i = \sum_n c_i^n N^n \tag{2.24a}$$

$$u_i = \sum_m a_i^m N^m. \tag{2.24b}$$

1.1.2.3 Assembly of Jacobian

Considering the divergence theorem for stresses in W, substituting our formulation for the weighting function (Equation 2.24), and recognizing that the equation of motion's weak form is equivalent to the strong form for arbitrary weighting function coefficients c_i^n allows us to rewrite Equation 2.23 as:

$$-\int_W \sigma_{ij} N^n_{,j} dW + \int_S T_i N^n dS + \int_W f_i N^n dW = 0. \tag{2.25}$$

We substitute forces, stresses, and tractions from the constitutive relation (Equation 4.2), our tidal loading formulation (Equations 2.14, 2.15, 2.16, and 2.17), and our numerical treatment of fault surfaces (Equations 2.20 and 2.22) into Equation 2.25 to formulate a Jacobian A_{ij}^{nm}. A_{ij}^{nm} is a superposition of tensors integrated over our domain volume ${}_W A_{ij}^{nm}$, outer surface ${}_{S_0} A_{ij}^{nm}$, inner surface ${}_{S_{int}} A_{ij}^{nm}$, and fault sufraces ${}_{S_f} A_{ij}^{nm}$. We replace the linear transformation H_{qw} and the radial position of the domain r with the rank-4 tensor H_{lknm} and the radial position of nodes r^n respectively:

$$A_{ij}^{nm} = {}_{W}A_{ij}^{nm} + {}_{S_0}A_{ij}^{nm} + {}_{S_{int}}A_{ij}^{nm} + {}_{S_f}A_{ij}^{nm} \tag{2.26}$$

$$\begin{aligned} {}_{W}A_{ij}^{nm} = \int_V (&\frac{1}{4}C_{ijqw}(N_{,w}^m + N_{,q}^m)(N_{,j}^n + N_{,i}^n) + (\rho_{ice}\nabla(\sum_l \sum_k \frac{4\pi\mathcal{G}r^n}{2l+1}((\rho_w - \rho_{ice}) \\ &H_{lknm}(\mathbf{e}_i \cdot \mathbf{e}_s)\big(\frac{R_0}{r^n}\big)^{l+2} + \rho_{ice}H_{lknm}(\mathbf{e}_i \cdot \mathbf{e}_s)\big(\frac{r^n}{R_0 - \tilde{d}_{ice}}\big)^{l-1})) \cdot \mathbf{e}_i)N^n N^m)dW \end{aligned} \tag{2.27a}$$

$$\begin{aligned} {}_{S_{int}}A_{ij}^{nm} = \int_{S_{int}} ((&\rho_w \sum_l \sum_k \frac{4\pi\mathcal{G}r^n}{2l+1}((\rho_w - \rho_{ice})H_{lknm}(\mathbf{e}_i \cdot \mathbf{e}_s)\big(\frac{R_0}{r^n}\big)^{l+2} + \rho_{ice}H_{lknm} \\ &(\mathbf{e}_i \cdot \mathbf{e}_s)\big(\frac{r^n}{R_0 - \tilde{d}_{ice}}\big)^{l-1}))(\mathbf{e}_s \cdot \mathbf{e}_i) + (\mathbf{e}_i \cdot \mathbf{e}_s)(\rho_{ice} - \rho_w)g_{int}(\mathbf{e}_s \cdot \mathbf{e}_i))N^n N^m dS \end{aligned} \tag{2.27b}$$

$${}_{S_0}A_{ij}^{nm} = \int_{S_0} (\mathbf{e}_i \cdot \mathbf{e}_s)\rho_{ice}g_0(\mathbf{e}_s \cdot \mathbf{e}_i)N^n N^m dS \tag{2.27c}$$

$${}_{S_f}A_{ij}^{nm} = \int_{S_f} C_{ijkl}M_{kli}(N^{m+} - N^{m-}) \cdot \mathbf{e}_i N^n dS, \tag{2.27d}$$

where N^{m+} and N^{m-} denote shape functions for split nodes on either side of a fault surface. We can also combine terms from Equations 2.14 and 2.15 to write a force vector b_i^n:

$$b_i^n = -\int_W (\rho_{ice}\nabla V \cdot \mathbf{e}_i)N^n dW - \int_{S_{int}} \rho_w V(\mathbf{e}_s \cdot \mathbf{e}_i)N^n dS. \tag{2.28}$$

Finally, we assemble Equations 2.26, 2.27, and 2.28 to form a linear system and solve for displacement coefficients a_i^m.

$$A_{ij}^{nm}a_i^m = b_i^n. \tag{2.29}$$

1.1.2.4 Solution Method

We solve Equation 2.29 using a multigrid method built into the PetSc solver package within Pylith (Aagaard et al., 2007). For the multigrid method, we apply preconditioners to A_{ij}^{nm} in Equation 2.29 to obtain solutions (i.e., coefficients a_i^m) for a series of increasingly fine mesh grids. We use Gaussian elimination to compute a_i^m for all grids except the coursest grid. To remove rigid body translational and rotational motion from solutions, we apply singular-value decomposition and discard computed a_i^m values at the coursest grid level (for details, see 4.1.5 of Aagaard et al., 2007). We are able to mesh geometries, run simulations, and post-process model results for a single time step (e.g., at t = 0) within 60 – 90 minutes on a computer equipped with two CPU cores using our finite-element method.

1.2 Benchmarking

We benchmark our tidal loading formulation on *Base* models against analytic solutions using the spectral solver software package SATStress, a widely used tool within the planetary science community to predict diurnal (and fluid) Love number values and stress fields on planetary bodies (Wahr et al., 2009). SATStress solves the equation of motion for tidally-loaded multi-layered spherically symmetric bodies accounting for self-gravitation and viscous effects. Figure 2.7 shows predictions of Love number values from SATStress across our range of modelled $\tilde{d}_{ice}$ values. Within SATStress, we specify a multi-layered body with an outer ice layer and underlying ocean consistent with the rheological parameters in Table 2.3 (see main text), a mean ice viscosity 10^{16} Pa-s (Friedson and Stevenson, 1983), an ocean shear modulus 10^{-20} Pa, and an ocean viscosity 10^{-20} Pa-s. Love number values between numerical and analytical models agree to within <0.1% across all $\tilde{d}_{ice}$ values. Possible additional minor differences between predictions from either set of results may result from our lack of accounting for changes in ice shell rheology due to volumetric expansion or contraction within the ice shell during tidal loading (for details see Wahr et al., 2006).

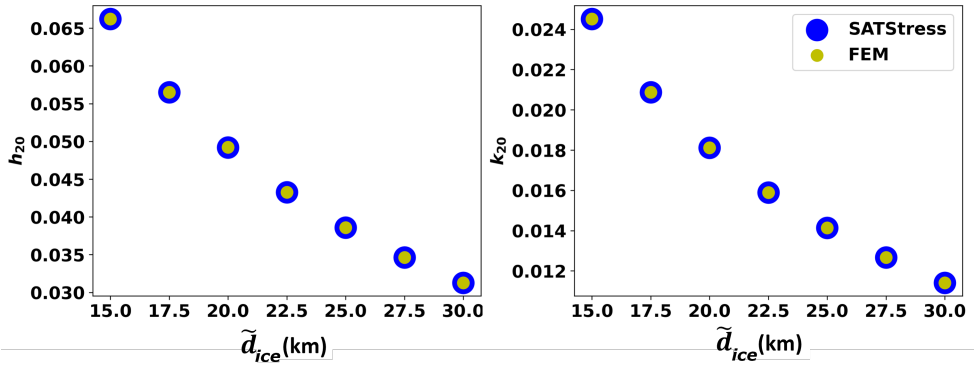

Figure 2.7: Comparison of analytic and FEM Love number results for several values of $\tilde{d}_{ice}$ on spherically symmetric (*Base*) models. Love numbers plotted against $\tilde{d}_{ice}$ for analytic models using SATStress (blue dots) and using the FEM formulated here (yellow dots).

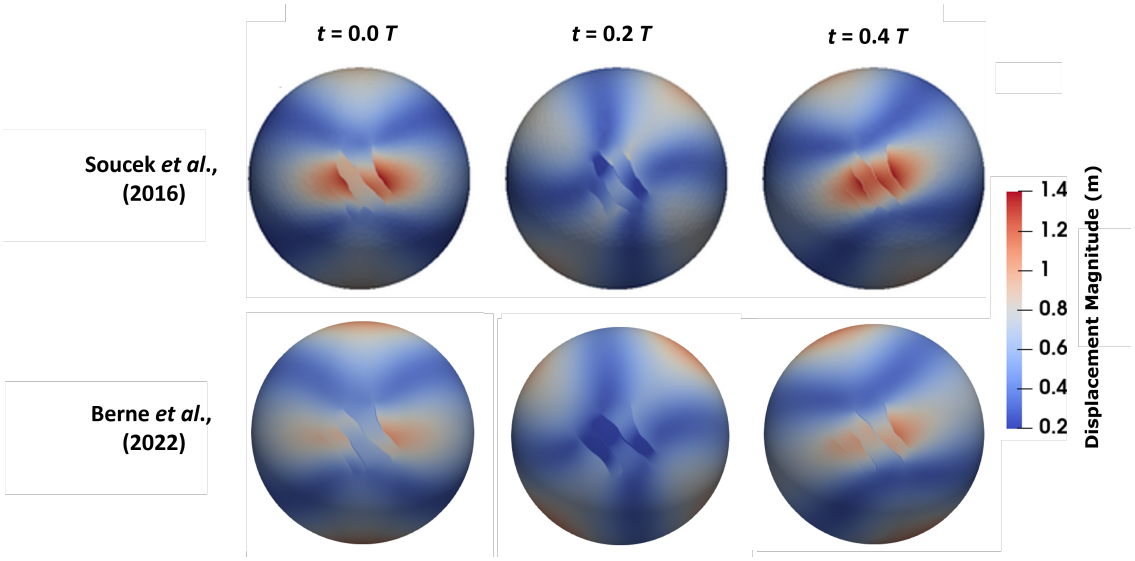

Figure 2.8: Qualitative comparison of our FEM results with results from Souček et al. (2016) (top row) and this work (bottom row) for models with weak zones at Tiger Stripe locations viewed facing the South Pole. Fields denote the magnitude of the displacement vector evaluated at the outer surface of deformed geometries. The top row and colorbar of this Figure are adapted from top row of Figure 3 of Souček et al. (2016). We assign weak zone bulk moduli μ_{WZ}/μ=10^{-5} and shear moduli G_{WZ}/G=10^{-5} for our simulations in accordance with the formulation of weak zones described in Souček et al. (2016).

We additionally compare model results from this work with results from Souček et al. (2016). Figure 2.8 shows displacement magnitude fields at three different time indices in the tidal cycle (t=0.0 T (periapse), 0.2 T, and 0.4 T, where T is the orbital period T = 33 hrs) for models in Souček et al. (2016) (top row) and this work (bottom). We deactivate self-gravitation on *Base* models and assign weak zones (with prescribed bulk modulus $\mu_{WZ} = 10^{-5}\mu$ and shear modulus $G_{WZ} = 10^{-5}G$) to regions surrounding the Tiger Stripes for model comparisons. We find we are able to largely reproduce results from Souček et al., (2016) both quantitatively (i.e., peak displacement magnitude values correspond to within <10%) and qualitatively. Slight differences in displacement field characteristics persist surrounding the weak zone regions likely due to methodological differences in the implementation of adaptive mesh sizing, the assignment of reduced elastic moduli (i.e., the location of the Tiger Stripes and the shear modulus reduction away from fault planes), or the use of different shape functions (i.e., linear vs. quadratic) between models.

1.3 Mesh Convergence Test

We perform a mesh convergence test to confirm that Love number results from models with structural heterogeneities are not sensitive to chosen mesh sizing parameters. Figure 2.9 shows Love number values evaluated from models with only weak zones at chasma, Tiger Stripe, and circum-tectonic boundary locations (i.e., *WZ* models) and $\tilde{d}_{ice}$ = 15 km meshed with specified minimum cell side lengths S_{min}= 6, 5, 4, 3, 2, and 1 km. We additionally show example snapshots of the radial displacement fields between our *WZ* model relative to our *Base* model for geometries with $\tilde{d}_{ice}$ = 15 km across our range of tested S_{min} values. Results from Figure 2.9 demonstrate that both Love number results and overall radial displacement fields are insensitive to chosen minimum cell size for values of $S_{min} < 3$ km. We accordingly assign S_{min} = 1 km for all models discussed in this work.

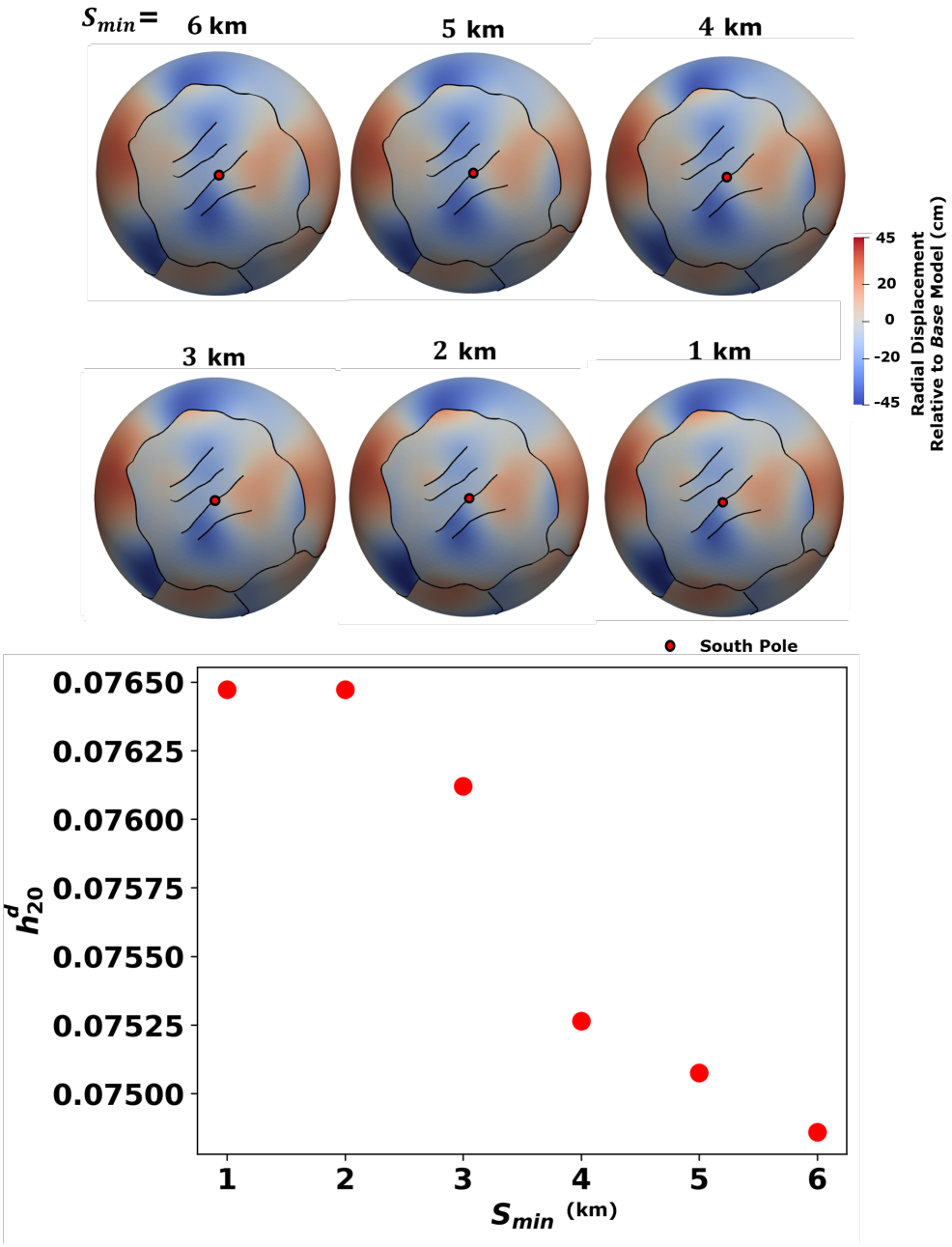

Figure 2.9: Results evaluated at periapse for *WZ* models ($\tilde{d}_{ice}$ = 15 km) for a range of S_{min}. We show radial displacement fields viewed facing upwards towards the South Pole (top) and h_{20}^d Love number results we use to track the sensitivity of results due to changes in S_{min} (bottom).

1.4 Choice of Weak Zone Elastic Parameters

We evaluate results from models with weak zones at chasma, Tiger Stripe, and circum-tectonic boundary locations (i.e., *WZ* models) to confirm that Love number outputs are not sensitive to our choice of weak zone shear modulus. Figure 2.10 shows Love number values evaluated from *WZ* models with $\tilde{d}_{ice}$ = 15 km and specified weak zone moduli across $10^{-8} < G_{WZ}/G < 10^{0}$. We additionally show example snapshots of radial displacement fields from our *WZ* models relative to our *Base* model with $\tilde{d}_{ice}$ = 15 km across our range of tested G_{WZ} values. Results from Figure 2.10 demonstrate that both Love number results and overall radial displacement fields are insensitive weak zone shear modulus for $G_{WZ}/G < 10^{-4}$. These results are consistent with those described in the supplementary documentation of Souček et al. (2016) but extend to inferences of displacement away from the Tiger Stripes and for instances of non-zero bulk modulus within weak zones.

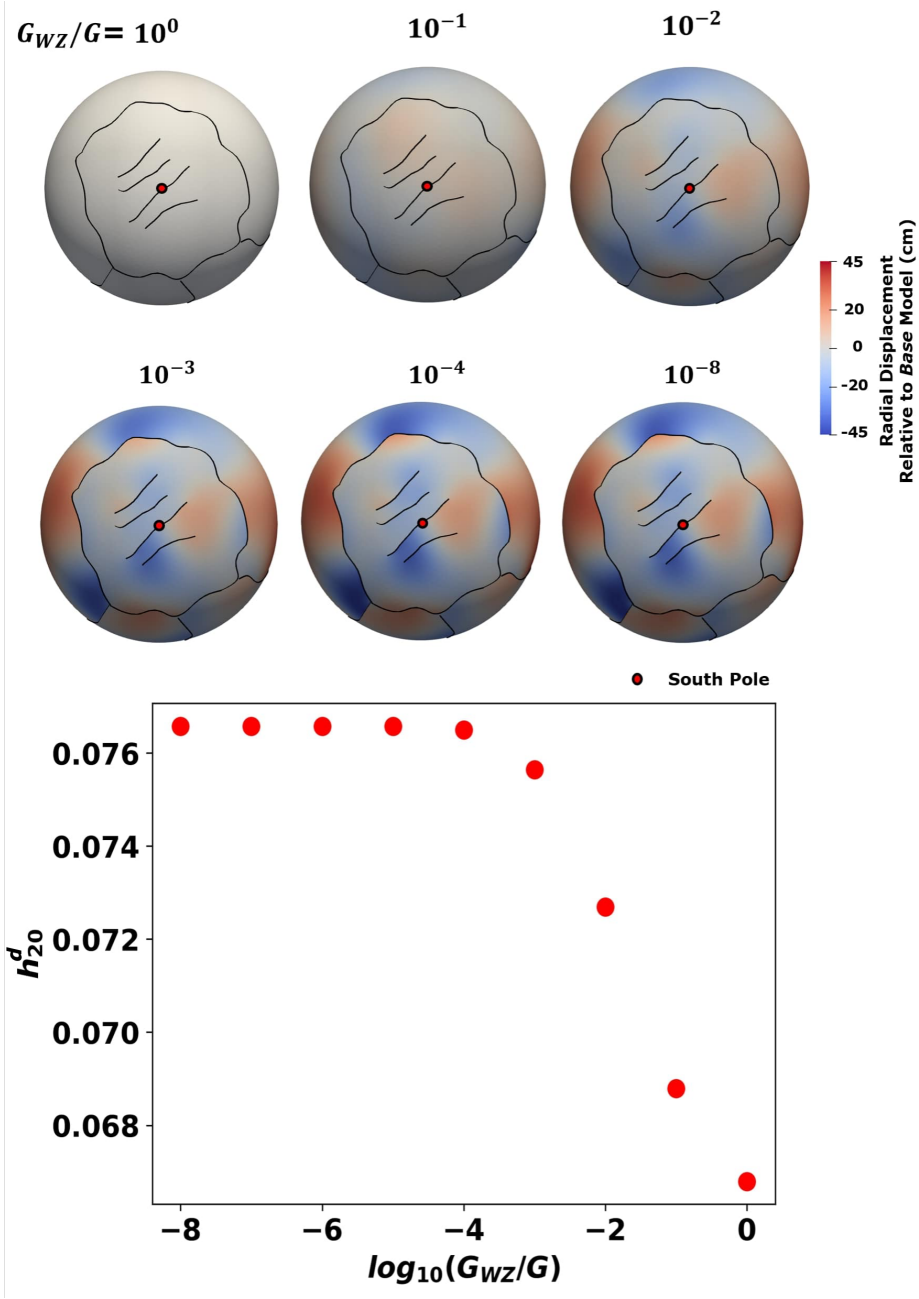

Figure 2.10: Results evaluated at periapse for *WZ* models ($\tilde{d}_{ice}$ = 15 km) across several values of G_{WZ}. We show radial displacement fields viewed facing upwards towards the SP (top) and h_{20}^d Love number results we use as a proxy for effective model stiffness.

1.5 Mode Coupling

We investigate the extent to which structural heterogeneities excite radial displacement patterns beyond degree-2 harmonics. For each model with structural heterogeneities, we treat radial displacement fields relative to the *Base* model (i.e., $u_r(\mathbf{\Omega})$, where $\mathbf{\Omega}$ is the position variable comprising the co-latitude longitude pair (θ, ϕ) in a reference frame fixed to Enceladus's center of mass). Note that $u^r(\mathbf{\Omega})$ is a sum over orthonormal spherical harmonic basis functions $Y_{lm}(\mathbf{\Omega})$ scaled by coefficients u^r_{lm} (l and m denote spherical harmonic degree and order):

$$u^r(\mathbf{\Omega}) \ = \sum_{l=0}^{\infty} \sum_{m=-l}^{l} u^r_{lm} Y_{lm}(\mathbf{\Omega}). \tag{2.30}$$

The power of $u^r(\mathbf{\Omega})$ at a given spatial scale (i.e., l) can be represented via the power spectral density. We evaluate power spectral density using the root-mean-square of coefficients u^r_{lm} in Equation 2.30 over order m:

$$\text{Power Spectral Density} = \left(\frac{\sum_m (u^r_{lm})^2}{2l+1} \right)^{1/2}. \tag{2.31}$$

Figure 2.11 shows power spectral density across l for *LTV*, *Faulted+LTV*, *Faulted*, *Faulted+ LTV+WZ*, and *WZ* models (See Figures 1 and 2 in the main text). Figure 2.11 demonstrates that structural heterogeneities stimulate mode coupling (i.e., non degree-2 deformation) across l = 2 - 20 with diminishing power at shorter wavelengths (i.e., higher l). Moreover, lateral variations in crustal thickness (i.e., in *LTV* and *WZ* models) and weak zones (i.e., in *WZ* and *Faulted + LTV + WZ* models) drive the most significant long-wavelength (l = 2 - 5) deformation across models. By contrast, deformation driven by faults (i.e., in *Faulted* models) is minimal at long-wavelengths but relatively more prominent at shorter wavelengths (l = 10 - 20) as compared to deformation in *LTV* models.

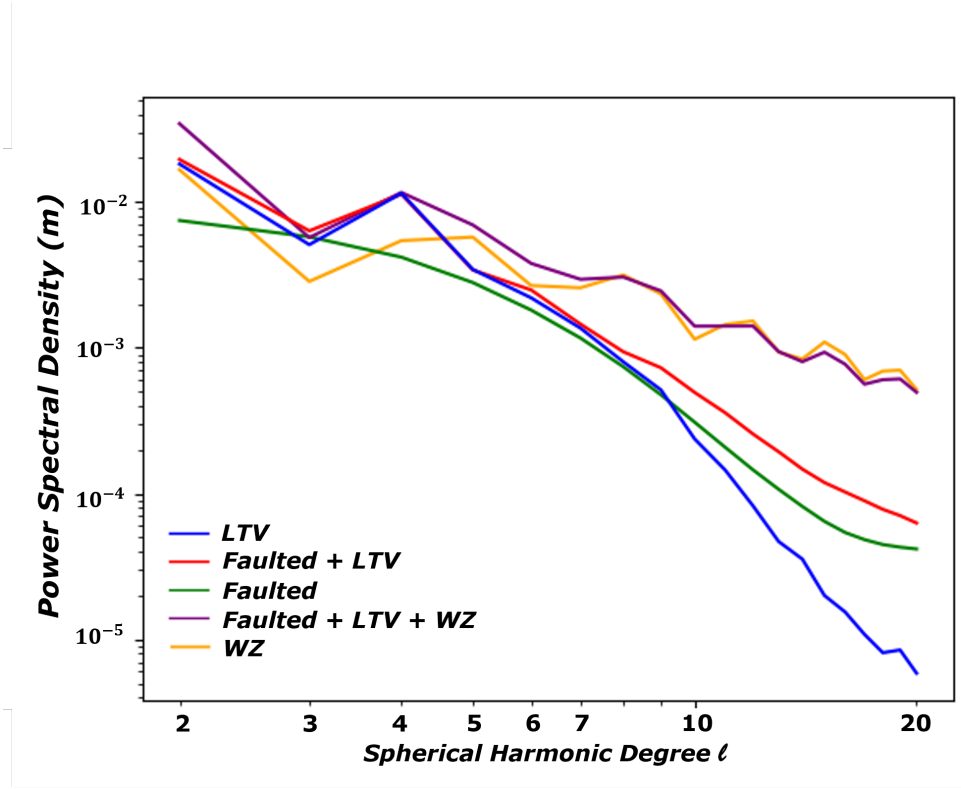

Figure 2.11: Power spectral density of surface radial displacements for models with structural heterogeneities described in this work. We compute power spectral density for each model using Equations 2.30 and 2.31. For a description of each model class, see Section 2.1 of the main text. Axes are plotted in $\log_{10}$ scale.

1.6 Ice Thickness and Thermal Thickness

We aim to describe the relationship between 1) the ice thickness $\tilde{d}_{ice}$ predicted from analyzing displacement over diurnal timescales at Enceladus and 2) the thermal thickness $\tilde{d}_t$ of ice between the surface and the water-ice phase transition at 273°K (i.e., the ice-ocean boundary). Note that the general (i.e., complex) form of the diurnal degree-2 shape Love number (for a spherically symmetric body) possesses both real $\Re(h_2^d)$ and imaginary $\Im(h_2^d)$ components. For a body that exhibits purely elastic deformation, $h_2^d = \Re(h_2^d)$ and $\Im(h_2^d) = 0$. However, we expect the 'thermal' portion of the ice shell to exhibit an additional viscous component of deformation such that $\Im(h_2^d) \neq 0$. We can therefore estimate the ratio between $\tilde{d}_t$ and $\tilde{d}_{ice}$ by comparing $\Re(h_2^d)$ and $\Im(h_2^d)$:

$$\tilde{d}_t/\tilde{d}_{ice} = \frac{(\Im(h_2^d)^2 + \Re(h_2^d)^2)^{1/2}}{\Re(h_2^d)}. \tag{2.32}$$

The imaginary Love number component $\Im(h_2^d)$ in Equation 2.32 is sensitive to the dynamic viscosity structure of the crust (Čadek et al., 2019). Viscosity $\eta(r)$ in the ice shell is a function of radial position r and $\tilde{d}_t$ (cf. Equations 56 and 57, Beuthe 2018):

$$\eta(r) = \eta_0 \cdot \exp\left(\frac{E}{R_g T_{io}}\left(\frac{T_{io}}{T_{io}^{(r-R)/(\tilde{d}_t)} T_s^{(r-R+\tilde{d}_t))/(\tilde{d}_t)}} - 1\right)\right), \tag{2.33}$$

where is $\eta_0 = 3{\cdot}10^{14}$ Pa-s is the minimum viscosity at the base of the ice shell (Čadek et al., 2019), $T_{io} = 273$ K and $T_s = 70$ K respectively are temperatures at the ice-ocean boundary and surface (Howett et al., 2010), $R = 252.1$ km is radius of the surface (Hemingway and Mittal, 2019), R_g is the gas constant, and $E = 59.4$ kJ mol^{-1} is the activation energy for diffusion creep of ice.

We solve for $\Im(h_2^d)$ and $\Re(h_2^d)$ using SATStress (Wahr et al., 2009, see also S1.2). Within SATStress, we specify a body with 100 equally thick layers of uniform rheology. For each layer, we linearly interpolate viscosity values from the radial viscosity structure described to Equation 2.33 and assign a constant shear modulus $G = 3.3$ GPa (Souček et al., 2016). Figure 2.12 shows results for computed $\Im(h_2^d)$, $\Re(h_2^d)$, and $\tilde{d}_t/\tilde{d}_{ice}$ (see Equation 2.32). Figure 2.12 demonstrates that $\tilde{d}_t/\tilde{d}_{ice} < 1.012$ for $\tilde{d}_t = 15-30$ km. In other words, estimates of mean ice thickness from Love numbers likely underestimate thermal thickness by less than $\sim 0.2\%$ at Enceladus (note that computed $\tilde{d}_t/\tilde{d}_{ice}$ are consistent with values expected when using complex Love numbers at Enceladus reported by Beuthe, 2018 cf. Figure 3).

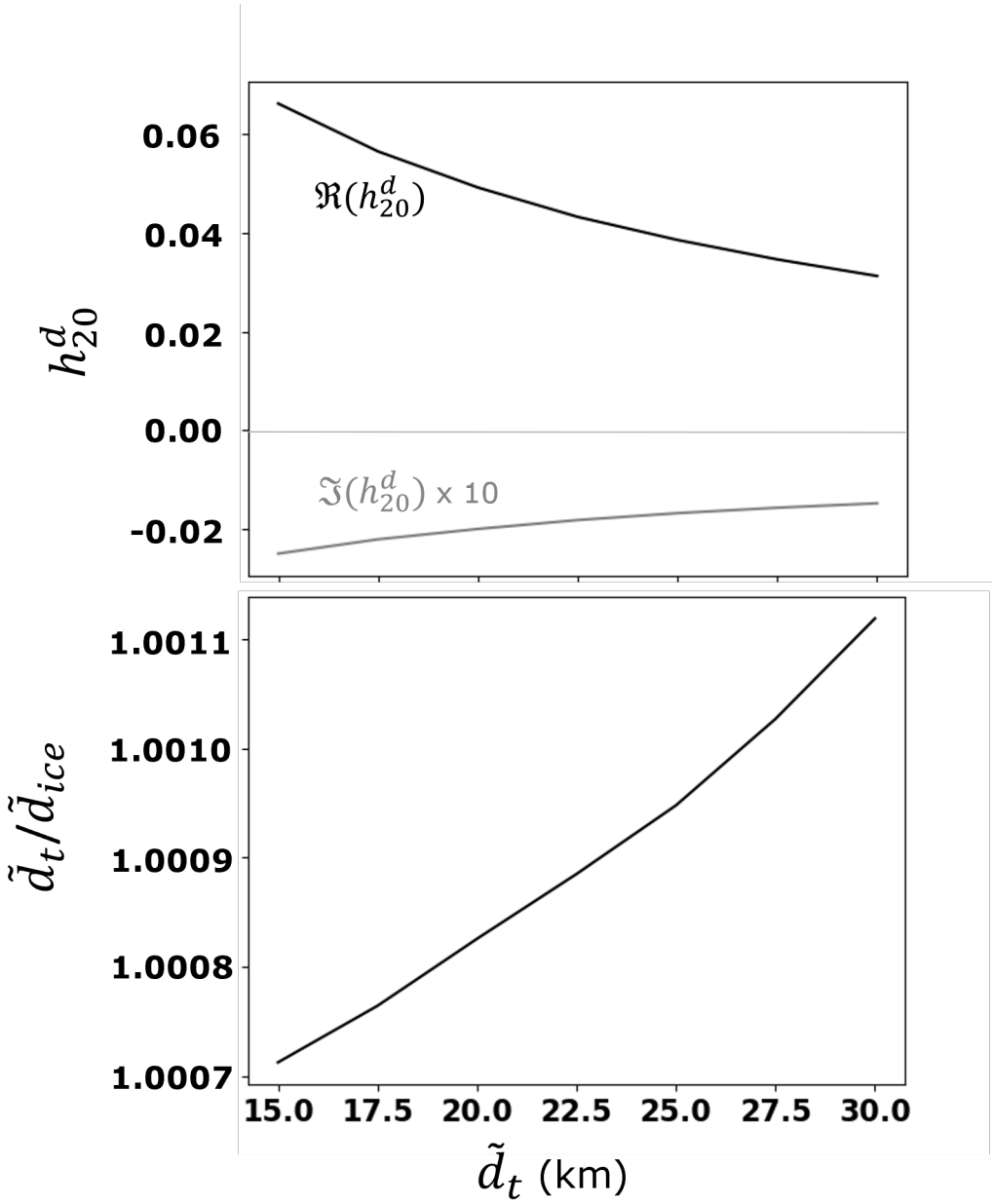

Figure 2.12: Computed complex Love number components $\Im(h_2^d)$ and $\Re(h_2^d)$ (top row), and associated $\tilde{d}_t/\tilde{d}_{ice}$ values (see Equation 2.32) (bottom row) across input mean crustal thicknesses $\tilde{d}_t$ = 15-30 km. We evaluate $\Im(h_2^d)$ and $\Re(h_2^d)$ using SATStress and following the procedure described in S1.6.

1.7 Impact of Structural Heterogeneities on Horizontal Displacements

Results for horizontal displacement (i.e., orthogonal to the radial direction and tangential to the outer surface) across a range of model classes (see section 2.1 in the main text) are shown in Figure 2.13. Figure 2.13 demonstrates that the magnitude of horizontal displacements produced by structural heterogeneities are comparable to (or greater than) the magnitude of horizontal displacements in *Base* models near the South Pole of Enceladus (see discussion).

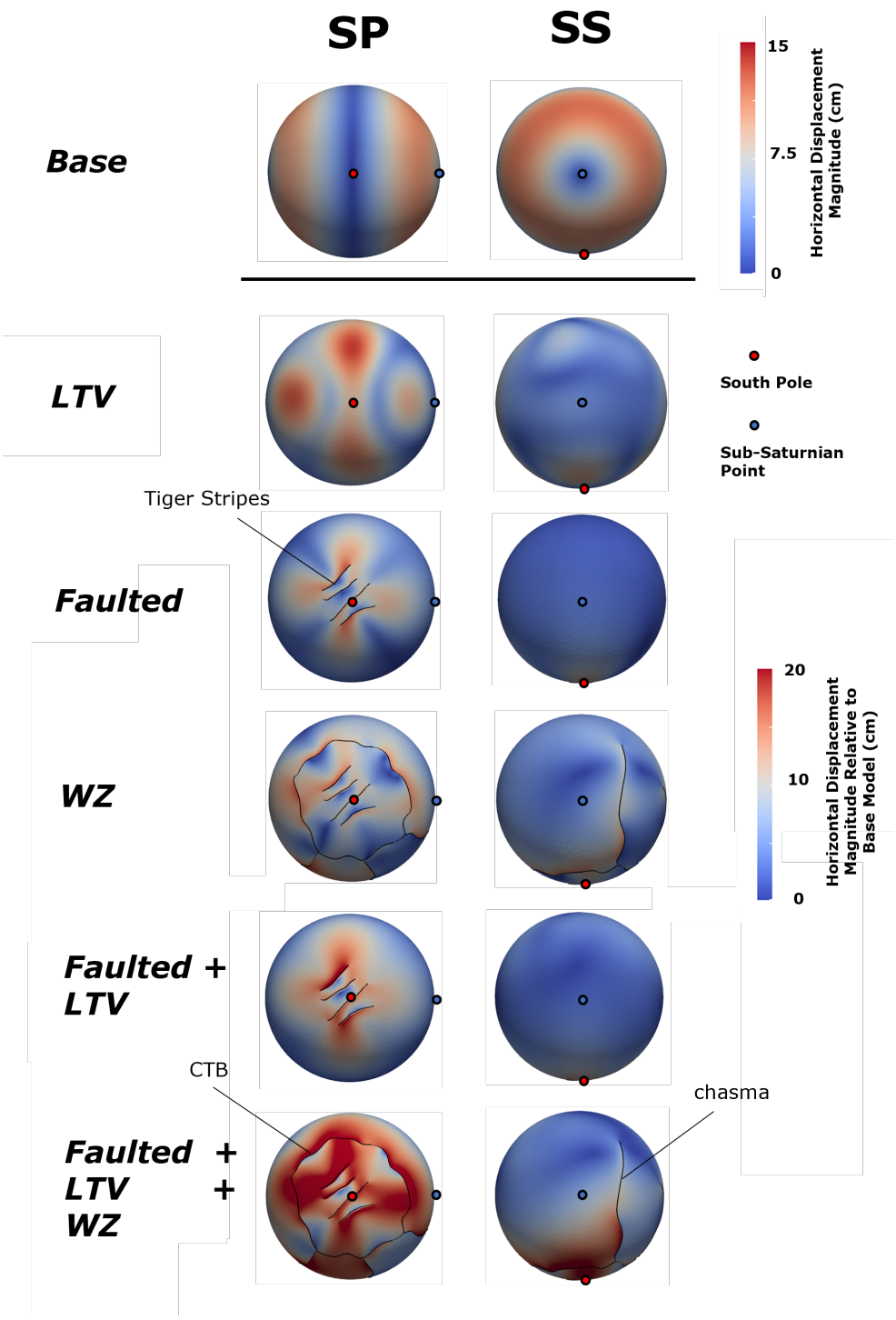

Figure 2.13: Snapshots of the magnitude of horizontal displacement from each model class viewed facing the south pole (SP, left column) and the sub-Saturnian point (SS, right column) evaluated at $t = 0$ (periapse). The top row shows the magnitude of horizontal displacement in the *Base* model due to tidal forcing. The remaining rows present the magnitude of the difference in horizontal displacement between models with structural heterogeneities and the *Base* model. Each model shown assumes $\tilde{d}_{ice} = 25$ km. Tiger Stripes, the south polar circum-tectonic boundary (CTB), and chasma are labelled.

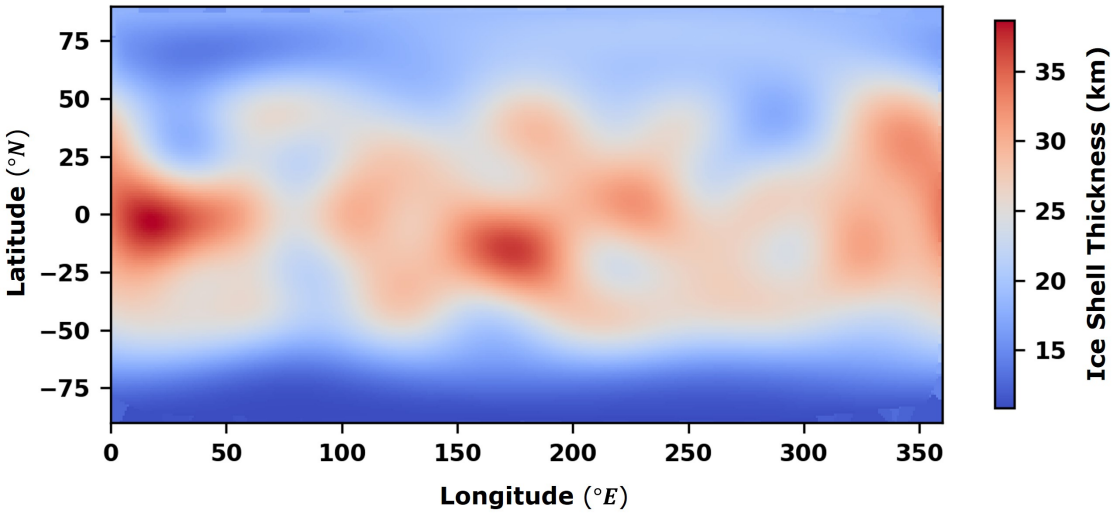

Figure 2.14: Crustal thickness variations for *LTV* models. For details regarding our methodology to generate crustal thickness variations, see Section 2.1 of the main text.

References

Aagaard, B., C. Williams, and M. Knepley (2007). "PyLith: A Finite-Element Code for Modeling Quasi-Static and Dynamic Crustal Deformation". In: *Eos* 88(52).

Beuthe, M. (2018). "Enceladus's crust as a non-uniform thin shell: I tidal deformations". In: *Icarus* 302. ISSN: 10902643. DOI: 10.1016/j.icarus.2017.11.009.

Čadek, O., O. Souček, M. Běhounková, G. Choblet, G. Tobie, and J. Hron (2019). "Long-term stability of Enceladus' uneven ice shell". In: *Icarus* 319. ISSN: 10902643. DOI: 10.1016/j.icarus.2018.10.003.

Friedson, A. J. and D. J. Stevenson (1983). "Viscosity of rock-ice mixtures and applications to the evolution of icy satellites". In: *Icarus* 56 (1). ISSN: 10902643. DOI: 10.1016/0019-1035(83)90124-0.

Hemingway, D. and T. Mittal (2019). "Enceladus's ice shell structure as a window on internal heat production". In: *Icarus* 332. ISSN: 10902643. DOI: 10.1016/j.icarus.2019.03.011.

Howett, C. J., J. R. Spencer, J. Pearl, and M. Segura (2010). "Thermal inertia and bolometric Bond albedo values for Mimas, Enceladus, Tethys, Dione, Rhea and Iapetus as derived from Cassini/CIRS measurements". In: *Icarus* 206 (2). ISSN: 00191035. DOI: 10.1016/j.icarus.2009.07.016.

Segall, P. (2010). *Earthquake and volcano deformation*. DOI: 10.5860/choice.48-0287.

Souček, O., J. Hron, M. Běhounková, and O. Čadek (2016). "Effect of the tiger stripes on the deformation of Saturn's moon Enceladus". In: *Geophysical Research Letters* 43.14. ISSN: 19448007. DOI: 10.1002/2016GL069415.

Wahr, J., Z. A. Selvans, M. E. Mullen, A. C. Barr, G. C. Collins, M. M. Selvans, and R. T. Pappalardo (2009). "Modeling stresses on satellites due to nonsynchronous rotation and orbital eccentricity using gravitational potential theory". In: *Icarus* 200.1. ISSN: 00191035. DOI: 10.1016/j.icarus.2008.11.002.

Wahr, J., M. T. Zuber, D. E. Smith, and J. I. Lunine (2006). "Tides on Europa, and the thickness of Europa's icy shell". In: *Journal of Geophysical Research E: Planets* 111.12. ISSN: 01480227. DOI: 10.1029/2006JE002729.

Chapter 3

USING TIDALLY-DRIVEN ELASTIC STRAINS TO INFER REGIONAL VARIATIONS IN CRUSTAL THICKNESS AT ENCELADUS

.

A. Berne et al. (2023). "Using Tidally-Driven Elastic Strains to Infer Regional Variations in Crustal Thickness at Enceladus". In: *Geophysical Research Letters* 50 (22)

3.1 Abstract

Constraining the spatial variability of the thickness of the ice shell of Enceladus (i.e., the crust) is central to our understanding of the internal dynamics and evolution of this small Saturnian moon. In this study, we develop a new methodology to infer regional variations in crustal thickness using measurements of tidally-driven elastic strain that could be made in the future. As proof of concept, we recover thickness variations from synthetic finite-element crustal models subjected to diurnal eccentricity tides. We demonstrate recovery of crustal thickness to within ∼2 km of true values across the crust with ∼10% error in derived spherical harmonic coefficients at degrees $l \leq 12$. Our computed uncertainty is significantly smaller than the inherent ∼10 km ambiguity associated with crustal thickness derived solely from gravity and topography measurements. Therefore, future measurements of elastic strain can provide a robust approach to probe crustal structure at Enceladus.

3.2 Introduction

Enceladus, a small moon of Saturn, is a geologically active and potentially habitable ocean world (e.g., Porco et al., 2006; Postberg et al., 2009). Enceladus possesses both highly cratered landscapes and regions with active resurfacing (e.g., the South Polar Terrain or SPT) (Yin and Pappalardo, 2015; Schenk et al., 2018). Based on incomplete spherical harmonic degree $l = 3$ gravity and topography fields derived primarily from three spacecraft flybys, the SPT is believed to have significantly thinner crust (∼4 – 14 km) relative to a mean crustal thickness (∼20 – 40 km) (Nimmo et al., 2011; Iess et al., 2014;, 2016; Beuthe et al., 2016; Hemingway et al., 2018). The SPT also possesses four large-scale fractures (informally known

as ‘Tiger Stripes’; Porco et al., 2006). Cryovolcanic jets along the Tiger Stripes are believed to supply material from a global subsurface ocean (Thomas et al., 2016; Iess et al., 2014) to a water-ice plume which exhibits diurnal variations in activity (e.g., Ingersoll et al., 2020). Diurnal eccentricity tides may correspondingly regulate crustal dynamics by cyclically deforming Enceladus over its 32.9 hr orbital period (Souček et al., 2016).

Characterizing the spatial variability of crustal thickness at Enceladus is crucial for studying processes which control the satellite’s long-term evolution and internal heating. It is believed that basal heating (and melting) of the ice shell maintains topography at the interface between the ice shell and ocean over geologic timescales (Čadek et al., 2019; D. Hemingway and Mittal, 2019; Ermakov et al., 2021). Viscous dissipation of tidal energy within the ice shell is likely insufficient to maintain significant ice-ocean topography at Enceladus (Čadek et al., 2019). Knowledge of crustal thickness may therefore constrain the location and magnitude of tidal heating within the ocean and core of the satellite (Hay and Matsuyama, 2019; Choblet et al., 2017). Crustal thickness also mediates possible non-eruptive material transport within the crust (e.g., localized refreezing of ocean material in thinned regions of the ice shell; Čadek et al., 2019) and the intra-crustal processing of erupted ocean material over the South Pole (Kite and Rubin, 2016; Ingersoll and Nakajima, 2016; Fifer et al., 2022).

Several methods have been proposed to infer spatially variable crustal thickness at Enceladus. Measurements of gravity and topography can provide constraints on variations in crustal thickness across regional spatial scales (i.e., $l = 2 – 20$) (e.g., Ermakov et al., 2021). However, previous geodetic studies at Enceladus (Iess et al., 2014; McKinnon, 2015; D. Hemingway and Mittal, 2019) predict a wide possible range of crustal thickness values across regional spatial scales (e.g., 4 – 14 km, or ∼10 km near the South Pole). Ambiguity in determinations of crustal thickness from existing geodetic surveys arises primarily from uncertain estimates of the impact of ocean and crustal densities on Enceladus’s gravity field (D. Hemingway and Mittal, 2019). Efforts to more precisely determine crustal structure using libration measurements (e.g., Thomas et al., 2016; Van Hoolst et al., 2016) or observations of local lithospheric flexure induced by the presence of surface topography (e.g., Giese et al., 2008) constrain only the mean thickness ($l = 0$) or variations in thickness at very short wavelengths ($l > 20$), respectively.

We develop a new method for inferring crustal thickness at Enceladus using proposed

measurements of tidally-driven elastic strain across regional spatial scales. From Hooke's law, strain along a loaded 1D system scales linearly with local stiffness (Figure 3.1). For an elastic layer, both layer thickness and elastic moduli influence the tendency for a medium to resist deformation in response to an applied force. We therefore anticipate that changes in the strain field produced by diurnal tides at a given location will exhibit a linear relationship with variations in the local thickness, provided that elastic moduli are uniform throughout the crust (see discussion section for a more detailed exploration of the possible effects of non-uniform elastic moduli). We expect that viscous effects (e.g., near the ice-ocean boundary) only minimally impact surface strain at Enceladus over the 32.9 hr orbital period (Shaw, 1985; Wahr et al., 2006; Neumeier, 2018). Thus, inferences of thickness from tidally-driven elastic strain closely approximate (to within $< 0.2\%$) true crustal thickness at Enceladus (for additional details, see Figure 3.7).

Gradients in material properties, such as crustal thickness and elastic moduli, induce additional complexity in the response of a 2D layer to applied tractions (Hsu et al., 2011 cf. Equation 4). We refer to this phenomenon as the 'gradient' effect, which we illustrate in Figure 3.1. Crustal thickness gradients can lead to biased estimates of crustal thickness when using a linear (one-to-one) interpretation of strain fields, particularly when gradients are high (e.g., when variations in crustal thickness are present at short wavelengths). Existing analytic and semi-analytic models of diurnal tides at Enceladus cannot easily predict deformation caused by short-wavelength variations in crustal thickness (Wahr et al., 2006; Qin et al., 2016; Beuthe, 2018; Rovira-Navarro et al., 2023). However, numerical Finite Element Models (FEMs) can accurately simulate deformation for ice shell geometries that incorporate variations in crustal thickness across a wide range of spatial scales (Souček et al., 2016; Behounkova et al., 2017; Souček et al., 2019; Berne et al., 2023a).

Here, we introduce an approach to determine crustal thickness at Enceladus through the application of Hooke's law to tidally-induced elastic strains (Section 3.3). Our approach utilizes numerical techniques to iteratively minimize differences between measured crustal strains and those predicted using FEMs of spatially heterogeneous ice shells subject to tidal loading. To account for potential gradient effects, our FEMs incorporate variations in crustal thickness at length scales down to $\sim$12 km or spherical harmonic degree $l \sim 60$. As proof of concept, we demonstrate recovering thickness using elastic strains from a synthetic model of Enceladus's ice

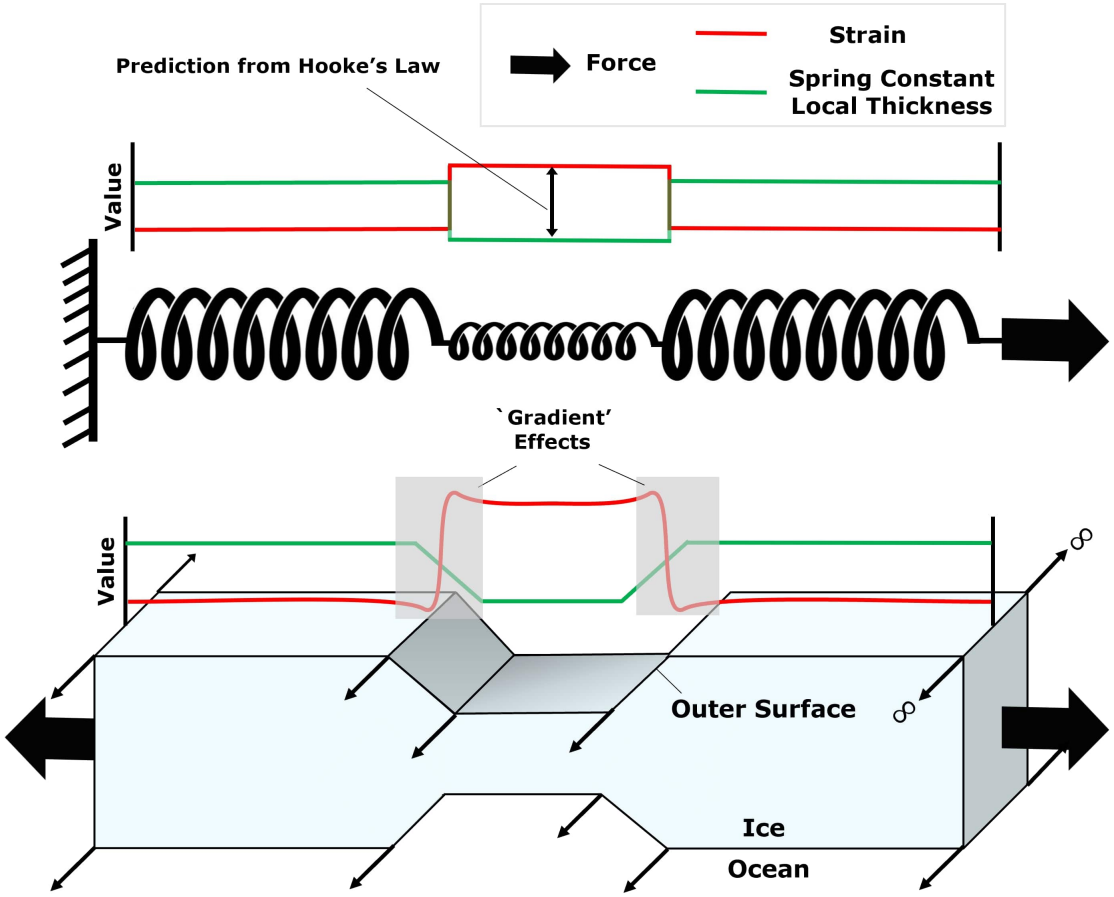

Figure 3.1: Crustal strain correlates with ice shell thickness. Top Panel: Example 1D elastic structure (i.e., springs in series) subject to an axial load. Hooke's law predicts that strain is relatively higher where springs have lower stiffness (i.e., smaller spring constants). Bottom Panel: Analogous 2D elastic layer subject to a transverse load. In this case, local layer thickness modulates the effective stiffness (and strain) of the medium. Proposed measurements of strain at the outer surface of the crust (labelled) would permit inferences of local thickness at Enceladus. Shaded regions denote locations where 'gradient effects' impact inferences of local thickness from strain fields.

shell using our methodology (Section 3.4). We assess uncertainty by comparing the discrepancy between thicknesses that are input into the synthetic models with thicknesses recovered from those models. We conclude by addressing the utility of using imaging geodesy (e.g., Interferometric Synthetic Apreture Radar) to carry out the strain measurements required to recover crustal thickness variations at Enceladus (Section 4).

3.3 Methods

Input Model Specification

We first construct a spherically symmetric model geometry that is broadly consistent with the elastic structure of the crust of Enceladus. Building on the methodology discussed in Berne et al. (2023) (see also section 2.1), we start with a hollow shell with prescribed outer radius R and uniform thickness $\tilde{D}$ (see Supplementary Table 3.1 for chosen values for parameters used throughout this work). Using the software package CUBIT (Skroch et al., 2019; CoreForm, 2020), we mesh our geometry with tetrahedral elements and assign a uniform shear modulus G and a bulk modulus value μ. We account for self-gravitational effects and ignore inertial forces. The deformation of the core may impact elastic strain at the outer surface by up to 5 – 10% but would require a shear modulus of rock which is orders of magnitude smaller than that associated with consolidated silicate material on Earth (Schubert et al., 2007; Rovira-Navarro et al.; 2020). We therefore treat the core as a rigid body for simulations, but recognize that an unconsolidated or fluid core could bias inference of crustal thickness using our analysis. We have benchmarked our methodology against the semi-analytic spectral method outlined in Rovira-Navarro and Matsuyama (2023) to ensure accurate FEM solutions.

For our analysis, we construct a synthetic 'true' crustal thickness model by modifying the surface and ice-ocean boundary of our spherically symmetric geometry. $D^{true}(\mathbf{\Omega})$ represents the spatially variable thickness of the outer ice shell of our synthetic model where $\mathbf{\Omega}$ is the position variable comprising the co-latitude longitude pair (θ, ϕ) in a body-fixed reference frame. Note that we can write the quantity $D^{true}(\mathbf{\Omega})$ as a sum over orthonormal spherical harmonic basis functions $Y_{lm}(\mathbf{\Omega})$ scaled by coefficients d_{lm}^{true} (where l and m denote spherical harmonic degree and order):

$$D^{true}(\mathbf{\Omega}) = \sum_{l=0}^{\infty} \sum_{m=-l}^{l} d_{lm}^{true} Y_{lm}(\mathbf{\Omega}). \tag{3.1}$$

We generate d_{lm}^{true} up to $l = 60$ by compensating observed surface topography using a modified form of Airy isostasy (D. Hemingway and Matsuyama, 2017). Further details of our procedure to generate thickness variations in the synthetic model are given in Supplementary section S1.1 of this chapter.

Tidal Loading

Following the formulation described in Supplementary section S1.1 of Berne et al., (2023a), we apply forces associated with the driving potential produced by time-dependent diurnal eccentricity tides $V(r, \theta, \phi, t)$ (to the first order in eccentricity) to model geometries (Murray and Dermott, 2000):

$$V(r,\theta,\phi) = r^2\omega^2 e \cdot (\sin(\omega t)\,\mathrm{P}_{22}(\lambda)\sin 2\phi - \frac{3}{4}\cos(\omega t)\ (2\,\mathrm{P}_{20}(\lambda) - \mathrm{P}_{22}(\lambda)\cos 2\phi)). \tag{3.2}$$

In Equation 3.2, ω is Enceladus's orbital angular velocity, e is the body's orbital eccentricity, and r is radial position in a body-fixed reference frame. Time $t = 0, \frac{2\pi}{\omega}$ corresponds to orbital periapse. $P_{20}(\mu)$ and $P_{22}(\mu)$ are associated Legendre Functions with the nested function $\mu = \cos(\theta)$. We use the 3D FEM code PyLith (Aagaard et al., 2007) for simulations. PyLith is a well-established geodynamic modelling tool which allows for complex bulk rheology and geometrical meshes. We have modified PyLith for modeling full spheres in a no-net-rotation/translation reference frame with central time-dependent body forces appropriate for eccentricity tides (see also section 2.2 of Berne et al., 2023a).

Strain Computation

Following the methodology described in Tape et al. (2009) (cf. Equation 20), for a deforming quasi-spherical body with a linear isotropic elastic rheology, we can compute components of the horizontal strain rate tensor $\boldsymbol{\epsilon}$ at the surface according to:

$$\epsilon_{ij} = \frac{1}{R}\begin{bmatrix} -\frac{3\mu-2G}{3\mu+4G}(2v_r + \frac{dv_\theta}{d\theta} + \cdots & 0 & 0 \\ \cdots v_\theta\cot\theta + \csc\theta\frac{dv_\phi}{d\phi}) & & \\ 0 & v_r + \frac{dv_\theta}{d\theta} & \frac{1}{2}(-v_\phi\cot\theta + \csc\theta\frac{dv_\theta}{d\phi} + \frac{dv_\phi}{d\theta}) \\ 0 & \frac{1}{2}(-v_\phi\cot\theta + \csc\theta\frac{dv_\theta}{d\phi} + \frac{dv_\phi}{d\theta}) & v_r + v_\theta\cot\theta + \csc\theta\frac{dv_\phi}{d\phi} \end{bmatrix}, \tag{3.3}$$

where quantities v_r, v_θ, and v_ϕ and subindices '1', '2', and '3' respectively denote surface velocities and tensor components in positive radial, co-latitude, and longitude directions. To compute v_r, v_θ and v_ϕ, we difference FEM displacement fields between 180 consecutive time points over the tidal cycle ($t = 0$ to $t = \frac{2\pi}{\omega}$ in Equation

3.2). We can also compute surface velocities (and strain rate tensor components) by combining radial, lateral, and toroidal shape Love numbers (evaluated across several values of l) with the driving potential described in Equation 3.2 (Wahr et al., 2006; Wahr et al., 2009; Rovira-Navarro and Matsuyama, 2023). Subtracting the dilatation of the strain tensor ϵ_h from diagonal components of ϵ_{ij} in Equation 3.3 permits computation of the horizontal deviatoric strain rate tensor $\tilde{\epsilon}_{ij}$:

$$\tilde{\epsilon}_{ij} = \epsilon_{ij} - \epsilon_h \delta_{ij}, \tag{3.4}$$

where δ_{ij} is the kronecker delta. ϵ_h is the average of the diagonal components of ϵ_{ij} in Equation 3.3:

$$\epsilon_h = \frac{\epsilon_{11} + \epsilon_{22} + \epsilon_{33}}{3}. \tag{3.5}$$

For convenience, we seek to parameterize strain rate at the surface of our models using a scalar quantity which is not sensitive to our choice of coordinate system, here called $E(\mathbf{\Omega})$ (see section 2.1 for the definition of $\mathbf{\Omega}$). Using matrix components $\tilde{\epsilon}_{ij}$ in Equation 3.4, we define $E(\mathbf{\Omega})$ as the time-averaged 2$^{\text{nd}}$ invariant of the deviatoric horizontal strain rate:

$$E(\mathbf{\Omega}) = \frac{\omega}{2\pi} \int_0^{\frac{2\pi}{\omega}} \left| \tilde{\epsilon}_{11}\tilde{\epsilon}_{22} + \tilde{\epsilon}_{22}\tilde{\epsilon}_{33} + \tilde{\epsilon}_{11}\tilde{\epsilon}_{33} - \tilde{\epsilon}_{23}\tilde{\epsilon}_{32} \right| \, dt, \tag{3.6}$$

3.4 Results

Initial Crustal Thickness Recovery

We perform an iterative analysis to recover thickness from strain fields. $D^n(\mathbf{\Omega})$ and $E^n(\mathbf{\Omega})$ respectively denote thickness and strain fields evaluated at a given iteration number n. To assess the discrepancy between thicknesses that are input and recovered from models for each iteration, we compute the mismatch $\delta D^n(\mathbf{\Omega})$ between $D^n(\mathbf{\Omega})$ and $D^{true}(\mathbf{\Omega})$:

$$\delta D^n(\mathbf{\Omega}) = D^n(\mathbf{\Omega}) - D^{true}(\mathbf{\Omega}). \tag{3.7}$$

We initially (i.e., $n = 0$) recover crustal thickness $D^0(\mathbf{\Omega})$ using 'observed' strains (i.e., $E^{obs}(\mathbf{\Omega})$) extracted from our FEM with thickness $D^{true}(\mathbf{\Omega})$. Hooke's law predicts that thickness is inversely proportional to strain in a 2D elastic medium

subject to a transverse load (as previously shown in Figure 3.1). It is therefore reasonable to assume the following relationship between $E^{obs}(\mathbf{\Omega})$ and $D^0(\mathbf{\Omega})$:

$$\frac{D^0(\mathbf{\Omega})}{\tilde{D}} = \kappa(\mathbf{\Omega})\frac{E^{Base}(\mathbf{\Omega})}{E^{obs}(\mathbf{\Omega})}, \tag{3.8}$$

where $\kappa(\mathbf{\Omega})$ is a transfer function and $E^{Base}(\mathbf{\Omega})$ is strain evaluated on a spherically symmetric Enceladus with uniform ice shell thickness $\tilde{D}$. The function $\kappa(\mathbf{\Omega})$ accounts for any non-linear dependence of strain fields on thickness variations at different $\mathbf{\Omega}$. We find that averaging strain values over the tidal cycle and assigning $E(\mathbf{\Omega})$ to the second invariant of the horizontal deviatoric strain rate tensor (see Equation 3.6) minimizes the impact of $\kappa(\mathbf{\Omega})$ using our approach (i.e., Equation 3.8 describes an approximately linear relationship). Nonetheless, we remove an empirical long-wavelength function from strain fields to account for $\kappa(\mathbf{\Omega})$ on inferences of thickness (for additional details, see Supplementary section S1.2 of this chapter).

Figure 3.2 shows snapshots of $D^{true}(\mathbf{\Omega})$, $E^{obs}(\mathbf{\Omega})$, $D^0(\mathbf{\Omega})$, and $\delta D^0(\mathbf{\Omega})$ from our analysis. For visualization, we plot the base-10 logarithm of $E^{obs}(\mathbf{\Omega})$ normalized by $E^{Base}(\mathbf{\Omega})$ (i.e., $\widehat{E}^{obs}(\mathbf{\Omega})$):

$$\widehat{E}^{obs}(\mathbf{\Omega}) = \log_{10}\frac{E^{obs}(\mathbf{\Omega})}{E^{Base}(\mathbf{\Omega})}. \tag{3.9}$$

As expected, patterns of $\widehat{E}^{obs}(\mathbf{\Omega})$ correlate with patterns of $D^{true}(\mathbf{\Omega})$. Computed $\widehat{E}^{obs}(\mathbf{\Omega})$ fields reflect regional thinning at North and South poles, a relatively thicker crust at low latitudes, and the significant asymmetry in crustal thinning between Northern and Southern hemispheres visible in $D^{true}(\mathbf{\Omega})$. Recovered crustal thickness patterns, $D^0(\mathbf{\Omega})$, more closely match $D^{true}(\mathbf{\Omega})$ than do $\widehat{E}^{obs}(\mathbf{\Omega})$. Slight differences between $D^{true}(\mathbf{\Omega})$ and $D^0(\mathbf{\Omega})$ (i.e., $\delta D^0(\mathbf{\Omega})$ in Equation 3.7) appear to localize near regions with short-wavelength variations in crustal thickness (i.e., high contour density) consistent with the influence of gradient effects on our analysis. In particular, we significantly overestimate crustal thickness ($\delta D^0(\mathbf{\Omega})$ values up to 25 km) along several prominent ridges over the Trailing and Southern Hemispheres.

Gradient Effect Correction

We iteratively adjust the amplitude of crustal thicknesses $D^n(\mathbf{\Omega})$ to minimize differences between strain produced by models with recovered crustal thickness fields

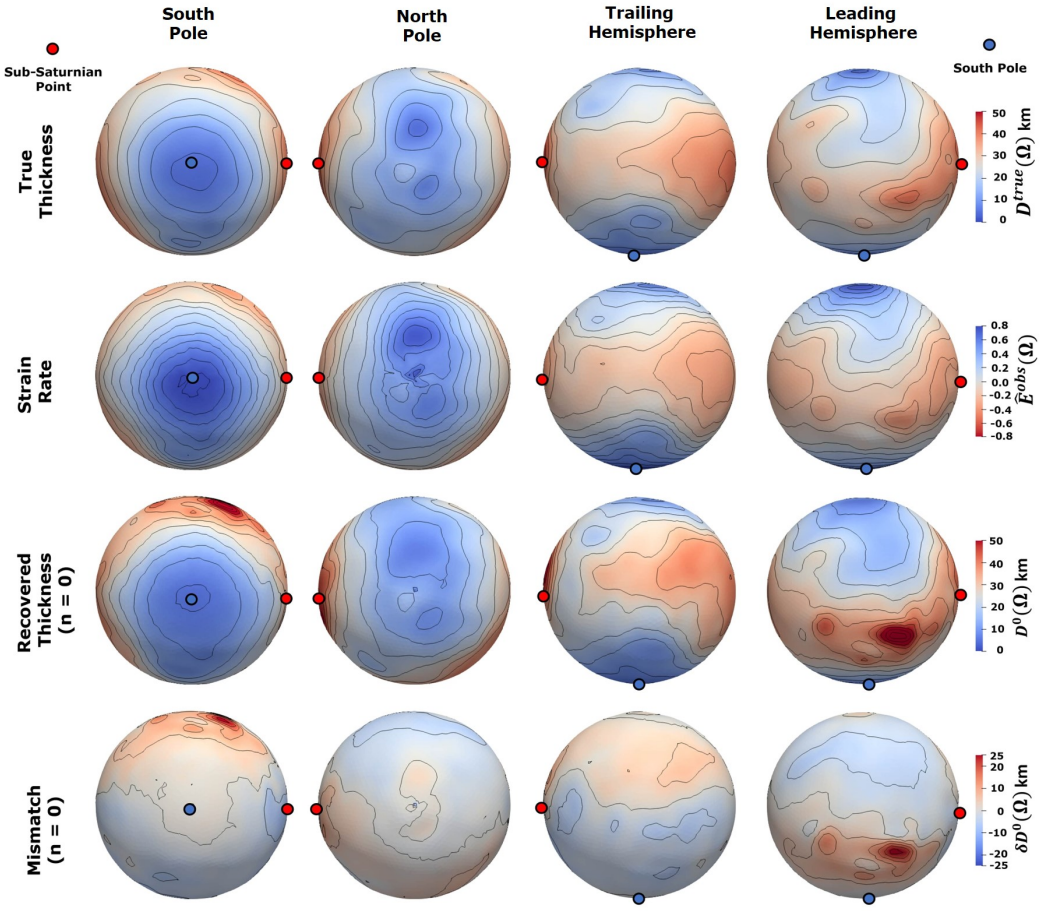

Figure 3.2: Snapshots of model input crustal thickness $D^{true}(\mathbf{\Omega})$ (first row), the simulated 2^{nd} invariant of time-averaged horizontal deviatoric strain rate $\widehat{E}^{obs}(\mathbf{\Omega})$ (see Equations 3.6 and 3.9) (second row), recovered crustal thickness $D^0(\mathbf{\Omega})$ evaluated from Equation 3.8 (third row), and mismatch between input and recovered thickness $\delta D^0(\mathbf{\Omega})$ (see Equation 3.7) for our initial recovery of crustal thickness (n = 0) viewed facing Southern, Northern, Leading, and Trailing hemispheres. See Supplementary S1.1 of this chapter for a description of how synthetic 'true' crustal thickness models are constructed. Plotted contours denote colorscale intervals of 0.05 (for $\widehat{E}^{obs}(\mathbf{\Omega})$ fields) and 5 km (for $D^n(\mathbf{\Omega})$ and $\delta D^n(\mathbf{\Omega})$ fields). Images are orthographic projections with labelled sub-Saturnian point and South Pole locations.

$E^n(\mathbf{\Omega})$ and 'true' strain $E^{obs}(\mathbf{\Omega})$ (see section 2.4). We define a cost function evaluated at a given iteration $\xi^E(n)$ as the integrated square of the difference between $E^{obs}(\mathbf{\Omega})$ and $E^n(\mathbf{\Omega})$:

$$\xi^E(n) = \int (E^n(\mathbf{\Omega}) - E^{obs}(\mathbf{\Omega}))^2 \cdot d\mathbf{\Omega}. \tag{3.10}$$

For comparison to $\xi^E(n)$, we additionally track the integrated square of the difference between true and recovered thicknesses $\xi^D(n)$:

$$\xi^D(n) = \int (D^n(\mathbf{\Omega}) - D^{true}(\mathbf{\Omega}))^2 \cdot d\mathbf{\Omega}. \tag{3.11}$$

We expect that the extent to which gradient effects distort strain fields at a given location scales with the magnitude of the local gradient in crustal thickness $||\nabla D^n(\mathbf{\Omega})||$. We therefore update $D^n(\mathbf{\Omega})$ to $D^{n+1}(\mathbf{\Omega})$ for iterations $n > 0$ following:

$$\log_{10}\left(\frac{D^{n+1}(\mathbf{\Omega})}{D^n(\mathbf{\Omega})}\right) = \eta(n) \cdot ||\nabla D^n(\mathbf{\Omega})|| \cdot M(\mathbf{\Omega}), \tag{3.12}$$

where $\eta(n)$ is the learning rate and $M(\mathbf{\Omega})$ is a spatially variable prefactor defined as:

$$M(\mathbf{\Omega}) = \kappa(\mathbf{\Omega})^{-1} \frac{E^n(\mathbf{\Omega}) - E^{obs}(\mathbf{\Omega})}{E^{Base}(\mathbf{\Omega})}. \tag{3.13}$$

We incorporate $M(\mathbf{\Omega})$ into Equation 3.12 to ensure modifications to $D^n(\mathbf{\Omega})$ only correct for over- (under-) predictions of local thickness in locations with reduced (elevated) $E^n(\mathbf{\Omega})$ relative to $E^{obs}(\mathbf{\Omega})$. We update $\eta(n)$ between iterations following an adaptive algorithm to ensure $\xi^E(n)$ converges to a local minimum (Barzilai and Borwein, 1988). Note that we can expand $D^n(\mathbf{\Omega})$ for each iteration in Equation 3.12 into spherical harmonic functions:

$$D^n(\mathbf{\Omega}) \ = \sum_{l=0}^{\infty} \sum_{m=-l}^{l} d^n_{lm} Y_{lm}(\mathbf{\Omega}), \tag{3.14}$$

where d^n_{lm} are spherical harmonic coefficients. We can examine mismatch in the spectral domain (i.e., spectral power) by evaluating the root-mean-square (RMS) of thickness coefficients d^n_{lm} in Equation 3.14 and d^{true}_{lm} in Equation 3.1 over l (i.e., d^n_l

and d_l^{true} respectively) as well as the RMS percentage difference between coefficients d_{lm}^n and d_{lm}^{true} (i.e., δd_l^n; note that $\delta D^n(\mathbf{\Omega})$ in Equation 3.7 considers δd_l^n across all spherical harmonic basis functions evaluated at an angular position $\mathbf{\Omega}$):

$$d_l^n = \left(\frac{1}{2l+1} \sum_m (d_{lm}^n)^2 \right)^{1/2} \tag{3.15a}$$

$$d_l^{true} = \left(\frac{1}{2l+1} \sum_m (d_{lm}^{true})^2 \right)^{1/2} \tag{3.15b}$$

$$\delta d_l^n = \left(\frac{1}{2l+1} \sum_m \left(\frac{d_{lm}^n - d_{lm}^{true}}{d_{lm}^{true}} \right)^2 \right)^{1/2} \cdot 100\%. \tag{3.15c}$$

Figure 3.3 shows snapshots of $D^{true}(\mathbf{\Omega})$, $D^1(\mathbf{\Omega})$, $\delta D^1(\mathbf{\Omega})$, $D^{12}(\mathbf{\Omega})$, and $\delta D^{12}(\mathbf{\Omega})$ (i.e., see Equations 3.7 and 3.12). In addition, Figure 3.4 shows $\delta D^n(\mathbf{\Omega})$, d_l^n, d_l^{true}, and δd_l^n for iterations n = 0, 1, and 12 (see Equation 3.15). The non-zero $\delta D^0(\mathbf{\Omega})$ observed in Figure 3.3 drives broad differences between recovered and true spectral powers d_l^0 and d_l^{true} as well as non-zero values of δd_l^0 across all wavelengths. Iterating through our analysis once (n = 1) reduces $\delta D^1(\mathbf{\Omega})$ to < 20 km along prominent ridges over the Trailing and Southern Hemispheres, lessens the mismatch between d_l^1 and d_l^{true} curves, and diminishes δd_l^1 values across all wavelengths. Further changes to crustal thickness for iterations n = 1 – 12 reduce δd_l^{12} to ~ 10% (< 0.4 km mismatch in recovered relative to input spherical harmonic coefficient values) across longer wavelengths (i.e., $l \leq 12$) and reduce $\delta D^{12}(\mathbf{\Omega})$ to ~2 km (1σ confidence) across the ice shell.

Figure 3.4 presents the strain mismatch cost function, $\xi^E(n)$, and integrated thickness mismatch, $\xi^D(n)$, for iterations n = 0 – 15. Our results demonstrate a slight increase in $\xi^E(n)$ from iterations n = 12 – 15, while $\xi^D(n)$ (as well as $\delta D^n(\mathbf{\Omega})$ and δd_l^n) values remain largely unchanged after $n \sim 12$. Bayesian approaches (e.g., Cawley and Talbot, 2007) enable determination of a suitable cutoff iteration number to avoid over-fitting strain fields (i.e., in the absence of knowledge of 'true' thickness) but are beyond the scope of the current study.

3.5 Discussion and Conclusion

We examine the relationship between tidally-driven elastic strains and spatially variable crustal thickness at Enceladus. Results show a broad correlation between strain fields and crustal thickness across the moon (see Figure 3.2). Gradient

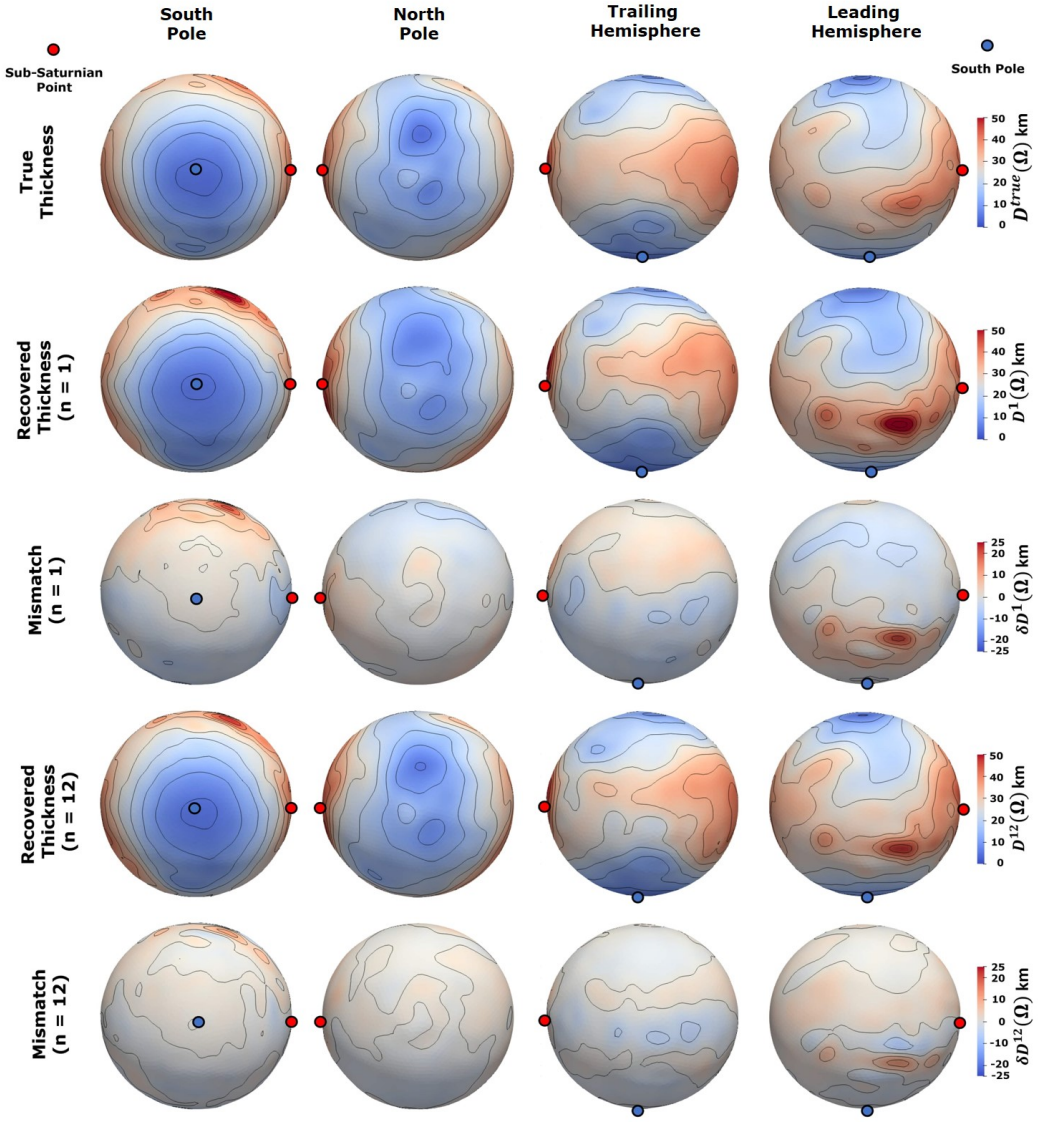

Figure 3.3: Snapshots of input crustal thickness $D^{true}(\mathbf{\Omega})$ (first row), recovered crustal thickness following $n = 1$ iteration $D^{1}(\mathbf{\Omega})$ (second row), mismatch between model and input crustal thickness following $n = 1$ iteration $\delta D^{1}(\mathbf{\Omega})$ (see Equations 3.7) (third row), recovered crustal thickness following $n = 12$ iterations $D^{12}(\mathbf{\Omega})$ (fourth row), and mismatch between model and input crustal thickness following $n = 12$ iterations $\delta D^{12}(\mathbf{\Omega})$ (fifth row) viewed facing the Southern, Northern, Leading, and Trailing hemispheres. Plotted contours denote colorscale intervals of 5 km for $\delta D^{n}(\mathbf{\Omega})$ and $D^{n}(\mathbf{\Omega})$ fields. Images are orthographic projections with labelled sub-Saturnian point and South Pole locations.

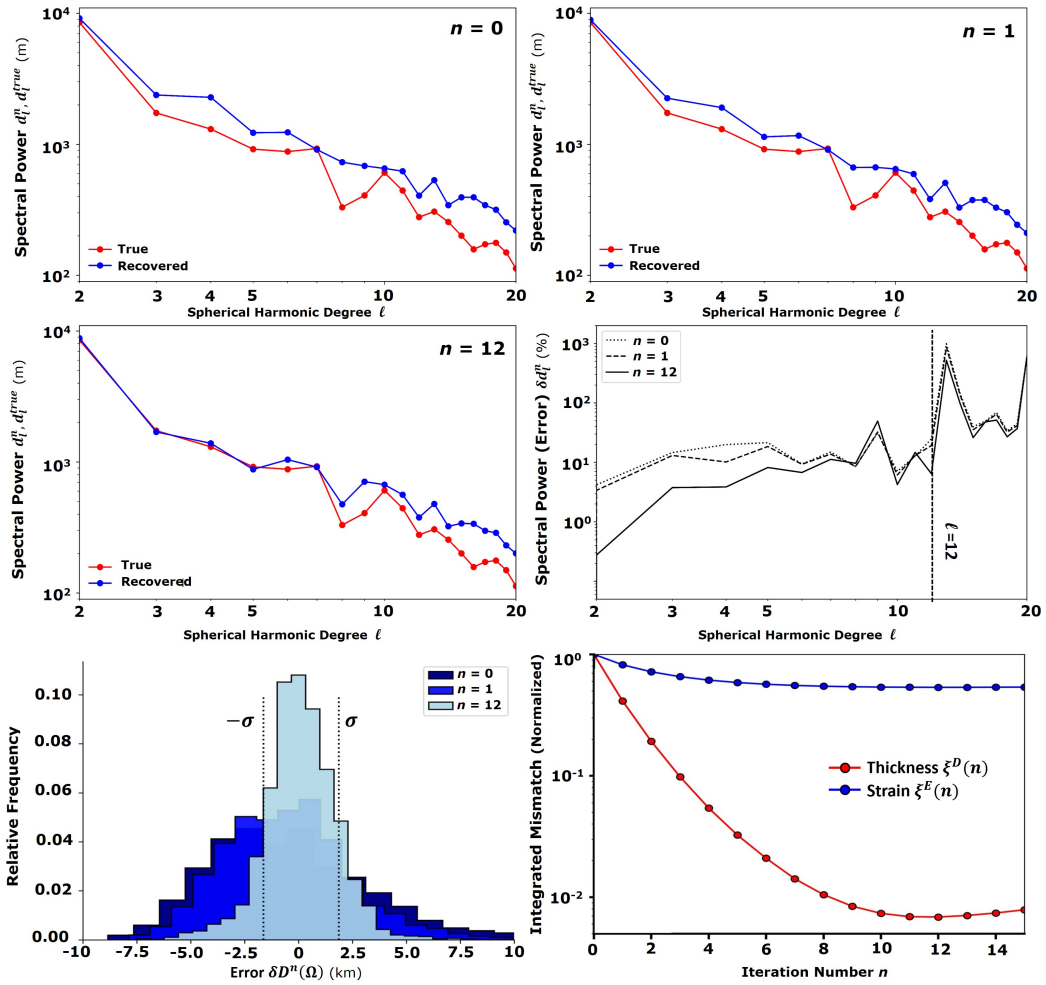

Figure 3.4: Analysis of mismatch between thickness fields that are input and recovered from models at a given iteration n using our analysis. Upper and center left panels show d_l^n and d_l^{true} evaluated for spherical harmonic degrees $l = 2 - 20$. d_l^n and d_l^{true} denote the spectral power of input and recovered thicknesses (see Equation 3.15ab; $d_l^n = d_l^{true}$ denotes a perfect recovery of crustal thickness). Note that the difference between d_l^n and d_l^{true} decreases (i.e., error decreases) after several iterations (i.e., increasing values of n). Center right panel shows δd_l^n evaluated for spherical harmonic degrees $l = 2 - 20$. δd_l^n is the spectral power of mismatch between input and recovered thicknesses at spherical harmonic degree l (see Equation 3.15c; $\delta d_l^n = 0$ denotes a perfect recovery of crustal thickness). Note that δd_l^n decreases (i.e., error decreases) after several iterations (i.e., increasing values of of n). Vertical dash-dot lines at $l = 12$ marked for reference. Lower left panel shows a histogram of $\delta D^n(\mathbf{\Omega})$ values (evaluated at FEM node locations) across recovered models for $n = 0$, 1, and 12. 1σ for the $n = 12$ case plotted as vertical dash-dot lines for reference. Lower right panel shows the cost function $\xi^E(n)$ (see Equation 3.10) and integrated thickness mismatch $\xi^D(n)$ (see Equation 3.11), normalized relative to the maximum value, for iterations $n = 0 - 15$. X-axes of upper and center panels are plotted in $\log_{10}$ scale.

effects modulate strain patterns (see Figures 3.3 and 3.4) with diminishing impact at longer wavelengths (see Figure 3.4). Our approach permits final recoveries of crustal thickness to within ~2 km of input values (1σ confidence) with minimal mismatch between the spherical harmonic coefficients (~10%) of expanded fields across spatial wavelengths $l \leq 12$ (i.e., corresponding to a half-wavelength of ~60 km; see Figure 3.4, iteration $n = 12$).

Our approach to correct for gradient effects minimally reduces error in crustal thickness estimates for $l > 12$ (see Figure 3.4). Note that length scales $l = 12 - 20$ (~60 – 40 km) approach the upper limit of input crustal thickness values for models (~50 km, see Figures 3.2 and 3.3). Moreover, bending effects (e.g., strain that is produced by non-local variations in elastic structure; see Beuthe, 2018 cf. Section 4.2.2) are expected to produce a more complex relationship between tidal strain and the amplitude of thickness variations than that considered by our approach (see Equations 3.8 and 3.12) at horizontal length scales that are comparable to the crustal thickness. To further examine the relationship between crustal thickness and the impact of bending effects on our analysis, we repeat our analysis with mean crustal thickness $\tilde{D} = 50$ km corresponding with maximum thickness values ~100 km. In this case, crustal thickness estimates become significantly less accurate across wavelengths $l \geq 8$ (i.e., ≤ 90 km; for further details see Supplementary Text S2 of this chapter).

Our initial analysis considers a crust with a uniform elastic rheology. However, fractures may reduce elastic shear modulus along fault zones (e.g., the Tiger Stripes) or highly damaged regions of the ice shell (Vaughan, 1995). Our modelling approach can readily account for localized reductions in shear modulus along fault zones if the surface and subsurface geometry (e.g., dip angle and penetration depth) of these structures is known *a priori* (for more information, see Berne et al., 2023a). However, resolving thickness over large-scale damage zones may require invoking additional assumptions regarding the expected shape of the crust at Enceladus. For example, local thickness exhibits a linear relationship with (Airy-) isostatically compensated surface topography over long- and regional- spatial scales (i.e., ice-ocean topography mirrors surface topography; D. Hemingway and Matsuyama, 2017). Variations in strain relative to topography (i.e., strain-topography admittance) may therefore be sensitive to (and permit correcting for) significant lateral variability in shear modulus over the crust (see Wahr et al., 2006; D. Hemingway and Mittal, 2019).

Our analysis also assumes *a priori* knowledge of $\tilde{D}$ (mean crustal thickness), G

(mean shear modulus), and ρ_w (ocean density) at Enceladus. $\tilde{D}$ is a crucial parameter for acquiring an initial estimate of variations in crustal thickness (i.e., $D^0(\mathbf{\Omega})$, see Equation 3.8). We find that our approach can correct for over- (under-) predictions of strain due to excessively low (high) initial estimates of $\tilde{D}$ (for details, see Supplementary Text S3 of this chapter). A reduced G (e.g., due to pervasive crustal fracturing) may also result in a derived value of $\tilde{D}$ that is inconsistent with constraints set by the amplitude of the forced libration of the ice shell (Van Hoolst et al., 2016; Beuthe, 2018; D. Hemingway and Mittal, 2019; Berne et al., 2023a). In this case, repeating our analysis with a lowered input G (see Table S1) should produce a derived $\tilde{D}$ that more closely matches the mean thickness expected for the satellite (D. Hemingway and Mittal, 2019). Traction at the ice-ocean boundary (which accounts for ~80% of tidally-driven surface strain for Enceladus, see Berne et al., 2023a) also scales with assumed ρ_w. The current ~50 kg/m^3 (i.e., 5%) range in expected ρ_w at Enceladus (Postberg et al., 2011; Glein et al., 2018) therefore corresponds to a ~4% uncertainty in derived crustal thickness using our approach.

In the future, geodetic imaging techniques (e.g., Interferometric Synthetic Aperture Radar or InSAR) at Enceladus could be used to determine crustal strain at high spatial resolution. InSAR measurements at Enceladus would be subject to uncertainty associated with imperfect spacecraft orbit determination but would not experience many of the sources of error experienced on Earth such as atmospheric propagation effects or temporal decorrelation due to vegetation, changing surface conditions, etc. over the orbital timescale (Simons and Rosen, 2015). Moreover, the sub-centimeter measurement noise typically associated with InSAR is smaller than the 1 - 10 cm signal produced by the presence of regional crustal thickness variations on Enceladus (see Supplementary Text S4 of this chapter). As such, we expect that InSAR measurements are ideally suited for inferring key characteristics of the interior structure and thus for improving our ability to understand the evolution and habitability of Enceladus.

3.6 Open Research

The data used in this study were generated using the software package PyLith (Aagaard et al., 2007; Aagaard et al., 2022). PyLith is an open-source finite element code for modeling geodynamic processes and is available on GitHub and Zenodo repositories (Aagaard et al., 2022). The specific PyLith version used in this study was v2.2.2. PyLith input files (including sample surface topography data), post-processing scripts, and selected output files for this work are available on (Berne

et al., 2023b). A full version of the forward FEM code, a user manual, and the workflow for inferring thickness from strain described in the current work is also available on (Berne et al., 2023b). The mesh geometries utilized in this study were created using CUBIT (v15.2), a node-locked licensed software which is available through the developer Sandia National Laboratories (Skroch et al., 2019; CoreForm, 2020).

3.7 Acknowledgements

This research was supported by the Future Investigators in NASA Earth and Space Science and Technology (FINESST) Program (80NSSC22K1318). We thank the Keck Institute for Space Studies (KISS) at the California Institute of Technology for organizing two workshops about "Next-Generation Planetary Geodesy" which provided insight, expertise, and discussions that inspired the research. We also thank Matthew Knepley, Brad Aagaard, and Charles Williams for providing valuable advice on how to modify PyLith for the simulations described in this work. A portion of this research was supported by a Strategic Research and Technology Development task led by James T. Keane and Ryan S. Park at the Jet Propulsion Laboratory, California Institute of Technology, under a contract with the National Aeronautics and Space Administration (80NM0018D0004)

References

Aagaard, B., C. Williams, and M. Knepley (2007). "PyLith: A Finite-Element Code for Modeling Quasi-Static and Dynamic Crustal Deformation". In: *Eos* 88(52).

Aagaard, B., C. Williams, and M. Knepley (2022). "PyLith: A Finite-Element Code for Modeling Quasi-Static and Dynamic Crustal Deformation". In: *geodynamics/pylith v2.2.2 (v2.2.2) [Computer software]. Zenodo,https://doi.org/10.5281/zenodo.3269486* .

Barzilai, J. and J. M. Borwein (1988). "Two-point step size gradient methods". In: *IMA Journal of Numerical Analysis* 8 (1). ISSN: 02724979. DOI: 10.1093/imanum/8.1.141.

Behounkova, M., O. Soucek, J. Hron, and O. Cadec (2017). "Plume activity and tidal deformation on enceladus influenced by faults and variable ice shell thickness". In: *Astrobiology* 17.9. ISSN: 15311074. DOI: 10.1089/ast.2016.1629.

Berne, A., M. Simons, J. Keane, and R. Park (2023b). "Using Tidally-Driven Elastic Strains to Infer Regional Variations in Crustal Thickness at Enceladus". In: *Geophysical Research Letters* 50 (22). DOI: 10.1029/2023GL106656.

Berne, A., M. Simons, J. Keane, and R. Park (2023a). “Inferring the Mean Thickness of the Outer Ice Shell of Enceladus from Diurnal Crustal Deformation”. In: *Journal of Geophysical Research E: Planets* . DOI: 10.1029/2022JE007712.

Berne, A., M. Simons, J. T. Keane, and R. S. Park (2023). “Using Tidally-Driven Elastic Strains to Infer Regional Variations in Crustal Thickness at Enceladus”. In: *Geophysical Research Letters* 50 (22).

Beuthe, M. (2018). “Enceladus’s crust as a non-uniform thin shell: I tidal deformations”. In: *Icarus* 302. ISSN: 10902643. DOI: 10.1016/j.icarus.2017.11.009.

Beuthe, M., A. Rivoldini, and A. Trinh (2016). “Enceladus’s and Dione’s floating ice shells supported by minimum stress isostasy”. In: *Geophysical Research Letters* 43 (19). ISSN: 19448007. DOI: 10.1002/2016GL070650.

Čadek, O., O. Souček, M. Běhounková, G. Choblet, G. Tobie, and J. Hron (2019). “Long-term stability of Enceladus’ uneven ice shell”. In: *Icarus* 319. ISSN: 10902643. DOI: 10.1016/j.icarus.2018.10.003.

Cawley, G. C. and N. L. Talbot (2007). “Preventing over-fitting during model selection via bayesian regularisation of the hyper-parameters”. In: *Journal of Machine Learning Research* 8. ISSN: 15324435.

Choblet, G., G. Tobie, C. Sotin, M. Běhounková, O. Čadek, F. Postberg, and O. Souček (2017). “Powering prolonged hydrothermal activity inside Enceladus”. In: *Nature Astronomy* 1 (12). ISSN: 23973366. DOI: 10.1038/s41550-017-0289-8.

CoreForm (2020). “ "CUBIT" https://coreform.com/products/coreform-cubit/ ”. In.

“Enceladus’s internal ocean and ice shell constrained from Cassini gravity, shape, and libration data” (2016). In: *Geophysical Research Letters* 43 (11). ISSN: 19448007. DOI: 10.1002/2016GL068634.

Ermakov, A. I., R. S. Park, J. Roa, J. C. Castillo-Rogez, J. T. Keane, F. Nimmo, E. S. Kite, C. Sotin, T. J. W. Lazio, G. Steinbrügge, S. M. Howell, B. G. Bills, D. J. Hemingway, V. Viswanathan, G. Tobie, and V. Lainey (2021). “A Recipe for the Geophysical Exploration of Enceladus”. In: *Planetary Science Journal* 2 (4). ISSN: 26323338. DOI: 10.3847/PSJ/ac06d2.

Fifer, L., D. Catling, and J. Toner (2022). “Chemical Fractionation Modeling of Plumes Indicates a Gas-rich, Moderately Alkaline Enceladus Ocean”. In: *The Planetary Science Journal* 3 (191). ISSN: DOI: 10.3847/PSJ/ac7a9f.

Giese, B., R. Wagner, H. Hussmann, G. Neukum, J. Perry, P. Helfenstein, and P. C. Thomas (2008). “Enceladus: An estimate of heat flux and lithospheric thickness from flexurally supported topography”. In: *Geophysical Research Letters* 35 (24). ISSN: 00948276. DOI: 10.1029/2008GL036149.

Glein, C. R., F. Postberg, and S. D. Vance (2018). *The Geochemistry of Enceladus: Composition and Controls*. DOI: 10.2458/azu_uapress_9780816537075-ch003.

Hay, H. C. and I. Matsuyama (2019). "Nonlinear tidal dissipation in the subsurface oceans of Enceladus and other icy satellites". In: *Icarus* 319. ISSN: 10902643. DOI: 10.1016/j.icarus.2018.09.019.

Hemingway, D. and I. Matsuyama (2017). "Isostatic equilibrium in spherical coordinates and implications for crustal thickness on the Moon, Mars, Enceladus, and elsewhere". In: *Geophysical Research Letters* 44.15. ISSN: 19448007. DOI: 10.1002/2017GL073334.

Hemingway, D. and T. Mittal (2019). "Enceladus's ice shell structure as a window on internal heat production". In: *Icarus* 332. ISSN: 10902643. DOI: 10.1016/j.icarus.2019.03.011.

Hemingway, L. Iess, R. Tajeddine, and G. Tobie (2018). "The Interior of Enceladus". In: *Enceladus and the icy moons of Saturn*. The University of Arizona Press in collaboration with Lunar and Planetary Institute, Houston.

Hsu, M. Simons, C. Williams, and E. Casarotti (2011). "Three-dimensional FEM derived elastic Green's functions for the coseismic deformation of the 2005 Mw 8.7 Nias-Simeulue, Sumatra earthquake". In: *Geochemistry, Geophysics, Geosystems* 12 (7). ISSN: 15252027. DOI: 10.1029/2011GC003553.

Iess, L., D. J. Stevenson, M. Parisi, D. Hemingway, R. A. Jacobson, J. I. Lunine, and P. Tortora (2014). "The gravity field and interior structure of Enceladus". In: *Science* 344.6179. ISSN: 10959203. DOI: 10.1126/science.1250551.

Ingersoll, S. P. Ewald, and S. K. Trumbo (2020). "Time variability of the Enceladus plumes: Orbital periods, decadal periods, and aperiodic change". In: *Icarus* 344. ISSN: 10902643. DOI: 10.1016/j.icarus.2019.06.006.

Ingersoll and M. Nakajima (2016). "Controlled boiling on Enceladus. 2. Model of the liquid-filled cracks". In: *Icarus* 272. ISSN: 10902643. DOI: 10.1016/j.icarus.2015.12.040.

Kite, E. S. and A. M. Rubin (2016). "Sustained eruptions on Enceladus explained by turbulent dissipation in tiger stripes". In: *Proceedings of the National Academy of Sciences of the United States of America* 113 (15). ISSN: 10916490. DOI: 10.1073/pnas.1520507113.

McKinnon, W. B. (2015). "Effect of Enceladus's rapid synchronous spin on interpretation of Cassini gravity". In: *Geophysical Research Letters* 42 (7). ISSN: 19448007. DOI: 10.1002/2015GL063384.

Murray, C. D. and S. F. Dermott (2000). *Solar System Dynamics*. DOI: 10.1017/cbo9781139174817.

Neumeier, J. J. (2018). "Elastic Constants, Bulk Modulus, and Compressibility of H2O Ice i h for the Temperature Range 50 K-273 K". In: *Journal of Physical and Chemical Reference Data* 47 (3). ISSN: 00472689. DOI: 10.1063/1.5030640.

Nimmo, F., B. G. Bills, and P. C. Thomas (2011). "Geophysical implications of the long-wavelength topography of the Saturnian satellites". In: *Journal of Geophysical Research E: Planets* 116.11. ISSN: 01480227. DOI: 10.1029/2011JE003835.

Porco, P. Helfenstein, P. C. Thomas, A. P. Ingersoll, J. Wisdom, R. West, and S. Squyres (2006). "Cassini observes the active south pole of enceladus". In: *Science* 311 (5766). ISSN: 00368075. DOI: 10.1126/science.1123013.

Postberg, F., S. Kempf, J. Schmidt, N. Brilliantov, A. Beinsen, B. Abel, U. Buck, and R. Srama (2009). "Sodium salts in E-ring ice grains from an ocean below the surface of Enceladus". In: *Nature* 459 (7250). ISSN: 00280836. DOI: 10.1038/nature08046.

Postberg, F., J. Schmidt, J. Hillier, S. Kempf, and R. Srama (2011). "A salt-water reservoir as the source of a compositionally stratified plume on Enceladus". In: *Nature* 474 (7353). ISSN: 00280836. DOI: 10.1038/nature10175.

Qin, C., S. Zhong, and J. Wahr (2016). "Elastic tidal response of a laterally heterogeneous planet: A complete perturbation formulation". In: *Geophysical Journal International* 207 (1). ISSN: 1365246X. DOI: 10.1093/gji/ggw257.

Rovira-Navarro, M., R. F. Katz, Y. Liao, W. van der Wal, and F. Nimmo (2022). "The Tides of Enceladus' Porous Core". In: *Journal of Geophysical Research: Planets* 127 (5). ISSN: 21699100. DOI: 10.1029/2021JE007117.

Rovira-Navarro, M. and I. Matsuyama (2022). "A Spectral Method to Study the Tides of Laterally Heterogenous Bodies". In: *AGU Fall Meeting Abstracts*.

Rovira-Navarro, M., I. Matsuyama, and H. C. F. C. Hay (2023). "Thin-shell Tidal Dynamics of Ocean Worlds". In: *The Planetary Science Journal* 4 (2). DOI: 10.3847/psj/acae9a.

Schenk, P. M., R. N. Clark, C. J. A. Howett, A. J. Verbiscer, and J. H. Waite (2018). *Enceladus and the Icy Moons of Saturn*. DOI: 10.2458/azu_uapress_9780816537075.

Schubert, G., J. D. Anderson, B. J. Travis, and J. Palguta (2007). "Enceladus: Present internal structure and differentiation by early and long-term radiogenic heating". In: *Icarus* 188.2. ISSN: 00191035. DOI: 10.1016/j.icarus.2006.12.012.

Shaw, G. H. (1985). "Elastic properties and equation of state of high pressure ice". In: *The Journal of Chemical Physics* 84 (1). ISSN: 00219606. DOI: 10.1063/1.449897.

Simons, M. and P. A. Rosen (2015). "Interferometric Synthetic Aperture Radar Geodesy". In: *Treatise on Geophysics: Second Edition*. Vol. 3. DOI: 10.1016/B978-0-444-53802-4.00061-0.

Skroch, M., S. Owen, M. Staten, R. Quadros, B. Hanks, B. Clark, and C. Stimpson (2019). *CUBIT Geometry and Mesh Generation Toolkit 15.4 User Documentation*.

Souček, O., M. Běhounková, O. Čadek, J. Hron, G. Tobie, and G. Choblet (2019). "Tidal dissipation in Enceladus' uneven, fractured ice shell". In: *Icarus* 328. ISSN: 10902643. DOI: 10.1016/j.icarus.2019.02.012.

Souček, O., J. Hron, M. Běhounková, and O. Čadek (2016). "Effect of the tiger stripes on the deformation of Saturn's moon Enceladus". In: *Geophysical Research Letters* 43.14. ISSN: 19448007. DOI: 10.1002/2016GL069415.

Tape, C., P. Musé, M. Simons, D. Dong, and F. Webb (2009). "Multiscale estimation of GPS velocity fields". In: *Geophysical Journal International* 179 (2). ISSN: 0956540X. DOI: 10.1111/j.1365-246X.2009.04337.x.

Thomas, P. C., R. Tajeddine, M. S. Tiscareno, J. A. Burns, J. Joseph, T. J. Loredo, and C. Porco (2016). "Enceladus's measured physical libration requires a global subsurface ocean". In: *Icarus* 264. ISSN: 10902643. DOI: 10.1016/j.icarus.2015.08.037.

Van Hoolst, T., R. M. Baland, and A. Trinh (2016). "The diurnal libration and interior structure of Enceladus". In: *Icarus* 277. ISSN: 10902643. DOI: 10.1016/j.icarus.2016.05.025.

Vaughan, D. G. (1995). "Tidal flexure at ice shelf margins". In: *Journal of Geophysical Research* 100 (B4). ISSN: 01480227. DOI: 10.1029/94JB02467.

Wahr, J., Z. A. Selvans, M. E. Mullen, A. C. Barr, G. C. Collins, M. M. Selvans, and R. T. Pappalardo (2009). "Modeling stresses on satellites due to nonsynchronous rotation and orbital eccentricity using gravitational potential theory". In: *Icarus* 200.1. ISSN: 00191035. DOI: 10.1016/j.icarus.2008.11.002.

Wahr, J., M. T. Zuber, D. E. Smith, and J. I. Lunine (2006). "Tides on Europa, and the thickness of Europa's icy shell". In: *Journal of Geophysical Research E: Planets* 111.12. ISSN: 01480227. DOI: 10.1029/2006JE002729.

Yin, A. and R. Pappalardo (2015). "Gravitational spreading, bookshelf faulting, and tectonic evolution of the South Polar Terrain of Saturn's moon Enceladus". In: *Icarus* 260. ISSN: 10902643. DOI: 10.1016/j.icarus.2015.07.017.

3.8 Supplementary Information

Contents

Introduction

In S1, we outline our methodology for generating synthetic 'true' models of Enceladus's crust (S1.1) and for calculating the transfer function $\kappa(\mathbf{\Omega})$ in Equation 3.7 from the main text (S1.2 and Figure 2.7). In S2, we present the results of our iterative procedure for recovering crustal thickness on a synthetic crustal model with a mean thickness $\tilde{D}$ = 50 km (S2.1 and Figure 3.6) and demonstrate that viscous effects within the ice shell are not expected to significantly impact total surface strain at Enceladus (Figure 3.7). In S3, we present results for recoveries of crustal thickness on a synthetic model for which we assume an incorrect initial estimate of mean thickness (S3.1 and Figure 3.4). In S4, we examine the effect of incorporating noise (both correlated and uncorrelated) and discuss the impact of imperfect measurement coverage on recoveries of crustal thickness using our approach (S4.1 and Figure 3.9).

Text S1

S1.1: Synthetic 'True' Crustal Thickness Model

To generate 'true' crustal thickness models (see Figures 2 and 3 of the main text), we first apply topography $H(\mathbf{\Omega})$ to the outer surface of spherically symmetric models. Note that we can write $H(\mathbf{\Omega})$ as a sum over spherical harmonic basis functions scaled by coefficients h_{lm}:

$$H(\mathbf{\Omega}) = \sum_{l=0}^{\infty} \sum_{m=-l}^{l} h_{lm} Y_{lm}(\mathbf{\Omega}). \tag{3.16}$$

We extract h_{lm} in Equation 4.21 for $l = 2 - 60$ from an updated version of topography at Enceladus using all available Cassini imagery (Park et al., personal communication). Our approach for inferring crustal thickness from strain is agnostic to the details of assumed topography. Details of the topography used in this study are therefore not important and are not intended to promote any particular model for

Enceladus's shape. From h_{lm}, we generate components d_{lm}^{true} in Equation 3.1 of the main text assuming a modified formulation for Airy-type compensation of surface topography (Hemingway and Matsuyama, 2017):

$$d_{lm}^{true} = h_{lm} + h_{lm} \frac{\rho_{ice}}{(\rho_w - \rho_{ice})} \frac{g}{g_{int}} \frac{R^2}{(R - \tilde{D})^2} (l-1)^{-N}, \tag{3.17}$$

where g_{int} is radial gravitational acceleration at the ice-ocean boundary, ρ_{ice} is the mean density of the ice shell, ρ_w is the mean density of the ocean (see Table 3.8 of the main text for assumed parameter values), and N is a dimensionless constant. Equation 3.17 demonstrates that the amplitude of variations in crustal thickness across l depends on the chosen value of N. As N decreases, the amplitude of variations in crustal thickness at large values of l (i.e., short-wavelengths) increases rapidly. For models with $\tilde{D}$ = 25 km, an assumed value of $N < 1.0$ produces negative (i.e., non-physical) crustal thickness near the South and North Poles. We aim to estimate the maximum extent that short-wavelength variations in crustal thickness bias inferences of crustal thickness via gradient effects. We therefore generate a model with N = 1.0 for this work.

S1.2: Computation of $\kappa(\mathbf{\Omega})$

The quantity $\kappa(\mathbf{\Omega})$ is a transfer function which captures any non-linear dependence of strain fields on thickness variations at different $\mathbf{\Omega}$. We compute $\kappa(\mathbf{\Omega})$ empirically for a given crustal model by re-arranging Equation 3.8 of the main text:

$$\kappa(\mathbf{\Omega}) = \frac{D^{\zeta}(\mathbf{\Omega})}{\tilde{D}} \frac{E^{\zeta}(\mathbf{\Omega})}{E^{base}(\mathbf{\Omega})}, \tag{3.18}$$

where $E^{\zeta}(\mathbf{\Omega})$ is the strain produced by a crustal thickness model $D^{\zeta}(\mathbf{\Omega})$. To ensure a minimal impact of potential gradient effects on computations of $\kappa(\mathbf{\Omega})$, we define $D^{\zeta}(\mathbf{\Omega})$ such that models exhibit a uniform thickness across the crust:

$$D^{\zeta}(\mathbf{\Omega}) = \tilde{D} + \zeta, \tag{3.19}$$

where ζ is a constant. We assign a value of ζ (i.e., 0.1 km) that is much smaller than $\tilde{D}$ for models in the current work. Note that in the case of a perfectly linear and inverse relationship between $D^{\zeta}(\mathbf{\Omega})$ and $E^{\zeta}(\mathbf{\Omega})$ Equation 3.18 would imply $\kappa(\mathbf{\Omega})$ = 1. For convenience, we compute $E^{\zeta}(\mathbf{\Omega})$ and $E^{base}(\mathbf{\Omega})$ using numerical FEMs but

could easily compute these functions using analytic methods (e.g., SatStress; Wahr et al., 2009).

Figure 3.5 shows images of $\kappa(\mathbf{\Omega})$ for the case of $\tilde{D}$ = 25 km as well as recoveries of crustal thickness (for the input model presented in Figure 3.2 of the main text) which assume $\kappa(\mathbf{\Omega}) = 1$. Deviations in $\kappa(\mathbf{\Omega})$ from unity reflect differences in the efficiency of 3D tidal forcing for producing strain for thickness variations located at different $\mathbf{\Omega}$. For example, thinning (i.e., which is analogous to lowering the shear modulus (Qin et al., 2016) of 5% at locations with two tidally-driven principal stresses of opposite sense (i.e., resulting in non-zero local shear stresses) may enhance $E^{obs}(\mathbf{\Omega})$ (or $E^{n}(\mathbf{\Omega})$) by 6% relative to $E^{Base}(\mathbf{\Omega})$ compared to only 4% if positioned at locations with two principal stresses of the same sense (i.e., resulting in zero local shear stress) (Segall, 2010). Such position-dependent effects principally occur over long-wavelengths (i.e., $l = 2 - 4$) due to changes in the spatial pattern of the $l = 2$ tidal forcing (see Equation 3.2 of the main text) over these scales.

Text S2

S2.1: Results for Model With $\tilde{D}$ = 50 km

We reproduce the center-right and lower-left panels of Figure 3.4 of the main text for recoveries of thickness on a synthetic crustal model with a mean thickness value $\tilde{D}$ = 50 km (see Figure 3.6). We find that increasing the value of $\tilde{D}$ increases the horizontal spatial scale below which bending effects prohibit accurate recoveries of crustal thickness (i.e., from $l = 12$ to $l = 8$).

Text S3

S3.1: Results for Model with Incorrect Initial Estimate of Mean Thickness

We reproduce the center-right and lower-left panels of Figure 3.4 of the main text for recoveries of thickness on models for which we assume a mean thickness of 50 km despite a true mean thickness $\tilde{D}$ = 25 km (Figure 3.8). We find that we are able to eventually converge to thickness values similar to those obtained when we initially assume a correct mean thickness value of $\tilde{D}$ = 25 km (see Figure 3.4 of the main text).

Text S4

S4.1: The Impact of Noise and Measurement Coverage on Recoveries of Crustal Thickness

We examine the impact of noise (correlated and uncorrelated) on recoveries of crustal thickness using our approach. For uncorrelated noise, we carry out a series of experiments for which we superimpose Gaussian noise source to 'measurements' (simulated velocities at the surface of Enceladus) prior to inputting these simulated data into our recovery technique (i.e., sections 3.1 and 3.2 of the main text). We assign a standard deviation σ_n of the Gaussian noise source that is a fraction of the magnitude of evaluated velocity at the surface $|v| = \sqrt{v_r^2 + v_\theta^2 + v_\phi^2}$ (see Equation 3.3 of the main text) at a given location such that there is a constant value for $|v|/\sigma_n$ for measurements across the body. We test $|v|/\sigma_n$ values ranging from 20 – 10000 and find that $|v|/\sigma_n < 10$ - 100 results in a significant decrease in the accuracy of recoveries of crustal thickness using our approach (see Figure 3.9 below). For peak-to-peak tidally-induced horizontal displacements of ± 1 m at Enceladus, a loss of coherence for $|v|/\sigma_n \sim 10$ - 100 indicates that the signal associated with variations in crustal thickness ranges from approximately 1 - 10 cm, which is larger than the typical sub-cm sensitivity of InSAR measurements. Regularization techniques (e.g., Tikhanov smoothing) could also potentially reduce the impact of uncorrelated measurement noise allowing for inference of crustal thickness for $|v|/\sigma_n < 10$ (Tarantola, 2005).

For correlated noise, we replace our Gaussian moise source with a constant horizontal (i.e., in the East direction) velocity v_{corr} across the body (Note: $|v|/v_{corr}$ is not constant and depends on the local value of $|v|$). We test values of v_{corr} ranging from 0.001 — 1 m per tidal cycle and find that recoveries of thickness lose coherence only for v_{corr} values approaching 1 m per tidal cycle. Note that correlated noise, as described above, does not produce gradients in surface velocity fields and so minimally impacts deviatoric strain components in Equations 3.3 and 3.4 of the main text. Incorporating uncorrelated noise correspondingly produces poorer recoveries of crustal thickness (i.e., for similar noise magnitudes) than incorporating correlated noise into simulated measurements does.

Regarding measurement coverage, orbiting platforms could feasibly acquire images of displacement that are each separated by ~50 km distance across the full surface of Enceladus (Benedikter et al., 2022). Aliasing below such 50 km horizontal distances (i.e., $l = 15$) would impact strain at spatial scales over which bending effects already

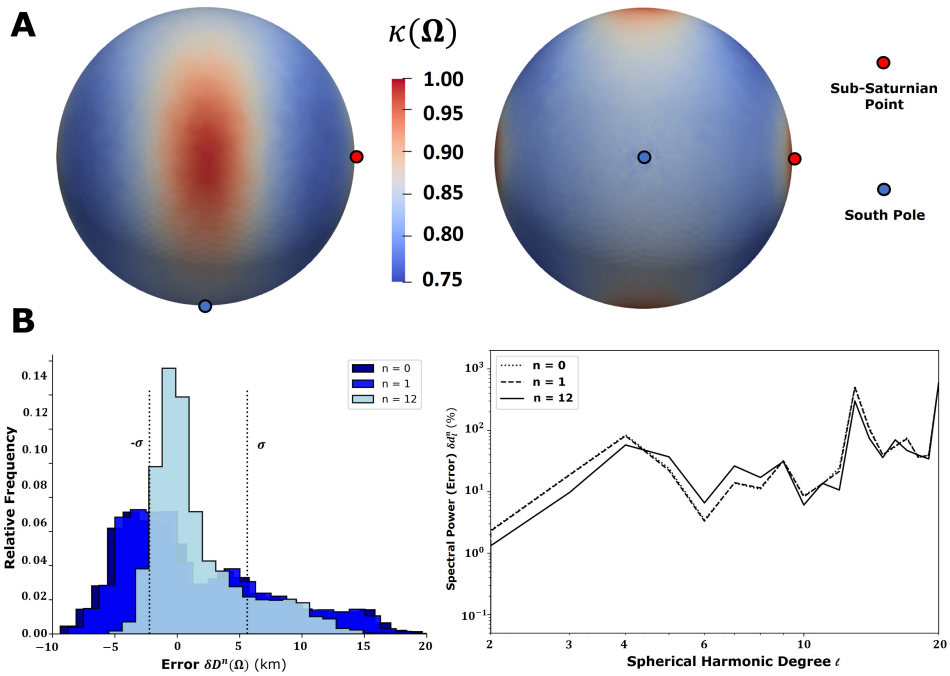

Figure 3.5: Panel A: Snapshots of the function $\kappa(\mathbf{\Omega})$ derived from Equations 3.18 and 3.19 viewed facing the Leading Hemisphere and the South Pole. Panel B: Similar to center-right and lower-left panels of Figure 3.4 of the main text except we assume $\kappa(\mathbf{\Omega}) = 1$ in Equations 3.8 and 3.13 for recoveries of crustal thickness.

prohibit accurate recoveries of crustal thickness (i.e., $l > 12$; see main text).

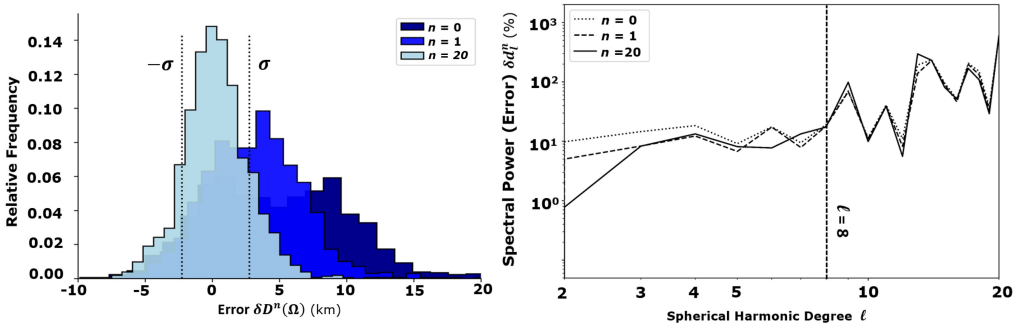

Figure 3.6: Similar to center-right and lower-left panels of Figure 3.4 of the main text except we assign a mean thickness $\tilde{D}$ = 50 km for 'true' models for iterations n = 0 – 20. Vertical dash-dot line at l = 8 marked for reference in the right panel.

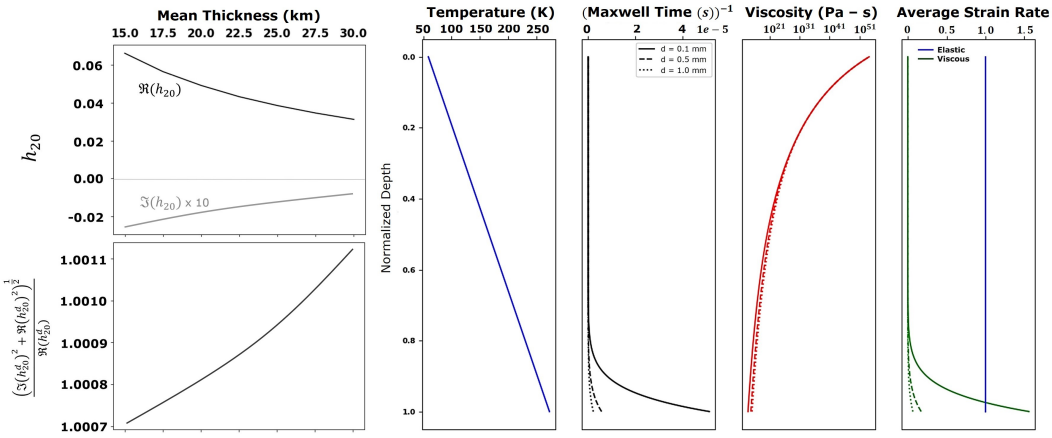

Figure 3.7: Complex diurnal Love number components (i.e., $\Im(h_{20})$ and $\Re(h_{20})$) for a spherically symmetric body with non-uniform radial viscosity structure. Viscosity structure is shown in the second plot from the right (grain size 0.1 mm; Brown et al., 2006) and is derived assuming grain size- and stress- dependent creep (diffusion, basal slip, and grain-boundary sliding mechanisms are considered; we extract molar volume, activation energy, Burger's vector, and viscous exponents for ice from Goldsby and Kohlstedt, 2001) and the conductive temperature profile shown in the fourth plot from the right. Maxwell times and average strain rates are shown in the third and first plots from the right, respectively. We assume a mean diurnal stress magnitude of 10 kPa for computations of viscosity. The lower left panel shows the total magnitude of h_{20} relative to that expected for a body which exhibits only elastic strain (i.e., a proxy for the relative impact of viscous deformation on surface strain fields; a value of 1 indicates that viscous strain does not modulate deformation at the surface). Note that viscous structure increases total strain at the outer surface by less than 0.2% for mean thicknesses ranging from 15 - 30 km (Van Hoolst et al., 2016). We solve for $\Im(h_2^d)$ and $\Re(h_2^d)$ using a 100-layer spherically symmetric model within SatStress (Wahr et al., 2009). For each layer, we linearly interpolate viscosity values and assign a constant shear modulus and bulk modulus (G = 3.3 GPa and μ = 8.8 GPa respectively).

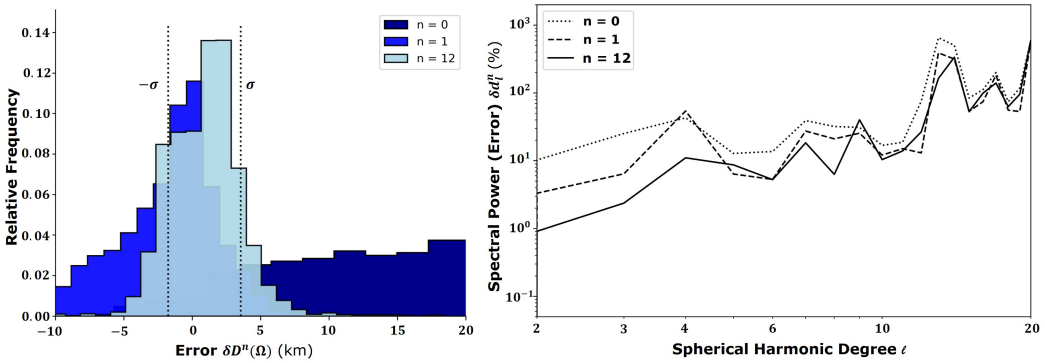

Figure 3.8: Similar to center-right and lower-left panels of Figure 3.4 of the main text except we assume an incorrect initial value for mean thickness (i.e., 50 km for 'true' mean thickness $\tilde{D} = 25$ km).

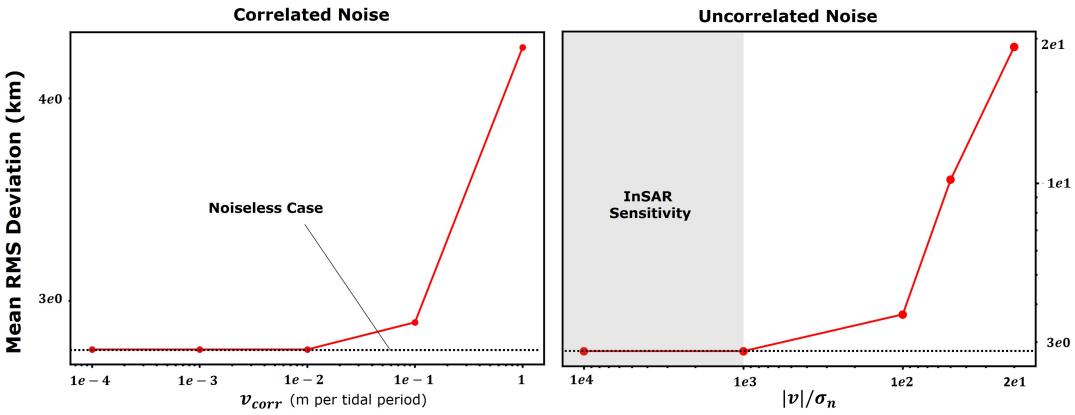

Figure 3.9: Mean RMS deviation (in km) of recovered relative to input thickness for recoveries of crustal thickness in the presence of measurement noise. Mean RMS deviation corresponds to the mean value of $|\delta D^{12}(\mathbf{\Omega})|$ (see Equation 3.7 of the main text) following our approach. Left Panel: Mean RMS deviation associated with correlated noise for applied v_{corr} (i.e., secular velocities) ranging from 0.0001 - 1 m over the tidal cycle. Right Panel: Mean RMS deviation associated with uncorrelated noise for $|v|/\sigma_n$ values ranging from 10000 - 20. Results for the noiseless case (i.e., Figure 3.4 of the main text) are shown as a horizontal dotted line at 2.1 km mean RMS deviation. Measurement resolution range that is achievable with InSAR based on Simons and Rosen (2015) is shown as a gray shaded box in the right panel for reference. X- and Y- axes are plotted in $\log_{10}$ scale.

Table 3.1: Assumed parameter values in Chapter 3. Parameter values extracted from Schenk et al. (2018); Iess et al. (2014); and Souček et al. (2016).

Parameter	**Value**	**Units**
R	252.1	km
$\tilde{D}$	25.0	km
G	3.3	GPa
μ	8.6	GPa
ρ_{ice}	925	kg/m^3
ρ_w	1007	kg/m^3
g	0.113	m/s^2
g_{int}	0.120	m/s^2
e	0.0047	N/A
ω	$5.307 \cdot 10^{-5}$	s^{-1}

References

Benedikter, A., K. Wickhusen, H. Hussmann, A. Stark, F. Damme, M. Rodriguez-Cassola, and G. Krieger (2022). "Periodic orbits for interferometric and tomographic radar imaging of Saturn's moon Enceladus". In: *Acta Astronautica* 191. ISSN: 00945765. DOI: 10.1016/j.actaastro.2021.10.041.

Brown, R. H., R. N. Clark, B. J. Buratti, D. P. Cruikshank, J. W. Barnes, R. M. Mastrapa, J. Bauer, S. Newman, T. Momary, K. H. Baines, G. Bellucci, F. Capaccioni, P. Cerroni, M. Combes, A. Coradini, P. Drossart, V. Formisano, R. Jaumann, Y. Langavin, D. L. Matson, T. B. McCord, R. M. Nelson, P. D. Nicholson, B. Sicardy, and C. Sotin (2006). "Composition and physical properties of Enceladus' surface". In: *Science* 311 (5766). ISSN: 00368075. DOI: 10.1126/science.1121031.

Goldsby, D. L. and D. L. Kohlstedt (2001). "Superplastic deformation of ice: Experimental observations". In: *Journal of Geophysical Research: Solid Earth* 106 (B6). ISSN: 21699356. DOI: 10.1029/2000jb900336.

Hemingway, D. and I. Matsuyama (2017). "Isostatic equilibrium in spherical coordinates and implications for crustal thickness on the Moon, Mars, Enceladus, and elsewhere". In: *Geophysical Research Letters* 44.15. ISSN: 19448007. DOI: 10.1002/2017GL073334.

Iess, L., D. J. Stevenson, M. Parisi, D. Hemingway, R. A. Jacobson, J. I. Lunine, and P. Tortora (2014). "The gravity field and interior structure of Enceladus". In: *Science* 344.6179. ISSN: 10959203. DOI: 10.1126/science.1250551.

Qin, C., S. Zhong, and J. Wahr (2016). "Elastic tidal response of a laterally heterogeneous planet: A complete perturbation formulation". In: *Geophysical Journal International* 207 (1). ISSN: 1365246X. DOI: 10.1093/gji/ggw257.

Schenk, P. M., R. N. Clark, C. J. A. Howett, A. J. Verbiscer, and J. H. Waite (2018). *Enceladus and the Icy Moons of Saturn*. DOI: 10.2458/azu_uapress_9780816537075.

Segall, P. (2010). *Earthquake and volcano deformation*. DOI: 10.5860/choice.48-0287.

Simons, M. and P. A. Rosen (2015). "Interferometric Synthetic Aperture Radar Geodesy". In: *Treatise on Geophysics: Second Edition*. Vol. 3. DOI: 10.1016/B978-0-444-53802-4.00061-0.

Souček, O., J. Hron, M. Běhounková, and O. Čadek (2016). "Effect of the tiger stripes on the deformation of Saturn's moon Enceladus". In: *Geophysical Research Letters* 43.14. ISSN: 19448007. DOI: 10.1002/2016GL069415.

Tarantola, A. (2005). *Inverse Problem Theory and Methods for Model Parameter Estimation*. DOI: 10.1137/1.9780898717921.

Van Hoolst, T., R. M. Baland, and A. Trinh (2016). "The diurnal libration and interior structure of Enceladus". In: *Icarus* 277. ISSN: 10902643. DOI: 10.1016/j.icarus.2016.05.025.

Wahr, J., Z. A. Selvans, M. E. Mullen, A. C. Barr, G. C. Collins, M. M. Selvans, and R. T. Pappalardo (2009). "Modeling stresses on satellites due to nonsynchronous rotation and orbital eccentricity using gravitational potential theory". In: *Icarus* 200.1. ISSN: 00191035. DOI: 10.1016/j.icarus.2008.11.002.

Chapter 4

JET ACTIVITY ON ENCELADUS LINKED TO TIDALLY-DRIVEN STRIKE-SLIP MOTION ALONG TIGER STRIPES

A. Berne et al. (2024). "Jet activity on Enceladus linked to tidally driven strike-slip motion along tiger stripes". In: *Nature Geoscience* 17.5.

4.1 Abstract

At Saturn's moon Enceladus, jets along four distinct fractures called 'Tiger Stripes' erupt ice crystals into a broad plume above the South Pole. The Tiger Stripes experience variations in tidally-driven shear and normal traction as Enceladus orbits Saturn. Here we use numerical finite-element modelling of a spherical ice shell subjected to tidal forces to show that this traction may produce quasi-periodic strike-slip motion in the Enceladus crust with two peaks in activity during each orbit. We suggest that friction modulates the response of Tiger Stripes to driving stresses, such that tidal traction on the faults results in a difference in the magnitudes of peak strike-slip and delays the first peak in fault motion following peak tidal stress. The simulated double-peaked and asymmetric strike-slip motion of the Tiger Stripes is consistent with diurnal variations in jet activity inferred from Cassini spacecraft images of plume brightness. The spatial distribution of strike-slip motion also matches Cassini infrared observations of heat flow. We hypothesize that strike-slip motion can extend transtensional bends (e.g., pull-apart structures) along geometric irregularities over the Tiger Stripes and thus modulate jet activity. Tidally-driven fault motion may also influence longer term tectonic evolution near the South Pole of the satellite.

4.2 Introduction

Enceladus is a small (~500 km diameter), dynamic, and potentially habitable moon of Saturn (Porco et al., 2006; Postberg et al., 2009). Flybys of Enceladus by the Cassini spacecraft between 2005-2015 revealed the presence of numerous jets which localize along four large-scale surface fractures (informally known as the 'Tiger Stripes') over the moon's highly tectonized South Polar Terrain (SPT) (Yin and Pappalardo, 2015; Spitale et al., 2025). The Tiger Stripes exhibit high heat flow

relative to other regions on Enceladus (Spencer et al., 2018) and are believed to tap material from a global (Thomas et al., 2016) or regional (Johnston and Montési, 2017) subsurface ocean to feed a broad, mostly water-ice plume visible above the South Pole (Porco et al., 2006).

Jet activity and plume brightness at Enceladus vary over a 32.9 hr period (Ingersoll et al., 2020). The coincidence of the plume brightness oscillation period and the orbital timescale suggests that diurnal tides (resulting from Enceladus's phase-locked and eccentric orbit about Saturn; Murray and Dermott, 2000; Nimmo et al., 2018) regulate heat and mass transport by cyclically deforming the satellite's outer icy crust (Hurford et al., 2007; Souček et al., 2016). Tidally-driven 'opening' along fractures has been hypothesized to modulate jet activity by exposing the liquid water interface within the Tiger Stripes (i.e., the water table) to the vacuum of space (Nakajima and Ingersoll, 2016; Hurford et al., 2007; Kite and Rubin, 2016; Behounková et al., 2015; Porco et al., 2014). Extension in a direction normal to Tiger Stripes oriented ~30° counter-clockwise from the sub-Saturn direction produces a single peak in fault-opening displacement over the tidal cycle near mean anomaly φ = 120° (Hurford et al., 2007). However, the plume of Enceladus exhibits peak brightness near φ = 200° as well as a smaller local peak in activity near φ = 30° (Ingersoll et al., 2020). Viscous effects within the crust could induce a 6-7 hr delay (i.e., 'phase lag') between the maximal response at φ = 200° and peak forcing at φ = 120° but only for a relatively thick ice shell (~50 km) with an extremely low mean viscosity (~10^{13} Pa-s) over the SPT (Behounková et al., 2015). Dynamic fluid inertia within faults has also been proposed to cause a delay in peak plume activity, but this process would require invoking an additional mechanism (e.g., turbulent, intra-fault fluid dissipation) to maintain Tiger Stripes that are nearly fully-open (Kite and Rubin, 2016) despite effective overburden pressures of at least ~100 kPa (Crawford and Stevenson, 1988). Models of jet activity that rely on pure opening displacement across the Tiger Stripes also cannot readily explain the occurrence of a second peak in plume brightness near φ = 30° (Ingersoll et al., 2020).

Strike-slip motion may also regulate jet activity at Enceladus. Initial interpretations of Cassini data suggested that shear heating along the tiger stripe faults may cause sublimation of icy material into the plume (Nimmo et al., 2007; Smith-Konter and Pappalardo, 2008). However, it is difficult to reconcile a shear heating-driven eruption mechanism with the discovery of salts in solid plume grains (Postberg et al., 2009; Postberg et al., 2011; Postberg et al., 2018). Nonetheless, an eruption

mechanism that is driven by strike-slip motion could result in two peaks in activity through the tidal cycle (Smith-Konter and Pappalardo, 2008; Sládková et al., 2021) and may not require the action of an additional process to delay the timing of maximal plume brightness by 6-7 hrs.

4.3 Tidal Deformation at Enceladus

Using a fully 3D numerical (finite-element) approach (Berne et al., 2023a; Berne et al., 2023b), we find that tidally-driven strike-slip motion along the Tiger Stripes closely tracks plume timing and heat flow at Enceladus. We simulate tidal forcing by subjecting a quasi-spherical ice shell to forces associated with time-variable eccentricity tides (Figures 4.1 and 4.2, see also Methods and Figure 4.6). We assume a shell with a mean thickness of 30 km (Thomas et al., 2016; Van Hoolst et al., 2016; Hemingway and Mittal, 2019; Park et al., 2024), a uniform elastic rheology (see Table 4.1; Ermakov et al., 2021), lateral variations in crustal thickness (local thickness near the South Pole is ~10 km; Hemingway et al., 2018), and radial, through-going fault surfaces at tiger stripe locations (see Figure 4.6). Fault slip is consistent with that expected from interfaces subject to Coulomb friction and hydrostatic normal stresses. We compute deformation over a sufficient number of orbital periods such that differences between displacements at a given mean anomaly between cycles are negligible (see Figure 4.8). We also assume that intraporous liquid water pressure counteracts the impact of hydrostatic normal stress on fault deformation below the ~1 km depth of the water table (Rozhko et al., 2007). Mean effective overburden pressures (~50 kPa) are much larger than maximum tidally-driven 'opening' tractions (~20 kPa, see Figure 4.2b) over the Tiger Stripes. Modelled fault interfaces therefore do not experience significant opening displacement (for details, see Methods).

We find that frictional fault interfaces at tiger stripe locations periodically slide and lock (i.e., exhibit stick-slip behavior) over the 32.9 hr orbital timescale (Figure 4.2c and Figure 4.2d). Laboratory experiments (Schulson and Fortt, 2012) indicate that the static coefficient of friction for ice-on-ice within the crust of Enceladus is probably between $\mu = 0.3 - 0.8$ but may be much lower ($\mu \sim 0.0$) if ice temperatures fall below 200K along faults (Schulson and Fortt, 2012). Liquid water generated by shear heating (Schulson and Fortt, 2012; Meyer et al., 2022) or below the water table (Kite and Rubin, 2016) could additionally lubricate frictional contacts over interfaces (Souček et al., 2016; Behounkova et al., 2017; Sládková et al., 2021). Lubrication will decrease the impact of friction during fault sliding (i.e., lower the

dynamic coefficient of friction to nearly zero). However, laboratory experiments (Maeno et al., 2003) and studies of sea ice rheology on Earth (Sukhorukov and Løset, 2013) do not indicate that lubrication impacts the failure stress necessary for the *onset* of sliding (allowing for potentially high values of μ, see also Figure 1 of Maeno et al., 2003). We therefore explore a range of values for the coefficient of static friction $\mu = 0.0 - 0.8$ and assume zero dynamic friction (i.e., lubricated contacts) for the tiger stripe faults.

The timing of peak resolved shear traction along the Tiger Stripes is sensitive to the orientation (i.e., strike direction) of the fault planes. Here, we assume traces of the Tiger Stripes derived from Schenk, 2008. Starting from periapse (mean anomaly $\varphi = 0°$), left-lateral shear tractions resolved along planes oriented $\sim$30° counter-clockwise (viewed facing the South Pole) from the sub-Saturnian point increase until reaching a maximum value near $\varphi = 15°$ (Figure 4.2a). As the tidally-driven principle stress directions subsequently rotate about the South Pole, shear tractions (Figure 4.2a) decrease ($\varphi = 15° - 105°$), change sign ($\varphi = 105°$), and induce right-lateral fault slip (Figure 4.2d) between $\varphi = 105° - 195°$. A second peak in resolved lateral shear traction occurs slightly after apoapse near $\varphi = 195°$.

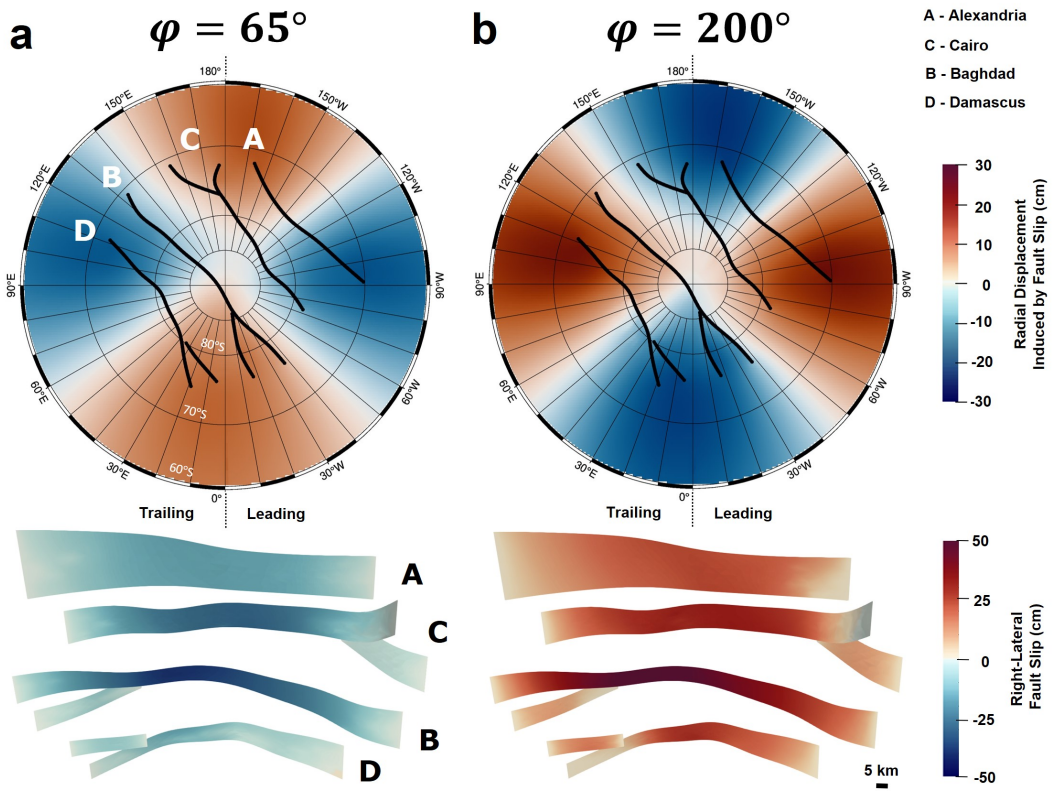

Figure 4.1: Examples of tidally-driven deformation at Enceladus during phases of peak left-lateral slip at $\varphi = 65°$ (panel a) and right-lateral slip at $\varphi = 200°$ (panel b). Top row: South Polar stereographic projections (Leading and Trailing hemispheres labelled) of radial displacement at the surface relative to that produced by models without Tiger Stripe faults. Bottom row: Perspective view of lateral slip along Tiger Stripe faults: 'A' Alexandria, 'C' Cairo, 'B' Baghdad, and 'D' Damascus. We assign $\mu = 0.4$ to Tiger Stripe faults for this example. Faults are viewed from 130°W, looking upward from 35° below the horizontal.

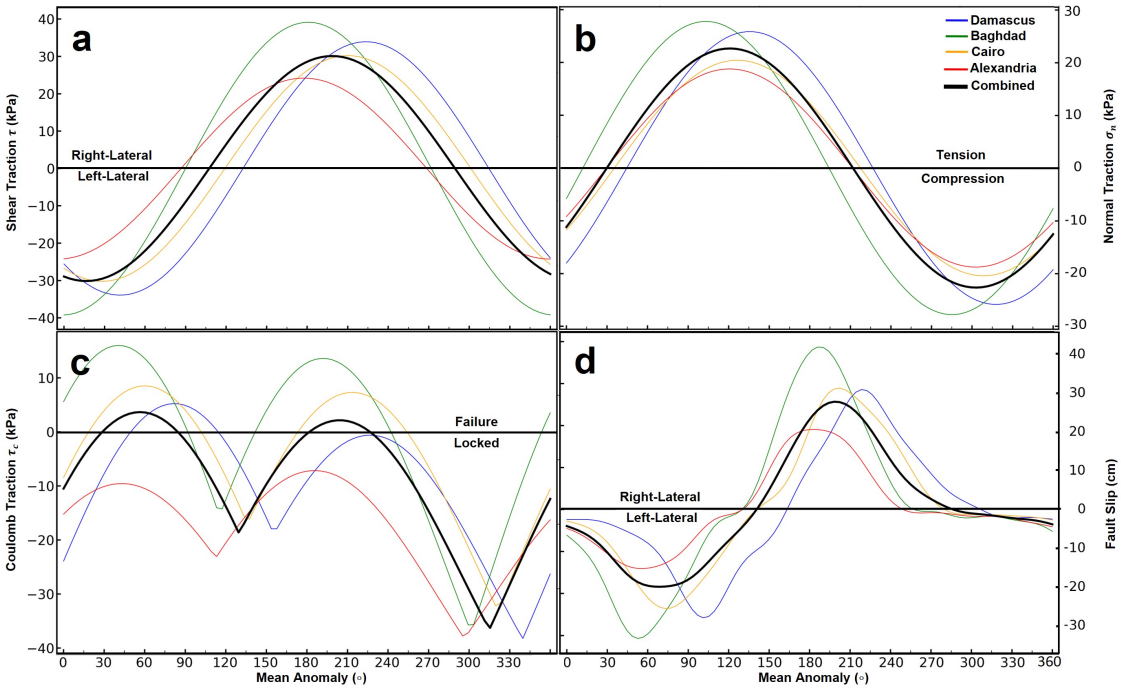

Figure 4.2: Modelled traction and lateral slip over Tiger Stripe faults as a function of mean anomaly. Driving shear traction τ (panel a), normal traction σ_n (panel b), Coulomb traction τ_c (panel c), and resultant accumulated lateral fault slip (panel d) are averaged over each respective Tiger Stripe and correspond to snapshots of deformation shown in Figure 4.1. Mean anomalies $\varphi = 0°$, $360°$ and $\varphi = 180°$ respectively correspond to periapse and apoapse. Normal tractions are evaluated relative to effective overburden pressures across fault interfaces. See Methods 'Fault Interfaces' for additional details regarding the computation of traction and slip from our models.

For a fault subject to static Coulomb friction, slip occurs when the local value of a shear traction τ ($\pm$ 30 kPa range over the tidal cycle, see Figure 4.2a) exceeds the total local normal traction σ_n scaled by μ (i.e., Coulomb traction, or $\tau_c = |\tau| - \mu\sigma_n$, is positive; Sládková et al., 2021). Diurnal tides drive approximately $\pm$ 20 kPa differences in mean σ_n (relative to a mean effective overburden pressures of ~50 kPa) with peak extension and compression at $\varphi = 120°$ and $\varphi = 300°$ (Figure 4.2b). Resulting mean τ_c is positive across the Tiger Stripes (for models with $\mu = 0.4$) during $\varphi \sim 30° - 80°$ and $180° - 225°$ (Figure 4.2c). Following the onset of failure near $\varphi = 30°$ and $\varphi = 180°$, tiger stripe faults accumulate lateral slip until reaching peak values at $\varphi = 65°$ and $\varphi = 200°$. As the magnitude of τ decreases (i.e., faults are unloaded), elastic strain in the crust surrounding fractures induces slip in an opposite sense until net lateral slip returns to nearly zero at $\varphi = 140°$ and $285°$ (Figure 4.2d). Note that peak left-lateral τ (Figure 4.2a) does not align with positive τ_c (Figure 4.2c), resulting in an inability of large portions of the Tiger Stripes to initiate slip until $\varphi \sim 30°$ (Figure 4.2d). Relatively smaller shear tractions resolved along the Tiger Stripes during $\varphi = 30° - 80°$ reduce the magnitude of peak left-lateral slip at $\varphi = 65°$ compared to that of peak right-lateral slip near $\varphi = 200°$ (i.e., when positive τ_c at $\varphi = 180° - 225°$ effectively coincides with peak right-lateral shear traction at $\varphi = 195°$). The resulting slip profile over the orbital period is double-peaked and asymmetric (for further discussion of the relationship between τ_c, τ, μ and slip for an analogous (1D) finite fault, see Figure 4.9). Increasing prescribed μ shifts the start of the first mean positive τ_c window (Figure 4.2c) forward in time relative to peak left-lateral τ (Figure 4.2a), further reducing and delaying peak left-lateral slip during Enceladus's tidal cycle.

4.4 Strike-Slip Motion Correlates with Jet Activity

We compare numerical results for the magnitude of deformation along the Tiger Stripes (i.e., the absolute value of lateral slip in Figure 4.1 and Figure 4.2d) with observations of plume brightness (Figure 4.3). Plume brightness is derived from Cassini Imaging Science Subsystem (ISS) images of particle densities within horizontal 'slabs' at ~100 km altitude above the South Pole of Enceladus (Ingersoll et al., 2020). Predicted strike-slip motion is generally correlated with plume brightness across the entire tidal cycle, regardless of the value of μ assigned to the Tiger Stripes (Pearson's correlation coefficient R ~ 0.5 - 0.9, see Figure 4.10). Maxima in model-predicted slip coincide with observations of peak plume brightness near $\varphi = 30°$ and $200°$. Nearly zero fault slip also occurs during periods of relatively low

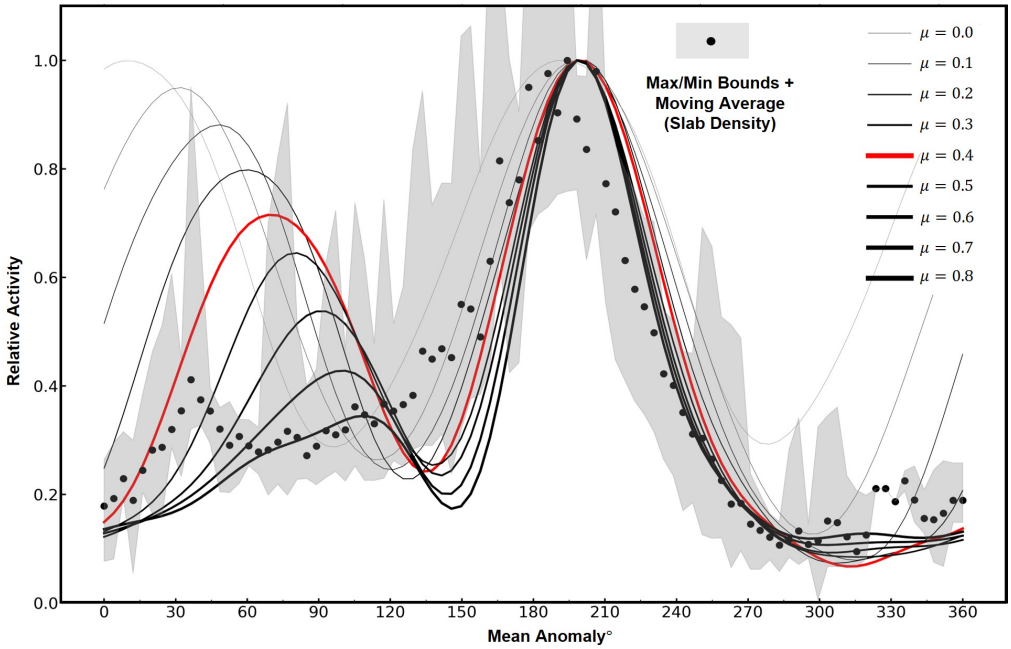

Figure 4.3: Comparison of predicted strike-slip motion along Tiger Stripes and observations of plume brightness. Individual solid lines correspond to magnitudes of strike-slip motion on Tiger Stripes with different prescribed μ ranging from 0.0 – 0.8 normalized to maximum values over the tidal cycle. Plume brightness data is extracted from Ingersoll et al., 2020. Scatter points and the gray shaded area respectively denote the normalized moving average (4° bin widths) and range of plume brightness derived from ISS images between 2005 - 2017. The red solid line ($\mu = 0.4$) corresponds to the model results shown in Figures 4.1, 4.2, and 4.4.

brightness near $\varphi = 315°$ (i.e., minimal values of τ_c, see Figure 4.2c). Correlation is most sensitive to assumed μ values during $\varphi = 0° - 180°$ but is highest for models with moderate-high ($\mu = 0.3 - 0.8$) levels of static friction (R > 0.7).

The magnitude of predicted strike-slip motion also depends on position along the Tiger Stripes. Tidally-driven shear tractions in the southern hemisphere of Enceladus decrease moving away from the South Pole due to spatial variations in the tidal forcing function (see Methods) as well as the ~50% variation in crustal thickness over 90°S - 70°S latitude (see Figure 4.11; Wahr et al., 2006; Park et al., 2024; Berne et al., 2023b). Ignoring the impact of the variations in crustal thickness on deformation, we expect the ordering of faults according to the value of peak shear traction (and strike-slip motion) to be (from greatest to least): 1. Baghdad (maximum southern latitude θ_{max} = 89°S); 2. Cairo (θ_{max} = 84°S); 3. Damascus (θ_{max} = 80°S); and 4. Alexandria (θ_{max} = 76°S) or 'B-C-D-A'. Note that the significantly thicker crust over Cairo Sulcus relative to Damascus Sulcus results in the ordering 'B-D-C-A' in Figure 4.2a and Figure 4.2d (Berne et al., 2023a; Berne et al., 2023b). Local spatial maxima and minima in model-predicted slip also occur near the southernmost and northernmost portions (i.e., near the center and tips/splays) of each fracture, respectively.

We compare the depth-integrated spatial distribution of strike-slip activity (averaged over the tidal cycle) with measurements of heat flow (i.e., radiated power per unit length) along the Tiger Stripes (Figure 4.4). Heat flow is derived from Cassini Composite Infrared Spectrometer (CIRS) measurements of mean temperature across finite-width segments of the Tiger Stripes (Spencer et al., 2018). The position of peak slip and heat flow align both globally (i.e., order 'B-D-C-A') and locally (near the center of each fracture, except Cairo Sulcus). Overall, heat flow correlates with strike-slip motion distributed across all faults (R ~ 0.45 - 0.6, see Figure 4.12). Correlation is only mildly sensitive to the assumed coefficient of friction for the Tiger Stripes but is noticeably lower for cases with very low (i.e., μ = 0.0) and high (i.e., μ = 0.8) levels of friction.

4.5 Eruptions Driven by Strike-Slip Motion

The models presented here predict a strong correlation between the timing of tidally-driven strike-slip motion along the Tiger Stripes and plume brightness as well as local fault slip and heating. However, our models do not describe a mechanism by which lateral fault motion regulates jet activity at Enceladus. Due to the thermal inertia of ice, the impact of shear heating on variations in plume brightness over the orbital timescale is probably negligible (Nimmo et al., 2007). Based on our model, we also predict that frictional shear heating produces < 1 GW or less than 20% of the thermal energy radiating from the SPT (Spencer et al., 2018). However, strike-slip

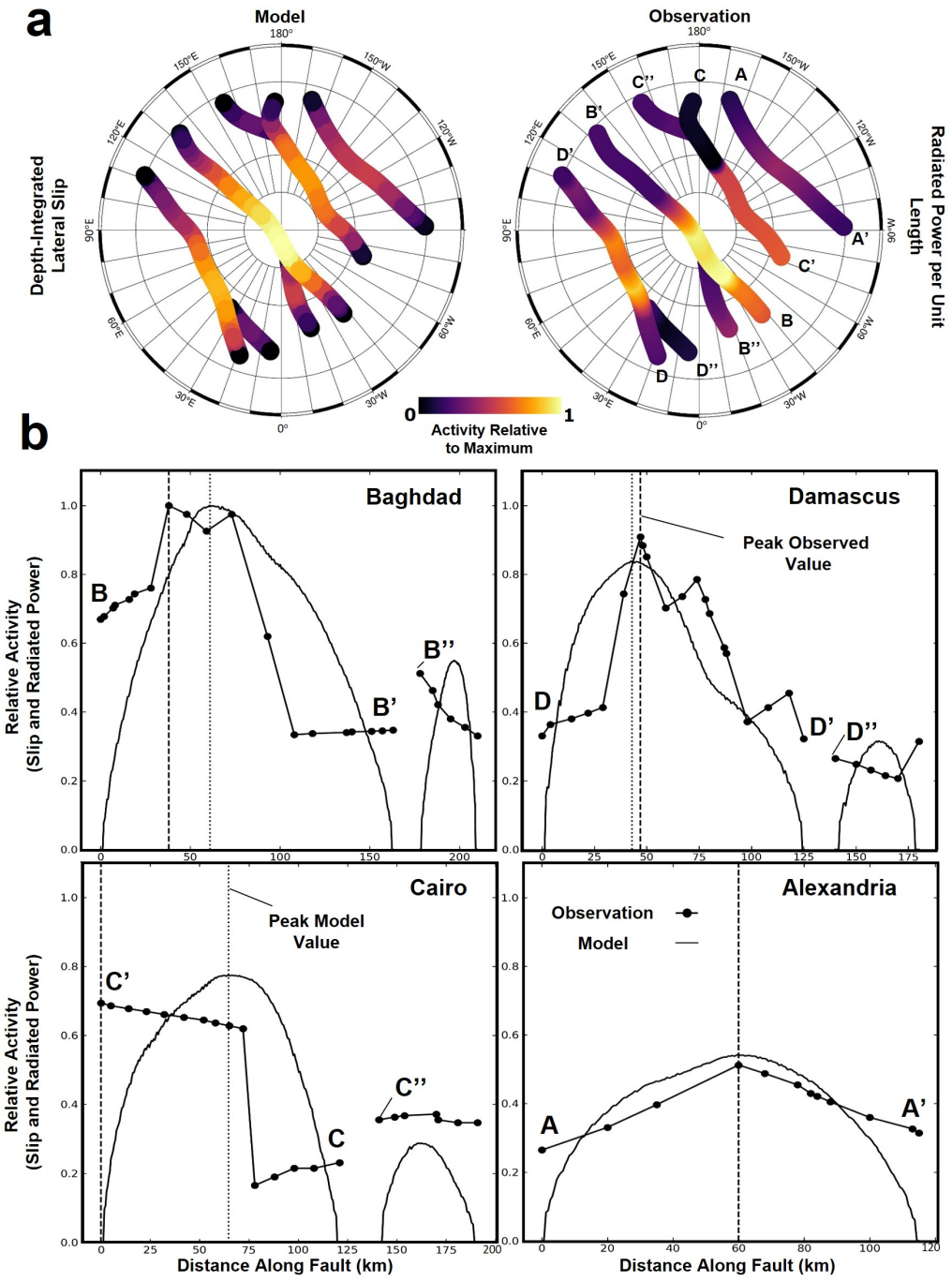

Figure 4.4: Comparison of the spatial distribution of strike-slip motion and heat flow along the Tiger Stripes. a: Spatial distribution of radiated power per unit length associated with heat flow (Spencer et al., 2018; right image) alongside depth-integrated lateral slip averaged over the tidal cycle for Tiger Stripes with $\mu = 0.4$ (left image) relative to global maximum values. b: 1-D profiles of heat flow (dash-dot) and strike-slip motion (solid) shown in panel 'a'. Local maxima for heat flow (observation) and lateral slip (model) marked with vertical dashed and dotted lines, respectively. Transect labels in panel 'a' correspond to endpoints of 1D profiles shown in panel 'b'.

motion could alternately deform left- and right- stepping transtensional bends (e.g., 'pull-aparts', see Figure 4.5) over a full tidal cycle. Under this scenario, focused extension over individual bends along the Tiger Stripes could facilitate water to rise and feed material (and latent heat) to jets, loosely analogous to volcanic processes commonly observed along Earth's large strike-slip fault bends subject to tectonic deformation (e.g., the Salton Sea; Han et al., 2016).

4.6 Tectonic Evolution of the South Polar Terrain

Beyond its impact on jet activity at tidal periods, we anticipate that friction-modulated slip along the Tiger Stripes influences the long-term evolution of the SPT. Anelasticity within the crust could diffuse tidally-driven strain via permanent fault slip, viscous flow, or material failure at crack tips. For example, if fault friction enhances peak right-lateral slip relative to peak left-lateral slip during each orbit, as predicted by this work (see Figures 4.1b, 4.2d, and 4.3) then tidal motion would favor permanent (i.e., long-term) right-lateral slip over Tiger Stripes. Sustained right-lateral slip would concentrate northward compression over the tip of Damascus Sulcus near 90°E (and Alexandria Sulcus near 90°W) (Figure 4.1) thereby promoting orthogonal extension along structures with north-south orientations centered over trailing (and leading) hemispheres (e.g., chasmata; Yin and Pappalardo, 2015). However, a past clockwise rotation of the SPT (Rossi et al., 2020; Yin and Pappalardo, 2015) could invert the favored sense of permanent tidally-driven deformation over the Tiger Stripes and support the formation of nearby geologic structure indicative of long-term left-lateral fault slip (e.g., eastward-bending horsetail structures; Yin and Pappalardo, 2015). Deformation expressed over the SPT could also result from a combination of different processes that have evolved through time (e.g., non-synchronous rotation; Patthoff and Kattenhorn, 2011) further complicating interpretations of current tiger stripe motion based solely on surrounding geomorphology. Testing the presented predictions may therefore require detailed geodetic observations of fault behavior over multiple tidal periods (e.g., using radar interferometry; Simons and Rosen, 2015). These observations could provide key constraints on the mechanical nature of the crust, tidal controls on jet activity, and the evolution of the South Polar Terrain.

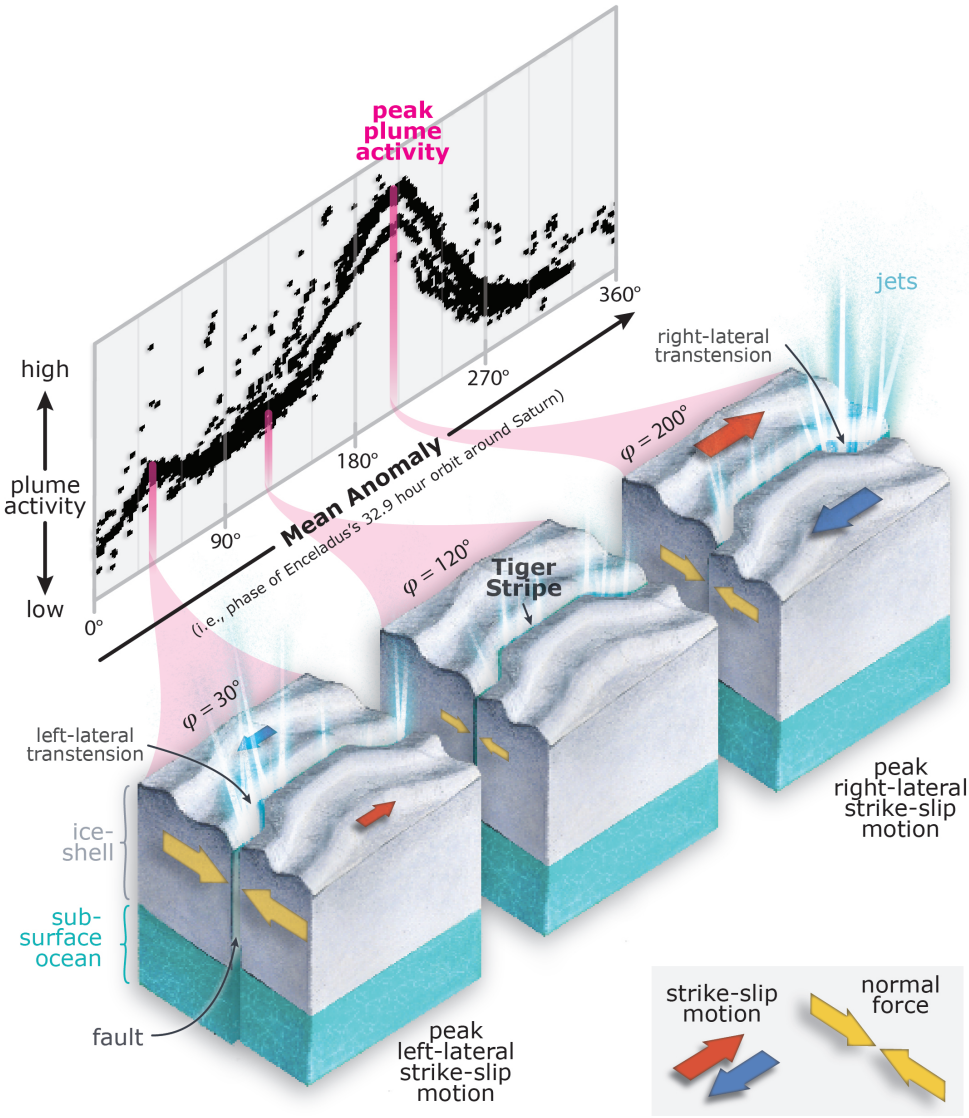

Figure 4.5: Conceptual relationship between tidally-driven normal tractions, strike-slip motion, and jet activity through the tidal cycle. Relatively higher compression near $\varphi = 30°$ (Figure 4.2b) reduces left-lateral motion compared to right lateral motion during $\varphi = 200°$ (Figure 4.2d). The resultant double-peaked and asymmetric variability of strike-slip motion correlates with plume brightness at Enceladus. Strike-slip motion may intermittently open left- and right-stepping transtensional bends (shown in the lower left and upper right crustal blocks) allowing water to rise through the ice shell and power jet activity along the Tiger Stripes. Graphics shown are not to scale.

Methods

Finite Element Model

Following the approach described in Supplementary section S1.1 of Berne et al., 2023a, we formulate and solve a boundary value problem appropriate for eccentricity tides on a quasi-spherical ice shell. We ignore the potential impact of viscous strain (Wahr et al., 2009), account for self-gravitational effects (Wahr et al., 2006), ignore inertial forces, and treat the core as a rigid body (Schubert et al., 2007). We find differences of <1% between results produced by our methodology and semi-analytic solutions for tidal deformation on ice shells with lateral variations in shear modulus (see Figure 2 of Rovira-Navarro and Matsuyama, 2022).

We start by defining the strong form of the quasi-static equation of motion:

$$\sigma_{ij,j} + f_i = 0 \ \text{ in } W \tag{4.1a}$$

$$\sigma_{ij} n_j = T_i \ \text{ on } S, \tag{4.1b}$$

where i describe cartesian directions for a body subject to stresses σ_{ij} and body forces f_i over the volume W, T_i describes tractions on surfaces S, and n_j is a unit vector. We subdivide S into the surface at the outer domain boundary S_{out}, the surface at the interior (i.e., ice-ocean) domain boundary S_{int}, and surfaces corresponding to fault interfaces S_f of our geometry.

For an elastic solid, we can write a constitutive relation (i.e., Hooke's law) using the rank-4 stiffness tensor C_{ijkl} to map displacements u to stresses σ_{ij}. We assign parameters in C_{ijkl} that are appropriate for a linear isotropic material with a shear modulus G and bulk modulus κ (see Supplementary Table 4.1; the symbol denotes derivative with respect to a direction):

$$\sigma_{ij} = \frac{1}{2} C_{ijkl}(u_{k,l} + u_{l,k}). \tag{4.2}$$

We apply forces associated with the time-dependant driving $V(r, \theta, \phi)$ and self-gravitational $V^{sg}(r, \theta, \phi)$ potentials. To the first order in eccentricity, we can formulate $V(r, \theta, \phi)$ at Enceladus following Murray and Dermott, 2000:

$$V(r, \theta, \phi) = r^2 \omega^2 e \cdot (\sin(\omega t)\, \mathrm{P}_{22}(\lambda) \sin 2\phi - \frac{3}{4} \cos(\omega t)\ (2\, \mathrm{P}_{20}(\lambda) - \mathrm{P}_{22}(\lambda) \cos 2\phi)), \tag{4.3}$$

where r, θ, ϕ are radial, co-latitude, and longitude positions in a reference frame fixed to the center of mass of Enceladus, ω is the orbital angular velocity, and e is the orbital eccentricity. Times $t = 0$, $\frac{2\pi}{\omega}$, $\frac{4\pi}{\omega}$ etc. correspond to orbital periapse for consecutive tidal cycles. $P_{20}(\lambda)$ and $P_{22}(\lambda)$ are associated Legendre Functions with the nested function $\lambda = \cos(\theta)$. To compute $V^{sg}(r, \theta, \phi)$, we self-consistently solve Poisson's equation for gravitational potential arising from mass movement at the boundaries (i.e., surfaces) of our geometry:

$$V^{sg}(r, \theta, \phi) = \mathcal{G}(r, \theta, \phi, r', \theta', \phi')\rho u_i(n_i \cdot n_o), \tag{4.4}$$

where n_o is the unit vector parallel to the direction normal to the local surface, ρ is the density of the ice shell, and $\mathcal{G}(r, \theta, \phi, r', \theta', \phi')$ is a Green's function relating mass at a given location r', θ', ϕ' with potential at r, θ, ϕ (see Supplementary S1.1.1.3 of Berne et al., 2023a for the definition $\mathcal{G}$; henceforth we drop the notation r, θ, ϕ and r', θ', ϕ' from V and V^{sg}) (Murray and Dermott, 2000).

We formulate the f_i on W in Equation 4.1 as a gradient of the sum of gravitational potentials in W:

$$f_i = -\nabla(V^{sg} + V) \cdot n_i \text{ in } W. \tag{4.5}$$

For T_i on S_{int}, we evaluate the restoring forces associated with the change in the geoid height and the change in the radial position of the ice-ocean boundary:

$$T_i = u_j(\rho - \rho_w)g_{int}(n_i \cdot n_o)(n_j \cdot n_o) + \rho_w(V + V^{sg})(n_i \cdot n_o) \text{ on } S_{int}, \tag{4.6}$$

where g_{int} is the radial gravitational acceleration at the ice-ocean boundary and ρ_w is the density of the ocean. For T_i on S_{out}, we only evaluate forces associated with changes in the radial position of the outer surface:

$$T_i = u_j\rho g_{out}(n_i \cdot n_o)(n_j \cdot n_o) \text{ on } S_{out}, \tag{4.7}$$

where g_{out} is the radial gravitational acceleration at the outer surface of Enceladus. The formulation for the boundary condition along S_f requires special consideration (see 'Fault Interfaces' below) but is functionally similar to boundary conditions along S_{out} and S_{int} in the context of Equation 4.1.

We use the 3D FEM code PyLith (Aagaard et al., 2007) to formulate and obtain solutions (i.e., u) for the boundary value problem described in Equations 4.1 - 4.7. PyLith is a well-established geodynamic modelling tool which allows for complex bulk rheology and geometrical meshes. PyLith also incorporates the highly parallelized numerical solver package PetSc (Balay et al., 2014). For this work, we have modified PetSc to solve for displacements in a no-net-rotation/translation reference frame appropriate for eccentricity tides (for additional details, see Supplementary S1.1.2.4 of Berne et al., 2023a).

Fault Interfaces

We simulate fault deformation by allowing duplicate sets of mesh nodes (i.e., 'split nodes'; Melosh and Raefsky, 1981) along prescribed interfaces to displace relative to each other when deformed by tidally-driven tractions. Our formulation for fault interfaces differs from the approach adopted by Sládková et al., 2021 which utilizes 'weak' zones with reduced viscosity as proxies for frictional behavior. By formulating faults as 2D surfaces instead of 3D volumes, we can compute strike-slip motion across fault structures in a manner which is far less sensitive to mesh discretization (Sládková et al., 2021) or our choice of solution basis functions (Melosh and Raefsky, 1981).

We constrain duplicate nodes on fault surfaces according to computed slip s following:

$$s_s = (u_i^+ - u_i^-)(n_i \cdot n_s) \text{ on } S_f, \tag{4.8}$$

where u_i^+ and u_i^- denote displacements on either side of a fault surface (the subscript s denotes a direction parallel to the local fault strike direction). Assigning friction along fault surfaces introduces a time-dependence to solutions for the elastic problem (Sládková et al., 2021). For this work, we discretize the time domain as a series of points (90 per tidal cycle) separated by finite intervals Δt. The temporal progression of slip depends on traction that is projected along the faults and the prescribed coefficient of static friction μ according to:

$$s_s(t + \Delta t) = s_s(t) + \Delta s_s \Leftrightarrow |T_i(t + \Delta t)(n_i \cdot n_s)| > \mu(T_i(t + \Delta t)(n_i \cdot n_o) + T^b) \tag{4.9a}$$

$$s_s(t + \Delta t) = s_s(t) \Leftrightarrow |T_i(t + \Delta t)(n_i \cdot n_s)| < \mu(T_i(t + \Delta t)(n_i \cdot n_o) + T^b), \tag{4.9b}$$

where T^b is a constant background effective overburden traction and:

$$\Delta s_s = 2M_{kls}^{-1} C_{ijkl}^{-1} (T_i(t + \Delta t) - T_i(t)) n_j, \tag{4.10}$$

where M_{kls} is a rank-3 tensor that relates strike-slip motion to equivalent co-local strain along a fault plane in a 3D elastic medium (Segall, 2010). Note that our formulation for fault rheology (Equations 4.9 and 4.10) allows for unrestricted slip only if shear tractions exceed normal tractions (scaled by μ) along the fault plane, which is consistent with the behavior expected for tiger stripe faults subject to static Coulomb friction and zero dynamic friction. Slip and traction are coupled to each other in a 3D elastic medium (e.g., slip generates a stress field, which induces additional slip, resulting in additional stress, etc.). Pylith/PetSc therefore utilizes a non-linear solver to iteratively and self-consistently resolve slip and traction at a given time step. To compute T^b, we consider the combined effect of normal hydrostatic stress and fluid pore pressure below the depth of the water table (Sládková et al., 2021):

$$T^b = \rho g_{out} d \Leftrightarrow d < D \frac{\rho_w - \rho}{\rho_w} \tag{4.11a}$$

$$T^b = \rho g_{out} d + (D \frac{\rho_w - \rho}{\rho_w} - d) \rho_w g_{out} \Leftrightarrow d > D \frac{\rho_w - \rho}{\rho_w}, \tag{4.11b}$$

where D is the local thickness of the ice shell derived from our crustal shape model (Figure 4.7, values range from 7 km to 15 km over the Tiger Stripes). The local distance from the outer surface d depends on the local radial position of the outer surface R and radial position r:

$$d = R - r. \tag{4.12}$$

To compute the area-mean of strike-slip motion at a given time point along a fault surface (i.e., potency $\Omega_s(t)$), we evaluate:

$$\Omega_s(t) = \frac{1}{A} \int_{S_f} s_s(t)\, dS, \tag{4.13}$$

where A is the total area of the fault surface. Similarly, to evaluate the area-mean of tractions along a fault surface $\Omega_T(t)$ we compute:

$$\Omega_T(t) = \frac{1}{A} \int_{S_f} T_i(t)(n_i \cdot n_f)\, dS, \tag{4.14}$$

where n_f can denote a vector in strike (n_s) or normal (n_o) directions. We compute driving tractions for a model with fully locked (non-slipping) interfaces at tiger stripe fault locations. However, slip produces additional stress in the surrounding medium resulting in ~10% more variability in shear and normal tractions relative to quantities presented in the upper panels of Figure 4.2 (for details, see Figure 4.6). To compute depth-integrated strike-slip potency Ω_s^d, we integrate strike-slip radially at a given lateral position through the ice shell and over tidal cycle b ($b = 0$ denotes the first tidal cycle):

$$\Omega_s^d = \int_{\frac{b}{2\pi\omega}}^{\frac{(b+1)}{2\pi\omega}} \int_{R-D}^{R} s_s(t)\, dr\, dt. \tag{4.15}$$

For faults with zero dynamic friction, strike-slip motion following the onset of failure does not result in energy dissipation along interfaces. Nonetheless, the maximum power P that *could* be transferred to frictional shear heating along the Tiger Stripes is the product of shear traction and the time-derivative of slip (i.e., $\frac{ds_s(t)}{dt}$) integrated along fault surfaces and averaged over the tidal cycle:

$$P = 2\pi\omega \int_{\frac{b}{2\pi\omega}}^{\frac{(b+1)}{2\pi\omega}} \int_{S_f} \frac{ds_s(t)}{dt} T_i(t)(n_i \cdot n_s)\, dS\, dt. \tag{4.16}$$

Increasing the impact of static friction decreases the amplitude of s_s but minimally affects $T_i(t)$. Values of P therefore negatively correlate with assigned μ in our models. We find that P ranges from 0.9 - 0.4 GW for prescribed μ values spanning 0.0 - 0.8.

Models permit fault opening s_o:

$$s_o = (u_i^+ - u_i^-)(n_i \cdot n_o) \text{ on } S_f, \tag{4.17}$$

if tidally driven normal tractions exceed effective overburden pressures:

$$s_o(t) \neq 0 \Leftrightarrow T_i(t)(n_i \cdot n_o) > T^b. \tag{4.18}$$

Fault opening does not result in a significant difference (<1%) in the modelled strike slip motion along Tiger Stripes (i.e., as compared to results for models which prohibit opening). Where faults do exhibit opening motion, peak s_o are typically about 20 times smaller than peak s_s and only occur locally near the outer surface and the ice-ocean boundary (strike-slip motion, by contrast, occurs over the entire fault; see Figure 4.1).

Model Geometry

To generate model geometries, we develop a mesh using the software package CUBIT (Skroch et al., 2019). Spherical shells are first defined with respective outer and inner surfaces at radii 252.1 km and 222.1 km as well as radial, through-going surfaces at tiger stripe locations. We then discretize geometries using tetrahedral elements and refine cell sizes near the tiger stripe faults. We assign a minimum cell size (i.e., tetrahedra cell edge length) of 1 km to tetrahedra to ensure simulation results are not subject to error due to poor mesh resolution surrounding fault structures (see Supplementary Figure S3 of Berne et al., 2023a). We also reduce numerical error by limiting maximum cell sizes to 8 km (i.e., so that at least 4 elements span the radial distance between inner and outer surfaces across geometries). Snapshots of our mesh geometry are shown in Figure 4.6.

To generate thickness variations, we apply topography at the outer and the interior surfaces (H_{out} and H_{int} respectively) of mesh geometries. H_{out} represents non-hydrostatic topography at Enceladus derived from the shape model described in Park et al., 2024 (up to a maximum spherical harmonic degree $L_{max} = 8$). We assume H_{int} tracks H_{out} following a formulation for Airy-type isostatic compensation (Hemingway and Matsuyama, 2017) (For a map of crustal thickness assumed for this work, see Figure 4.11):

$$H_{out} = H_{int} \frac{\rho}{(\rho - \rho_w)} \frac{g}{g_{int}}. \tag{4.19}$$

Model Spin-Up

To ensure that our time-dependant solutions for displacement are insensitive to initial conditions (see Equation 4.9), we conduct simulations over several tidal cycles until differences in slip along the tiger stripe faults (at a given mean anomaly) are minimal. We prescribe zero slip and zero traction initial conditions to fault surfaces:

$$s_i(t) = 0 \Leftrightarrow t < 0 \tag{4.20a}$$

$$T_i(t) = 0 \Leftrightarrow t < 0. \tag{4.20b}$$

We can evaluate a spin-up parameter $\Xi(t)$ which describes the normalized mismatch of $\Omega_s(t)$ (see Equation 4.13) over all tiger stripe faults (as a function of time) with values over the subsequent tidal cycle:

$$\Xi(t) = \frac{\Omega_s(t) - \Omega_s(t + \frac{2\pi}{\omega})}{\Omega_s(t)}. \tag{4.21}$$

We find that $\Xi(t)$ converges to effectively zero after ~3-4 tidal cycles (see Figure 4.8). Spin-up is slightly more rapid (i.e., ~2-3 tidal cycles) for low prescribed coefficients of static friction ($\mu = 0.1 - 0.3$). We evaluate final results following 7 tidal cycles for the current work.

4.7 Acknowledgements

This research was supported by the Future Investigators in NASA Earth and Space Science and Technology (FINESST) Program (80NSSC22K1318)(A.B., M.S.). We thank the Keck Institute for Space Studies (KISS) at the California Institute of Technology for organizing two workshops about "Next-Generation Planetary Geodesy" which provided insight, expertise, and discussions that inspired this research. We also thank Matthew Knepley, Brad Aagaard, and Charles Williams for providing valuable advice on how to modify PyLith for our simulations. A portion of this research was supported by a Strategic Research and Technology Development task led by James T. Keane and Ryan S. Park at the Jet Propulsion Laboratory, California Institute of Technology, under a contract with the National Aeronautics and Space Administration (80NM0018D0004) (J.T.K., R.S.P.).

4.8 Contributions

A.B. conceived and designed this study under the supervision of M.S.. A.B. drafted the article and constructed Figures 4.1-4.4. M.S., J.T.K., and A.B., developed numerical models used in the study. R.S.P. provided the shape model necessary for numerical simulations. J.T.K., with the aid of A.B., constructed Figure 4.5. E.J.L. provided expertise regarding the geological evolution of the SPT. All authors discussed the results of the study and commented on the manuscript at each stage of revision.

4.9 Data Availability

Data used for Figure 4.3 (slab densities derived from Cassini ISS images) is publicly available via `https://doi.org/10.1016/j.icarus.2019.06.006` (Ingersoll et al., 2020). Data used for Figure 4.4 (heat flow along the tiger stripe faults derived from Cassini CIRS measurements) is publicly available via `https://doi.org/10.2458/azu_uapress_9780816537075-ch008` (Spencer et al., 2018).

References

Aagaard, B., C. Williams, and M. Knepley (2007). "PyLith: A Finite-Element Code for Modeling Quasi-Static and Dynamic Crustal Deformation". In: *Eos* 88(52).

Balay, S., J. Brown, K. Buschelman, V. Eijkhout, W. Gropp, D. Kaushik, M. Knepley, L. C. McInnes, B. Smith, and H. Zhang (2014). "PETSc Users Manual Revision 3.4". In: *Computer, Computational, and Statistical Sciences Division2014*.

Behounkova, M., O. Soucek, J. Hron, and O. Cadec (2017). "Plume activity and tidal deformation on enceladus influenced by faults and variable ice shell thickness". In: *Astrobiology* 17.9. ISSN: 15311074. DOI: 10.1089/ast.2016.1629.

Behounková, M., G. Tobie, O. Cadek, G. Choblet, C. Porco, and F. Nimmo (2015). "Timing of water plume eruptions on Enceladus explained by interior viscosity structure". In: *Nature Geoscience* 8 (8). ISSN: 17520908. DOI: 10.1038/ngeo2475.

Berne, A., M. Simons, J. Keane, and R. Park (2023b). "Using Tidally-Driven Elastic Strains to Infer Regional Variations in Crustal Thickness at Enceladus". In: *Geophysical Research Letters* 50 (22). DOI: 10.1029/2023GL106656.

Berne, A., M. Simons, J. Keane, and R. Park (2023a). "Inferring the Mean Thickness of the Outer Ice Shell of Enceladus from Diurnal Crustal Deformation". In: *Journal of Geophysical Research E: Planets* . DOI: 10.1029/2022JE007712.

Berne, A., M. Simons, J. T. Keane, E. S. Leonard, and R. S. Park (2024). "Jet activity on Enceladus linked to tidally driven strike-slip motion along tiger stripes". In: *Nature Geoscience* 17.5.

Crawford, G. and D. Stevenson (1988). "Gas-driven water volcanism and the resurfacing of Europa". In: *Icarus* 73 (1). ISSN: 10902643. DOI: 10.1016/0019-1035(88)90085-1.

Ermakov, A. I., R. S. Park, J. Roa, J. C. Castillo-Rogez, J. T. Keane, F. Nimmo, E. S. Kite, C. Sotin, T. J. W. Lazio, G. Steinbrügge, S. M. Howell, B. G. Bills, D. J. Hemingway, V. Viswanathan, G. Tobie, and V. Lainey (2021). "A Recipe for the Geophysical Exploration of Enceladus". In: *Planetary Science Journal* 2 (4). ISSN: 26323338. DOI: 10.3847/PSJ/ac06d2.

Han, L., J. Hole, J. Stock, G. Fuis, A. Kell, N. Driscoll, G. Kent, A. Harding, M. Rymer, A. González-Fernández, and O. Lázaro-Mancilla (2016). "Continental rupture and the creation of new crust in the Salton Trough rift, Southern California and northern Mexico: Results from the Salton Seismic Imaging Project". In: *Journal of Geophysical Research: Solid Earth* 121 (10). ISSN: 21699356. DOI: 10.1002/2016JB013139.

Hemingway, D., L. Iess, R. Tajeddine, and G. Tobie (2018). *The Interior of Enceladus*. University of Arizona Press. DOI: 10.2458/azu_uapress_9780816537075-ch004.

Hemingway, D. and I. Matsuyama (2017). "Isostatic equilibrium in spherical coordinates and implications for crustal thickness on the Moon, Mars, Enceladus, and elsewhere". In: *Geophysical Research Letters* 44.15. ISSN: 19448007. DOI: 10.1002/2017GL073334.

Hemingway, D. and T. Mittal (2019). "Enceladus's ice shell structure as a window on internal heat production". In: *Icarus* 332. ISSN: 10902643. DOI: 10.1016/j.icarus.2019.03.011.

Hurford, T. A., P. Helfenstein, G. V. Hoppa, R. Greenberg, and B. G. Bills (2007). "Eruptions arising from tidally controlled periodic openings of rifts on Enceladus". In: *Nature* 447 (7142). ISSN: 14764687. DOI: 10.1038/nature05821.

Ingersoll, S. P. Ewald, and S. K. Trumbo (2020). "Time variability of the Enceladus plumes: Orbital periods, decadal periods, and aperiodic change". In: *Icarus* 344. ISSN: 10902643. DOI: 10.1016/j.icarus.2019.06.006.

Johnston, S. and L. Montési (2017). "The impact of a pressurized regional sea or global ocean on stresses on Enceladus". In: *Journal of Geophysical Research: Planets* 122 (6). ISSN: 21699100. DOI: 10.1002/2016JE005217.

Kite, E. S. and A. M. Rubin (2016). "Sustained eruptions on Enceladus explained by turbulent dissipation in tiger stripes". In: *Proceedings of the National Academy of Sciences of the United States of America* 113 (15). ISSN: 10916490. DOI: 10.1073/pnas.1520507113.

Maeno, N., M. Arakawa, A. Yasutome, N. Mizukami, and S. Kanazawa (2003). "Ice-ice friction measurements, and water lubrication and adhesion-shear mechanisms". In: *Canadian Journal of Physics* 81 (1-2). ISSN: 00084204. DOI: 10.1139/p03-023.

Melosh, H. J. and A. Raefsky (1981). "A simple and efficient method for introducing faults into finite element computations". In: *Bulletin of the Seismological Society of America* 71.5. ISSN: 0037-1106. DOI: 10.1785/bssa0710051391.

Meyer, C., J. Buffo, F. Nimmo, A. Wells, S. Boury, T. Tomlinson, J. Parkinson, and G. Vasil (2022). "A mushy source for the geysers of Enceladus". In: *Preprint at https://arxiv.org/abs/2208.06714*.

Murray, C. D. and S. F. Dermott (2000). *Solar System Dynamics*. DOI: 10.1017/cbo9781139174817.

Nakajima, M. and Ingersoll (2016). "Controlled boiling on Enceladus. 1. Model of the vapor-driven jets". In: *Icarus* 272. ISSN: 10902643. DOI: 10.1016/j.icarus.2016.02.027.

Nimmo, F., A. Barr, M. Behounkova, and W. McKinnon (2018). *The Thermal and Orbital Evolution of Enceladus*. University of Arizona Press. DOI: 10.2458/azu_uapress_9780816537075-ch005.

Nimmo, F., P. C. Thomas, R. T. Pappalardo, and W. B. Moore (2007). "The global shape of Europa: Constraints on lateral shell thickness variations". In: *Icarus* 191 (1). ISSN: 00191035. DOI: 10.1016/j.icarus.2007.04.021.

Park, R., N. Mastrodemos, R. Jacobsen, A. Berne, A. Vaughan, D. Hemingway, J. Castillo-Rogez, J. Keane, A. Konopliv, E. Leonard, F. Nimmo, J. Riedel, M. Simons, and S. Vance (2024). "The global shape, gravity field, and libration of Enceladus". In: *Journal of Geophysical Research, Planets* 125 (1). DOI: 10.1029/2023JE008054.

Patthoff, A. and S. Kattenhorn (2011). "A fracture history on Enceladus provides evidence for a global ocean". In: *Geophysical Research Letters* 38 (18). ISSN: 00948276. DOI: 10.1029/2011GL048387.

Porco, D. Dinino, and F. Nimmo (2014). "How the geysers, tidal stresses, and thermal emission across the south polar terrain of Enceladus are related". In: *Astronomical Journal* 148 (3). ISSN: 00046256. DOI: 10.1088/0004-6256/148/3/45.

Porco, P. Helfenstein, P. C. Thomas, A. P. Ingersoll, J. Wisdom, R. West, and S. Squyres (2006). "Cassini observes the active south pole of enceladus". In: *Science* 311 (5766). ISSN: 00368075. DOI: 10.1126/science.1123013.

Postberg, F., R. Clark, C. Hansen, A. Coates, C. D. Ore, F. Scipioni, M. Hedman, and J. Waite (2018). *Plume and Surface Composition of Enceladus*. University of Arizona Press. DOI: 10.2458/azu_uapress_9780816537075-ch007.

Postberg, F., S. Kempf, J. Schmidt, N. Brilliantov, A. Beinsen, B. Abel, U. Buck, and R. Srama (2009). "Sodium salts in E-ring ice grains from an ocean below the surface of Enceladus". In: *Nature* 459 (7250). ISSN: 00280836. DOI: 10.1038/nature08046.

Postberg, F., J. Schmidt, J. Hillier, S. Kempf, and R. Srama (2011). "A salt-water reservoir as the source of a compositionally stratified plume on Enceladus". In: *Nature* 474 (7353). ISSN: 00280836. DOI: 10.1038/nature10175.

Rossi, C., P. Cianfarra, F. Salvini, O. Bourgeois, and G. Tobie (2020). "Tectonics of Enceladus' South Pole: Block Rotation of the Tiger Stripes". In: *Journal of Geophysical Research: Planets* 125 (12). ISSN: 21699100. DOI: 10.1029/2020JE006471.

Rovira-Navarro, M. and I. Matsuyama (2022). "A Spectral Method to Study the Tides of Laterally Heterogenous Bodies". In: *AGU Fall Meeting Abstracts*.

Rozhko, A., Y. Podladchikov, and F. Renard (2007). "Failure patterns caused by localized rise in pore-fluid overpressure and effective strength of rocks". In: *Geophysical Research Letters* 34 (22). ISSN: 00948276. DOI: 10.1029/2007GL031696.

Schenk, P. M. (2008). "Cartographic and Topographic Mapping of the Icy Satellites of the Outer Solar System". In: *International Archives of the Photogrammetry, Remote Sensing and Spatial Information Sciences* 37.

Schubert, G., J. D. Anderson, B. J. Travis, and J. Palguta (2007). "Enceladus: Present internal structure and differentiation by early and long-term radiogenic heating". In: *Icarus* 188.2. ISSN: 00191035. DOI: 10.1016/j.icarus.2006.12.012.

Schulson, E. and A. Fortt (2012). "Friction of ice on ice". In: *Journal of Geophysical Research: Solid Earth* 117 (12). ISSN: 21699356. DOI: 10.1029/2012JB009219.

Segall, P. (2010). *Earthquake and volcano deformation*. DOI: 10.5860/choice.48-0287.

Simons, M. and P. A. Rosen (2015). "Interferometric Synthetic Aperture Radar Geodesy". In: *Treatise on Geophysics: Second Edition*. Vol. 3. DOI: 10.1016/B978-0-444-53802-4.00061-0.

Skroch, M., S. Owen, M. Staten, R. Quadros, B. Hanks, B. Clark, and C. Stimpson (2019). *CUBIT Geometry and Mesh Generation Toolkit 15.4 User Documentation*.

Sládková, K. P., O. Souček, and M. Běhounková (2021). "Enceladus' Tiger Stripes as Frictional Faults: Effect on Stress and Heat Production". In: *Geophysical Research Letters* 48 (19). ISSN: 19448007. DOI: 10.1029/2021GL094849.

Smith-Konter, B. and R. Pappalardo (2008). "Tidally driven stress accumulation and shear failure of Enceladus's tiger stripes". In: *Icarus* 198 (2). ISSN: 00191035. DOI: 10.1016/j.icarus.2008.07.005.

Souček, O., J. Hron, M. Běhounková, and O. Čadek (2016). "Effect of the tiger stripes on the deformation of Saturn's moon Enceladus". In: *Geophysical Research Letters* 43.14. ISSN: 19448007. DOI: 10.1002/2016GL069415.

Spencer, J., F. Nimmo, A. Ingersoll, T. Hurford, E. Kite, A. Rhoden, J. Schmidt, and C. Howett (2018). *Plume Origins and Plumbing (Ocean to Surface)*. University of Arizona Press, p. 166. DOI: 10.2458/azu_uapress_9780816537075-ch008.

Spitale, J. N., M. D. Tigges, A. Berne, A. Rhoden, T. A. Hurford, and K. D. Webster (Mar. 2025). "Curtain-based Maps of Eruptive Activity in Enceladus's South-polar Terrain at 15 Cassini Epochs". In: *The Planetary Science Journal* 6 (3), p. 67. ISSN: 2632-3338. DOI: 10.3847/PSJ/adb7d7. URL: https://iopscience.iop.org/article/10.3847/PSJ/adb7d7.

Sukhorukov, S. and S. Løset (2013). "Friction of sea ice on sea ice". In: *Cold Regions Science and Technology* 94. ISSN: 0165232X. DOI: 10.1016/j.coldregions.2013.06.005.

Thomas, P. C., R. Tajeddine, M. S. Tiscareno, J. A. Burns, J. Joseph, T. J. Loredo, and C. Porco (2016). "Enceladus's measured physical libration requires a global subsurface ocean". In: *Icarus* 264. ISSN: 10902643. DOI: 10.1016/j.icarus.2015.08.037.

Van Hoolst, T., R. M. Baland, and A. Trinh (2016). "The diurnal libration and interior structure of Enceladus". In: *Icarus* 277. ISSN: 10902643. DOI: 10.1016/j.icarus.2016.05.025.

Wahr, J., Z. A. Selvans, M. E. Mullen, A. C. Barr, G. C. Collins, M. M. Selvans, and R. T. Pappalardo (2009). “Modeling stresses on satellites due to nonsynchronous rotation and orbital eccentricity using gravitational potential theory”. In: *Icarus* 200.1. ISSN: 00191035. DOI: 10.1016/j.icarus.2008.11.002.

Wahr, J., M. T. Zuber, D. E. Smith, and J. I. Lunine (2006). “Tides on Europa, and the thickness of Europa’s icy shell”. In: *Journal of Geophysical Research E: Planets* 111.12. ISSN: 01480227. DOI: 10.1029/2006JE002729.

Yin, A. and R. Pappalardo (2015). “Gravitational spreading, bookshelf faulting, and tectonic evolution of the South Polar Terrain of Saturn’s moon Enceladus”. In: *Icarus* 260. ISSN: 10902643. DOI: 10.1016/j.icarus.2015.07.017.

4.10 Supplementary Information

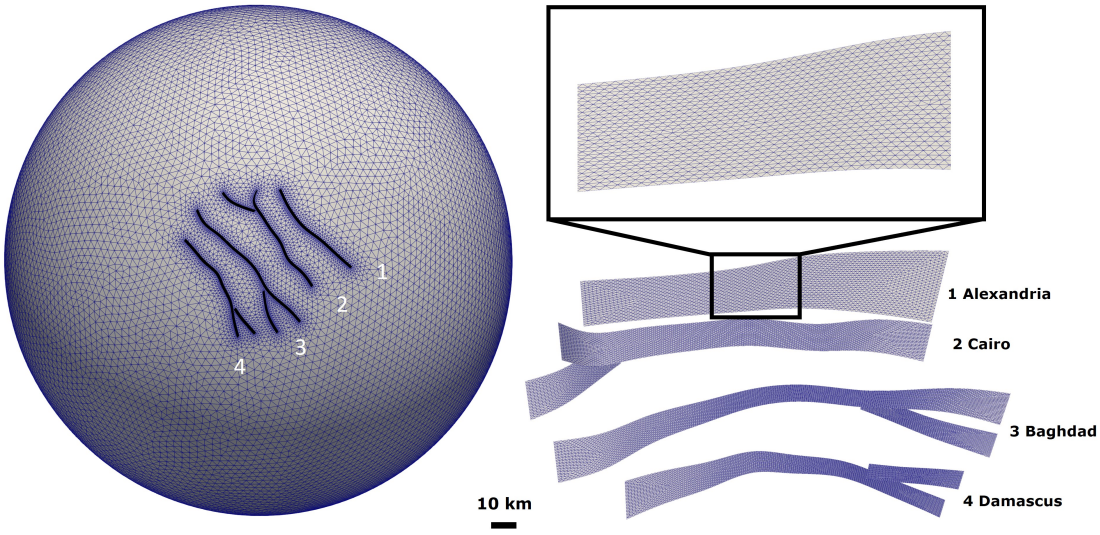

Figure 4.6: Example snapshots of mesh geometry. Left: South Polar (orthographic) view of mesh geometry showing labelled Tiger Stripe faults (black traces). Right: perspective view of Tiger Stripe surfaces with inset closeup image of Alexandria sulcus. Tetrahedra cell edges are colored in blue and range in size from 1 km (over the Tiger Stripe faults) to 8 km. Approximate distance scale is shown in the lower right panel for reference.

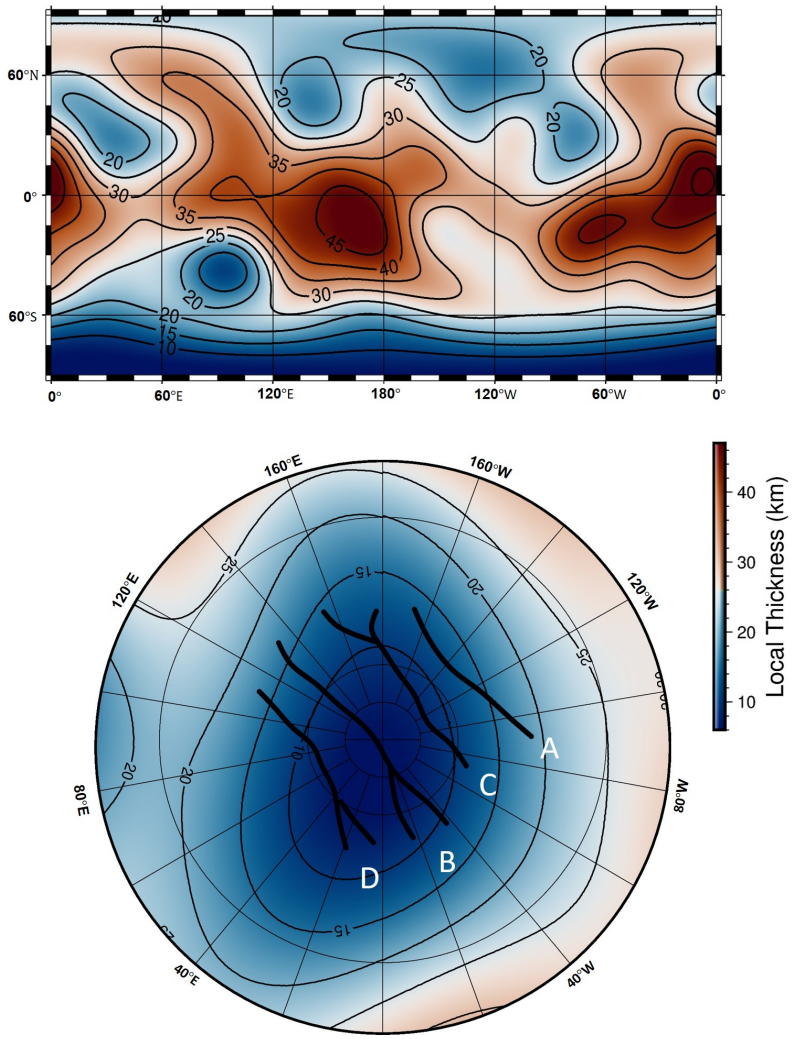

Figure 4.7: Crustal thickness assumed for finite element models. The top and bottom images respectively show crustal thickness in cylindrical equidistant and South Polar stereographic projections. We compensate non-hydrostatic surface topography at Enceladus using a formulation for Airy isostatic compensation to generate thickness variations (for details, see Methods 'Model Geometry'). Surface topography is extracted from a shape model of the full outer surface of Enceladus described in Park et al., 2024. Contours denote intervals of 5 km in thickness for both map projections. The labelled thick black lines plotted in the bottom image denote Tiger Stripes ('A' ⇔ Alexandria, 'C' ⇔ Cairo, 'B' ⇔ Baghdad, and 'D' ⇔ Damascus).

Table 4.1: Assumed parameter values in Chapter 4. Parameter values are extracted from Hemingway et al. (2018); Nimmo et al. (2018); Ermakov et al. (2021).

Parameter	**Value**	**Units**
ρ	925	kg/m^3
ρ_w	1007	kg/m^3
g_{out}	0.113	m/s^2
g_{int}	0.120	m/s^2
G	3.3	GPa
κ	8.8	GPa
e	0.0047	—
ω	$5.307 \cdot 10^{-5}$	s^{-1}

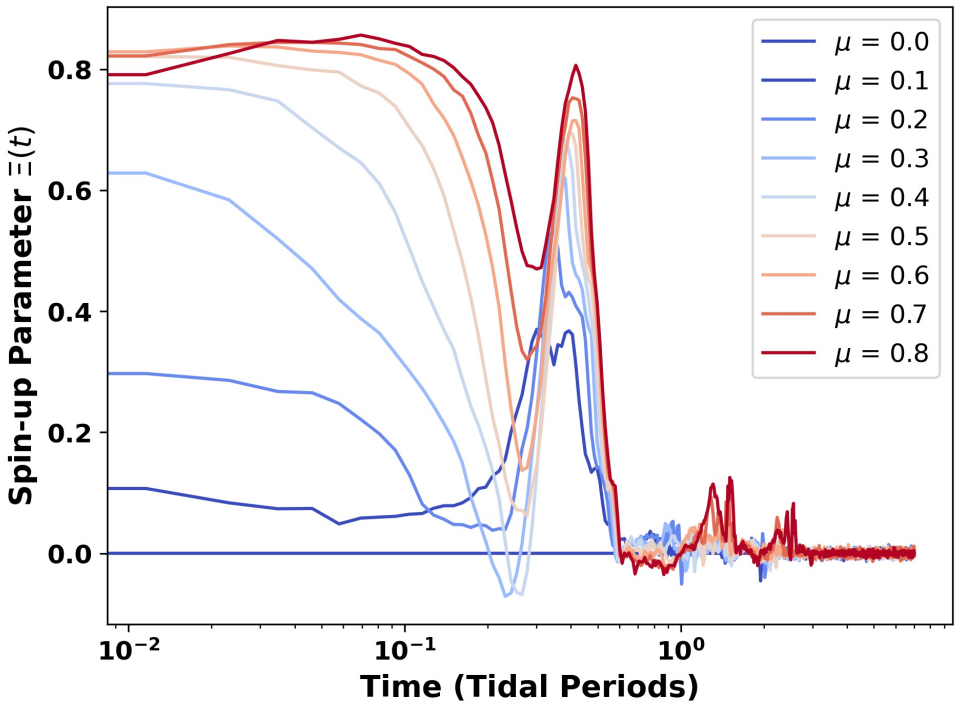

Figure 4.8: Spin-up parameter $\Xi(t)$ (see Equation 4.21) modelled as a function of time (in units of Tidal Periods) for several prescribed values for the static coefficient of friction μ. $\Xi(t) = 0$ indicates that differences between values at a given mean anomaly are zero (i.e., model is fully 'spun-up'). Plotted lines are colored by value of modelled coefficient of static friction. The x-axis is plotted in log-10 scale.

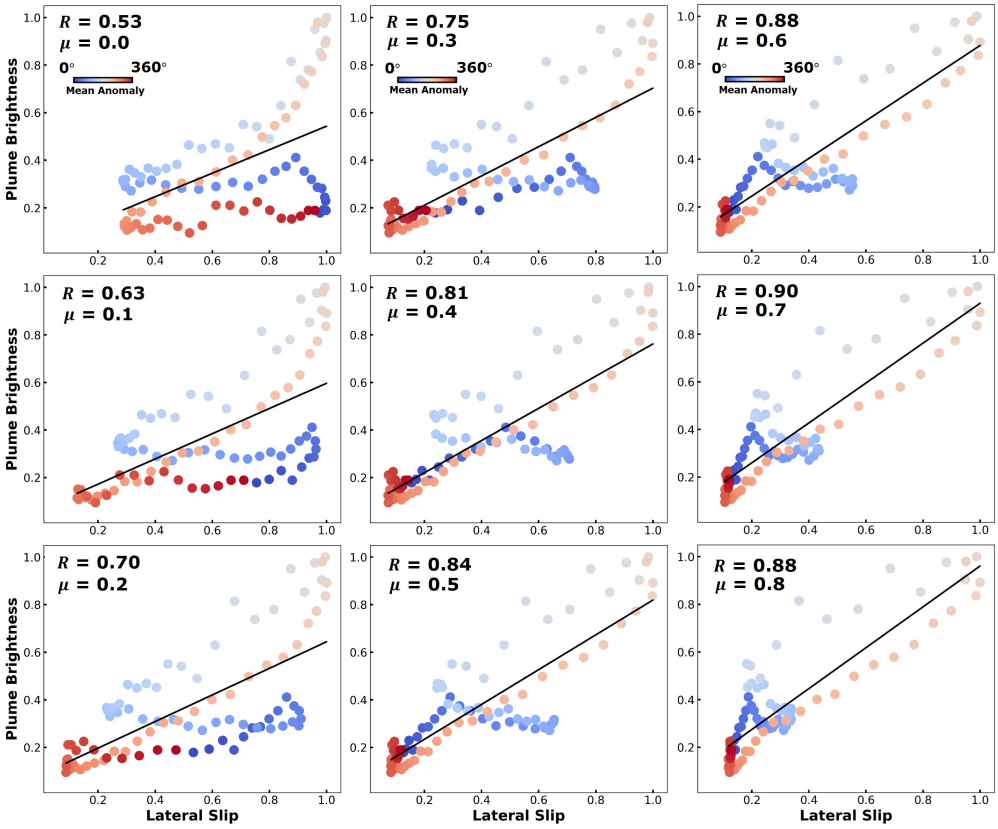

Figure 4.9: Correlation of timing of lateral slip and plume brightness (Ingersoll et al., 2020) for several values of modelled μ. Values are plotted for corresponding values of mean anomaly and are each normalized by maxima over the tidal cycle. Linear regression lines and associated Pearson Correlation Coefficients ($R = 1$ indicates perfect correlation) shown for reference. Scatter points are colored by value of mean anomaly ranging from 0° to 360° (i.e., periapse to periapse).

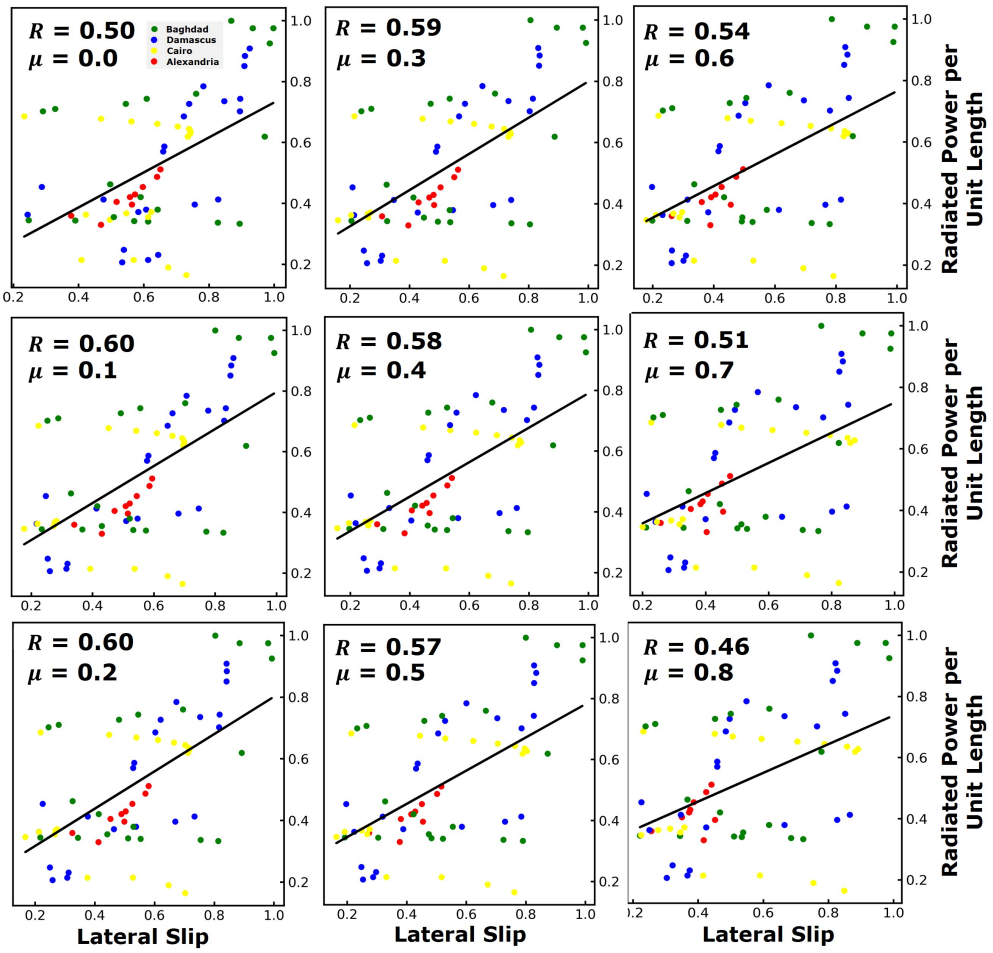

Figure 4.10: Correlation of spatial distribution of lateral slip and radiated power per unit length (Spencer et al., 2018) for several values of modelled μ. Values are plotted for corresponding values of surface location (i.e., along the Tiger Stripe faults) and are each normalized by maxima over all interfaces. Linear regression lines and Pearson Correlation Coefficient ($R = 1$ indicates perfect correlation) shown for reference. Scatter points are colored according to associated fault (Green $\Leftrightarrow$ Baghdad, Blue $\Leftrightarrow$ Damascus, Yellow $\Leftrightarrow$ Cairo, and Red $\Leftrightarrow$ Alexandria). Values from the endpoints of fault structures are excluded from plots and the computation of R values.

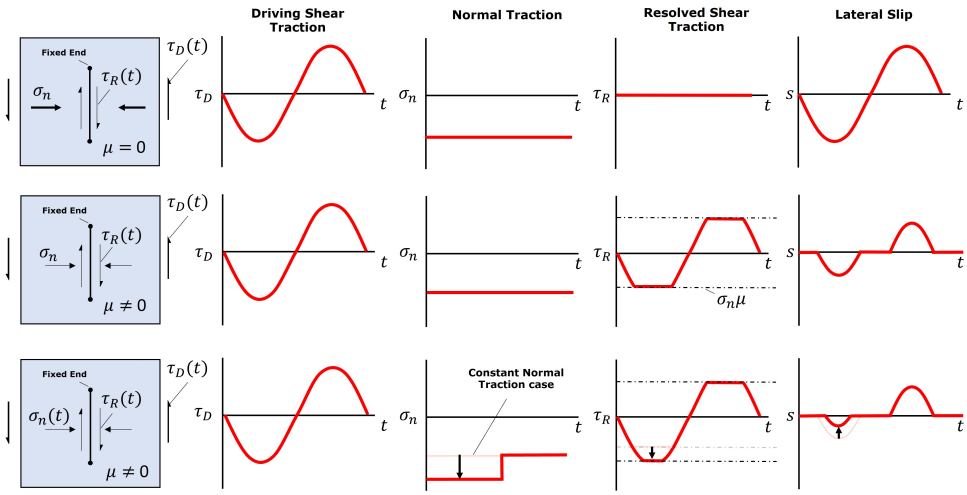

Figure 4.11: Simplified model relating driving shear traction τ_D, normal traction σ_n, μ, and slip s along the Tiger Stripe faults. Upper row: Frictionless fault subject to driving tractions. In this case, the fault cannot support shear traction (i.e., resolved shear traction $\tau_R = 0$) and driving traction τ_D is fully resolved via slip along interfaces (i.e., $s \neq 0$) regardless of the applied σ_n. Slip results in a concentration of elastic strain at the fixed ends of the fault. The subsequent unloading of the driving shear traction results in a return to zero slip. Center row: frictional fault with time-variable driving shear traction and constant normal traction. In this case, $s \neq 0$ when $|\tau_D| > \sigma_n\mu$ (i.e., $\tau_c = |\tau_D| - \sigma_n\mu > 0$). Constant values of σ_n result in symmetric slip profiles following the onset of sliding. Bottom row: frictional fault with time-variable driving shear and normal tractions. In this case, variable σ_n results in an increase in τ_D required to initiate sliding and an associated decrease in the amplitude of s during the first occurrence of $\tau_c > 0$. The resulting slip profile is double-peaked and asymmetric.

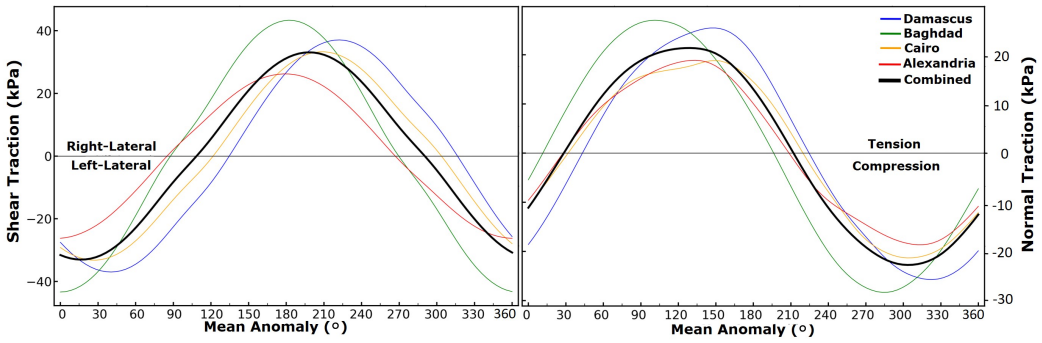

Figure 4.12: Similar to upper right and upper left panels of Figure 4.2 of the main text except values (i.e., driving tractions) are evaluated for a model with slipping faults ($\mu = 0.4$). We find that slip along Tiger Stripe faults induces up to ~10% variability in tractions relative to values evaluated for the case of fully-locked interfaces.

References

Ermakov, A. I., R. S. Park, J. Roa, J. C. Castillo-Rogez, J. T. Keane, F. Nimmo, E. S. Kite, C. Sotin, T. J. W. Lazio, G. Steinbrügge, S. M. Howell, B. G. Bills, D. J. Hemingway, V. Viswanathan, G. Tobie, and V. Lainey (2021). "A Recipe for the Geophysical Exploration of Enceladus". In: *Planetary Science Journal* 2 (4). ISSN: 26323338. DOI: 10.3847/PSJ/ac06d2.

Hemingway, D., L. Iess, R. Tajeddine, and G. Tobie (2018). *The Interior of Enceladus*. University of Arizona Press. DOI: 10.2458/azu_uapress_9780816537075-ch004.

Ingersoll, S. P. Ewald, and S. K. Trumbo (2020). "Time variability of the Enceladus plumes: Orbital periods, decadal periods, and aperiodic change". In: *Icarus* 344. ISSN: 10902643. DOI: 10.1016/j.icarus.2019.06.006.

Nimmo, F., A. Barr, M. Behounkova, and W. McKinnon (2018). *The Thermal and Orbital Evolution of Enceladus*. University of Arizona Press. DOI: 10.2458/azu_uapress_9780816537075-ch005.

Park, R., N. Mastrodemos, R. Jacobsen, A. Berne, A. Vaughan, D. Hemingway, J. Castillo-Rogez, J. Keane, A. Konopliv, E. Leonard, F. Nimmo, J. Riedel, M. Simons, and S. Vance (2024). "The global shape, gravity field, and libration of Enceladus". In: *Journal of Geophysical Research, Planets* 125 (1). DOI: 10.1029/2023JE008054.

Spencer, J., F. Nimmo, A. Ingersoll, T. Hurford, E. Kite, A. Rhoden, J. Schmidt, and C. Howett (2018). *Plume Origins and Plumbing (Ocean to Surface)*. University of Arizona Press, p. 166. DOI: 10.2458/azu_uapress_9780816537075-ch008.

Chapter 5

THERMAL ASYMMETRY IN THE MOON'S MANTLE INFERRED FROM MONTHLY TIDAL RESPONSE

R. S. Park et al. (2025). "Thermal Asymmetry in the Moon's Mantle Inferred from Monthly Tidal Response". In: *Nature* 641.8065.
The material presented in this chapter represents portions of the above paper that were contributed by A.B..

5.1 Abstract

The Moon undergoes periodic tidal forcing due to its eccentric and oblique orbit around the Earth (Park et al., 2021). The response to this tidal interaction drives temporal changes in the lunar gravity field and is sensitive to the satellite's internal structure (Qin et al., 2012; Rovira-Navarro et al., 2024; Zhong et al., 2012). We use data from the NASA GRAIL spacecraft (Konopliv et al., 2013; Konopliv et al., 2014; Lemoine et al., 2013; Lemoine et al., 2014; Zuber et al., 2013) to recover the time-varying lunar gravity field, including a degree-3 gravitational tidal Love number, k_3. Here, we report our estimated value of k_3=0.0163±0.0007 which is about 72% higher than that expected for a spherically symmetric Moon (Williams et al., 2014). Such a large k_3 can be explained if the elastic shear modulus of the mantle varies by about 2-3% between the nearside and farside (Zhong et al., 2012), providing the first observational demonstration of lateral heterogeneities in the deep lunar interior. This asymmetric structure suggests preservation of a predominantly thermal anomaly of approximately 100-200 K in the nearside mantle which formed surface mare regions 3-4 Gya (Laneuville et al., 2013) and could influence the spatial distribution of deep moonquakes (Frohlich and Nakamura, 2009).

5.2 Introduction

The Moon has well-known nearside-farside differences as expressed in the offset between the satellite's center of mass and center of figure as well as asymmetries in topography, crustal thickness, concentration of radiogenic elements at the surface, and geology (Jolliff et al., 2000). Various hypotheses have been proposed to explain these asymmetries, though their origin remains widely debated. Some studies suggest that the Moon's asymmetries are linked to variations in its deep

internal structure, including the distribution of radiogenic heat-producing elements which could sustain long-lived temperature differences between the nearside and farside (Zhong et al., 2000; Laneuville et al., 2013). These models can explain the concentration of volcanism on the Moon's nearside and provide constraints on the poorly understood bulk concentrations of lunar radiogenic elements (Taylor et al., 2006). However, to date, no observational evidence for such temperature differences or variations in deep internal structure has been unambiguously detected. In this study, we aim to determine the magnitude of these differences at depth by analyzing the Moon's gravitational response to its periodic tidal interactions with Earth.

The gravity field of the Moon is typically expressed in terms of spherical harmonic coefficients of degree l and order m (Kaula, 1963). The spatial resolution of the gravity field is inversely proportional to l, with the full wavelength usually defined as approximately $2\pi R/l$, where lunar radius R=1,738 km. Temporal changes in the lunar gravity field can be quantified using gravitational tidal Love numbers, k_{lm}, which represent the ratio of the induced potential from the deformation of the Moon to the imposed gravitational potential from Earth at a given degree and order (Love, 1909). Thus, k_{lm} scales the lunar gravity field as the relative positions of the Moon and Earth vary over the course of a month.

For spherically symmetric bodies, forcing at a given degree and order induces deformation only at the same degree and order. However, if the Moon is laterally heterogeneous, then forcing at a given degree and order can drive deformation at other degrees and orders (Dahlen and Tromp, 1998). A laterally heterogeneous Moon subject to tidal forcing at $l = 2$ will therefore exhibit deformation at all degrees ($l \geq 2$) as well as anomalous degree-3 Love numbers, k_{3m} (Figure 5.7). Moreover, unlike with static gravity—which is most sensitive to structures in the uppermost crust—time-varying long-wavelength gravity is strongly sensitive to deep-seated asymmetries in the lunar mantle (Qin et al., 2016). This sensitivity to deep lateral heterogeneity makes the analysis of gravitational tidal Love numbers a powerful tool for probing the structure of the lunar interior (Zhong et al., 2000; Zhong et al., 2012).

5.3 Recovery of internal nearside-farside structure

We reconstruct the lunar gravity field recover degree-2 and degree-3 Love numbers from an analysis of GRAIL Ka-band range rate data. We recover k_{2m} and k_{3m} for two separate cases, which are shown in Table 5.1. In the first case, $l = 3$ Love numbers

are assumed not to depend on m and we recover $k_3 = k_{3m} = 0.0163 \pm 0.0007$. In the second case, k_{3m} are estimated independently yielding $k_{30} = 0.0159 \pm 0.0011$, $k_{31} = 0.0141 \pm 0.0015$, $k_{32} = 0.0173 \pm 0.0015$, and $k_{33} = 0.0145 \pm 0.0024$ (Table 5.1 and Figure 5.1).

Parameter	**Value**	**15x formal 1-σ**	**Notes**
Case 1			
k_{20}	0.024223	0.000037	
k_{21}	0.024223	0.000037	
k_{22}	0.024223	0.000037	
k_3	0.0163	0.0007	The expected values of k_2 and k_3 for a spherically symmetric Moon are 0.0234 and 0.00945, respectively (Weber et al., 2011; Garcia et al., 2011).
Case 2			
k_{20}	0.024237	0.000037	
k_{21}	0.024236	0.000037	
k_{22}	0.024236	0.000037	
k_{30}	0.0159	0.0011	
k_{31}	0.0141	0.0015	
k_{32}	0.0173	0.0015	
k_{33}	0.0145	0.0024	

Table 5.1: Recovered gravitational tidal Love numbers, k_{2m} and k_{3m}. Case 1 shows recovered $k_3 = 0.0163 \pm 0.0007$ which is approximately 72% larger than the value expected for a spherically symmetric Moon (Figure 5.1). Case 2 shows individual k_{2m} and k_{3m} when values at each order are estimated independently. The magnitudes of the recovered order-dependent k_{3m} are comparable to the recovered k_3 value in Case 1.

Our recovered k_{3m} are approximately 72% larger than the values expected for a spherically symmetric interior (Williams et al., 2014; Figure 5.1 and Methods), suggesting substantial lateral heterogeneity within the Moon (Figure 5.2). To constrain the nature of this asymmetry, we perform a Markov Chain Monte Carlo (MCMC) inversion to predict k_{2m} and k_{3m} (Figure 5.8 and Methods) using the observational constraints shown in Case 2 of Table 5.1. The parameter set we explore includes shear modulus perturbations to a one-dimensional (1D) reference model derived

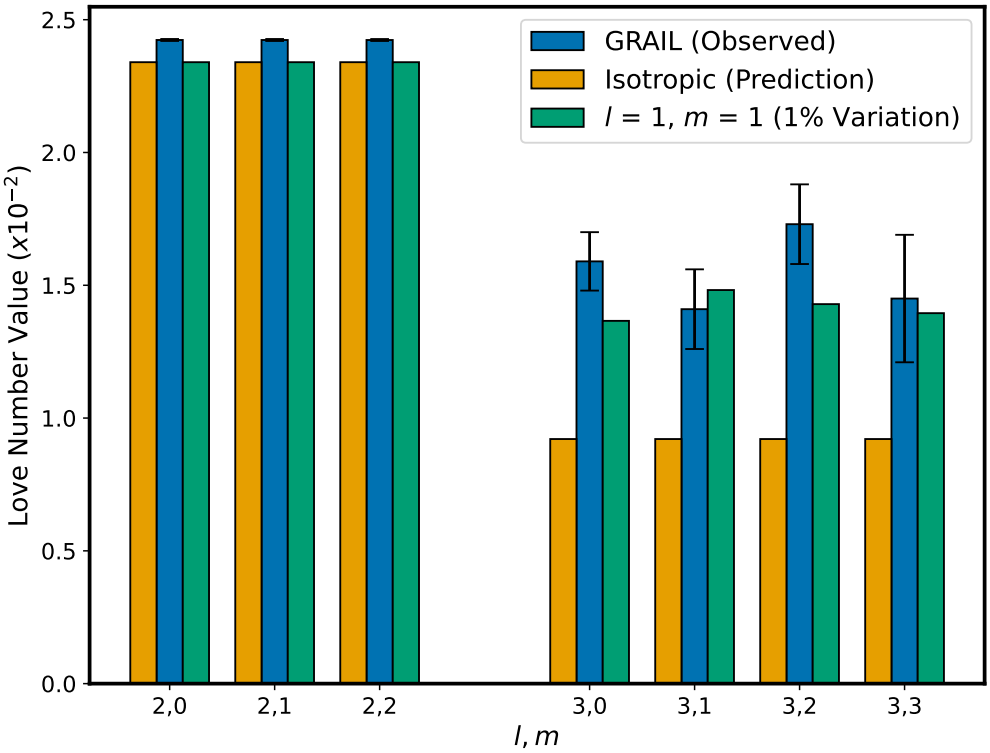

Figure 5.1: Bar chart showing k_{2m} and k_{3m} values expected for an isotropic Moon (orange), observed Love number values with 15× formal 1-σ uncertainties error bars (blue), and values predicted for a lunar interior with an imposed 1% nearside-farside ($l = 1$, $m = 1$) variation in mantle shear modulus (green). Love Numbers for the isotropic case represent values predicted for the 1D lunar interior derived from seismic travel time data in Weber et al., 2011.

from seismic travel-time data (Table 5.2). The reference models also incorporate lateral crustal thickness and density variations derived from lunar static gravity and topography data (Wieczorek et al., 2013) (5.9a, and 5.9c) but do not include lateral variations in shear modulus *a priori* for any layer. We use spherical harmonics up to $l = 3$ to parameterize perturbations for two internal layers: the crust (0–34 km depth) and the mantle (34–1,407 km depth). Lateral heterogeneity in the core minimally (<1%) impacts lunar time-variable gravity fields (Figure 5.2); therefore, models assume a laterally homogeneous elastic structure below 1,407 km depth. For the inversion, we use LOV3D (Rovira-Navarro et al., 2024), a semi-analytical spectral method to forward compute gravitational tidal Love numbers from candidate interior structures (Methods).

We find that positive ($l = 1, m = 1$) shear modulus structure, which corresponds

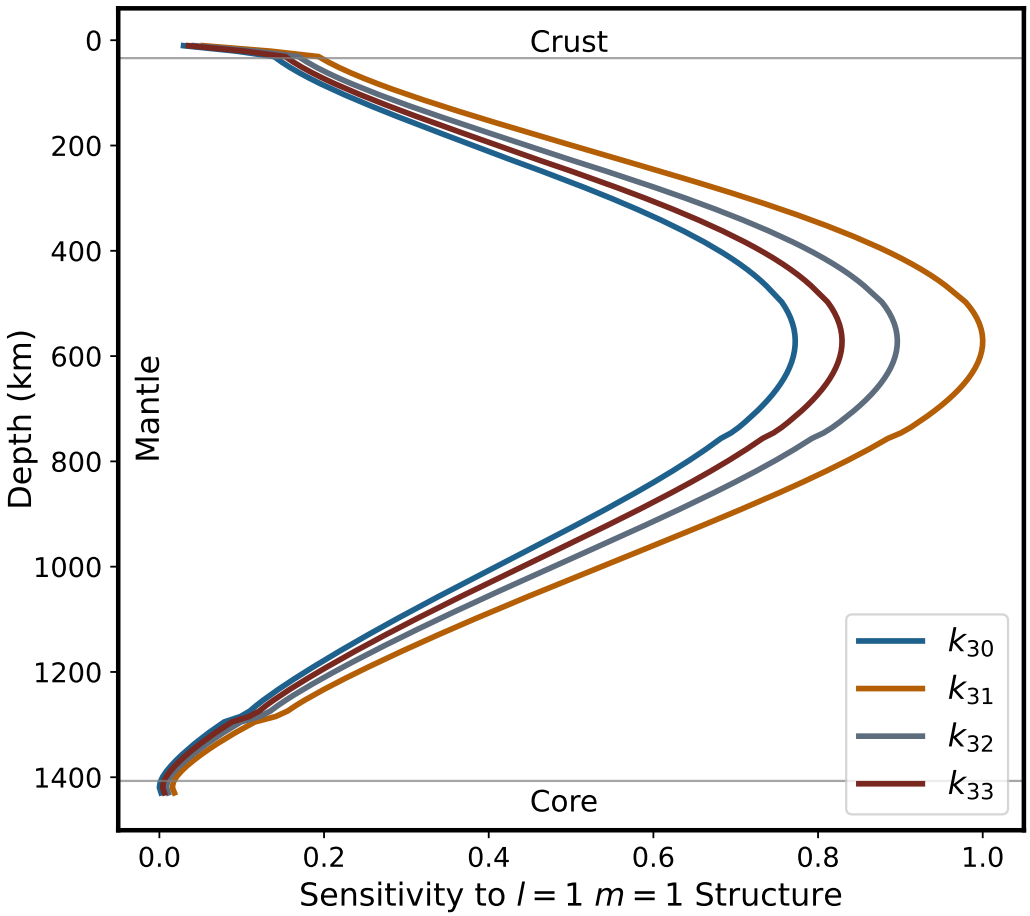

Figure 5.2: Normalized sensitivity of k_{30} (blue), k_{31} (orange), k_{32} (gray), and k_{33} (red) Love numbers to (l = 1, m = 1) perturbations (i.e., a nearside-farside pattern) in shear modulus placed at depths ranging from the surface (0 km) to the core-mantle boundary (1,407 km) for reference lunar interiors (Weber et al., 2011) subject to l = 2 forcing (e.g., eccentricity tides expected for the lunar orbit). Labels refer to vertical regions spanning the crust (0–34 km), the mantle (34–1,407 km), and the core (1,407–1,737 km).

to a nearside-farside pattern, increases all k_{3m} Love numbers for lunar interiors subject to monthly tidal forcing at $l = 2$ (green bars in Figure 5.1). For example, the combination of $(l = 2, m = 2)$ and $(l = 2, m = 0)$ harmonics in the Earth-Moon eccentricity tide interacts with lower (or higher) shear modulus values on the lunar nearside or farside to broadly increase (or decrease) outward radial deformation in these regions (Figure 5.7). The resulting mass displacement yields $(l = 3, m = 1)$ and $(l = 3, m = 3)$ gravity signatures that enhance the existing response to forcing at these harmonics, increasing the k_{31} and k_{33} Love numbers. Similarly, interaction between the $(l = 2, m = 1)$ Earth-Moon obliquity tide and nearside-farside structure produces $(l = 3, m = 0)$ and $(l = 3, m = 2)$ gravity signatures that increase the k_{30} and k_{32} Love numbers (Methods). Note that the eccentricity and obliquity components of the driving tidal potential and their associated coupling to degree-3 harmonics are comparable in magnitude, resulting in similar values for k_{3m} across all values of m.

The depth of lunar asymmetries modulates their impact on Love number values. For example, k_{3m} exhibit peak sensitivity to nearside-farside variations in shear modulus at approximately 600 km depth and are largely insensitive to structure close to the surface (Figure 5.2). Inversions consequently do not distinguish nearside-farside structure in the crust (< 34 km depth) (Table 5.3). Variations in crustal layer thickness are also insufficient to explain k_{3m}, as the approximately 50% variation in nearside-farside Moho depth alters $l = 3$ Love numbers by only about 30% (i.e., approximately 0.003) relative to values predicted for a laterally isotropic Moon. Moreover, crustal thinning below mare regions tends to increase the effective shear modulus of the nearside hemisphere and decrease degree-3 Love numbers, opposite to the observed trend of k_{3m} values in Table 5.1 (Figure 5.9c).

Our inversions predict a 2–3% mean difference in shear modulus between nearside and farside hemispheres for the entire lunar mantle, with >99.7% confidence (Figure 5.3). When we further subdivide the mantle into distinct regions for inversions, we find a slight preference for $(l = 1, m = 1)$ structure localized to approximately the upper 800 km of the interior. This is due to the relatively higher sensitivity of k_{3m} to $l = 1$ structure in this region (Figure 5.2). Nonetheless, the magnitude of heterogeneities derived for different mantle regions can trade off with one another to produce an overall 2–3% variation in $(l = 1, m = 1)$ mantle shear modulus. This non-uniqueness prevents statistically significant constraints on the extent to which asymmetries localize within these layers.

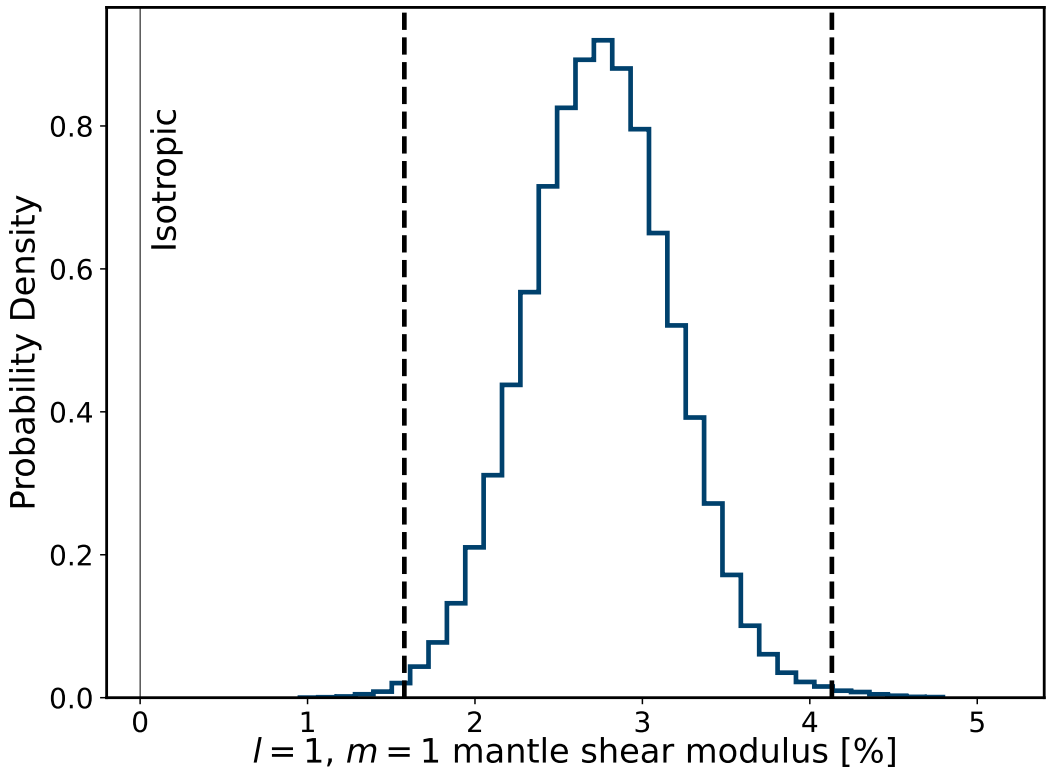

Figure 5.3: Recovered nearside-farside structure in the lunar mantle using independently recovered k_{3m}. Histogram showing inverted coefficient value that describes internal ($l = 1, m = 1$) variations in shear modulus (in % relative to the bulk value) for the lunar mantle. Dashed lines show 0.3% and 99.7% quantiles (i.e., 3-σ confidence bounds). Thin vertical gray line denotes value expected for an isotropic mantle. The preferred value and 3-σ bounds for ($l = 1, m = 1$) mantle shear modulus structure is 2.74±1.3%. A full list of derived harmonic coefficients describing 3D structure are shown in Table 5.3.

In addition to impacting k_{3m}, shear modulus structure is expected to drive variation in $l = 2$ Love numbers. The minimal observed differences between k_{2m} values across spherical harmonic order m correspondingly imply a lack of detectable $l = 2$ variation in internal shear modulus (Figure 5.1 and see also Figure 5.6 of ref. Rovira-Navarro et al., 2024). The coupled response at degree-2 due to inferred ($l = 1, m = 1$) shear modulus variation (Figure 5.3) also impacts k_{2m} at the 10^{-6}–10^{-7} level—approximately an order of magnitude smaller than observational uncertainty for these parameters (Table 5.1). However, the mean value of k_{2m} is approximately 5% higher than that expected for lunar interiors derived from seismic travel time data (Figure 5.1) (Williams et al., 2014; Garcia et al., 2011; Weber et al., 2011). This increase in monthly k_{2m} can be explained by an approximately global 97% reduction in effective shear modulus at tidal timescales between depths of 1,257–1,407 km. Consistent with results from several previous studies (Briaud et al., 2023; Matsumoto et al., 2015), this low effective shear modulus value corresponds with a local Maxwell viscosity of approximately 10^{15}–10^{16} Pa·s and can be explained by the presence of globally distributed partial melt in the lower mantle (Table 5.3 and Figure 5.9b).

5.4 Thermal asymmetry in the lunar mantle

Our modeling suggests that the Moon's large k_{3m} is the result of a substantial 2–3% difference between the shear modulus of the nearside and farside mantle. What could produce this difference? At a specified pressure, the shear modulus of rock depends on its composition and temperature. However, large changes in the mantle composition likely cannot explain the derived asymmetries due to their associated impact on internal density. For example, decreasing the shear modulus by the required 2–3% solely through changes in iron content would necessitate a >5% enrichment of dense iron-endmember olivine (i.e., fayalite) and a corresponding increase in the density of the nearside mantle by >50 kg/m^3 relative to the density of the farside mantle. Such a scenario would produce a COM-COF offset of the Moon that is at least 15 times larger than the observed value (Figure 5.4). Similarly, invoking a nearside enrichment in water content to explain the observed shear modulus variation would induce a COM-COF offset 5–10 times larger than the observed value (Figure 5.10; Jacobsen et al., 2008). In contrast, a temperature difference of approximately 100–200 K between the two hemispheres can produce the required variation in shear modulus with a sufficiently small change in mantle density and in the COM-COF offset. Thus, we favor a predominantly thermal explanation for these derived asymmetries.

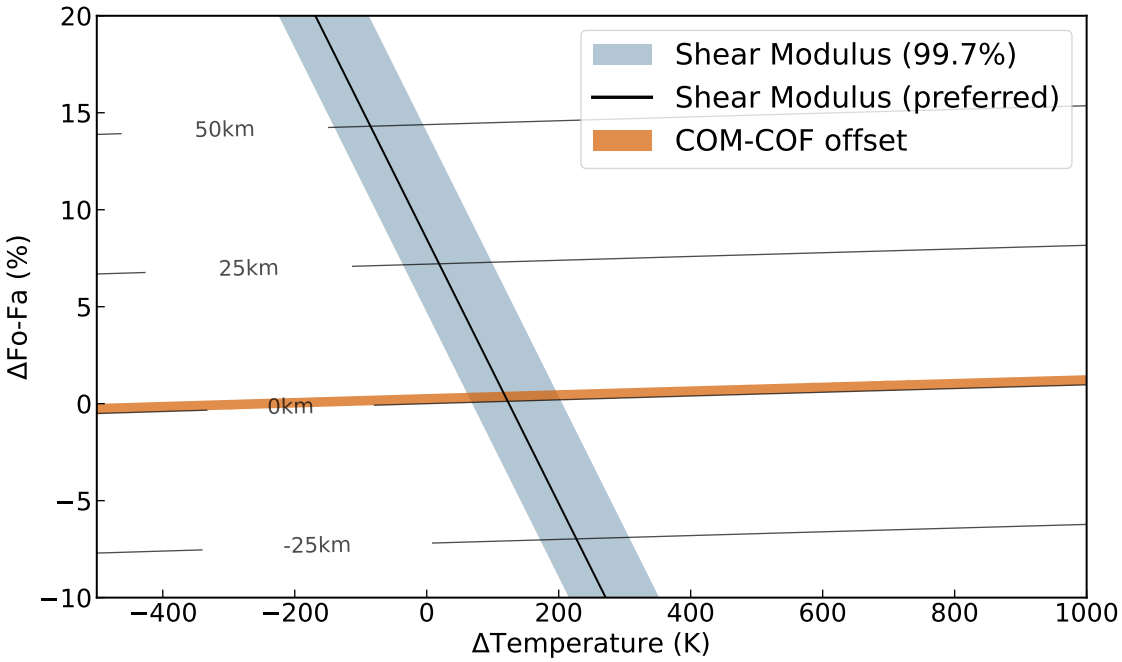

Figure 5.4: Impact of asymmetric temperature or composition on the lunar mantle. Lunar COM-COF offset and shear modulus change as a function of temperature change (assuming a volume expansion coefficient $\beta = 3 \times 10^{-5}$ K^{-1} and $\Delta\mu/\Delta T = -1.35 \times 10^{-2}$ GPa/K where T is temperature and μ is shear modulus Isaak, 1992; Suzuki, 1975) and iron content (i.e., percentage changes in the mol fraction of iron-endmember olivine (fayalite) relative to forsterite, or $\Delta Fo\text{-}Fa$, assuming $\Delta\rho/\Delta Fo\text{-}Fa = 9.7$ kg/%-m^3, where ρ is density and $\Delta\mu/\Delta Fo\text{-}Fa = -0.3$ GPa/% Chung, 1970) in the nearside mantle. The solid red region and thin black lines respectively denote the observed COM-COF offset Barker et al., 2016 and contours for computed COM-COF offset values. The blue shaded area and thick solid black line respectively denote 99.7% confidence bounds and preferred values for the nearside-farside shear modulus differences inferred from gravity data in this work. We infer a temperature anomaly of approximately 100–200 K between the lunar near and far side hemispheres by identifying overlapping portions of the $\Delta Fo\text{-}Fa$ - ΔTemperature parameter space that satisfy both the shear modulus difference (within 99.7% confidence bounds) and the COM-COF offset.

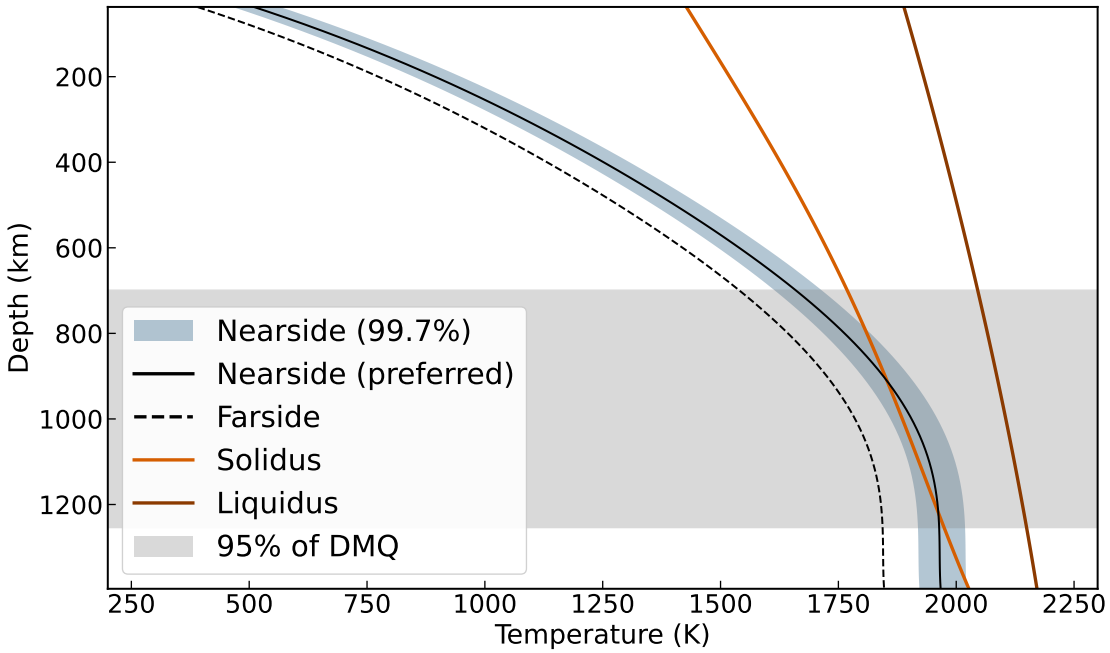

Figure 5.5: Internal temperature structure for the present-day lunar nearside based on predicted shear modulus change (99.7% confidence bound and preferred model are blue shaded region and solid black line respectively). The nearside profile is computed by uniformly increasing the temperature of a reference farside conductive model for the Moon (black dashed line, extracted from Fig. 5 of Laneuville et al., 2013) by the inferred 100–200 K anomaly (i.e., assuming zero lateral variation in mantle composition). The lunar mantle solidus and liquidus are shown as brown and orange lines, respectively. Since the predicted nearside model exceeds the solidus, we expect present-day melt production in the lunar mantle. The gray shaded region denotes the location of 95% of observed deep moonquakes (DMQ) (Frohlich and Nakamura, 2009).

It is important to note that our result implies a present-day thermal anomaly between the nearside and farside of the lunar mantle. This hemispheric thermal dichotomy may be sustained by the high abundance of radiogenic heat sources observed in the nearside crust, such as thorium and titanium, which constitute a negligible mass fraction of lunar material (Zhang et al., 2023). Models of lunar evolution that invoke radiogenic heating as a driver for nearside-farside differences in temperature predict a partially-molten mantle 3–4 Gya (Zhong et al., 2000; Laneuville et al., 2013). Based on our results, present-day magma production may still occur at 800–1,250 km depth in the nearside (Figure 5.5 and Figure 5.6) and further reduce the effective rigidity of this region relative to that of the deep farside interior (Takei, 2017).

A persistent thermal anomaly in the lunar mantle may also influence the evolution

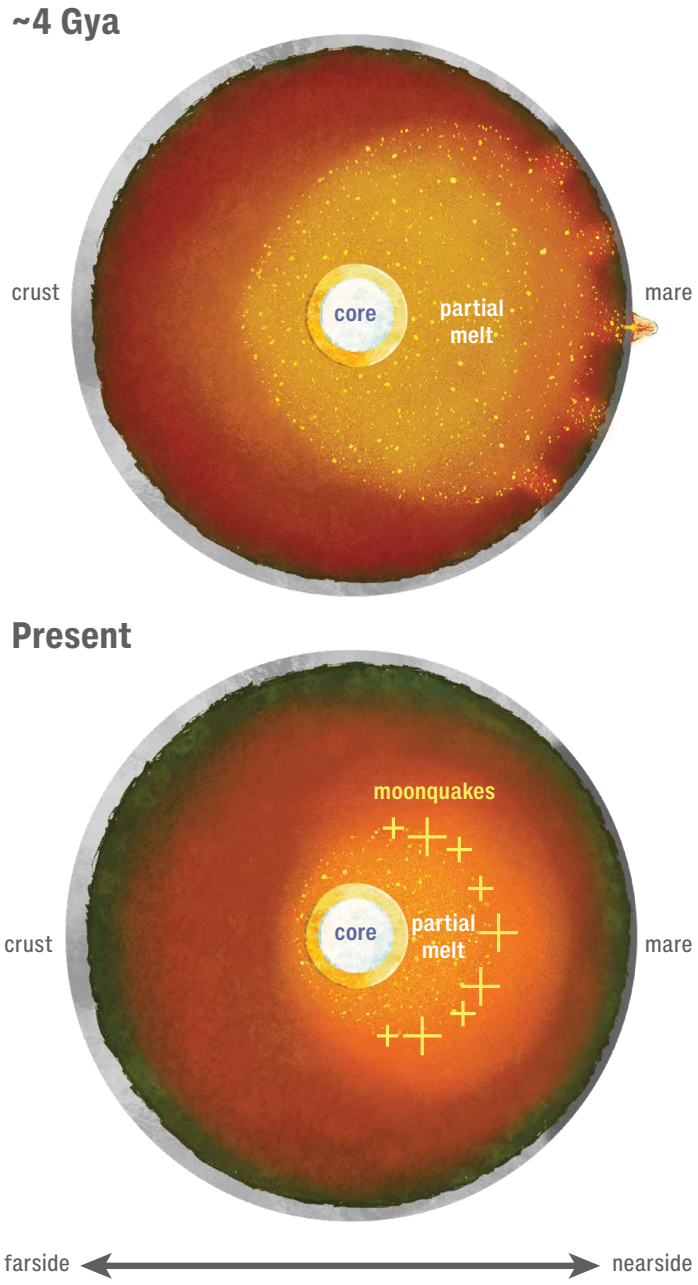

Figure 5.6: Conceptual model for the evolution of the lunar interior. Partial melt associated with the inferred nearside thermal anomaly erupts onto the surface to form mare regions approximately 4 Gya (top). As the interior cools, the partial melting associated with the inferred nearside thermal anomaly descends until localizing to depths of 800–1,200 km in the present-day (bottom). The color scale denotes mantle temperature (decreasing from light yellow to dark orange to dark green). Yellow crosses denote moonquakes which localize within or slightly above partially melted regions of the present-day lunar mantle. For a similar conceptual model that additionally considers compositional variations in water vapor and ilmenite in the lunar interior (see Fig. 4 of Qin et al., 2012).

of the overlying crust. For example, the upward migration of magma in the mantle is expected to deflect the Moho and drive crustal thinning (Neumann et al., 1996). A small fraction of this magma should also erupt on the surface to form mare regions (Laneuville et al., 2013). Comparing our result with independent thermochemical evolution models (Laneuville et al., 2013), we speculate that surface volcanic activity would have peaked 3–4 Gya and diminished over time as the interior cools and the depth of partial melting increases (Figure 5.5 and Figure 5.6). This gradual cooling of the lunar interior is consistent with the possible recent discovery of young (approximately 120 Mya) volcanic beads from Chang'e-5 samples (for alternative hypotheses on the formation of lunar beads see Long et al., 2022). The formation of polygonal fractures surrounding mare regions may also accommodate the long-term thermal contraction of the nearside hemisphere (Figure 5.6 of Andrews-Hanna et al., 2014).

Our inferred location of partial melt (Figure 5.5 and Figure 5.6) coincides with the lower bound of the radial extent of deep moonquakes (DMQ) (Qin et al., 2016). This correlation suggests that small amounts of partial melt (<5% by mass) may promote brittle failure by increasing the prevalence of stress concentrations in tidally-deforming regions of the lunar interior (Rushmer, 1995; Frohlich and Nakamura, 2009; Qin et al., 2012;Wilding et al., 2023). Small amounts of water (< 0.1% by mass, Figure 5.10) may also reduce the freezing point of rock and further encourage seismicity in the lower mantle (Qin et al., 2012). Alternatively, the enhanced ductility of very warm mantle rock may reduce its susceptibility to brittle failure and arrest DMQs at approximately 1,000-1,250 km depth (Figure 5.5). A link between DMQs and partial melt could be tested by measuring induced components of the Moon's magnetic field which form through interactions between the solar wind and deep magma. Moreover, a mantle-wide thermal asymmetry may imply lateral variations DMQ depth or frequency. While few farside DMQs are observed in Apollo data, it is unclear whether this is due to a difference in seismicity or due to attenuation at depth. This ambiguity may be resolved with the upcoming deployment of seismometers on the Moon with the Farside Seismic Suite planned for 2026 (Panning et al., 2022), the Lunar Environment Monitoring Station planned for Artemis III, and the proposed Lunar Geophysical Network mission (Weber et al., 2020).

5.5 Tidal tomography and future measurements

While so-called "tidal tomography" has been used to probe the deep structure of the Earth (Lau et al., 2017), our result provides the first example of extraterrestrial tidal tomography. The tidal signatures of planetary bodies are generally extremely small, making them challenging to detect. However, continued advancements in measurement techniques (Rummel et al., 2011; Zuber et al., 2013; Landerer et al., 2020; Park et al., 2020) will allow the recovery of these faint signals at a level meaningful for tidal tomography, thus providing a novel way to probe the deep interior. In the future, these techniques can be applied to other planetary objects exhibiting pronounced low-order surface variations, such as Mars (Zhong and Zuber, 2001), Enceladus (Berne et al., 2024), and Ganymede (Palguta et al., 2006). Because tidal tomography does not require a landed spacecraft, unlike seismology, it should be an important component of future missions that include an orbiter around the target body.

5.6 Methods

The lunar gravity field

The gravitational field potential, $U(r, \lambda, \phi)$, associated with the Moon is expressed as a spherical harmonic expansion (Kaula, 1963; Heiskanen and Moritz, 1967):

$$U(r, \lambda, \phi) = \frac{GM}{r} \sum_{l=0}^{\infty} \sum_{m=0}^{l} \left(\frac{R}{r}\right)^{l} \bar{P}_{lm}(\sin\phi) \left[\bar{C}_{lm} \cos(m\lambda) + \bar{S}_{lm} \sin(m\lambda)\right], \quad (5.1)$$

where GM is the mass parameter of the Moon, l is the spherical harmonic degree, m is the order, $\bar{P}_{lm}$ are the normalized associated Legendre polynomials, $\bar{C}_{lm}$ and $\bar{S}_{lm}$ are the normalized spherical harmonic coefficients, R is the reference radius of the Moon (1738 km), λ is longitude, ϕ is latitude, and r is the radius evaluated at the spacecraft position relative to a Moon's body-fixed frame. In this formulation, zonal coefficients are defined as $\bar{J}_l = -\bar{C}_{l0}$. The gravity field is modeled in the lunar Principal Axis frame. Since we are assuming that the origin of the Moon's body-fixed frame is defined to be the Moon's center of mass, the degree-1 coefficients are identically zero. The unnormalized spherical harmonic coefficients, (C_{lm}, S_{lm}), are related to the normalized spherical harmonic coefficients as follows:

$$(\bar{C}_{lm}, \bar{S}_{lm}) = (C_{lm}, S_{lm})/N_{lm},$$

where the normalization factor N_{lm} is defined as:

$$N_{lm} = \sqrt{\frac{(l-m)!(2-\delta_{0m})(2l+1)}{(l+m)!}}. \tag{5.2}$$

The Moon's tidal gravity field is modeled as corrections to the spherical harmonic coefficients (Konopliv et al., 2013; Lemoine et al., 2013):

$$\Delta C_{lm} - i\Delta S_{lm} = \frac{k_{lm}}{2l+1} \sum_j \frac{GM_j}{GM} \frac{R^{l+1}}{r_j^{l+1}} P_{lm}(\sin\phi_j) e^{-im\lambda_j}, \tag{5.3}$$

where GM_j is the mass parameter of body j and (λ_j, ϕ_j, r_j) represents the longitude, latitude, and distance of the body j in the lunar body-fixed frame (Konopliv et al., 2013; Kaula, 1963). Equation 5.3 accounts for Earth-Moon tides, where $j = 1$ arises from both the Moon's orbital eccentricity and its fixed approximately 6.7° obliquity around the Earth as well as $j = 2$ for the Sun-Moon tides. The Sun-Moon tides generate forcing potentials that are approximately 5–10 times and 1000 times smaller than the Earth-Moon tides at $l = 2$ and $l = 3$, respectively, and act over a shorter period. Moreover, for a laterally heterogeneous Moon, combinations of Sun-Moon and Earth-Moon tides induce temporal changes in the k_{3m} based on Equation 5.3. However, these variations are 2–3 times smaller than the effective uncertainties in k_{3m} derived from gravity field inversions (Table 5.1) and are, therefore, disregarded in our analysis.

Inversion Procedure

To constrain the structure of the lunar interior using Love numbers, we carry out a Bayesian inversion using Markov Chain Monte Carlo (MCMC) with a Metropolis-Hastings sampling algorithm using PyMC. For our inversion, we vary elastic parameters relative to a reference Lunar interior to fit observed k_{2m} and k_{3m} Love numbers (Table 5.1; Patil et al., 2010). Our detailed procedure is described below.

Our reference model incorporates both 1D structure and lateral variations in crustal thickness (and density) *a priori*. We extract 1D (i.e., radial) elastic parameters and density for reference models from Weber et al., 2011 which constrains lunar structure using the satellite's mean density and seismic wave arrival times (see Table 5.2 for assumed mean shear modulus, bulk modulus, and density values for each internal layer). While moment of inertia (MOI) can be used to further refine the interior structure of reference models, this constraint primarily informs the size of the lunar core (at > 1400 km depth) and therefore has minimal impact on interpretations of k_{2m} or k_{3m} in this study (see Figure 5.2; Williams et al., 2014; Matsumoto et al.,

2015; Garcia et al., 2011; Matsuyama et al., 2016). Nominal viscosity for each layer is set to effectively infinite values (10^{30} Pa-s). To account for variations in crustal structure (Wieczorek et al., 2013), we vary spherical harmonic coefficients describing shear modulus, bulk modulus, and density for two adjacent internal layers (extending from 0-34 km and 34-62 km depth) following the method described in Qin et al., 2016 (see Figure 5.9 for assumed coefficient values).

We consider both 1D and 3D perturbations to the shear modulus and do not consider changes in density (i.e., which may violate constraints from static gravity measurements, see Figure 5.4 or Wieczorek et al., 2013) or bulk modulus (which have a negligible effect on k_{2m} or k_{3m}, see Qin et al., 2016). Since shear modulus (μ) is related to shear wave speed (V_s) and density (ρ) via $\mu = \rho V_s^2$, our approach effectively perturbs V_s while maintaining fixed ρ within each model layer. We consider a total of 34 parameters: 30 parameters describing 3D variations of shear modulus (μ'_{lm}) (i.e., l = 1–3 spherical harmonic coefficients for the crust and mantle) and 4 parameters describing 1D structure (μ'_{00}) (i.e., $l = 0$ coefficients for the crust, the 34-734 km region, the 734-1,257 km region, and the 1,257-1,407 km region). These model parameters are sampled as coefficients for spherical harmonic basis functions which comprise the base-10 logarithm (denoted by the symbol $'$) of the ratio of the spatially variable shear modulus μ to that of the reference model μ_{ref} for each internal layer.

$$\log_{10} \frac{\mu}{\mu_{\text{ref}}} = \sum_{l=0}^{3} \sum_{m=-l}^{l} \mu'_{lm} Y_{lm}(\theta, \lambda), \tag{5.4}$$

where μ'_{lm} are sampled coefficients and $Y_{lm}(\lambda, \theta)$ are real form, ortho-normalized spherical harmonic basis functions (λ is the longitude, and θ is the co-latitude in the center of mass reference frame):

$$Y_{lm}(\theta, \lambda) = \begin{cases} \sqrt{\frac{1}{2\pi}} N_{lm}\, \bar{P}_{lm}(\cos\theta) \cos(m\lambda), & \text{for } m > 0 \\ \sqrt{\frac{1}{4\pi}} N_{lm}\, \bar{P}_{lm}(\cos\theta), & \text{for } m = 0 \\ \sqrt{\frac{1}{2\pi}} N_{l|m|}\, \bar{P}_{lm}(\cos\theta) \sin(|m|\lambda), & \text{for } m < 0. \end{cases} \tag{5.5}$$

We expand shear modulus structures for accepted candidate models into spherical harmonics (in post-processing) to compute percentage perturbations μ_{lm} (i.e., values presented in Figure 5.3 and Table 5.3):

$$\frac{\mu}{\mu_{\text{ref}}} = 1 + 10^{-2} \sum_{l=0}^{3} \sum_{m=-l}^{l} \mu_{lm} Y_{lm}. \tag{5.6}$$

The Maxwell viscosity η of the 1,257-1,407 km depth layer is computed by assuming $l = 0$ perturbations to the shear modulus of this layer correspond to changes in this layer's effective shear modulus μ_{eff} (i.e., the amplitude of the complex shear modulus at the monthly timescale):

$$\eta = \frac{\mu_{\text{ref}}}{\omega \sqrt{\left(\frac{\mu_{\text{ref}}}{\mu_{\text{eff}}} - 1\right)}}, \tag{5.7}$$

where $\omega = 2.661{\times}10^{-6}\text{s}^{-1}$ is the angular frequency corresponding to the lunar sidereal monthly period and:

$$\mu_{\text{eff}} = \mu_{\text{ref}} \left(1 + 10^{-2}\sqrt{4\pi}\mu_{00}\right). \tag{5.8}$$

Coefficients for sampled $l = 1$ to $l = 3$ structure (i.e., μ'_{lm} in Equation 5.6) are assumed to have uniform (i.e., flat) prior probability distributions. Note that our method does not necessarily require the use of spherical harmonics as basis functions for calculations. For example, a 2-3% amplitude spherical cap (placed at the sub-Earth point) spanning the nearside hemisphere is sufficient to explain the observed 2-3% ($l = 1, m = 1$) variation in mantle shear modulus derived in this work. By contrast, we assume sampled μ'_{00} coefficients have Gaussian prior distributions with variances extracted from Weber et al., 2011. We separately sample μ'_{00} coefficients for regions between 34-734 km, 734-1,257 km, and 1,257-1,407 km depth (i.e., the lunar low velocity zone or LVZ) to account for differences in mean shear modulus uncertainty for these regions (the variance for μ'_{00} in the LVZ is set to infinity). Increasing the variances of the μ'_{00} coefficients tends to distribute reductions in the mean shear modulus (required to explain high degree-2 Love numbers; see Figure 5.1) to each layer, thereby increasing the inferred Maxwell viscosity of the LVZ from Equation 5.7. Moreover, changing the assumed model for viscoelasticity (e.g., from Maxwell to Kevin-Voigt) alters the inferred viscosity value(s) associated with a $\sim$ 97% reduction in the effective shear modulus of the LVZ at the sidereal monthly period (relative to the effective shear modulus at seismic timescales, see Table 5.3) by up to an order of magnitude. Note that all sampled coefficients μ'_{lm} (i.e., not just μ'_{00}) could, in principle, represent changes in effective shear modulus

μ_{eff} and (by extension) variations in internal viscosity. However, only significant lateral changes in viscosity in the LVZ (i.e., due to variations in temperature near the lunar mantle's solidus in this region) are likely to drive substantial variation in μ_{eff} as per Equation 5.7. This suggests that the inferred variations in mantle shear modulus may reflect a pronounced lateral viscosity variation within the LVZ. However, without additional constraints, it remains unclear to what extent inferred asymmetries localize to any region of the deep interior or are indicative of a broader (e.g., mantle-wide) anomaly (see main text discussion).

We generate an ensemble of internal structure models for Markov chains by sampling prior probability distributions for model parameters and forward computing Love numbers using these values. Each ensemble consists of ~1000 individual accepted model realizations (i.e., 50,000 samples total from 50 walkers). To speed up convergence, we consider only shear modulus perturbations and sample harmonic coefficients describing this structure up to $l = 3$ for inversions (see earlier discussion). We also adopt an adaptive sampling approach (the 'tune' functionality in PyMC) which dynamically adjusts step sizes based on the sensitivity of model outputs to input parameters (Patil et al., 2010). We visually inspect Markov chains to discard initial burn-in steps (i.e., typically the first ~ 10-20% of samples) and terminate inversions when parameter autocorrelations are > 0.99. Walker positions are updated based on a likelihood function that considers only degree-2 and degree-3 Love number values (Case 2 of Table 5.1):

$$\log L \propto -\frac{1}{2}(\mathbf{X} - \mathbf{Y})^T \mathbf{\Sigma}^{-1} (\mathbf{X} - \mathbf{Y}), \tag{5.9}$$

where $\mathbf{X}$ is the vector of observed Love numbers and $\mathbf{Y}$ is the vector of model-predicted Love numbers. $\mathbf{\Sigma}$ is a matrix that considers both observational and model covariances ($\mathbf{\Sigma} = \mathbf{\Sigma}_{obs} + \mathbf{\Sigma}_{mod}$). Both $\mathbf{\Sigma}_{obs}$ and $\mathbf{\Sigma}_{mod}$ are assumed to be diagonal (i.e., each Love number observation and model parameter is independent). Note that differences between observations and modeled Love numbers ($\mathbf{X} - \mathbf{Y}$) yield maximum L values of ~ 0.8 (out of a possible 1) across our ensemble of accepted models, supporting our interpretation that k_{3m} observations can be adequately explained by a nearside-farside asymmetry in the interior (see also Figure 5.8). Other system constraints (e.g., mean density, moment of inertia, or quality factors) are not incorporated into vectors $\mathbf{X}$ or $\mathbf{Y}$ in Equation 5.9.

Modelling Tidal Deformation

We compute lunar Love numbers using the semi-analytic spectral method LOV3D (Rovira-Navarro et al., 2024), which solves mass conservation, momentum, and Poisson's equations in the Fourier domain for a laterally heterogeneous body subject to tidal loading:

$$\rho' = -\rho_0(\nabla \cdot \mathbf{u}) - \mathbf{u} \cdot \nabla\rho_0 \tag{5.10}$$

$$\nabla \cdot \boldsymbol{\sigma}' - \rho_0\nabla(g\mathbf{u} \cdot \mathbf{e}_r) + g\rho_0(\nabla \cdot \mathbf{u})\mathbf{e}_r - \rho_0\nabla\varphi' = 0 \tag{5.11}$$

$$\nabla^2\varphi' = 4\pi G\rho', \tag{5.12}$$

where $\mathbf{u}$ is the displacement vector, $\boldsymbol{\sigma}'$ is the incremental material stress tensor, $\mathbf{e}_r$ is the radial unit vector, g the gravitational acceleration of the unperturbed body, ρ' is the incremental local density, G is the universal gravitational constant, ρ_0 is the density of the unperturbed body, and φ' is the gravitational potential arising from tides and mass movement driven by deformation. We use the constitutive equation for isotropic linear elasticity to relate $\boldsymbol{\sigma}'$ and $\mathbf{u}$:

$$\boldsymbol{\sigma}' = \left(\kappa - \frac{2}{3}\mu\right)(\nabla \cdot \mathbf{u})\mathbf{I} + \mu(\nabla\mathbf{u} \cdot \nabla\mathbf{u}^T), \tag{5.13}$$

where $\mathbf{I}$ is the identity matrix and μ and κ are the shear and bulk moduli. We find minimal differences (<0.01%) between results produced by our methodology and numerical (i.e., finite-element) solutions for displacement on a laterally heterogeneous Moon subject to tidal loading. Moreover, our results for perturbations to the lunar gravity field for lunar interiors with $l = 1, m = 1$ shear modulus structure are broadly consistent with results presented in Fig. 1 of Zhong et al., 2012.

We discount the influence of polar motion—the movement of a planetary body's rotational axis relative to its surface—on calculations of degree-2 and degree-3 Love numbers. This simplification is based on our expectation that the body tides considered in our work induce only minimal changes to the Moon's moment of inertia tensor over the GRAIL observation period. To verify this assumption, we computed the amplitude of polar motion resulting from a static degree-2, order-1 bulge of 1 cm height. The resulting value, approximately 10^{-3} degrees, is orders of magnitude smaller than the Moon's $\sim 6.7°$ obliquity (i.e., which is the dominant driver of degree-2, order-1 forcing for the Moon). Nonetheless, we expect that polar motion may substantially influence longer-term response to surface loading (e.g., see Figs. 3a and 3b in Zhong et al., 2022).

LOV3D explicitly computes coefficients $K^{l,m}_{l',m'}$, or 'Extended Love numbers' (distinct from the 'traditional' Love numbers k_{lm} described in Equation 5.3). $K^{l,m}_{l',m'}$ represents coupling between forcing at one harmonic (at l', m') and gravitational response to this forcing at another harmonic (at l, m) for a given interior structure. For a laterally heterogeneous body, Equation 5.3 can be derived considering a general expression for perturbations to gravity field coefficients ΔC_{lm} and ΔS_{lm} in terms of real-form $K^{l,m}_{l',m'}$:

$$\begin{aligned}\Delta C_{lm} - i\Delta S_{lm} = \sum_{l'=2}^{3}\sum_{m'=0}^{l}\frac{1}{2l'+1}\sum_{j}\frac{GM_j}{GM}\frac{R^{l'+1}}{r_j^{l'+1}}P_{l'm'}(\sin\phi_j) \\ \times\Big[\Big(K^{l,m}_{l',m'}\cos(m'\lambda_j) + K^{l,m}_{l',-m'}\sin(m'\lambda_j)\Big) \\ - i\Big(K^{l,-m}_{l',m'}\cos(m'\lambda_j) + K^{l,-m}_{l',-m'}\sin(m'\lambda_j)\Big)\Big]. \qquad (5.14)\end{aligned}$$

In this work, we make the following simplifications:

1. Gravity field inversions assume that perturbations ΔC_{30}, ΔC_{31}, ΔC_{32}, ΔC_{33}, ΔS_{31}, ΔS_{32}, ΔS_{33} are not impacted by coupling that is temporally out of phase with forcing at these harmonics. We correspondingly set $K^{l,m}_{l',-m'}$, $K^{l,-m}_{l',m'}$, and $K^{3,1}_{2,1}$, $K^{3,3}_{2,1}$, $K^{3,2}_{2,0}$, $K^{3,2}_{2,2}$, $K^{3,2}_{2,-2}$, $K^{3,-3}_{2,-1}$, $K^{3,-3}_{2,-1}$ to zero *a priori*.
2. To improve computational efficiency, we assume $K^{l,m}_{l',m'} = K^{l,-m}_{l',-m'}$. However, we note that limited MCMC results (approximately 5000 accepted candidate models) indicate that separate computations of Love numbers that assume $K^{l,-m}_{l',-m'} \neq K^{l,m}_{l',m'}$ does not substantially (<1%) alter results presented in Figs. 2-4, Figure 5.9b, and Figure 5.10.

Based on these assumptions, we can rewrite Equation 5.14:

$$\Delta C_{lm} - i\Delta S_{lm} = \sum_{l'=2}^{3}\sum_{m'=0}^{l}\frac{K^{l,m}_{l',m'}}{2l'+1}\sum_{j}\frac{GM_j}{GM}\frac{R^{l'+1}}{r_j^{l'+1}}P_{l',m'}(\sin\phi_j)e^{-im\lambda_j}. \qquad (5.15)$$

Note that we can compute individual components of the tidal forcing potential $V_{l'm'}$ from Equation 5.15:

$$V_{l',m'} = \frac{1}{2l'+1}\sum_{j}\frac{GM_j}{GM}\frac{R^{l'+1}}{r_j^{l'+1}}P_{l',m'}(\sin\phi_j)e^{-im\lambda_j}. \qquad (5.16)$$

Comparing Equations 5.16, 5.15, and 5.3, it becomes apparent that traditional Love numbers k_{lm} represent the ratio of tidal (i.e., forcing) potentials at (l', m') and response at (l, m) (i.e., $V_{l'm'}$ and V_{lm} from Equation 5.16) scaled by $K^{l,m}_{l',m'}$:

$$k_{lm} = \sum_{l'=2}^{3} \sum_{m'=0}^{l} K^{lm}_{l',m'} \frac{V_{l',m'}}{V_{lm}}. \tag{5.17}$$

In the case of a spherically symmetric Moon, Extended Love numbers simplify to k_{lm} when $l = l'$ and $m = m'$ (e.g., $K^{30}_{30} = K^{31}_{31} = K^{32}_{32} = K^{33}_{33} = k_3$ and $K^{20}_{20} = K^{21}_{21} = K^{22}_{22} = k_2$). However, for lunar interiors with degree-1 order-1 shear modulus variations, additional coupling terms become significant such that $k_{31} \approx K^{31}_{31} + K^{31}_{20}V_{20}/V_{31} + K^{31}_{22}V_{22}/V_{31}$ and $k_{33} \approx K^{33}_{33} + K^{33}_{22}V_{22}/V_{33}$ (see Eqn. 5.17; Zhong et al., 2012). Note that Zhong et al., 2012 approximates $V_{3m}/V_{2m} = 1/220$. Using our exact numerical approach to compute tidal potentials (Eqn. 5.16), we find V_{3m}/V_{2m} ranges from approximately $1/200 - 1/300$.

Using our MCMC method, we additionally examine whether an unconstrained spherically symmetric lunar interior (i.e., with all 1-σ bounds on mean shear modulus values for internal layers in Table 5.2 set to infinity) could theoretically explain observed Love number values. We find that these inversions require a 70–100% reduction in mean μ_{eff} within the uppermost 100–200 km of the Moon relative to values presented in Table 5.2 to explain k_{3m} and k_{2m} in Table 5.1 (the required perturbations are shallow because k_{3m} are more sensitive to such perturbations than k_{2m}). Such reductions suggest an unrealistically weak upper mantle or crust (e.g., viscosities in Equation 5.7 ranging from 10^9–10^{16} Pa·s, which falls at least five orders of magnitude below expected values for this region).

Modelling Temperature Change

Our inference of a 100–200 K temperature difference (Figure 5.4) relies on linear relationships between temperature, shear modulus, density, and composition ($\beta, \Delta\mu/\Delta T, \Delta\rho/\Delta Fo\text{-}Fa, \Delta\mu/\Delta Fo\text{-}Fa$) based on experimental studies of olivine. However, the lunar mantle likely contains at least approximately 5% pyroxene (Treiman and Semprich, 2023) which may very slightly alter $\beta, \Delta\mu/\Delta T, \Delta\rho/\Delta Fo\text{-}Fa$, and $\Delta\mu/\Delta Fo\text{-}Fa$ (Reynard et al., 2010). Phase changes could also cause deviations from this linear behavior described by $\beta, \Delta\mu/\Delta T, \Delta\rho/\Delta Fo\text{-}Fa$, and $\Delta\mu/\Delta Fo\text{-}Fa$; though such variations are likely confined to the low-velocity zone (LVZ). Minor phases (e.g., ilmenite) may also be present in low concentrations throughout

the lunar mantle (Wieczorek et al., 2006) but likely have a negligible effect on results presented in Figure 5.4.

5.7 Acknowledgements

A portion of this research was carried out at the Jet Propulsion Laboratory, California Institute of Technology, under a contract with the National Aeronautics and Space Administration (80NM0018D0004). A.B. and M.S. were partially supported by the Future Investigators in NASA Earth and Space Science and Technology (FINESST) Program (80NSSC22K1318). M.R.N. and I.M. were partially supported by the National Aeronautics and Space Administration under grant No. 80NSSC20K0570 issued through the NASA Solar System Workings program. We gratefully acknowledge the use of the Ames Pleiades Supercomputer that was used to generate the GL1800F gravity solutions of this paper. The authors would like to thank Prof. Shijie Zhong and an anonymous referee for providing very helpful review comments and suggestions that improved the overall content of this study.

References

Andrews-Hanna, J. C., J. Besserer, J. W. Head, C. J. Howett, W. S. Kiefer, P. J. Lucey, P. J. McGovern, H. J. Melosh, G. A. Neumann, R. J. Phillips, P. M. Schenk, D. E. Smith, S. C. Solomon, and M. T. Zuber (2014). "Structure and evolution of the lunar Procellarum region as revealed by GRAIL gravity data". In: *Nature* 514 (7520). ISSN: 14764687. DOI: 10.1038/nature13697.

Barker, M. K., E. Mazarico, G. A. Neumann, M. T. Zuber, J. Haruyama, and D. E. Smith (2016). "A new lunar digital elevation model from the Lunar Orbiter Laser Altimeter and SELENE Terrain Camera". In: *Icarus* 273. ISSN: 10902643. DOI: 10.1016/j.icarus.2015.07.039.

Berne, A., M. Simons, J. T. Keane, E. J. Leonard, and R. S. Park (May 2024). "Jet activity on Enceladus linked to tidally driven strike-slip motion along tiger stripes". In: *Nature Geoscience* 17 (5), pp. 385–391. ISSN: 17520908. DOI: 10.1038/s41561-024-01418-0.

Briaud, A., C. Ganino, A. Fienga, A. Mémin, and N. Rambaux (2023). "The lunar solid inner core and the mantle overturn". In: *Nature* 617 (7962). ISSN: 14764687. DOI: 10.1038/s41586-023-05935-7.

Chung (1970). "Effects of iron/magnesium ratio on P- and S- wave velocities in olivine". In: *J Geophys Res* 75 (35). DOI: 10.1029/jb075i035p07353.

Dahlen, F. A. and J. Tromp (1998). *Theoretical global seismology*. DOI: 10.1063/1.882788.

Frohlich, C. and Y. Nakamura (2009). "The physical mechanisms of deep moonquakes and intermediate-depth earthquakes: How similar and how different?" In: *Physics of the Earth and Planetary Interiors* 173 (3-4). ISSN: 00319201. DOI: 10.1016/j.pepi.2009.02.004.

Garcia, R. F., J. Gagnepain-Beyneix, S. Chevrot, and P. Lognonné (2011). "Very preliminary reference Moon model". In: *Physics of the Earth and Planetary Interiors* 188 (1-2). ISSN: 00319201. DOI: 10.1016/j.pepi.2011.06.015.

Heiskanen, W. A. and H. Moritz (1967). "Physical geodesy". In: *Bulletin Géodésique* 41 (4). ISSN: 00074632. DOI: 10.1007/BF02525647.

Isaak, D. G. (1992). "High-temperature elasticity of iron-bearing olivines". In: *Journal of Geophysical Research* 97 (B2). ISSN: 01480227. DOI: 10.1029/91JB02675.

Jacobsen, S. D., F. Jiang, Z. Mao, T. S. Duffy, J. R. Smyth, C. M. Holl, and D. J. Frost (2008). "Effects of hydration on the elastic properties of olivine". In: *Geophysical Research Letters* 35 (14). ISSN: 00948276. DOI: 10.1029/2008GL034398.

Jolliff, B. L., J. J. Gillis, L. A. Haskin, R. L. Korotev, and M. A. Wieczorek (2000). "Major lunar crustal terranes: Surface expressions and crust-mantle origins". In: *Journal of Geophysical Research: Planets* 105 (E2). ISSN: 01480227. DOI: 10.1029/1999JE001103.

Kaula, W. M. (1963). *Determination of the Earth's gravitational field*. DOI: 10.1029/RG001i004p00507.

Konopliv, A. S., R. S. Park, D. N. Yuan, S. W. Asmar, M. M. Watkins, J. G. Williams, E. Fahnestock, G. Kruizinga, M. Paik, D. Strekalov, N. Harvey, D. E. Smith, and M. T. Zuber (2013). "The JPL lunar gravity field to spherical harmonic degree 660 from the GRAIL Primary Mission". In: *Journal of Geophysical Research: Planets* 118 (7). ISSN: 21699100. DOI: 10.1002/jgre.20097.

Konopliv, A. S., R. S. Park, D. N. Yuan, S. W. Asmar, M. M. Watkins, J. G. Williams, E. Fahnestock, G. Kruizinga, M. Paik, D. Strekalov, N. Harvey, D. E. Smith, and M. T. Zuber (2014). "High-resolution lunar gravity fields from the GRAIL Primary and Extended Missions". In: *Geophysical Research Letters* 41 (5). ISSN: 19448007. DOI: 10.1002/2013GL059066.

Landerer, F. W., F. M. Flechtner, H. Save, F. H. Webb, T. Bandikova, W. I. Bertiger, S. V. Bettadpur, S. H. Byun, C. Dahle, H. Dobslaw, E. Fahnestock, N. Harvey, Z. Kang, G. L. Kruizinga, B. D. Loomis, C. McCullough, M. Murböck, P. Nagel, M. Paik, N. Pie, S. Poole, D. Strekalov, M. E. Tamisiea, F. Wang, M. M. Watkins, H. Y. Wen, D. N. Wiese, and D. N. Yuan (2020). "Extending the Global Mass Change Data Record: GRACE Follow-On Instrument and Science Data Performance". In: *Geophysical Research Letters* 47 (12). ISSN: 19448007. DOI: 10.1029/2020GL088306.

Laneuville, M., M. A. Wieczorek, D. Breuer, and N. Tosi (2013). "Asymmetric thermal evolution of the Moon". In: *Journal of Geophysical Research: Planets* 118 (7). ISSN: 21699100. DOI: 10.1002/jgre.20103.

Lau, H. C., J. X. Mitrovica, J. L. Davis, J. Tromp, H. Y. Yang, and D. Al-Attar (2017). "Tidal tomography constrains Earth's deep-mantle buoyancy". In: *Nature* 551 (7680). ISSN: 14764687. DOI: 10.1038/nature24452.

Lemoine, F. G., S. Goossens, T. J. Sabaka, J. B. Nicholas, E. Mazarico, D. D. Rowlands, B. D. Loomis, D. S. Chinn, D. S. Caprette, G. A. Neumann, D. E. Smith, and M. T. Zuber (2013). "High-degree gravity models from GRAIL primary mission data". In: *Journal of Geophysical Research: Planets* 118 (8). ISSN: 21699100. DOI: 10.1002/jgre.20118.

Lemoine, F. G., S. Goossens, T. J. Sabaka, J. B. Nicholas, E. Mazarico, D. D. Rowlands, B. D. Loomis, D. S. Chinn, G. A. Neumann, D. E. Smith, and M. T. Zuber (2014). "GRGM900C: A degree 900 lunar gravity model from GRAIL primary and extended mission data". In: *Geophysical Research Letters* 41 (10). ISSN: 19448007. DOI: 10.1002/2014GL060027.

Long, T., Y. Qian, M. D. Norman, K. Miljkovic, C. Crow, J. W. Head, X. Che, R. Tartèse, N. Zellner, X. Yu, S. Xie, M. Whitehouse, K. H. Joy, C. R. Neal, J. F. Snape, G. Zhou, S. Liu, C. Yang, Z. Yang, C. Wang, L. Xiao, D. Liu, and A. Nemchin (2022). "Constraining the formation and transport of lunar impact glasses using the ages and chemical compositions of Chang'e-5 glass beads". In: *Science Advances* 8 (39). ISSN: 23752548. DOI: 10.1126/sciadv.abq2542.

Love, A. E. H. (1909). "The yielding of the earth to disturbing forces". In: *Proceedings of the Royal Society of London. Series A, Containing Papers of a Mathematical and Physical Character* 82 (551). ISSN: 0950-1207. DOI: 10.1098/rspa.1909.0008.

Matsumoto, K., R. Yamada, F. Kikuchi, S. Kamata, Y. Ishihara, T. Iwata, H. Hanada, and S. Sasaki (2015). "Internal structure of the Moon inferred from Apollo seismic data and selenodetic data from GRAIL and LLR". In: *Geophysical Research Letters* 42 (18). ISSN: 19448007. DOI: 10.1002/2015GL065335.

Matsuyama, I., F. Nimmo, J. T. Keane, N. H. Chan, G. J. Taylor, M. A. Wieczorek, W. S. Kiefer, and J. G. Williams (2016). "GRAIL, LLR, and LOLA constraints on the interior structure of the Moon". In: *Geophysical Research Letters* 43 (16). ISSN: 19448007. DOI: 10.1002/2016GL069952.

Neumann, G. A., M. T. Zuber, D. E. Smith, and F. G. Lemoine (1996). "The lunar crust: global structure and signature of major basins". In: *Journal of Geophysical Research* 101 E7. ISSN: 01480227. DOI: 10.1029/96je01246.

Palguta, J., J. D. Anderson, G. Schubert, and W. B. Moore (2006). "Mass anomalies on Ganymede". In: *Icarus* 180 (2). ISSN: 00191035. DOI: 10.1016/j.icarus.2005.08.020.

Panning, M. P., S. Kedar, N. Bowles, D. Bugby, S. Calcutt, J. Cutler, J. Elliott, R. F. Garcia, T. Kawamura, P. Lognonné, E. Miller, C. Nunn, W. T. Pike, G. Pont, S. D. Raucourt, I. Standley, W. Walsh, R. Weber, and C. Yana (2022). "Farside Seismic Suite (FSS): Surviving the Lunar Night and Delivering the First Seismic Data from the Farside of the Moon". In: *53rd Lunar and Planetary Science Conference (LSPC); 7-11 March 2022; The Woodlands, TX*.

Park, R. S., A. Berne, A. S. Konopliv, J. T. Keane, I. Matsuyama, F. Nimmo, M. Rovira-Navarro, M. P. Panning, M. Simons, D. J. Stevenson, and R. C. Weber (2025). "Thermal Asymmetry in the Moon's Mantle Inferred from Monthly Tidal Response". In: *Nature* 641.8065.
The material presented in this chapter represents portions of the above paper that were contributed by A.B..

Park, R. S., W. M. Folkner, J. G. Williams, and D. H. Boggs (2021). "The JPL Planetary and Lunar Ephemerides DE440 and DE441". In: *The Astronomical Journal* 161 (3). ISSN: 0004-6256. DOI: 10.3847/1538-3881/abd414.

Park, R. S., J. E. Riedel, A. I. Ermakov, J. Roa, J. Castillo-Rogez, A. G. Davies, A. S. McEwen, and M. M. Watkins (2020). "Advanced Pointing Imaging Camera (APIC) for planetary science and mission opportunities". In: *Planetary and Space Science* 194. ISSN: 00320633. DOI: 10.1016/j.pss.2020.105095.

Patil, A., D. Huard, and C. J. Fonnesbeck (2010). "PyMC: Bayesian Stochastic modelling in Python". In: *Journal of Statistical Software* 35 (4). ISSN: 15487660. DOI: 10.18637/jss.v035.i04.

Qin, C., A. C. Muirhead, and S. Zhong (2012). "Correlation of deep moonquakes and mare basalts: Implications for lunar mantle structure and evolution". In: *Icarus* 220 (1). ISSN: 00191035. DOI: 10.1016/j.icarus.2012.04.023.

Qin, C., S. Zhong, and J. Wahr (2016). "Elastic tidal response of a laterally heterogeneous planet: A complete perturbation formulation". In: *Geophysical Journal International* 207 (1). ISSN: 1365246X. DOI: 10.1093/gji/ggw257.

Reynard, B., J. D. Bass, and J. Brenizer (2010). "High-temperature elastic softening of orthopyroxene and seismic properties of the lithospheric upper mantle". In: *Geophysical Journal International* 181 (1). ISSN: 1365246X. DOI: 10.1111/j.1365-246X.2010.04524.x.

Rovira-Navarro, M., I. Matsuyama, and A. Berne (May 2024). "A Spectral Method to Compute the Tides of Laterally Heterogeneous Bodies". In: *Planetary Science Journal* 5 (5). ISSN: 26323338. DOI: 10.3847/PSJ/ad381f.

Rummel, R., W. Yi, and C. Stummer (2011). "GOCE gravitational gradiometry". In: *Journal of Geodesy* 85 (11). ISSN: 09497714. DOI: 10.1007/s00190-011-0500-0.

Rushmer, T. (1995). "An experimental deformation study of partially molten amphibolite: application to low-melt fraction segregation". In: *Journal of Geophysical Research* 100 (B8). ISSN: 01480227. DOI: 10.1029/95jb00077.

Suzuki, I. (1975). "Thermal expansion of periclase and olivine, and their anharmonic properties". In: *Journal of Physics of the Earth* 23 (2). ISSN: 00223743. DOI: 10.4294/jpe1952.23.145.

Takei, Y. (2017). "Effects of Partial Melting on Seismic Velocity and Attenuation: A New Insight from Experiments". In: *Annual Review of Earth and Planetary Sciences* 45. ISSN: 00846597. DOI: 10.1146/annurev-earth-063016-015820.

Taylor, S. R., G. J. Taylor, and L. A. Taylor (2006). "The Moon: A Taylor perspective". In: *Geochimica et Cosmochimica Acta* 70 (24). ISSN: 00167037. DOI: 10.1016/j.gca.2006.06.262.

Treiman, A. H. and J. Semprich (2023). "A dunite fragment in meteorite Northwest Africa (NWA) 11421: A piece of the Moon's mantle". In: *American Mineralogist* 108 (12). ISSN: 19453027. DOI: 10.2138/am-2022-8911.

Weber, R. C., C. Neal, B. Banerdt, C. Beghein, P. Chi, D. Currie, S. Dell'Agnello, R. Garcia, I. Garrick-Bethell, R. Grimm, M. Grott, H. Haviland, T. Kawamura, S. Kedar, P. Lognonné, S. Nagihara, Y. Nakamura, C. Nunn, L. Ostrach, M. Panning, N. Petro, N. Schmerr, M. Siegler, T. Watters, M. Wieczorek, and K. Zacny (2020). "The lunar geophysical network mission". In: *SEG Technical Program Expanded Abstracts*. Vol. 2020-October. DOI: 10.1190/segam2020-3416702.1.

Weber, R. C., P. Y. Lin, E. J. Garnero, Q. Williams, and P. Lognonné (2011). "Seismic detection of the lunar core". In: *Science* 331 (6015). ISSN: 00368075. DOI: 10.1126/science.1199375.

Wieczorek, M. A., B. L. Jolliff, A. Khan, M. E. Pritchard, B. P. Weiss, J. G. Williams, L. L. Hood, K. Righter, C. R. Neal, C. K. Shearer, I. S. McCallum, S. Tompkins, B. R. Hawke, C. Peterson, J. J. Gillis, and B. Bussey (2006). *The constitution and structure of the Lunar interior*. DOI: 10.2138/rmg.2006.60.3.

Wieczorek, M. A., G. A. Neumann, F. Nimmo, W. S. Kiefer, G. J. Taylor, H. J. Melosh, R. J. Phillips, S. C. Solomon, J. C. Andrews-Hanna, S. W. Asmar, A. S. Konopliv, F. G. Lemoine, D. E. Smith, M. M. Watkins, J. G. Williams, and M. T. Zuber (2013). "The crust of the moon as seen by GRAIL". In: *Science* 339 (6120). ISSN: 10959203. DOI: 10.1126/science.1231530.

Wilding, J. D., W. Zhu, Z. E. Ross, and J. M. Jackson (2023). "The magmatic web beneath Hawai'i". In: *Science* 379 (6631). ISSN: 10959203. DOI: 10.1126/science.ade5755.

Williams, J. G., A. S. Konopliv, D. H. Boggs, R. S. Park, D. N. Yuan, F. G. Lemoine, S. Goossens, E. Mazarico, F. Nimmo, R. C. Weber, S. W. Asmar, H. J. Melosh, G. A. Neumann, R. J. Phillips, D. E. Smith, S. C. Solomon, M. M. Watkins, M. A. Wieczorek, J. C. Andrews-Hanna, J. W. Head, W. S. Kiefer, I. Matsuyama, P. J. McGovern, G. J. Taylor, and M. T. Zuber (2014). "Lunar interior properties from the GRAIL mission". In: *Journal of Geophysical Research: Planets* 119 (7). ISSN: 21699100. DOI: 10.1002/2013JE004559.

Zhang, J., J. W. Head, J. Liu, and R. W. Potter (2023). "Lunar Procellarum KREEP Terrane (PKT) Stratigraphy and Structure with Depth: Evidence for Significantly Decreased Th Concentrations and Thermal Evolution Consequences". In: *Remote Sensing* 15 (7). ISSN: 20724292. DOI: 10.3390/rs15071861.

Zhong, S., K. Kang, A. Geruo, and C. Qin (2022). "CitcomSVE: A Three-Dimensional Finite Element Software Package for Modeling Planetary Mantle's Viscoelastic Deformation in Response to Surface and Tidal Loads". In: *Geochemistry, Geophysics, Geosystems* 23 (10). ISSN: 15252027. DOI: 10.1029/2022GC010359.

Zhong, S., E. M. Parmentier, and M. T. Zuber (2000). "A dynamic origin for the global asymmetry of lunar mare basalts". In: *Earth and Planetary Science Letters* 177 (3-4). ISSN: 0012821X. DOI: 10.1016/S0012-821X(00)00041-8.

Zhong, S., C. Qin, G. Geruo, and J. Wahr (2012). "Can tidal tomography be used to unravel the long-wavelength structure of the lunar interior?" In: *Geophysical Research Letters* 39 (15). ISSN: 00948276. DOI: 10.1029/2012GL052362.

Zhong, S. and M. T. Zuber (2001). "Degree-1 mantle convection and the crustal dichotomy on Mars". In: *Earth and Planetary Science Letters* 189 (1-2). ISSN: 0012821X. DOI: 10.1016/S0012-821X(01)00345-4.

Zuber, M. T., D. E. Smith, M. M. Watkins, S. W. Asmar, A. S. Konopliv, F. G. Lemoine, H. J. Melosh, G. A. Neumann, R. J. Phillips, S. C. Solomon, M. A. Wieczorek, J. G. Williams, S. J. Goossens, G. Kruizinga, E. Mazarico, R. S. Park, and D. N. Yuan (2013). "Gravity field of the moon from the Gravity Recovery and Interior Laboratory (GRAIL) mission". In: *Science* 339 (6120). ISSN: 10959203. DOI: 10.1126/science.1231507.

5.8 Supplementary Information

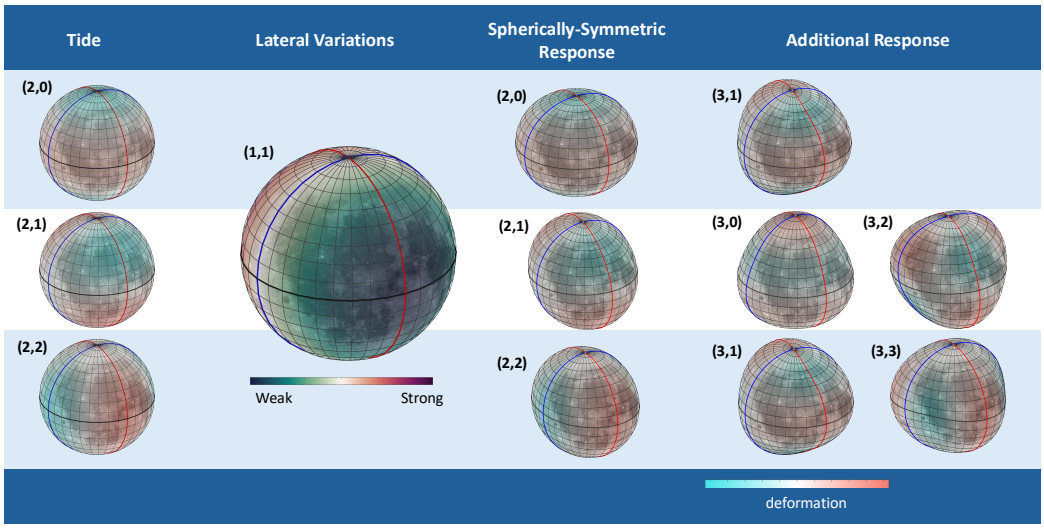

Figure 5.7: Conceptual relationship between lunar 3D structure and response to tidal forcing. The left column shows the spatial pattern of gravitational potentials associated with eccentricity tides at degree-2, order-0,2 (i.e., (2,0) and (2,2)) and obliquity tides degree-2, order-1 (2,1) acting on the Moon. The second column shows the spatial pattern of a degree-1, order-1 (i.e., (1,1) or nearside farside) lateral heterogeneity in shear modulus imposed onto the lunar interior. The third column shows response at (2,0), (2,1), and (2,2) expected for a spherically symmetric interior (i.e., also the main components of the response for a laterally heterogeneous interior). The fourth and fifth columns show additional modes of deformation at degree-3 (i.e., (3,0), (3,1), (3,2), and (3,3)) expected for the laterally heterogeneous interior shown in the second column. Rows in the third, fourth, and fifth columns correspond to response associated with forcing in the same row in column 1. For example, (2,1) forcing stimulates response at (3,0) and (3,2), (2,0) forcing stimulates response at (3,1), and (2,2) forcing stimulates response at (3,1) and (3,3).

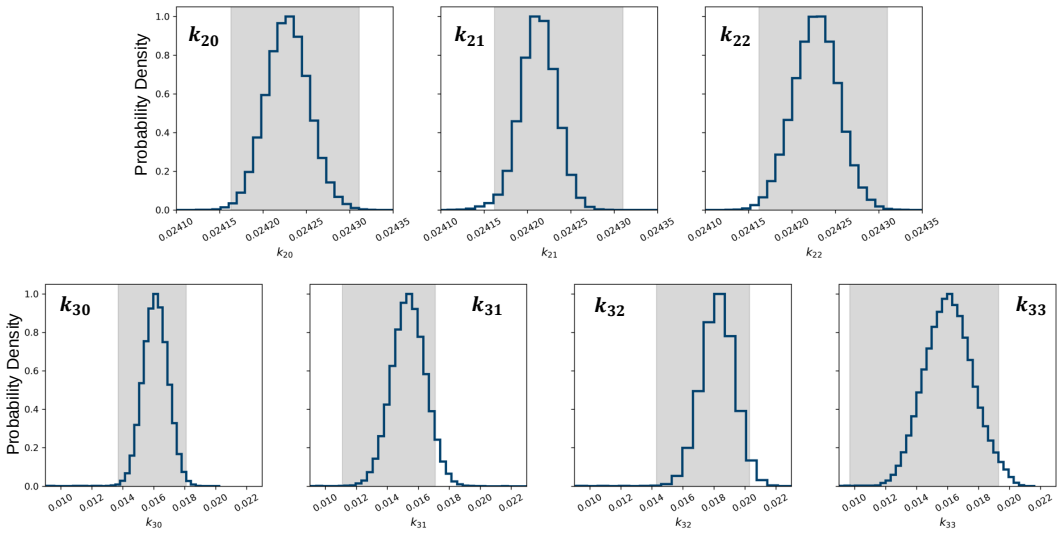

Figure 5.8: Distributions of modeled Love numbers k_{2m} and k_{3m} corresponding to the ensemble of accepted candidate models. Grey boxes represent observational constraints, where the box width is 15 times the formal uncertainty for each value as presented in Table 5.1.

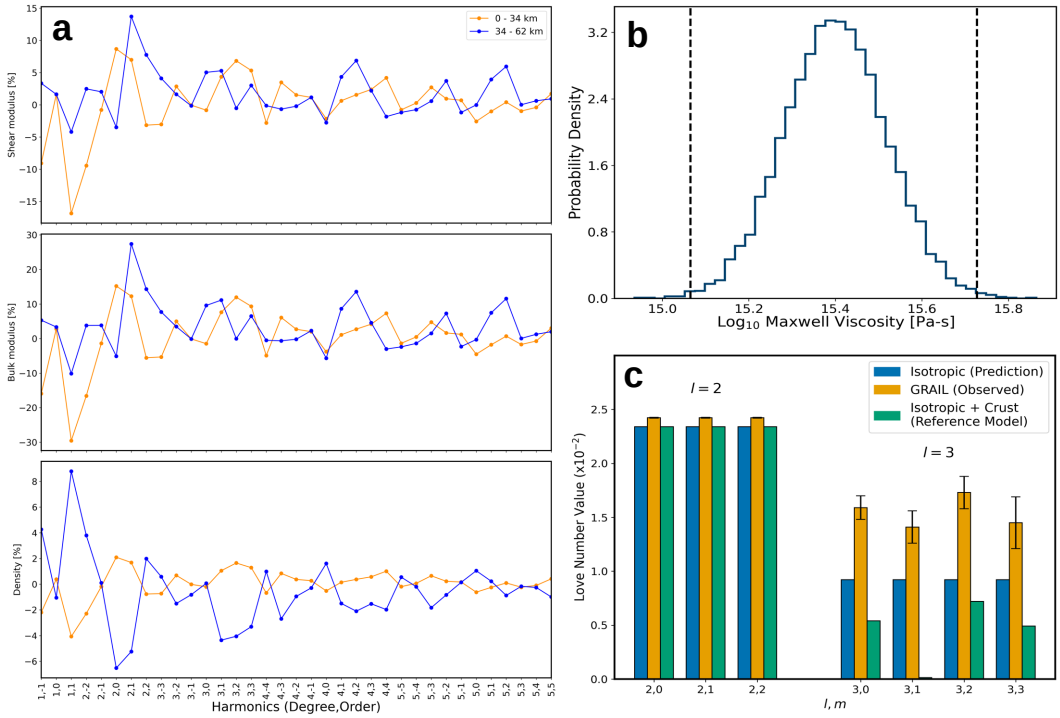

Figure 5.9: **(a)** Lateral variations in crustal structure assumed for reference models. Line plots with scatter points show shear modulus (top), bulk modulus (middle), and density (bottom) perturbations (parameterized as spherical harmonic coefficients up to degree-5, normalized as a percentage of the mean value (see Equation 5.6)) for two vertical regions of the lunar interior spanning 0-34 km (orange line) and 34-62 km (blue line). Coefficient values are derived by linearly mapping lateral variations in crustal properties from Wieczorek et al., 2013 to variations in bulk/shear moduli and density (see Eqn. 75 of Qin et al., 2016). Note that density variations reflect both observed variations in the density of the crust (Wieczorek et al., 2013) and effective density variations due to lateral variability in the depth of the Moho whereas bulk/shear moduli variations only reflect variations in Moho depth. **(b)** Inferred Maxwell viscosity for 1,257-1,407 km depth. Histogram shows Maxwell viscosity values corresponding to the inverted reduction in the degree-0 shear modulus value of the region spanning 1,257-1,407 km depth (Table 5.3 and Equation 5.8). Dashed lines show 0.003, and 0.997 quantiles (i.e., 3-σ confidence bounds). **(c)** Similar to Figure 5.2 except including models with crustal thickness and density variations. Note that the green bar above the $l = 3$, $m = 1$ harmonic is very close to zero.

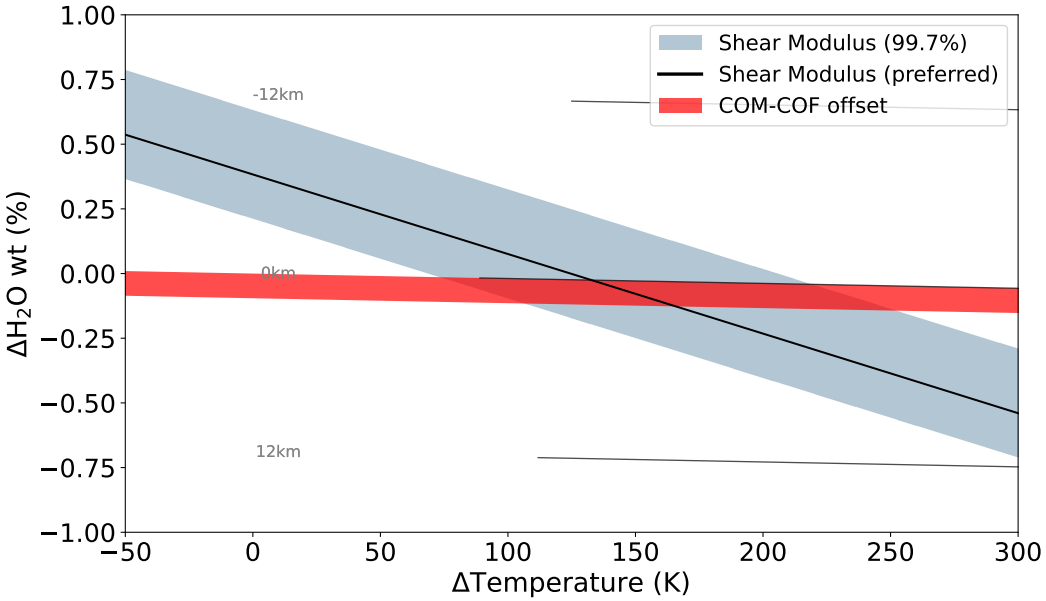

Figure 5.10: Similar to Figure 5.4 except considering the impact of water content (as a weight percentage) on the shear modulus and density of lunar mantle olivine and assuming $\beta = 3 \times 10^{-5}$ K^{-1}, $\Delta\mu/\Delta T = -1.35 \times 10^{-2}$ GPa/K, $\Delta\rho/\Delta H_2O = -50.56$ kg/%$-$m^3, and $\Delta\mu/\Delta H_2O = -6.63$ GPa/% in the nearside mantle (Jacobsen et al., 2008). While our analysis suggests a limited water mass fraction difference of approximately 0.1% between the nearside and farside, superimposed compositional variations, such as iron and ilmenite content (Qin et al., 2012), could influence the overall density structure and may reconcile a water-enriched nearside mantle with the small observed COM-COF offset.

Radius (km)	Density (kg/m^3)	Bulk Modulus (GPa)	Shear Modulus (GPa)
0-240	8000	91.5	42.3
240-330	5100	85.7	0
330-480	3400	144.8	34.8
480-999.1	3400	153.8	68.8 ± 3.06
999.1-1,249.1	3400	108.6	65.8 ± 2.09
1,249.1-1,499.1	3400	120.3	64.9 ± 2.08
1,499.1-1,675.1	3220	106.3	63.5 ± 1.13
1,675.1-1,703.1	3220	106.3	63.5 ± 1.13
1,703.1-1,738	2800	46.5	28.7 ± 1.79

Table 5.2: Radial (1D) elastic structure (density, bulk modulus, and shear modulus) assumed for reference models. Data extracted from Weber et al., 2011. Bounds for regions at radii >480 km denote 1-σ uncertainties from Weber et al., 2011.

Parameters	Median	0.3 Percentile	99.7 Percentile
$\sqrt{4\pi}\mu_{00}^{C}$, 0 - 34 km	0.065653	-3.6205	4.0836
μ_{11}^{C}	-1.4229	-44.0530	29.1940
μ_{10}^{C}	-0.3063	-26.0100	34.4690
μ_{1-1}^{C}	0.9097	-37.9210	41.4050
μ_{2-2}^{C}	-0.0271	-40.7510	52.7740
μ_{2-1}^{C}	-1.2886	-33.3990	36.0380
μ_{20}^{C}	0.5234	-27.5670	31.0460
μ_{21}^{C}	-0.6511	-27.0570	36.5800
μ_{22}^{C}	2.1510	-31.1770	39.4600
μ_{3-3}^{C}	-0.5627	-45.1440	25.3410
μ_{3-2}^{C}	2.1697	-34.2600	45.9770
μ_{3-1}^{C}	5.1384	-37.5470	44.7200
μ_{30}^{C}	2.7226	-34.0430	41.5320
μ_{31}^{C}	-1.3253	-42.1530	23.8930
μ_{32}^{C}	0.2102	-31.7710	34.2010
μ_{33}^{C}	1.5966	-33.2250	38.9190
$\sqrt{4\pi}\mu_{00}^{M}$, 34 - 734 km	0.62337	-1.6036	4.5446
$\sqrt{4\pi}\mu_{00}^{M}$, 734 - 1,257 km	0.94006	-2.6956	3.5210
$\sqrt{4\pi}\mu_{00}^{M}$, 1,257 - 1,407 km	-96.560	-99.803	-73.100
μ_{11}^{M}	2.7403	1.6198	4.0439
μ_{10}^{M}	-0.10086	-1.2421	0.82273
μ_{1-1}^{M}	0.44328	-5.1940	4.5035
μ_{2-2}^{M}	0.009699	-3.4384	4.3829
μ_{2-1}^{M}	-0.02862	-3.7696	5.6615
μ_{20}^{M}	0.059821	-4.7254	3.1454
μ_{21}^{M}	0.020556	-3.9083	2.1802
μ_{22}^{M}	-0.34836	-2.7808	3.2809
μ_{3-3}^{M}	-0.09964	-4.1147	5.2624
μ_{3-2}^{M}	-0.05283	-3.3548	6.1057
μ_{3-1}^{M}	0.050182	-5.1317	6.9248
μ_{30}^{M}	0.089398	-3.7133	4.5336
μ_{31}^{M}	0.23411	-4.9441	4.5442
μ_{32}^{M}	0.12678	-1.9470	2.7009
μ_{33}^{M}	0.032167	-4.8334	8.7238

Table 5.3: Inverted median, standard deviation, 0.3%, and 99.7% of coefficient values describing 3D structure in the lunar crust (superscript C, see Equation 5.7) and the lunar mantle (superscript M). The $\sqrt{4\pi}$ factor is included to account for ortho-normalization of the degree-0 harmonic.

References

Jacobsen, S. D., F. Jiang, Z. Mao, T. S. Duffy, J. R. Smyth, C. M. Holl, and D. J. Frost (2008). "Effects of hydration on the elastic properties of olivine". In: *Geophysical Research Letters* 35 (14). ISSN: 00948276. DOI: 10.1029/2008GL034398.

Qin, C., A. C. Muirhead, and S. Zhong (2012). "Correlation of deep moonquakes and mare basalts: Implications for lunar mantle structure and evolution". In: *Icarus* 220 (1). ISSN: 00191035. DOI: 10.1016/j.icarus.2012.04.023.

Qin, C., S. Zhong, and J. Wahr (2016). "Elastic tidal response of a laterally heterogeneous planet: A complete perturbation formulation". In: *Geophysical Journal International* 207 (1). ISSN: 1365246X. DOI: 10.1093/gji/ggw257.

Weber, R. C., P. Y. Lin, E. J. Garnero, Q. Williams, and P. Lognonné (2011). "Seismic detection of the lunar core". In: *Science* 331 (6015). ISSN: 00368075. DOI: 10.1126/science.1199375.

Wieczorek, M. A., G. A. Neumann, F. Nimmo, W. S. Kiefer, G. J. Taylor, H. J. Melosh, R. J. Phillips, S. C. Solomon, J. C. Andrews-Hanna, S. W. Asmar, A. S. Konopliv, F. G. Lemoine, D. E. Smith, M. M. Watkins, J. G. Williams, and M. T. Zuber (2013). "The crust of the moon as seen by GRAIL". In: *Science* 339 (6120). ISSN: 10959203. DOI: 10.1126/science.1231530.

Chapter 6

CONCLUSION

6.1 Summary

This thesis explored the impact of structural heterogeneity on the dynamics of planetary bodies across a wide range of spatial and temporal scales. In Chapter 2, we presented a 3D finite element model of the crust of Enceladus to predict the low-order response of the body to eccentricity tides. In Chapters 3 and 4, we extended this numerical model to explore the viability of characterizing short-wavelength structure as well as the geodynamics of Enceladus' Tiger Stripe faults. Finally, in Chapter 5 we described a real-world application of tidal tomography to characterize a long-lived thermal asymmetry in the lunar mantle.

6.2 Enceladus

Enceladus is a high-priority target for future missions to the outer solar system due to the potential for habitable conditions within the satellite's subsurface ocean. Enceladus' habitability is not static but varies over time, encompassing both short-term (instantaneous) and long-term (sustained) components (Cockell et al., 2024). Instantaneous habitability depends on the ocean's chemical composition, particularly the availability of key bioessential elements such as Carbon, Hydrogen, Nitrogen, Oxygen, Phosphorus, and Sulfur (CHNOPS; Postberg et al., 2018). In contrast, sustained habitability is governed by the stability of the ocean layer and the cycling of material between the surface and the deep interior, processes that are essential for maintaining potential metabolic activity over geologic timescales (Bagheri et al., 2024; Simons et al., 2024).

Crustal thickness places key constraints on the sustained habitability of Enceladus' ocean. For example, whereas Enceladus' mean crustal thickness is sensitive to the satellite's overall tidal dissipation (Ojakangas and Stevenson, 1989), the presence of variations in crustal thickness indicates long-term energy exchange and localized melting at the ocean-crust boundary (Čadek et al., 2019). We demonstrate that a combination of very low-order measurements of Enceladus' time-variable gravity field (Chapter 2) and finer-scale observations of periodic surface motion (Chapter 3) enable determinations of crustal thickness. If the core of Enceladus is hydrostatic, then combinations of surface strain observations and additional measurements of

the $l \geq 2$ static gravity signal (i.e., the extent of isostatic compensation of thickness variations) may bound the density (and by extension, the composition and temperature) of Enceladus' ocean (Vance et al., 2021; Meyer et al., 2025; Vance et al., 2024; Vance et al., 2023). Modern gravimetry (Park et al., 2025) may also be sufficiently precise to measure the temporal phase lag in Enceladus' degree-2 response relative to forcing (i.e., the imaginary component of k_{2m} or $\Im(k_{2m})$; Ermakov et al., 2021; Rovira-Navarro et al., 2023). An $\Im(k_{2m})$ that is comparable to the real component $\Re(k_{2m})$ would require significant viscous dissipation within Enceladus' ice shell or core and suggest that the satellite's subsurface ocean persists over ~Myr timescales (Nimmo et al., 2023).

In contrast, the dynamics of the Tiger Stripes inform Enceladus' instantaneous habitability. In Chapter 4, we propose that strike-slip motion generates localized extension along rifts (e.g., pull-aparts) to influence jet activity. This localized extension can be reconciled with controlled boiling of a water-vacuum interface within fractures. Under this scenario, diurnal wall motion within the Tiger Stripes alters the height the water-vacuum interface to vary jet activity through Enceladus' tidal cycle (Nakajima and Ingersoll, 2016). Crucially, controlled boiling would chemically fractionate Enceladus' jet material as it ascends through the ice shell (Fifer et al., 2022). As such, integrating tectonic and jet models will be essential for accurately characterizing Enceladus' astrobiological potential through future *in situ* analysis of plume samples (Spitale et al., 2025; Nelson et al., 2024a; Nelson et al., 2024b; Berne et al., 2022).

Detailed descriptions Enceladus' sustained or instantaneous habitability will likely require a dedicated future mission to the satellite (Bagheri et al., 2025; Berne et al., 2021). Throughout this thesis, we highlight the potential of incorporating interferometric radar (InSAR) measurements into such a mission. InSAR has proven highly effective at providing high-resolution observations of seismic and post-seismic deformation on Earth and should therefore be well-suited for measuring the approximately 50–100 cm of diurnal crustal displacement expected across Enceladus' surface (Simons and Rosen, 2015; Benedikter et al., 2022; Simons et al., 2023). The more localized 10–20 cm deformation along the Tiger Stripes should also be readily observable via InSAR, though optimizing viewing geometries will be crucial in order to enhance sensitivity to the predominantly horizontal displacement produced by these fractures (see Figure 2.13) (Tam et al., 2023; Keane et al., 2022; Berne et al., 2023).

6.3 The Moon

We propose a relationship between a present-day thermal anomaly in the lunar mantle and crustal nearside-farside heterogeneities (Chapter 5). However, a radially uniform temperature anomaly distributed throughout the lunar mantle is almost certainly an oversimplification of the true nature internal asymmetries. Theoretical thermo-chemical evolution models of the lunar interior (e.g., Laneuville et al., 2013; Zhong et al., 2000) suggest that elevated temperatures and partial melt are primarily concentrated in the upper nearside mantle due to this region's affinity to radiogenic material in the nearside crust. Additionally, detected asymmetries may reflect a slight depletion ($< 0.1\%$) of water in the nearside mantle, as predicted by some evolution models (Qin et al., 2012). Future reconciliation of our results (i.e., the detection of an overall 2–3% asymmetry in structure) with viable evolution models may correspondingly refine estimates of trace incompatible element and volatile abundances in the deep lunar interior.

The Moon represents a unique case among extraterrestrial planetary bodies for which future gravity field observations are unlikely to yield substantial new insight into deep interior processes. For example, while reducing uncertainties for degree-3 gravity Love numbers could reveal additional very small-amplitude variations in internal structure (e.g., north-south, east-west asymmetries in shear modulus), this inference would require gravity field observations with a precision better than that achieved by the GRAIL spacecraft (Zuber et al., 2013). In contrast, even limited future seismological data could offer much more detailed descriptions of the Moon's deep 3D structure. NASA's upcoming farside seismic suite (scheduled for 2027) and the Chinese Space Agency's planned seismometer deployment at the lunar South Pole (targeted for 2028) could each determine whether deep moonquakes exist in the farside mantle. Coordinating these seismological observations may also shed light on whether the depth of deep moonquakes varies with longitude, and, by extension, whether degree-1 asymmetries influence lunar seismicity.

6.4 Closing Thoughts

Planetary bodies are complicated, and the work presented in this thesis is a starting point for future investigations to characterize this complexity from observations of tidal deformation. Arguably, the first application of tidal tomography occurred at Caltech in 2011 to constrain the structure of the asthenosphere using the Earth's response to ocean tidal loads (Ito and Simons, 2011). Subsequent work at Harvard University in 2017 determined the buoyancy of compositional anomalies at the base

of the Earth's mantle using k_2 (Lau et al., 2017). Since 2016, continued efforts at Caltech and the University of Montana have identified spatially correlated residuals between predictions for periodic displacement associated with ocean tidal loading and GPS observations in South America, suggesting the presence of regional-scale 3D structure in the lithosphere (e.g., a subducting slab below the western edge of the continent; Martens et al., 2016; Martens et al., 2024; Martens et al., 2025).

If the Earth serves as a representative example of solar system objects, then clearly much remains to be learned from future geodetic observations elsewhere. In fact, Earth is likely an outlier among rocky bodies due to its relatively high gravity and warm interior, which should erase heterogeneities over time. In contrast, smaller bodies like Ceres ($g \approx \frac{1}{40} g_{Earth}$), Enceladus ($g \approx \frac{1}{100} g_{Earth}$), and Mimas ($g \approx \frac{1}{200} g_{Earth}$) are more likely to retain substantial internal variations in structure. Although this complexity likely poses challenges for future studies of these bodies, I expect it also presents new opportunities for understanding their formation, evolution, and dynamics.

References

Bagheri, A., M. Simons, R. S. Park, A. Berne, S. D. Vance, and M. M. Daswani (2025). *Geodetic Exploration of the Interior Structure of Enceladus*. arXiv preprint arXiv:2505.14743.

Bagheri, A., M. Simons, S. Vance, R. S. Park, A. Berne, and M. M. Daswani (2024). "Determining the Optimal Measurements Required to Infer the Geophysical Characteristics of Enceladus". In: *AGU Fall Meeting Abstracts*. Vol. 2024. 3069, P23A–3069.

Benedikter, A., K. Wickhusen, H. Hussmann, A. Stark, F. Damme, M. Rodriguez-Cassola, and G. Krieger (2022). "Periodic orbits for interferometric and tomographic radar imaging of Saturn's moon Enceladus". In: *Acta Astronautica* 191. ISSN: 00945765. DOI: 10.1016/j.actaastro.2021.10.041.

Berne, A., N. Chung, J. M. Stock, and F. M. Schwandner (Dec. 2022). "An Inverse Approach to UAV-Based Ground Gas Flux Monitoring at Volcanic Systems". In: *AGU Fall Meeting Abstracts*. Vol. 2022, NS24A–06.

Berne, A., M. Simons, J. T. Keane, and R. S. Park (2021). "Modelling Tidally-Driven Crustal Dynamics of Enceladus". In: *AGU Fall Meeting 2021*. AGU.

Berne, A., M. Simons, J. T. Keane, and R. S. Park (2023). "Using Tidally Driven Elastic Strains to Infer Regional Crustal Thickness and Ocean Salinity at Enceladus". In: *54th Lunar and Planetary Science Conference*. Vol. 2806, p. 1899.

Čadek, O., O. Souček, M. Běhounková, G. Choblet, G. Tobie, and J. Hron (2019). "Long-term stability of Enceladus' uneven ice shell". In: *Icarus* 319. ISSN: 10902643. DOI: 10.1016/j.icarus.2018.10.003.

Cockell, C. S., M. Simons, J. Castillo-Rogez, P. M. Higgins, L. Kaltenegger, J. T. Keane, E. J. Leonard, K. L. Mitchell, R. S. Park, S. M. Perl, and S. D. Vance (2024). "Sustained and comparative habitability beyond Earth". In: *Nature Astronomy* 8 (1). ISSN: 23973366. DOI: 10.1038/s41550-023-02158-8.

Ermakov, A. I., R. S. Park, J. Roa, J. C. Castillo-Rogez, J. T. Keane, F. Nimmo, E. S. Kite, C. Sotin, T. J. W. Lazio, G. Steinbrügge, S. M. Howell, B. G. Bills, D. J. Hemingway, V. Viswanathan, G. Tobie, and V. Lainey (2021). "A Recipe for the Geophysical Exploration of Enceladus". In: *Planetary Science Journal* 2 (4). ISSN: 26323338. DOI: 10.3847/PSJ/ac06d2.

Fifer, L., D. Catling, and J. Toner (2022). "Chemical Fractionation Modeling of Plumes Indicates a Gas-rich, Moderately Alkaline Enceladus Ocean". In: *The Planetary Science Journal* 3 (191). ISSN: DOI: 10.3847/PSJ/ac7a9f.

Ito, T. and M. Simons (2011). "Probing asthenospheric density, temperature, and elastic moduli below the western United States". In: *Science* 332 (6032). ISSN: 00368075. DOI: 10.1126/science.1202584.

Keane, J. T., M. M. Sori, A. I. Ermakov, A. Austin, J. Bapst, A. Berne, C. J. Bierson, et al. (2022). "Next-Generation Planetary Geodesy: Results from the 2021 Keck Institute for Space Studies Workshops". In: *53rd Lunar and Planetary Science Conference*. Vol. 2678, p. 1622.

Laneuville, M., M. A. Wieczorek, D. Breuer, and N. Tosi (2013). "Asymmetric thermal evolution of the Moon". In: *Journal of Geophysical Research: Planets* 118 (7). ISSN: 21699100. DOI: 10.1002/jgre.20103.

Lau, H. C., J. X. Mitrovica, J. L. Davis, J. Tromp, H. Y. Yang, and D. Al-Attar (2017). "Tidal tomography constrains Earth's deep-mantle buoyancy". In: *Nature* 551 (7680). ISSN: 14764687. DOI: 10.1038/nature24452.

Martens, H. R., M. Simons, S. Owen, and L. Rivera (2016). "Observations of ocean tidal load response in South America from subdaily GPS positions". In: *Geophysical Journal International* 205 (3). ISSN: 1365246X. DOI: 10.1093/gji/ggw087.

Martens, H. R., M. Simons, E. Serviss, L. A. Rivera, A. Moore, C. Boehm, A. Dmitrovskii, et al. (2024). "Insights into Solid-Earth Structure from GNSS Geodesy and Ocean Tidal Loading". In: *AGU Fall Meeting Abstracts*. Vol. 2024, G12A–04.

Martens, H. R., Z. M. Young, D. F. Argus, M. J. Swarr, W. P. Gardner, N. Lau, A. A. Borsa, Z. Hoylman, Q. Cao, A. M. Wilson, M. Pan, E. Knappe, F. M. Ralph, S. Puel, A. Berne, M. Simons, and Y. Fu (Mar. 2025). "Geodetic Insights into Water Resources and Drought Dynamics in the Western United States". In: *EGU General Assembly 2025*. Abstract EGU25-13419. Copernicus Meetings.

Meyer, C. R., A. G. Stubblefield, B. M. Minchew, S. S. Pegler, A. Berne, J. J. Buffo, and T. C. Tomlinson (2025). *Implications of Shallow-Shell Models for Topographic Relaxation on Icy Satellites*. arXiv preprint arXiv:2504.20095.

Nakajima, M. and Ingersoll (2016). "Controlled boiling on Enceladus. 1. Model of the vapor-driven jets". In: *Icarus* 272. ISSN: 10902643. DOI: 10.1016/j.icarus.2016.02.027.

Nelson, K. M., C. Jiménez, C. D. Deering, M. J. de Moor, J. M. Blackstock, S. P. Broccardo, F. M. Schwandner, et al. (2024a). "Total CO_2 Budget Estimate and Degassing Dynamics for an Active Stratovolcano: Turrialba Volcano, Costa Rica". In: *Journal of Volcanology and Geothermal Research* 450, p. 108075.

Nelson, K. M., C. Jiménez, C. D. Deering, M. J. de Moor, J. M. Blackstock, S. P. Broccardo, F. M. Schwandner, et al. (2024b). "Total CO_2 Budget Estimate and Degassing Dynamics for an Active Stratovolcano: Turrialba Volcano, Costa Rica". In: *Journal of Volcanology and Geothermal Research* 450, p. 108075.

Nimmo, F., M. Neveu, and C. Howett (2023). *Origin and Evolution of Enceladus's Tidal Dissipation*. DOI: 10.1007/s11214-023-01007-4.

Ojakangas, G. W. and D. J. Stevenson (1989). "Thermal state of an ice shell on Europa". In: *Icarus* 81 (2). ISSN: 10902643. DOI: 10.1016/0019-1035(89)90052-3.

Park, R. S., J. E. Riedel, E. J. Brandon, N. E. Harvey, S. Manafi, M. C. Smart, Z. J. Towfic, et al. (2025). "Gravity Imaging Radio Observer (GIRO) for Planetary Science and Mission Opportunities". In: *The Planetary Science Journal* 6.5, p. 127.

Postberg, F., R. Clark, C. Hansen, A. Coates, C. D. Ore, F. Scipioni, M. Hedman, and J. Waite (2018). *Plume and Surface Composition of Enceladus*. University of Arizona Press. DOI: 10.2458/azu_uapress_9780816537075-ch007.

Qin, C., A. C. Muirhead, and S. Zhong (2012). "Correlation of deep moonquakes and mare basalts: Implications for lunar mantle structure and evolution". In: *Icarus* 220 (1). ISSN: 00191035. DOI: 10.1016/j.icarus.2012.04.023.

Rovira-Navarro, M., I. Matsuyama, and A. Berne (Dec. 2023). "Revealing Lateral Structures in the Interiors of Planets and Moons from Tidal Observations". In: *AGU Fall Meeting Abstracts*. Vol. 2023. 3166, P33C–3166.

Simons, M. and P. A. Rosen (2015). "Interferometric Synthetic Aperture Radar Geodesy". In: *Treatise on Geophysics: Second Edition*. Vol. 3. DOI: 10.1016/B978-0-444-53802-4.00061-0.

Simons, M., B. Anderson, A. Benedikter, S. Bhaskaran, A. Berne, S. Horst, K. Hurst, D. Jones, J. Keane, G. Krieger, and E. Leonard (Oct. 2023). "Crustal Deformation Derived from Repeat-Pass Interferometric SAR at Enceladus–Why and How?" In: *AAS/Division for Planetary Sciences Meeting Abstracts #55*. Vol. 55. 8, pp. 210–07.

Simons, M., A. Berne, A. Bagheri, S. Puel, and R. S. Park (2024). "Does Enceladus Have a Global Ocean?" In: *AGU Fall Meeting Abstracts*. Vol. 2024. 307, P23A–307.

Spitale, J. N., M. D. Tigges, A. Berne, A. Rhoden, T. A. Hurford, and K. D. Webster (2025). "Curtain-Based Maps of Eruptive Activity in Enceladus's South-Polar Terrain at 15 Cassini Epochs". In: *The Planetary Science Journal* 6.3, p. 67.

Tam, R., A. Berne, T. Köhne, and M. Simons (Dec. 2023). "Inferring Crustal Thickness for Enceladus from Tidal Strain Fields Through Multi-Scale Inversion". In: *AGU Fall Meeting Abstracts*. Vol. 2023. 3323, P43E–3323.

Vance, S., M. Behounkova, B. G. Bills, P. Byrne, O. Cadek, J. Castillo-Rogez, G. Choblet, K. Hughson, T. Hurford, S. Kedar, J. Keane, E. Kite, A. H. Lobo, A. G. Marusiak, M. M. Daswani, M. P. Panning, R. S. Park, B. E. Schmidt, K. Sladkova, K. M. Soderlund, C. Sotin, O. Soucek, S. Stähler, G. Steinbrügge, S. Tharimena, A. Thompson, G. Tobie, W. Song, and S. Wang (2021). "Distributed Geophysical Exploration of Enceladus and Other Ocean Worlds". In: *Bulletin of the AAS* 53 (4). DOI: 10.3847/25c2cfeb.a07234f4.

Vance, S., A. Berne, J. C. Castillo-Rogez, J. T. Keane, E. J. Leonard, K. L. Mitchell, R. S. Park, M. Simons, and A. Bagheri (2024). "Assessing the Habitability of Enceladus with a Suite of Geophysical Investigations". In: *2024 Astrobiology Science Conference*. AGU.

Vance, S., J. Castillo-Rogez, A. Berne, A. Hendrix, J. Keane, E. Leonard, K. Mitchell, F. Nimmo, R. Park, and M. Simons (2023). "Does Enceladus Have an Active Core with Hydrothermal Circulation?" In: *AAS/Division for Planetary Sciences Meeting Abstracts #55*. Vol. 55. 8, pp. 509–08.

Zhong, S., E. M. Parmentier, and M. T. Zuber (2000). "A dynamic origin for the global asymmetry of lunar mare basalts". In: *Earth and Planetary Science Letters* 177 (3-4). ISSN: 0012821X. DOI: 10.1016/S0012-821X(00)00041-8.

Zuber, M. T., D. E. Smith, M. M. Watkins, S. W. Asmar, A. S. Konopliv, F. G. Lemoine, H. J. Melosh, G. A. Neumann, R. J. Phillips, S. C. Solomon, M. A. Wieczorek, J. G. Williams, S. J. Goossens, G. Kruizinga, E. Mazarico, R. S. Park, and D. N. Yuan (2013). "Gravity field of the moon from the Gravity Recovery and Interior Laboratory (GRAIL) mission". In: *Science* 339 (6120). ISSN: 10959203. DOI: 10.1126/science.1231507.